Universität Hamburg
DER FORSCHUNG | DER LEHRE | DER BILDUNG

Crown Ether-Polymers for Lithium Recovery: From Molecular Binding to Solid-State Architecture

Dissertation

submitted by

Sabrina Jaehnke

Hamburg 2025

Faculty of Mathematics, Informatics, and Natural Science

Department of Chemistry

In conformity with requirements for

the degree of *Doctor rerum naturalium* (Dr. rer. nat.)

submitted to the University of Hamburg

“*Wenn wir uns erlauben, zu scheitern, erlauben wir uns gleichzeitig, uns selbst zu übertreffen.”*

Eloise Ristad

Supervisor: Prof. Dr. Volker Abetz

1st Referee: Prof. Dr. Volker Abetz

2nd Referee: Dr. Werner Pauer

Defense committee:

Prof. Dr. Volker Abetz

Priv. Doz. Dr. Christoph Wutz

Dr. Thomas Hackl

Date of oral defense: 23.01.2026

This dissertation was created under the supervision of Prof. Dr. Volker Abetz at the Institute of Physical Chemistry (Department of Chemistry, Faculty of Mathematics, Informatics, and Natural Sciences) of the University of Hamburg. The work was started in September 2021 and the dissertation was submitted in November 2025.

PUBLICATIONS

This cumulative dissertation includes three first-author publications. These publications are reprinted in the original form in Chapter 5.

1) Lithium Selectivity of Crown Ethers: The Effect of Heteroatoms and Cavity Size
   Iklima Oral*, Sabrina Tamm*[i], Carmen Herrmann, Volker Abetz
   *: Both authors contributed equally to this project.
   Separation and Purification Technology **2022**, *294*, 121142.
   doi.org/10.1016/j.seppur.2022.121142
   Impact Factor (2022): 8.6

2) Systematic Investigation of a Crown Ether Functionalized PS-*b*-PMAA Block Copolymer for Optimized Lithium Extraction from Aqueous Media
   Sabrina Jaehnke, Joachim von Chamier Gliszczynski, Birgit Hankiewicz, Volker Abetz
   Journal of Polymer Science **2025**; n/a.
   doi.org/10.1002/pol.20250060
   Impact Factor (2024): 3.6

3) Electrospun, Crown Ether Functionalized PS-*b*-PMAA Block Copolymer Fibers for Li Extraction from Aqueous Media
   Sabrina Jaehnke, Volker Abetz
   Desalination **2025**, 616, 119343.
   doi.org/10.1016/j.desal.2025.119343
   Impact Factor (2024): 9.8

[i]To avoid any misunderstanding, it should be mentioned that the author's surname changed from Tamm to Jaehnke during the course of this work.

CONTENTS

Publications 4
Contents 6
Abbreviations 8
Constants and Variables 12
1. Zusammenfassung 16
2. Abstract 18
3. Introduction 20
3.1. Lithium – Value, Demand and Recovery 21
3.1.1. Lithium in Applications 21
3.1.2. Lithium Ion Batteries 23
3.1.3. Natural Occurrence and Extraction 24
3.1.4. Sustainable Recovery Methods 28
3.2. Crown ethers 29
3.3. Computational Methods in Quantum Chemistry 41
3.4. Polymers 52
3.4.1. Polymer Architectures and Block Copolymers 52
3.4.2. (Controlled) Radical Polymerization 54
3.4.3. RAFT Polymerization 56
3.4.4. CE-Polymer Linkage 59
3.5. Polymer Manufacturing and Self-Assembly 63
3.5.1. Thermodynamics of Block Copolymers 63
3.5.2. Microphase Separation of Block Copolymers 65
3.5.3. Membranes 67
3.5.4. Cubosomes 69
3.5.5. Electrospinning 70
4. Objectives of this Work 73
5. Cumulative Part 75
5.1. Publication 1 75
5.2. Publication 2 87
5.3. Publication 3 99
6. Unpublished Results 106
6.1. Membrane Preparation 106
6.1.1. PS-*b*-PMAA Membrane 106
6.1.2. B9C3-Membrane 108
6.1.3. Additives for Membrane Formation 109

6.1.4. B12C4-Membrane 111
6.1.5. Experimental Section 112
6.2. Cubosome Preparation 113
6.2.1. B9C3 Cubosomes 113
6.2.2. Experimental Section 116
7. Discussion 117
7.1. Computational Modeling of CEs 117
7.2. CE-Polymers in Solution 118
7.3. CE-Polymers in Solid-State 119
7.4. Outlook 120
8. References 123
9. Appendix 134
9.1. Author contributions 134
9.2. Supporting information for Publication 1 135
9.3. Supporting information for Publication 2 153
9.4. Supporting information for Publication 3 179
9.5. Safety 193
10. Danksagung 197
11. Eidesstattliche Versicherung 199

ABBREVIATIONS

The abbreviations used in this work are defined in alphabetical order in the following.

12C4	12-crown-4
14C4	14-crown-4
15C5	15-crown-5
18C6	18-crown-6
6FDA	Difunctional phthalic anhydride
9C3	9-crown-3
AAS	Atom absorption spectrometer
AB15C5	*Aza*-benzo-15-crown-5
ac	After extraction
ACN	Acetonitrile
AcOH	Acetic acid
ACVA	4,4'-Azobis(4-cyanopentanoic acid)
AIBN	Azobis(isobutyronitrile)
ATRP	Atom-transfer radical polymerization
B12C4	Benzo-12-crown-4
B3LYP	Becke 3-parameter hybrid functional using Lee–Yang–Parr correlation
B9C3	Benzo-9-crown-3
bc	Before extraction
bcc	Body-centered cubic
BCEEM	2-(benzo-12-crown-4-ether)ethyl meth acrylamide
BEV	Battery electric vehicle
C	Cylindrical
CaF	Fuchsin calcium salt
CDI	Capacitive deionization
CE	Crown Ether
CE3MA	Benzo-9-crown-3 functionalized methacrylic acid
CN	Coordination number
CPCM	Conductor like PCM
CTA	Chain transfer agent
CTPPA	4-Cyano-4-thioylthiopropylsulfanyl pentanoic acid
CUI	Cluster of excellence
Cyclam	Tetra*aza*-14-crown-4
D	Double diamond
DCM	Dichloromethane

def2-TZVP	Second-generation, triple-zeta valence basis set with polarization functions
DFG	Deutsche Forschungsgemeinschaft
DFT	Density functional theory
DIAD	Diisopropyl azodicarboxylate
DLS	Dynamic light scattering
DMF	Dimethylformamide
DOSY	Diffusion ordered spectroscopy
DOX	1,4-Dioxane
DP	Degree of polymerization
EHT	Acceleration voltage
EISA	Evaporation induced self-assembly
EM	Electron microscopy
fcc	Face-centered cubic
G	Double-gyroid
GBL	*γ*-Butyrolactone
GGA	Generalized gradient approximation
GTO	Gaussian-type orbital
$HClO_4$	Perchloric acid
H-GGA	Hybrid generalized gradient approximation
HNO_3	Nitric acid
HSAB	Hard and Soft Acids and Bases
IPCM	Integral Equation Formalism
IR	Infrared
ISR	Intermediate segregation regime
IUPAC	International union of pure and applied chemistry
KEE	Potassium ethyl eosin
KS	Kohn-Sham
L	Lamellar
LAM	Less-activated monomer
LDA	Local Density Approximation
Li_2CO_3	Lithium carbonate
$LiAlSi_2O_6$	Spodumene
LIB	Lithium ion battery
$LiCoO_2$	Lithium cobalt oxide
$LiNiMnCoO_2$	Lithium nickel manganese cobalt oxide
LiOH	Lithium hydroxide
LIS	Lithium 3,5-diiodo-salicylic acid

LLE	Liquid-liquid extraction
LMO	Lithium manganese oxide ($LiMn_2O_4$)
LMTO	Lithium manganese titanium oxide
LP	Lone pair
LTO	Lithium titanium oxide ($Li_4Ti_5O_{12}$)
M_2L	Dinuclear complex
M_2L_3	Club sandwich complex
mag	Magnification
MAM	More-activated monomer
MeOH	Methanol
MgA	8-Anilino-1-naphthalene sulfonic acid hemimagnesium salt
ML	Metal-ligand complex
ML_2	Sandwich complex
MOF	Metal-organic framework
MW	Molecular Weight
n.d.	Not defined
NaEE	Sodium ethyl eosin
$NaHCO_3$	Sodium bicarbonate
NAO	Natural atomic orbital
NASICON	Sodium super ionic conductor
NBO	Natural bond orbital
NEt_3	Triethylamine
NHO	Natural hybrid orbital
NiPAAm	*N*-isopropylacrylamide
NLMO	Natural (semi-)localized molecular orbital
NMP	Nitroxide-mediated radical polymerization
NMR	Nuclear magnetic resonance
NOESY	Nuclear Overhauser effect spectroscopy
ODT	Order-disorder transition
P4VP	Poly-4-vinylpyridine
PAA	Polyacrylic acid
PCM	Polarizable continuum models
PDI	Polydispersity index
PES	Potential energy surface
PGMA	Poly(glycidyl methacrylate)
PI-RAFT	Photoiniferter reversible-addition-fragmentation chain-transfer radical
PISA	Polymerization induced self-assembly

PL	Perforated lamellae
PMAA	Poly(methacrylic acid)
PS	Poly styrene
PSF	Polysulfone
PTFE	Polytetrafluoroethylene
r.t.	Room temperature
RAFT	Reversible-addition-fragmentation chain-transfer radical
S	Spherical
SAS	Solvent accessible surface
SCF	Self-consistent field
SCFT	Self-consistent field theory
SDEMS	Solution diffusion evaporation mediation
SE	Schrödinger equation
SEC	Size exclusion chromatography
S-ED	Selective electrodialysis
SEM	Scanning electron microscopy
SES	Solvent excluded surface
SI	Supporting information
SLE	Solid-liquid extraction
SNIPS	Self-assembly and nonsolvent-induced phase separation
SSL	Strong segregation limit
TEM	Transmission electron microscopy
TFA	Trifluoroacetic acid
THF	Tetrahydrofuran
TPP	Triphenylphosphine
UV	Ultraviolet
Vis	Visible
WSL	Weak segregation limit
λ-MnO_2	Manganese(IV) oxide

CONSTANTS AND VARIABLES

The constants and variables mentioned in this work are defined alphabetically in the following.

A	Absorbance
Å	Ångstrom
[A]	Concentration of the monomer A
$a_{\pm}$	Activity coefficient
a_0	Headgroup area
b_X	Occupancy of the donor orbital
[B]	Concentration of the monomer B
c	Concentration
c_A	Polarization effect of atom A
c_B	Polarization effects of atom B
cm	centimeter
d	Path length
$Đ$	Dispersity
d_{CE}	Cavity size
$d_{X\text{-}M}^{n+}$	Distance between the heteroatom and the metal ion
E	Energy
e	Electron (charge)
$E[\varrho]$	Density functional
E_C	Correlation energy
E_{el}	Electronic energy
E_J	Electron-electron (Coulomb) interaction energy
E_T	Kinetic energy of the electrons
E_{tot}	Total energy of the system
E_V	Interaction energy of the electrons with the nuclear field
E_X	Electron-electron exchange energy
$E_{xc}[\varrho]$	Exchange-correlation functional
$\hat{F}$	Fock operator
f_i	Volume fraction of the component i
g	gram
h	Planck constant
$\hbar$	Reduced Planck constant (h/2π)
$\hat{H}$	Hamiltonian
h_A	Natural hybrid orbital of atom A
h_B	Natural hybrid orbital of atom B

$\hat{H}_{el}$	Electronic Hamiltonian
hv	Energy of a photon
Hz	hertz
i	Metal ion's stochiometric factor
I	Nucleus
i	Electron
I·	Initiator radical
I_0	Initial light intensity
I_1	Intensity of the transmitted light
I_s	Ionic strength
$J[\varrho]$	Coulomb fractions of the electron interactions
K	Equilibrium constant (or complexation constant)
K	Nuclei
k_{AA}	Rate constant of the addition of monomer A to A-type growing chain end
k_{AB}	Rate constant of the addition of monomer A to B-type growing chain end
k_B	Boltzmann constant
k_{BA}	Rate constant of the addition of monomer B to A-type growing chain end
k_{BB}	Rate constant of the addition of monomer B to B-type growing chain end
kcal	kilokalorie
kDa	kilodalton
kg	kilogram
kV	kilovolt
L	liter
l_c	Length of the hydrophobic block
m	meter
M	Metal ion
m	Mass of the electron
M	Mass of the nucleus
mg	milligram
M_n	Number average molecular weight
mol	molar
MΩ	megaohm
n	Crown ether's stochiometric factor
n_{CE}	Amount of crown ether
Ni	Degree of polymerization
p	Packing parameters
$\cdot P^i$ and $\cdot P^j$	Polymer radical

pm	picometer
pM	picomolar
q	Capacity
Q	Stoichiometric factor for Debye-Hückel theory
q_{CE}	Capacity per amount of crown ether
q_i	Hirshfeld charge
q_{poly}	Capacity per mass of the material
R	Coordinates of the nucleus
r	Coordinates of the electron
R	Universal gas constant
R·	Radical
$\vec{r}$	Spatial coordinate of the electron
r^{-1}	Distance
r_1 and r_2	Reactivity ratios
R_h	Hydrodynamic Radius
S_c	Conformational entropy
S_T	Translational entropy
t	tonne
T	Temperature
t	time
T_e	Kinetic energy of the electron
T_K	Kinetic energy of the nuclei
$T_s[\varrho]$	Functional of the kinetic energy
v-	Counter ion's charge
V	Volume
v	Volume of the chain
V_{ee}	Potential energy of the electron-electron interaction
V_{eK}	Potential energy of the electron-nucleus interaction
V_{ext}	External potential
V_{KK}	Potential energy of the nucleus-nucleus interaction (Coulomb repulsion)
$w_i^{Hirsh}(\vec{r})$	Hirshfeld weighting factor
wt%	Weight percentage
Y	Counter ion
y	Counterion's stochiometric factor
z+	Metal ion's charge
Z	Charges of the nucleus
Z_n	Number of nearest neighbors in the lattice

γ_-	Activity coefficient of the anion
γ_+	Activity coefficient of the cation
$\gamma_\pm$	Mean activity coefficient
δ	Chemical shift
ε	Dielectric constant
ε_λ	Molar extinction coefficient
λ	Wave length
ψ	Wave function
ψ_{el}	Electronic wave function
χ	Flory-Huggins-Staverman interaction parameter
χN	Degree of segregation
Ψ_k	Kohn-Sham-orbital
ϱ	Electron density
$(M_iCE_n)^{iz+}(Y_y)^{yv-}$	Complex
$\Delta E^{(2)}_{\sigma\rightarrow\sigma^*}$	Stabilization energy
ΔG_{mix}	Free enthalpy of mixing
ΔH_{mix}	Enthalpy of mixing
ΔS_{mix}	Entropy of mixing
ε_X and $\varepsilon_{M^{n+}}$	Diagonal elements
$d\vec{r}_1$	Volume element
σ_{AB}	Bonding natural bond orbital
σ^*_{AB}	Antibonding natural bond orbital
φ_i	Volume fraction of the component i
ϵ	Interaction energy
ϵ_σ	Energy of the acceptor natural bond orbital
ϵ_{σ^*}	Energy of the donor natural bond orbital
$\varrho^{def}(\vec{r})$	Molecular deformation density
$\varrho_i(\vec{r})$	Individual electron densities
$\varrho_i^{def}(\vec{r})$	Atomic deformation density
$\varrho_i^{free}(\vec{r})$	Electron density of “free” atoms
$\varrho^{in}(\vec{r})$	Estimated electron density
$\varrho^{out}(\vec{r})$	New electron density
$\varrho^{pro}(\vec{r})$	Electron density of the promolecule
∇	Nabla
°C	degrees Celsius
µm	micrometer (micron)

1. ZUSAMMENFASSUNG

Lithium ist ein Schlüsselrohstoff der Energiewende und essenziel für die Herstellung von Lithium-Ionen-Batterien - einer Technologie die vor allem in Elektrofahrzeugen sowie in mobilen Endgeräten, medizinischer Technik, Elektrowerkzeugen und stationären Energiespeichersystemen angewendet wird. Die weltweite Lithium-Nachfrage steigt rasant, maßgeblich getrieben durch den Ausbau klimafreundlicher Elektromobilität zur Erreichung globaler Nachhaltigkeitsziele. Dem gegenüber steht eine industrielle Gewinnung, welche bislang mit erheblichen sozialen und ökologischen Problemen verbunden ist. Konventionelle Gewinnungstechniken, wie die Erschließung über Bergbau, der Gewinnung aus Tonmineralien oder Salzseen sind energieintensiv, stark wasserverbrauchend und beeinträchtigen teilweise empfindliche Ökosysteme erheblich. Insbesondere in stark betroffenen Regionen, wie Südamerika, führt dies zunehmend zu politischen Unruhen und massiver globaler Kritik. Die Entwicklung innovativer, nachhaltiger Gewinnungsmethoden ist unabdingbar um dem steigenden Lithiumbedarf ökologisch verantwortungsvoll gerecht zu werden. Als alternative, hochergiebige Quelle bietet sich Meerwasser an, welches mit einer Gesamtmasse von über 231 Milliarden Tonnen Lithium landbasierte Ressourcen weit übersteigt.

Diese Dissertation beschäftigt sich mit der (Weiter-)Entwicklung eines solchen alternativen Ansatzes zur selektiven Bindung und Gewinnung von Lithium aus geringkonzentrierten, wässrigen Ressourcen, in Anwesenheit konkurrierender Ionen. Die Grundvoraussetzung an dieses Material ist die Kombination molekularer Selektivität mit materialtechnischer Umsetzbarkeit zur Schaffung eines ökologisch und ökonomisch tragbaren Extraktionsverfahrens.

Im ersten Teil dieser Dissertation werden verschiedene Kronenether mittels Dichtefunktionaltheorie-Simulationen hinsichtlich ihres Komplexierungsverhaltens gegenüber Lithium und konkurrierender Alkali- und Erdalkali-Metallionen wie Natrium, Kalium, Magnesium und Calcium untersucht. Unter einer Auswahl an 9-, 12-, und 15-gliedrigen Kronenethern mit jeweils einem durch Stickstoff oder Schwefel substituierten Sauerstoffatoms zeigte der 15-gliedrige *thio*-Kronenether eine besonders hohe Selektivität gegenüber Lithium. Die Simulationsergebnisse wurden experimentell mit *aza*-15-Krone-5 validiert und bestätigen die Eignung rechnergestützter Methoden zur Vorauswahl geeigneter Kronenether-Strukturen. Die Notwendigkeit zeitintensiver, kostenintensiver und gegebenenfalls gesundheitsschädlicher Synthesemethoden, bei ungewissem Erfolg, wird dadurch drastisch reduziert. Diese Erkenntnisse leisten einen grundlegenden Betrag zum Verständnis von Wirt-Gast-Komplexen und ermöglichen eine gezielte Optimierung des Systems.

Der zweite Teil dieser Dissertation widmet sich der praktischen Umsetzung des Konzeptes durch eine systematische Entwicklung des funktionalisierten Polymermaterials. Eine

amphiphile Block-Copolymer-Matrix aus Polystyrol als hydrophober Hauptteil und Polymethacrylsäure als hydrophilen Minoritätsblock (PS-*b*-PMAA) wurde mit dem 9-gliedrigen Kronenether Benzo-9-Krone-3 (B9C3) modifiziert um die Bildung von ML_2-typ Sandwich-Komplexierung mit Lithiumionen zu ermöglichen. Die systematische Variation des Polymerisationsgrades, der Länge des hydrophoben Blockes sowie des Funktionalisierungsgrades führte zu der Entwicklung eines hochselektiven Systems mit optimaler Lithiumbindung. Über Flüssig-Flüssig-Extraktionen in einem Dichlormethan/Wasser-System sowie dynamischer Lichtstreuung konnte die hohe Effizienz des Systems untermauert werden.

Um näher in den industriellen Anwendungskontext zu gelangen, in dem große Lösemittelmengen zur Extraktion weder praktikabel noch nachhaltig wären, wird das System im dritten Teil dieser Arbeit in eine feste, lösemittelfreie Form überführt. Die polymere Matrix dient dabei als idealer Ausgangspunkt. Drei Verarbeitungsmethoden, die Materialien mit hohen Oberflächen-zu-Volumenverhältnissen ergeben, wurden untersucht: Membranen, Cubosome und elektrogesponnene Fasern.

Membranen wurden mittels SNIPS (*self-assembly and nonsolvent-induced phase separation*)-Prozess und Cubosome durch Nanofällung hergestellt – beide Verfahren basieren auf kontrollierter Selbstorganisation des Blockcopolymers und Phasentrennung. Cubosome konnten erfolgreich aus B9C3-funktionalisierten Polymeren produziert werden, wobei die Ausbeute mit etwa 200 mg pro Fällungsprozess Optimierungspotenzial bietet. Die Herstellung der isoporösen, integral asymmetrischen PS-*b*-PMAA Membran gelang. Nach erfolgreicher Funktionalisierung des PMAA-Blockes mit den aromatischen Kronenethern B9C3 und Benzo-12-Krone-4 (B12C4) wurde die Polymerselbstorganisation und damit die Membranmorphologie jedoch erheblich gestört.

Die vielversprechendste und in dieser Arbeit erfolgreichste Methode war die Herstellung elektrogesponnener Fasern aus funktionalisierten Polymeren. Die Herstellung feiner Fasern war sowohl mit B9C3 als auch B12C4 und 12-Krone-4-funktionalsierten Blockcopolymeren technisch unkompliziert und skalierbar. Besonders das B12C4-basierte Polymer wies eine hohe Lithiumkapazität bei optimaler Selektivität gegenüber Natrium auf. Daraus lässt sich schließen, dass bei Fest-Flüssig-Extraktionen ML-Komplexierung gegenüber ML_2-Komplexierungen bevorzugt werden. Dieses Verhalten, bestätigt durch die geringe Lithium-Komplexierung der B9C3-basierten Fasern, ist eine interessante Abweichung zu dem bisher bekannten Verhalten in Lösung. Im Rahmen dieser Arbeit war es nicht nur möglich nähere Einblicke in die molekularen Wechselwirkungen des Systems zu gewinnen, sondern ein Material in einer festen, technologisch relevanten Form, mit effektiver Lithium-Komplexierung in Anwesenheit konkurrierender Natriumionen herzustellen.

2. ABSTRACT

Lithium is a key raw material for the energy transition and essential for the production of lithium-ion batteries—a technology used primarily in electric vehicles, mobile devices, medical technology, power tools, and stationary energy storage systems. Global demand for lithium is rising rapidly, driven predominantly by the expansion of climate-friendly electric mobility to achieve global sustainability goals. This is contrasted by industrial extraction, which has so far been associated with considerable social and environmental problems. Conventional extraction techniques, such as mining, extraction from clay minerals, or salt lakes, are energy-intensive, consume large amounts of water, and in some cases significantly impact sensitive ecosystems. In severely affected regions such as South America, this is increasingly leading to political instability and massive global criticism. The development of innovative, sustainable extraction methods is indispensable in order to meet the growing demand for lithium in an ecologically responsible manner. Seawater offers an alternative, highly productive source, which, with a total mass of over 231 billion tons of lithium, far exceeds land-based resources.

This dissertation explores the continued development of an alternative approach for the selective binding and extraction of lithium from low-concentration aqueous resources in the presence of competing ions. The basic requirement for this material is the combination of molecular selectivity with material-technical feasibility to create an ecologically and economically viable extraction process.

In the first part of this work, various crown ethers are investigated using density functional theory simulations concerning their complexation behavior towards lithium and competing alkali and alkaline earth metal ions such as sodium, potassium, magnesium, and calcium. Among a selection of 9-, 12-, and 15-membered crown ethers, partially with an oxygen atom substituted by nitrogen or sulfur, the 15-membered *thio*-crown ether showed particularly high selectivity toward lithium. The simulation results were experimentally validated with *aza*-15-crown-5 and confirm the suitability of computer-aided methods for preselecting suitable crown ether structures. This drastically reduces the need for time-consuming, cost-intensive, and potentially harmful synthesis methods with uncertain success. These findings make a fundamental contribution to the understanding of host-guest complexes and enable targeted optimization of the system.

The second part of this study is dedicated to the practical implementation of the concept through the systematic evolution of the functionalized polymer material. An amphiphilic block copolymer matrix consisting of polystyrene as the hydrophobic majority block and poly(methacrylic acid) as the hydrophilic minority block (PS-*b*-PMAA) was modified with the 9-membered crown ether benzo-9-crown-3 (B9C3) to enable the formation of ML_2-type sandwich complexation with lithium ions. Systematic variation of the degree of polymerization, the length

of the hydrophobic block, and the degree of functionalization led to the development of a highly selective system with optimal lithium binding. The high efficiency of the system was confirmed by liquid-liquid extractions in a dichloromethane/water system and dynamic light scattering.

In order to get closer to the industrial application context, in which large quantities of solvents would be neither practical nor sustainable for extraction, the system is converted into a solid, solvent-free form in the third part of this work. The polymer matrix serves as an ideal starting point in this regard. Three processing methods that result in materials with high surface-to-volume ratios were investigated: membranes, cubosomes, and electrospun fibers.

Membranes were produced using the SNIPS (self-assembly and nonsolvent-induced phase separation) process and cubosomes by nanoprecipitation – both methods are based on controlled self-organization of the block copolymer and phase separation. Cubosomes were successfully produced from B9C3-functionalized polymers, with a yield of approximately 200 mg per precipitation process offering potential for optimization. The production of the isoporous, integrally asymmetric PS-*b*-PMAA membrane was successful. However, after successful functionalization of the PMAA block with the aromatic crown ethers B9C3 and benzo-12-crown-4 (B12C4), polymer self-organization and thus membrane morphology were significantly disturbed.

The most promising and successful method in this work was the production of electrospun fibers from functionalized polymers. The production of fine fibers was technically straightforward and scalable with both B9C3 and B12C4 and 12-crown-4-functionalized block copolymers. The B12C4-based polymer in particular exhibited high lithium capacity with optimal selectivity towards sodium. This suggests that ML complexation is preferred over ML_2 complexation in solid-liquid extractions. This behavior, confirmed by the low lithium complexation of the B9C3-based fibers, is an interesting deviation from the previously known behavior in solution. Within the scope of this work, it was not only possible to gain deeper insights into the molecular interactions of the system, but also to produce a material in a solid, technologically relevant form with effective lithium complexation in the presence of competing sodium ions.

3. INTRODUCTION

This thesis addresses the sustainable extraction and use of lithium (Li), a strategically important element for modern energy storage technologies. The starting point of this introduction is an analysis of its physical and chemical properties as well as current extraction methods, whose ecological and geopolitical challenges necessitate an urgent search for alternative approaches. Subsequently, innovative concepts for environmentally friendly lithium extraction are presented, with one specific approach being examined in depth within the scope of this thesis. The main part is divided into two thematic areas: Quantum chemical modeling of crown ether (CE) cation complexes and polymer-based implementation of the concept in the application context.

In context of publication 1, the structure and binding properties of CEs and their lithium complexes are first analyzed. Building on this, an introduction to the theoretical fundamentals of density functional theory (DFT) is provided, particularly with regard to geometry optimizations and electronic population analyses.

To emphasize the relevance of polymer-supported systems, the integration of CEs is presented as groundwork for publications 2 and 3. The focus is on the synthesis of functionalized polymers using controlled radical polymerization, their self-organization in solution and in the solid state, and the formation of hierarchical structures. This is followed by a discussion of production methods of complex polymer-based structures such as membranes, cubosomes, and electrospun fibers.

3.1. LITHIUM – VALUE, DEMAND AND RECOVERY

Li belongs to the group of alkali metals and is characterized (in its pure form) by its silvery-white color, low density (0.53 g cm^{-1}), small ionic diameter (1.58 Å), and high reactivity. With an atomic weight of approximately 6.94 u, Li is the lightest metal and the lightest solid element under standard conditions.[1–4] In terms of electrochemical properties, Li is distinguished by its high electrochemical potential and energy density.[4–6] Its ability to store large amounts of energy in a compact form is a key reason for its widespread use in Li-ion batteries (LIBs). Its application in LIBs has revolutionized energy storage technology, essential for electric vehicles, stationary power storage systems for intermittent energy sources (e.g. solar and wind), and mobile electronic devices.[2,7–9] Therefore, Li is crucial in modern technologies and the transition to renewable energy.[9] As the demand for such technologies continues to rise, the global need for Li also increases. Apart from LIBs, Li applications include ceramics and glasses, lubricating greases, air treatment, continuous casting mold flux powders, medical applications, polymer production, and aerospace applications.[9–11]

3.1.1. LITHIUM IN APPLICATIONS

Figure 1 illustrates the proportions of the primary Li usage in 2022 and 2024. In addition to the remarkably high share of LIBs in the global end-user market of Li of 74% in 2022, the tremendous increase in this industry by 13% to 87% within just 2 years illustrates the rapidly developing interest in LIBs.[9,10] In fact, this even exceeds forecasts that predicted an increase to 65% by 2025 just a few years earlier.[12]

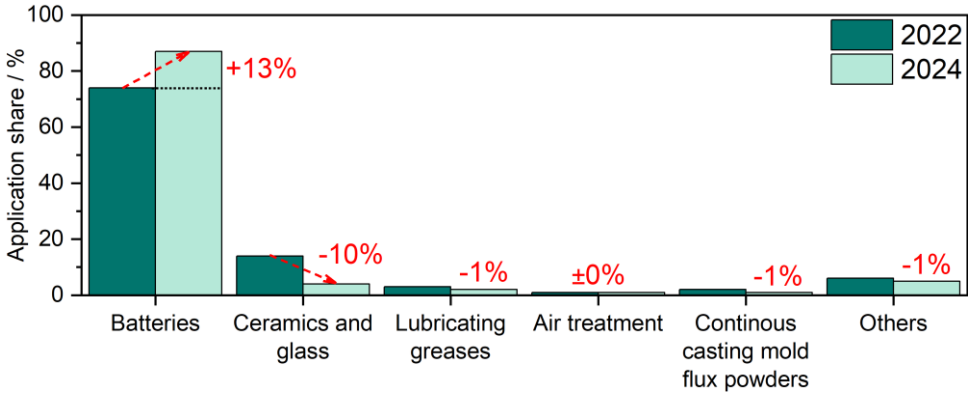

Figure 1: Year-on-year change in the share of Li applications in the global end-user market from 2022 to 2024. Created by the author with data from Ref. [9,10].

Several factors are propelling the use of LIBs. To combat climate change, governments and non-governmental organizations have signed a number of agreements that commit to reducing global, anthropogenic CO_2 emissions. As the two largest sources of greenhouse gases, the transportation and power generation sectors are pivotal in attaining these goals. This transition towards renewable energies and the corresponding need for high-performance batteries for

energy storage is accelerating the emergence of LIBs. In addition, fluctuating prices for fossil fuels and escalating geopolitical conflicts in the context of these energy sources are major factors in the high demand for LIBs.[2,5,7,13]

Li appears in a wide variety of forms in industry. Li aluminum silicates are alloyed with glass-ceramics to adjust their melting and processing temperatures. The resulting ceramics have a high resistance to temperature and thermal expansion, making them particularly suitable for elevated-temperature applications such as stoves and ovens. The low expansion coefficient of the integrated Li compounds results in higher dimensional stability of the ceramics.[1,2,14] Li carbonates, hydroxides, and chlorides are added to lubricating greases to improve their viscosity. Li-based fatty acids, like palmitic, stearic, oleic, and linoleic acids, assist in maintaining the stability of the lubricating grease, enhance water repellence and insensitivity to oxygen, enable high-temperature resistance, and consistent lubricity in low-temperature ranges.[2,15–17] Due to the low weight of Li and corresponding Li alloys with e.g. aluminum, cadmium, copper, magnesium or manganese, the latter are used in aeronautical engineering. In addition to their low weight, the resulting materials exhibit high mechanical strength and corrosion resistance.[2,18] Alkyl Li compounds are used in the polymer industry for initiation reactions to produce styrene-butadiene rubbers, which in turn are raw materials for tires due to their high abrasion resistance.[2] Patients suffering from mental health conditions such as depression or bipolar disorders are medicated with Li carbonates and Li citrates, in acute therapy and as a prophylactic treatment to prevent the recurrence of depressive or manic episodes.[19,20]

3.1.2. LITHIUM ION BATTERIES

LIBs are a key technology in the energy transition and make up the lion's share of the Li end-use market. Their role is pivotal in electromobility and in the storage of renewable energies. This section provides a more detailed picture of the role of Li in LIBs.[2,6,13] The approximate mass of Li in different types of LIB applications is shown in Figure 2.

The mode of action of LIBs is based on the reversible exchange of Li ions between two electrodes. Graphite or silicon electrodes, where Li ions can be reversibly intercalated, generally serve as the anode material. The absorption capacity of nanostructured silicon is thereby considerably greater. A wide variety of Li oxides serve as cathode materials in combination with transition metals such as nickel, manganese or cobalt.[7]

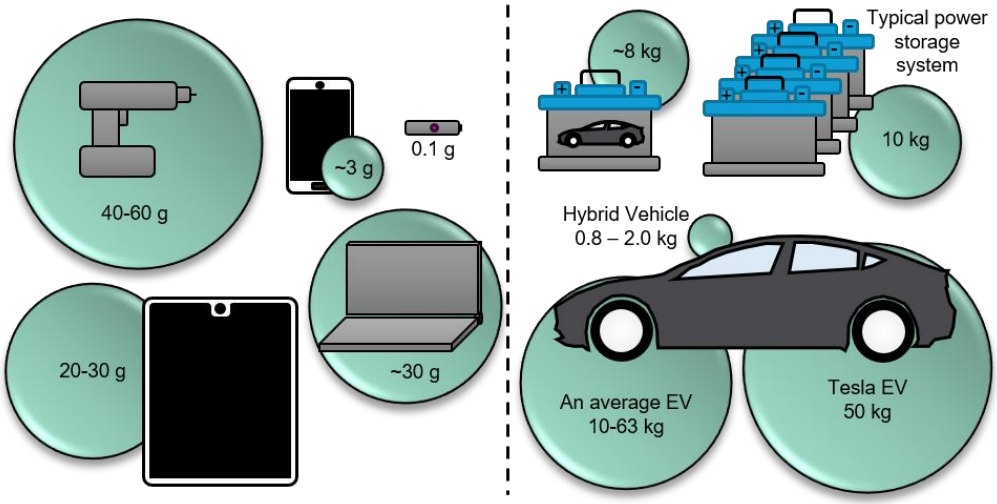

Figure 2: Overview of the average mass of lithium in a range of lithium ion battery applications. Created by the author with data from Ref. [2].

Depending on the battery type, LIBs have enormously high energy capacities of 120–200 Wh/kg.[7] With a global market share of 37.2%, 29.0% and 21.0% respectively, Li cobalt oxide ($LiCoO_2$), Li nickel manganese cobalt oxide ($LiNiMnCoO_2$) and Li manganese oxide ($LiMn_2O_4$) batteries are dominating the market for LIBs.[7] In practice, a combination of several transition metals, as in the $LiNiMnCoO_2$ electrode, often proves to be a more cost-effective alternative to a pure $LiCoO_2$ electrode.[1] The anode and cathode are separated by an electron-insulating, Li ion-conducting electrolyte. The cell reactions proceed as follows in Figure 3:

anode	$Li_xC_n \rightleftharpoons C_n + xLi^+ + xe^-$
cathode	$Li_{1-x}MO_2 + xLi^+ + xe^- \rightleftharpoons LiMO_2$
reaction	$Li_{1-x}MO_2 + Li_xC_n \rightleftharpoons LiMO_2 + C_n$

Figure 3: Cell reactions and overall reaction in lithium ion batteries.[21]

During the discharge process in this galvanic cell, the Li ions move from the anode (Li_xC_n) through the Li ion-conducting electrolyte to the cathode, where they are incorporated into the host lattice, the $Li_{1-x}MO_2$ structure. During this oxidation process, electrons are freed and migrate *via* the energy consumer to the anode, where the reduction occurs. The reverse process describes the charging process.[11,21]

The rapidly growing demand for Li makes it necessary to take a critical look at the Li sources and the methods of Li extraction, with particular attention to their environmental impacts and geopolitical implications.[11,13]

3.1.3. NATURAL OCCURRENCE AND EXTRACTION

While Li concentrations in the earth's crust are around 17–46 ppm[2,22], it is enriched in certain geological formations such as pegmatites, salt lakes (salars) and clay minerals. The type of deposit determines the choice of extraction method, in turn having a significant impact on the environment, energy consumption and economic viability.[2] The main natural Li deposits and common extraction methods are systematically presented in this section and evaluated in terms of their efficiency and sustainability.

To estimate the global stock of Li, a distinction must first be made between resources and reserves. The terminus *resources* refers to the entirety of all global occurrences of a mineral. These can only be potentially mined, including all known and suspected deposits.[8,9]

Reserves are the economically viable fraction of a mineral resource, recoverable with current mining technologies. They include those parts of the resource that meet both economic and socio-economic criteria for extraction.[8,9] Irrespective of the type of deposit, which varies depending on location, the economically significant Li deposits are globally very unevenly distributed. This leads to the monopolization of Li availability by certain countries, which is particularly evident in light of the looming Li shortage. This unbalanced distribution can entail price manipulation, geopolitical dependencies, barriers to innovation, and a lack of environmental and social standards caused by the absence of competitive pressure. The global distribution of Li reserves and Li resources (year: 2024) is shown in Figure 4.[2,7,11,23,24]

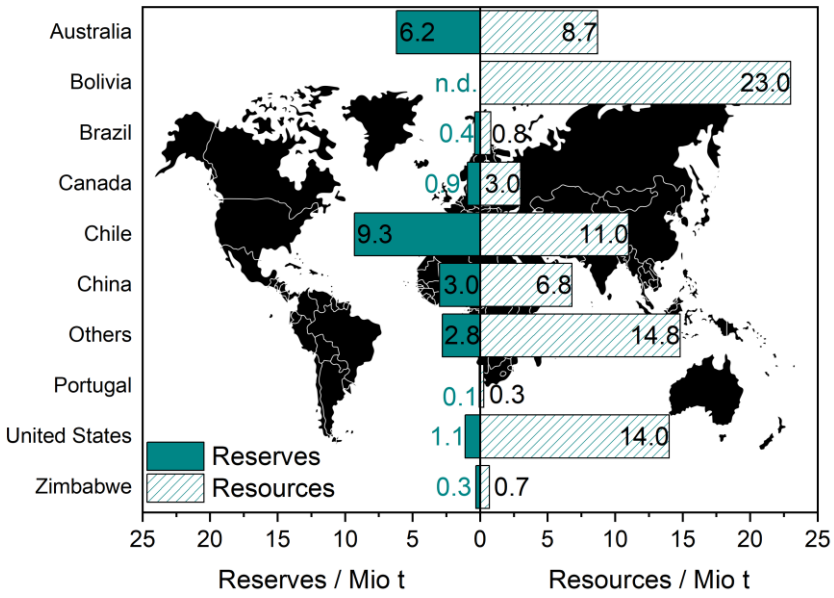

Figure 4: Distribution of global lithium reserves (total 28 million tons) and resources (total 105 million tons) in the year 2024. Created by the author with data from Ref. [9].

Li deposits can be generally categorized into three main areas:

1. **aqueous deposits** such as salars that contain brines with high Li concentrations, accounting for 64% of the world's Li deposits,
2. **igneous rocks** (e.g. pegmatites), with 26% of global Li share, in which the Li is embedded in minerals such as spodumene, and
3. **clay minerals**, representing 9% of global Li deposits.[2,3,9]

In addition to traditional sources, Li can be extracted from red mud, borate deposits, geothermal wastewater, coal and fly ash, mine water, and *via* the recycling of end-of-life LIBs.[2] For example, there is plenty of potential for development when it comes to the Li recovery from disused energy storage devices – currently barely 5% of LIBs worldwide are being recycled.[25,26]

Aqueous Deposits – The so-called *Lithium Triangle* is one of the world's most important and prominent regions for Li mining. This region in South America spans over 400.000 km^2 including parts of Chile, Argentina and Bolivia. Mining in this area mainly takes place from aqueous sources with Li concentrations around 18–1750 mg/L, localized in the high altitudes of the Andes, the Salar de Atacama (Chile), the Salar de Uyuni (Bolivia) and the Salar del Hombre Muerto (Argentina). Apart from the occurrence of Li, these regions are characterized by a hot, extremely dry climate with high annual solar radiation.[2,3,23] Extraction from highly concentrated, aqueous resources is possible *via* a range of processes, including evaporation, direct precipitation, membrane processes such as nanofiltration, liquid membranes or

electrodialysis, solvent extraction, surface adsorption, and ion exchange.[ii] Solar evaporation is presently the most established method of extracting Li from aqueous media due to the arid conditions in the main deposits. Therefore, and to enable a better understanding of this type of process, an exemplary procedure is presented in the following.[2,3]

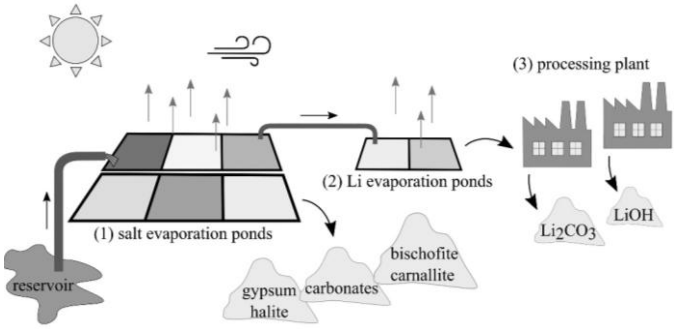

Figure 5: Evaporation process of conventionally mined brines for lithium recovery. Reprinted from Ref. [3], © 2022, with permission of Informa UK Limited, trading as Taylor & Francis Group.

Li-containing brines have formed over millions of years in underground aquifers through complex geological and hydrological processes. The brine is pumped to the surface *via* boreholes and transferred to large evaporation basins, as depicted in Figure 5. Over several months, the brine concentrates as a result of the intense solar radiation of the arid regions. During the evaporation process, various salts of competing ions are gradually precipitated. Initially, the salts with low solubilities are removed by precipitation, such as the sodium salt halite, the calcium salt gypsum, the potassium-magnesium salt carnallite, the magnesium salt bischofite and various carbonates (Ca, Mg, Fe). As a result of evaporation, the Li ion concentration rises to up to 6wt%. In order to remove other interfering ions including magnesium, calcium and borate trioxide, precipitants are deliberately used to maximize the Li concentration in the aqueous medium. Minor premature Li losses occur, for example, through the co-precipitation of Li carnallite. Ultimately, Li carbonate is salted out with a purity of up to 99.9% by adding sodium carbonate. Strongly dependent on initial salt composition, this process allows around 50–80% of the Li in the brine to be recovered.[3] The benefits of this approach are low costs (2000–5700 \$/t Li_2CO_3 and low energy requirements, provided the climatic conditions allow solar evaporation. However, the evaporation process is very time-consuming (several months or years) and large areas are required for the evaporation basins. Furthermore, the consumption of fresh water is quite high at 5–50 m^3/t Li_2CO_3, which can lead to an increase in water scarcity and subsequent political and ecological problems, especially in extremely arid climatic regions. Moreover, this process is not suitable for all aqueous media.[3,13,23,27]

[ii] Further details can be found in Reich *et al*. (2023).[3]

Igneous Rocks – The Greenbushes mine in western Australia is one of the largest exploitation areas for Li-bearing pegmatitic rocks (total of 1.34 Mt Li), accounting for 42% of the total Li supply generated by mining.[11,23,28,29] Pegmatite deposits are formed by magma containing minerals, which entered the earth's crust millions of years ago through magma chambers, slowly began to cool and crystallize. Pegmatitic rocks are not only a source of Li, but also tin, tantalum, niobium, beryllium, cesium, rubidium, scandium, thorium, uranium, and rare earth metals, with Li contents of 1–4 wt% (10-40 g/kg) and high recovery rates (60–70%).[2,7,11,29] The Li-containing mineral spodumene ($LiAlSi_2O_6$) can be extracted from these pegmatites and is characteristic of the occurrences in the Greenbushes mine. A classic extraction process will be briefly illustrated on the basis of spodumene. First, the mineral is mechanically ground and then calcined at temperatures of >1000 °C. As a result of this process, the unreactive a-spodumene is converted to the more reactive b-spodumene. Other Li-containing minerals are not decrepitated thereby. Acid digestion of b-spodumene is possible, allowing the $LiAlSi_2O_6$ to react with sulfuric acid at temperatures of 200–300 °C to form the water-soluble Li sulphate. The sulfate can then simply be leached out with water and subsequently used or further processed into other Li compounds such as carbonates or chlorides.[2,23,27,30,31] Compared to extraction from brines, this process is significantly faster, more location independent and still yields a high Li output. However, the energy consumption and therefore the carbon footprint of the produced Li is significantly weaker. With costs around 3000–6000 \$/t Li_2CO_3 the process is less economical.[23]

Clay Minerals – The third and “newest” method for industrial-scale Li production is extraction from sediments and clays. Large deposits of these Li-containing deposits have been discovered in Serbia, China, Tanzania and Mexico.[23] Li extraction from sedimentary rocks is in part similar to the processes applied for extraction from pegmatites. This is demonstrated by the patent from Rabe *et al.* (year: 2020)[32]. After grinding and suspending the sedimentary materials, a Li containing slurry is separated. The Li is dissolved from the sediment by adding acid (usually sulfuric acid as in pegmatite processing), precipitates are formed which are subsequently removed. Undesired ions (magnesium, potassium, iron and aluminum) are removed from the aqueous Li sulfate solution in several steps. These include leaching, crystallization *via* the different solubilities, chemical purification by the addition of calcium oxide, soda or oxalic acid and eventually an ion exchange. Finally, a high-purity Li sulphate solution is obtained.[2,11,32] With high energy costs and complex purification steps, the current extraction from clays at 7000-10000 \$/t Li_2CO_3 is the least economical of the presented methods for Li extraction. However, as this method is still relatively unexplored, it offers great potential for optimization.[23,31]

All these processes have in common that they can cause considerable challenges due to high energy or water consumption, intensive land requirements or geopolitically sensitive

dependencies, which are becoming even more acute in view of the increasing scarcity of Li. The development of alternative, sustainable extraction methods is therefore fundamental to reducing negative ecological impacts and ensuring the strategic availability of Li.[4,13,33]

3.1.4. SUSTAINABLE RECOVERY METHODS

This chapter contrasts two approaches, intended to contribute to a more sustainable recovery of Li: The recycling of spent LIBs and the extraction of Li from seawater. Particular emphasis is placed on the latter due to the relevance for this thesis. Additionally, a multitude of other unconventional Li resources exist, such as geothermal brines, waste streams, submarine deposits and extra-terrestrial materials.[11]

Recycling of LIBs – The recycling of spent LIBs is an excellent opportunity not only for extracting Li, but also for reducing the increasing pressure on primary resources and minimizing waste generation. Given the high quantities of Li in electric vehicles (Figure 2), its potential is significant. The economic efficiency of the process is increased by recovering not only Li but additional valuable metals such as cobalt, copper, and nickel.

The method proceeds as follows: The collection of the LIBs is followed by dismantling and separation of the components into cathode, anode and electrolyte material.[11,13,26,34] The hydrometallurgical process involves battery discharge to prevent self-ignition or explosion with subsequent fragmentation. After separation by magnetic and density-dependent flotation processes, the remaining matter is chemically dissolved *via* leaching and/or being precipitated as salts or oxides.[11,26,35] In the pyrometallurgical process, thermal melting (>1200 °C) is performed to recover metals (nickel, cobalt, copper, and iron) from LIBs. However, most pyrometallurgical processes are not economically suitable for the recovery of Li yet, as Li remains in the slag or dust.[11] At the same time, research shows that modern pyrolysis processes can actually recover Li, which requires a change in large-scale industrial processes.[4] Responsible handling of the toxic battery components and waste is essential for the ecological sustainability of LIB recycling, yet is admittedly lacking, especially in private households. The recycling of LIBs represents an excellent opportunity to build a circular economy in which resources can be used efficiently and waste minimized.[13] However, the actual recycling rate remains low due to safety risks, technical complexity, poor sorting practices, and high costs (five times as high as brine-based recovery).[11,26]

Recovery from Seawater – The extraction of Li from seawater is an interesting and promising way of meeting the demand for Li in the long term and in a sustainable manner. The total amount of Li in the world's oceans is estimated at 231–260 billion tons, massively exceeding the 133 million tons of Li on land. In addition, it is distributed relatively evenly across the globe, preventing the formation of monopolies by single countries. However, as Li concentrations in

seawater are very low (0.18 mg/L; for comparison: 18–1750 mg/L Li in brines), a highly efficient recovery system is required. Conventional methods such as evaporation and precipitation are not suitable.[8,11,12,36] This problem is exacerbated by the presence of competing ions in significantly higher concentrations, such as sodium (10.5 g/L), magnesium (1.3 g/L), calcium (0.4 g/L) and potassium (0.4 g/L).[8,36] Due to the high relevance of the topic, intensive research has been carried out in recent years. This includes research on electrochemical processes such as ion pumps, capacitive deionization (CDI – membrane-based or hybrid systems), electrodialysis (in combination with ionic liquids, monovalent-selective membranes or bipolar membranes) and electrochemically assisted Li extraction using ion sieves (e.g. λ-MnO_2). Furthermore, a wide range of adsorptive materials is being investigated, including nature-based minerals (e.g. zeolites, clays and silicotitanates), metal-based lattice structures (e.g. aluminum-, manganese-, or titanium-based), metal-organic frameworks (MOFs) such as UiO-66, HKUST-1, and ZIF-8, organic materials or functional polymers (e.g. polymeric glycidyl methacrylate, hydrogels, or polysulfone-*graft*-4′-aminobenzo-15-crown-5-ether), and supra-molecular structures (e.g. CE, ion-imprinted polymers, or porous silica).[8,36–42] In addition, ion sieves (Aluminum Hydroxide, Li Manganese Oxide, Li Titanate, and Li Manganese Titanate Oxide), further membrane-based and liquid-phase separation processes, including nanofiltration, membrane distillation or crystallization, supported liquid membranes, and liquid-liquid extraction are possible methods for lithium recovery.[8,36]

Besides electrochemically supported methods, absorption processes are one of the more promising methods of extracting Li from low-concentration aqueous media due to their high efficiency, low environmental impact and high purity of the Li extracted. The requirement for this is a high selectivity of the system towards Li, which can be realized by the use of supramolecular structures. Supramolecular structures enable selective binding of specific ions by targeted molecular recognition. This molecular recognition is based on the specific formation of several non-covalent interactions (such as hydrogen bonds, von der Waals forces, π–π interactions and coordinative bonds). CEs are a classic representative of this group as they are able to selectively complex certain cations, depending on charge and size. Since the complexation behavior of CEs is an elementary component of the system presented in this work, the following chapter is devoted to this topic.

3.2. CROWN ETHERS

The macrocyclic polyethers, first discovered by C. J. Pedersen in 1967, represent an outstanding class of molecules. In their shape resembling a crown, they received the term *Crown Ether*, commonly used today. Their preorganized, circular structure of (traditionally) several ethylene-oxy units enables the formation of non-covalent host-guest complexes with a variety of cations.[8,43,44] The CE's structural variance, including substituents, branches, and the

replacement of oxygen with nitrogen or sulfur, will be discussed. This chapter is intended to establish basic knowledge in this field in order to understand the structural characteristics of CEs in all their variance, as well as to provide an overview of the opportunities for cation complexation.

3.2.1. FUNDAMENTALS OF CROWN ETHERS

Pedersen, Lehn, and Cram were awarded the Nobel Prize in Chemistry in 1987 for their discovery of the structural class of CE almost 60 years ago. In the study of multidentate ligands, Pedersen utilized monoprotected pyrocatechol, comprising a minor portion unprotected pyrocatechol. The cyclic ether dibenzo-18-crown-6 (Figure 6) was formed in 0.4% yield as a by-product of the Williamson ether synthesis with bis-2-chloroethyl ether. The easily crystallizable solid exhibited exceptional solubility behavior. It could not be dissolved in methanol until the addition of sodium hydroxide, and potassium permanganate could not be completely dissolved in organic solvents such as benzene or chloroform until the addition of dibenzo-18-crown-6. Pedersen recognized the potential of the novel macrocyclic structure and thus laid the foundation for numerous innovations in chemistry, materials science, and biology.[43–46]

The total number of ring atoms and the number of heteroatoms in the macrocycle are of critical importance regarding the size, bonding properties, and potential applicability of the CEs. With the potential for complicated names, the IUPAC-compliant naming of CE structures can be a challenge. Therefore, a much more intuitive and simpler naming scheme is used: [number of atoms in the ring]-**crown**-[number of oxygen atoms], (Figure 6).[43,45]

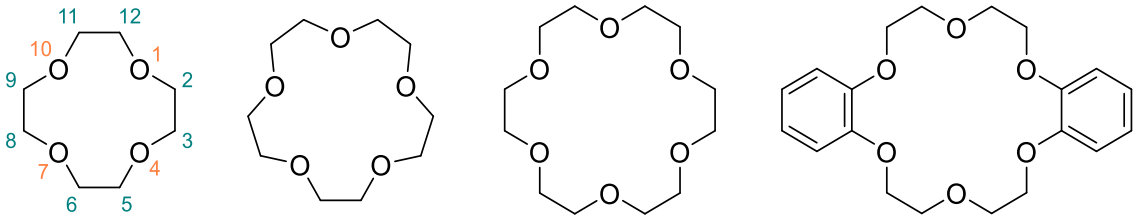

Figure 6: Structures of crown ethers (CEs) of different ring sizes (12-, 15- and 18-membered) as well as the first discovered CE dibenzo-18-crown-6. The numbering is illustrated in color for 12-crown-4 exemplarily (created by the author with data from Ref. [47,48]).

The characteristic structure of CE – consisting of hydrophilic heteroatoms and a hydrophobic carbon backbone – gives rise to a number of potential applications of CEs. One example are phase transfer catalysts. Depending on the solvent environment, the structural conformation and spatial orientation of the CEs changes drastically, and consequently, the flexibility, cavity size and host-guest binding affinity change as well. Furthermore, CEs are able to form stable complexes (so-called *coronates*) with a large number of cations, whereby the ions are trapped in the ring opening of CEs by non-covalent interactions. Thus, CEs can act as carrier molecules

transferring cations from one phase to another, immiscible with the former phase, in which these cations would not be soluble without support (Figure 7). This effect is not only beneficial for circumventing solubility difficulties, but can also have a favorable effect on the reaction rate of specific reactions.[43,44,49]

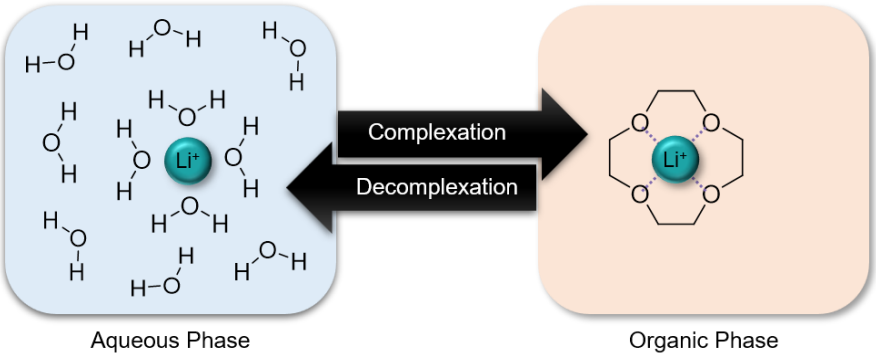

Figure 7: Phase transfer of Li^+ between an aqueous and an organic phase. Dehydration of Li^+ enables complexation (created by the author).

A prominent example is potassium fluoride being part of a reaction in which the anion functions as a nucleophile. In solution, the fluoride ion is typically present as a closely associated ion pair with the potassium cation, which significantly limits its reactivity due to electrostatic interactions and solvation. However, once the potassium ion is encapsulated in a CE structure, coordination is reduced and the fluoride ion is present as a *naked anion* – the nucleophilicity and thus the reactivity is drastically increased.[49] Furthermore, CEs are used in chromatographic applications[50,51], antibiotics[52,53], ion channels[54], sensors[55,56], electrodes[57], and membranes[58–60]. Since cation complexation is of fundamental importance in most applications, it is discussed in more detail in the following chapter.

3.2.2. CATION COMPLEXATION AND SELECTIVITY

The selective cation complexation by CEs is based on their specific structural and electronic properties. Their preorganized ring-like structure leads to a spatially defined arrangement of oxygen donors, which enables optimal cation complexation. Some structural characteristics are of key importance for intermolecular host-guest interactions, for example:

- the size of the CE cavity[46,47,61–64],
- the number and type of donor atoms in the CE[46,62–64],
- the charge and size of the cation (as well as the counterion)[46,47,61,63],
- preorganization[46,47,65],
- conformational flexibility[46],
- substitutions of electron withdrawing or donating groups[46,62–64] and,
- solvation[43,45,61,63,65].

The bond between CE and cation is created by non-covalent interactions, however, these are manifold: Electrostatic interactions (cation–anion, ion–dipole, dipole–dipole), hydrogen bonds, π interactions (π–π, cation–π, and anion–π), Van der Waal's forces (dispersion and inductive effects), halogen bonds (less relevant in this context), as well as hydrophobic or solvophobic effects.[66] The principle of optimal spatial fit is a central concept for explaining the cation selectivity of certain CEs and describes the compatibility of the size ratios of cation and CE cavity. Put simply, the better the cation fits into the cavity of the CE, the more stable the resulting host-guest complex. To illustrate this, the cavity sizes of a number of different large *oxa*-CEs and the diameters of various mono- or divalent cations are summarized in Table 1.[iii] The term "*oxa"* refers to the oxygen donor atoms in the ring, the variation of which is discussed in section 3.2.3.

Table 1: Cavity sizes of a number of crown ethers and ion diameters of various mono- and divalent cations. The diameters refer to a coordination number (CN) of 6.[21,43,47,48]

CE	Cavity Size /pm [43,47]	Cation	Diameter /pm [21,48]	Cation	Diameter /pm [21,48]
12-crown-4	120–150	Li^+	152	Mg^{2+}	144
15-crown-5	170–220	Na^+	204	Ca^{2+}	200
18-crown-6	260–320	K^+	276	Sr^{2+}	236
21-crown-7	340–430	Cs^+	334	Ba^{2+}	270

A classic example is the high affinity of 18-crown-6 (18C6) for potassium and barium ions. With a cavity size of 260-320 pm, the 18C6 CE encloses the potassium ion or barium ion with ion diameters (with a coordination number of 6) of 276 pm and 270 pm respectively in an optimal

[iii] Please note: The cation diameter varies depending on the coordination number CN.

spatial fit (Figure 8, A). This almost perfect size complementarity enables highly symmetrical coordination of the ions by the donor atoms, which results in the formation of stable non-covalent interactions. These contribute significantly to the enthalpy of complex formation and increase the thermodynamic stability of the resulting host-guest complex. This behavior is particularly pronounced in complex formation with the double-charged barium ion, whose charge density significantly exceeds that of the potassium ion, yet the ion diameter is almost identical. The improved electrostatic interactions with the negatively polarized donor atoms of the CE result in a strong complex structure.[43,46,47,65]

Three effects are of central importance for cation-CE complexes – the chelate effect, the macrocyclic effect, and the cryptate effect. The *chelate effect* describes the improved complex stability of multidentate ligands compared to ligands with fewer ligation sites.[45,48,65,67] The reasons for this include the entropy gain when replacing several ligands with a single ligand, the forced spatial proximity of the ligands, and the formation of stable chelate rings. An example for the *macrocyclic effect* is cyclam (tetra*aza*-14-crown-4), exhibiting a three orders of magnitude higher complex stability compared to its noncyclic analogue 2,3,2-tetramine.[45,48] Owing to their reduced degrees of freedom, macrocycles exhibit a lower entropy loss during complex formation than open-chain analogues. In addition, they are often less solvated, which renders desolvation energetically more favorable and promotes complex formation enthalpically. Complex formation can be further enhanced by the so-called *cryptate effect* – closely related to the chelate effect. The integration of a bridging arm with additional coordination sites creates a so-called cryptand, which forms a three-dimensional cage system. This enables particularly effective confinement of the cation.[45,46,49] In fact, these preorganizing effects are very conducive to CE synthesis. Interestingly, cations are often added to the synthesis that correspond in diameter to the cavity size of the desired CE. By preferential arrangement of the reactants around this cation, the synthesis of the desired macrocycle is usually far more effective than in the absence of such an ion.[46]

The structural flexibility of the CE allows the formation of complexes with cations whose diameter exceeds or falls below the cavity size of the CE, due to conformational distortion. If the cation diameter exceeds the cavity size of the CE, the cation can be forced out of the ring plane and be localized above or below the CE (Figure 8, B). If the cation diameter is too small for an ideal spatial fit, a partial (Figure 8, C) or complete (Figure 8, D) distortion of the CE framework towards increased coordination leads to better donor-acceptor interactions. This gain in enthalpy can compensate for the conformational tension.[43]

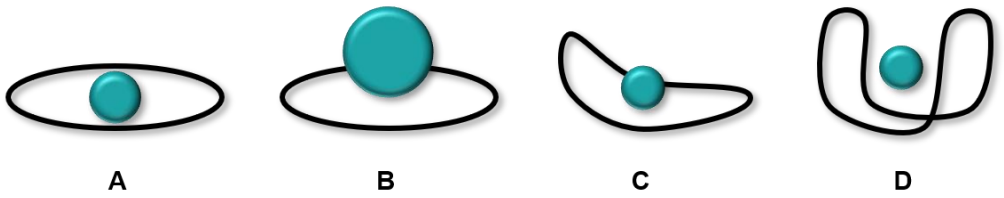

Figure 8: Schematic diagram of mononuclear complex structures. The crown ether (CE; black line) ideally encloses the cation (turquoise sphere; A), the cation can be located outside of the CE plane (B), the CE can be distorted and partially (C) or completely (D) enclose the cation (created by the author with data from Ref. [43]).

In addition to this classical single complexation of the ML (M=metal, L=ligand) type, dinuclear complexes of the M_2L type (Figure 9, left) can be formed if the cavity size exceeds the ion diameter by a multiple. Building on the complex B (Figure 8), a second CE is able to coordinate to the exposed side of the "oversized" ion. Complexes of this ML_2 type (Figure 9, middle), in which the ion is enclosed by two CEs, can be referred to as sandwich complexes. Extending this stacking by another layer (Figure 9, right), more complex structures such as M_2L_3 complexes can be built, which are termed "club sandwich complexes". Two ions are coordinated by two terminal ligands and a central bridging ligand.[33,43,48,62,65]

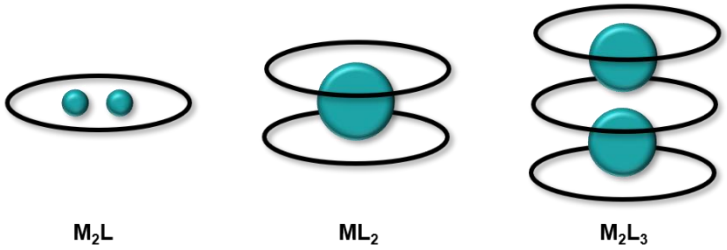

Figure 9: Schematic representation of dinuclear complexes M_2L, sandwich complexes ML_2 and club-sandwich complexes M_2L_3 (black line = crown ether (L), turquoise sphere = cation (M); created by the author with data from Ref. [43,65]).

This is illustrated by an example that is of particular relevance in the context of this work: Compared to other CEs, 12C4 or 14-crown-4 (14C4) have a high affinity for Li ions, which is due to the almost ideal size ratio of CE cavity to Li ion diameter. However, these CEs are also capable of coordinating larger ions such as sodium or potassium, as part of a distorted structure or ML_2 sandwich complexation. The latter is enthalpically favored by the increased number of donor-acceptor interactions.[33,59,68,69] Since this work is essentially addressing the efficiency of Li ion-selective systems, the question arises regarding maximizing selectivity towards other alkali metal ions. One possible approach is the introduction of sterically demanding substituents to the CE structure in order to suppress the coordination of more than one of these ligands.[69,70] An alternative and particularly interesting approach is the targeted utilization of sandwich complexation through the use of smaller CEs such as 9-crown-3 (9C3). 9C3 forms ML_2 complexes with Li ions, the coordination of larger ions is virtually eliminated by the small cavity. The result is an effective selectivity mechanism benefiting Li ions. The ion selectivity of some CEs (9- to 18-membered) with respect to the alkali metal ions Li, Na and K based on the size fit criterion is shown in Figure 10.

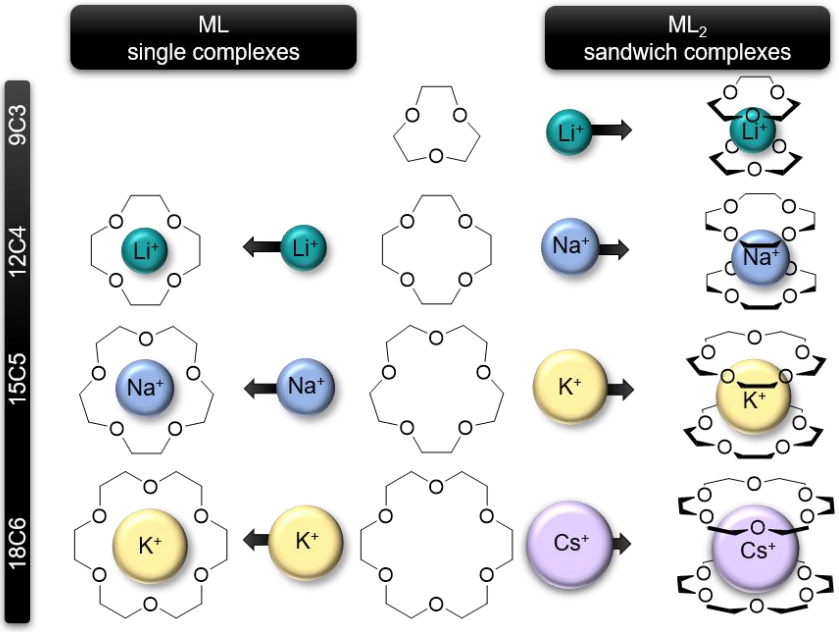

Figure 10: Visualization of the size fit criterion: Crown ethers of different sizes (9C3, 12C4, 15C5, and 18C6) with lithium, sodium, potassium, and cesium ions. ML or ML_2 complexes are formed (created by the author with data from Ref. [43,71,72]).

The attentive reader will certainly wonder whether there is a conflict with the formation of ML structures with the divalent beryllium ions (ion diameter 54 pm for CN 4).[73] This would indeed be conceivable, but is neglected in the context of this work, as the concentration of beryllium ions in seawater is insignificantly small at around 2–30 pM.[74] A greater selectivity problem is posed by the magnesium ion, which is very similar to Li in diameter (144 pm) but, as in the potassium-barium comparison, has a higher charge density due to its divalence.[75] This problem is addressed in particular in publication 1.

3.2.3. Structural Variants of Crown Ethers

Traditionally, the classical structure of a CE is often considered to be the crown-like, cyclically alternating arrangement of ethylene groups and oxygen units. However, the structural variety of CEs is far more diverse. A comprehensive description of these (and their terminology) is beyond the scope of this thesis, but some important examples will be highlighted including the specific effect of the ligands on the coordination of Li ions.[iv]

A comparatively simple but effective modification of CEs is the exchange of heteroatoms in the macrocycle. Classically, oxygen atoms are substituted with nitrogen, sulfur, or phosphorus in order to tailor the electronic properties and coordination preference of the ligand. The nomenclature of such CEs follows the subsequent rules: The number of substituted heteroatoms is indicated by numerical prefixes (di-, tri-, tetra-, etc.), the type of heteroatoms

[iv] Further information regarding the nomenclature of CEs can be found in the literature.[46,48,195]

by the Hantzsch-Widman nomenclature as heteroatom prefix (*aza*=N, *oxa*=O, or *thia*=S; e.g., 1,10-di*aza*-18-crown-6 in Figure 11, A). This strategy is of central importance in publication 1, in which, *inter alia*, the Li selectivity of mixed donor CEs of different diameters was investigated. Based on the concept of *Hard and Soft Acids and Bases* (HSAB), the selectivity towards different cations can be specifically influenced by replacing one or more donor atoms in the ring. The general idea is that "hard" ions with low polarizability are most efficiently coordinated by similarly "hard" donors. "Softer", more polarizable ions with low charge density are correspondingly better coordinated by donors that are "softer" and have a higher polarizability. For example, the "harder" K^+ is preferentially complexed with 18C6, while a donor substitution with only two nitrogen or sulfur atoms leads to a more favorable complexation of Ag^+ or Pb^{2+}.[43,45,46,48,76,77]

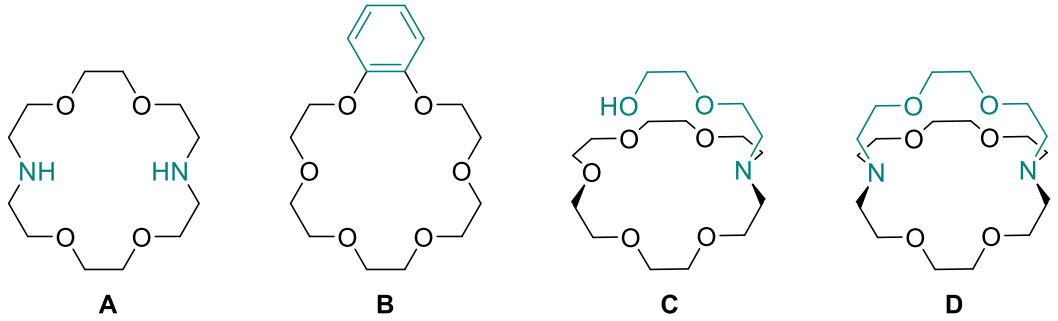

Figure 11: Schematic representation of various crown ethers with structural characteristics (highlighted in turquoise) of a heteroatom substitution by nitrogen (A, 1,10-di*aza*-18-crown-6), an aromatic substituent (B, benzo-18-crown-6), an *N*-pivot Lariat ether (C), and a cryptand (D, [2.2.2] cryptand; Created by the author with data from Ref. [46,48,69]).

Introducing substituents to the basic CE structure greatly expands the structural diversity of supramolecular systems and allows tailoring of CEs to specific applications. Depending on the desired reactivity, electron density, functionality, conformation, steric requirements, suitable substituents can be chosen to achieve the desired motif. An example is the introduction of one or more benzene substituents (Figure 11, B), which serve as sites for covalent attachment and enable aromatic interactions. Benzene rings also stabilize the structure by reducing the polyether ring's flexibility, which can affect cation selectivity. For instance, Swain *et al.* showed 12C4 and B12C4 had similar Li^+/Na^+ recovery ratios in extraction experiments, while 14C4 demonstrated a 4-fold higher Li selectivity compared to its aromatic analogue benzo-14C4.[33] The smaller Li fits well with the 12-membered CEs, but requires a slight conformational change with the 14-membered CEs, likely limited by the rigid benzene substituent. Additionally, electron-shifting substituents on the benzene ring can modulate the CE affinity for specific cations. The substituents are named according to classical nomenclature and prefixed to the CE name.[33,43,46–48,78]

Another structural variation of the classical CE structure is the *lariat ether*, a term introduced by G. Gokel in 1980.[79] The name derives from the long side chains covalently bound to the CE

framework (Figure 11, C). The designation *N*-pivot or *C*-pivot specifies the connecting atom. These lariat-like arms, often functionalized, extend into or over the ring and can support cation complexation, increasing both the stability and the selectivity of the host-guest complex. For example, Wakita *et al*. synthesized a variety of Li-selective *C*-pivot lariat ethers bearing an electron-donating side arm. In particular, the introduction of a quinolinyloxy pendant to 13-crown-4 was very successful in terms of selective Li coordination.[80] Lariat ethers with two or three branches are also known from literature to be bibracchial or tribracchial lariat ethers.[46,69,79,81–83]

Cryptands, which are already known from the introduction of the cryptate effect in section 3.2.2, build exceptionally stable complexes. As a reminder, these CE structures have a lateral chain that bridges the cavity and contains donor functions for the coordination of cations. Coordination in three spatial dimensions enables multiple enthalpically favored ligand-cation interactions. Unlike lariat ethers, cryptands are not kinetically inhibited, as the interacting arm is fixed on both sides of the CE. The cryptand acts as a pre-organized, macrocyclic ligand that encapsulates the cation in a cage-like structure, enabling particularly stable complex formation. The nomenclature of the cryptands is given by the prefix [x,y,z] where x, y and z represent the number of ethyleneoxy units of the linker arms.[43,45–48,83] This is illustrated in Figure 11, D. For example, the cryptand [2.1.1] with a cavity size of 150–168 pm provides the perfect binding cavity for the Li ion with very high selectivity towards sodium or magnesium ions. By completely enclosing the ion, interactions are maximized and the cryptate effect can be observed, since the complex stability is 200 000 times that of 12C4.[83] In order to embed cations as effectively as possible in the CE, it would therefore appear reasonable to utilize cryptands. However, identifying a suitable mechanism for the decomplexation of the cation, as would be necessary for a reusable material, is significantly more challenging. For this reason, conventional CEs were utilized in this study.

3.2.4. Quantification of Complex Stability

In the previous section, the suitability of CEs as Li absorbers from aqueous media was described. The terms efficiency and selectivity were used. However, the question arises concerning the quantitative description of these parameters. For this purpose, two quantities are to be introduced, the equilibrium constant *K* and the capacity *q*. *K* was determined in publications 1 and 2, *q* in publication 3.

A typical set-up of a liquid-liquid extraction (LLE) is shown in Figure 12 to provide a better understanding of the process and to demonstrate the calculation of *K* and *q*. An organic solution (usually in dichloromethane (DCM)) of the CE or CE-containing material is overlaid with an aqueous solution of a Li salt (here lithium 3,5-diiodo-salicylic acid (LIS)). The phase interface is enlarged by mechanical mixing. Through interaction of the CE and the Li ion, the

hydrate shell is partially or completely removed and the ion is coordinated by the CE. The Li ion is transferred into the organic phase along with the UV active anion. After the termination of mixing and complete phase separation, the aqueous phase is analyzed *via* UV-Vis spectroscopy.[62,71,84]

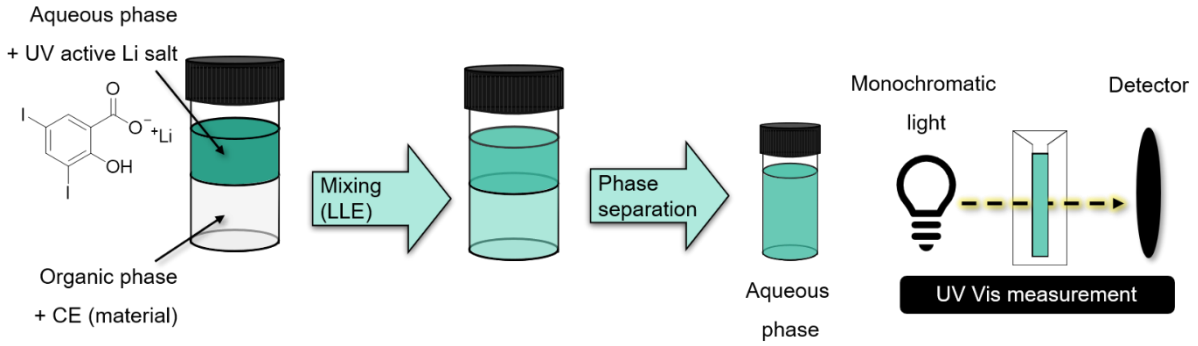

Figure 12: Liquid-liquid extraction for the quantification of the complexation of lithium ions from aqueous media with subsequent UV-Vis measurement of the aqueous phase to determine the concentration of 3,5-diiodo salicylate (created by the author according to Ref. [62]).

A typical complex formation of CE and metal salt can be described by Scheme 3.2.1, where M is the metal of charge *z* and Y is the counterion of charge *v*. *i, y,* and *n* are the stoichiometric factors of metal ions, counterions, and CEs respectively.[62,71]

$$(iM)^{z+}+(yY)^{v-}+nCE\rightarrow(M_iCE_n)^{iz+}(Y_y)^{yv-} \qquad 3.2.1$$

The equilibrium constant *K* (or complexation constant) can be determined from the law of mass action. For the reaction presented, this equation corresponds to equation 3.2.2. The concentration of the complex formed $(M_iCE_n)^{iz+}(Y_y)^{yv-}$, the formal concentrations of metal ion (corresponding to the concentration of the counterion), and the concentration of the CE must be known. In order to calculate the effective concentration from the formal concentration of the ions, the ion concentrations must be weighted by the ion activity (activity coefficient $a_\pm$). This can be calculated with the Davies equation for highly concentrated solutions (>0.5 mol L^{-1}). However, since in this work highly diluted solutions were used, the calculation of $a_\pm$ is carried out using the simplified Debye-Hückel equation, which is suitable for low ionic strengths (up to 0.01 mol L^{-1}), as in equation 3.2.3 with the stoichiometric factor *Q*, the mean activity coefficient $\gamma_\pm$, and the concentration *c*.[66,85,86]

$$K = \frac{[(M_i CE_n)^{iz+} Y_y^{yv-}]}{a_{\pm} \cdot [M^{z+}]^i \cdot [Y^{v-}]^y \cdot [CE]^n} \qquad 3.2.2$$

$$a_{\pm} = Q \cdot \gamma_{\pm} \cdot c \qquad 3.2.3$$

Q can be calculated *via* equation 3.2.4, applying the stoichiometric factors of the ions, i and y. $\gamma_{\pm}$ is calculated by equation 3.2.5, applying the ionic charges of the salt, the ionic strength I_s, and the dimensionless factor A, whereby A is 0.509 for water under standard conditions. I_s can in turn be calculated from equation 3.2.6.[66,87]

$$Q = \left(i^i \cdot y^y\right)^{\frac{1}{i+y}} \qquad 3.2.4$$

$$\gamma_{\pm} = 10^{-A|z_+ \cdot v_-| \cdot \sqrt{I_s}} \qquad 3.2.5$$

$$\sqrt{I_s} = \sum_i c \cdot z_+ \cdot v_- \qquad 3.2.6$$

With the equation 3.2.4, 3.2.5, and 3.2.6, equation 3.2.2 can be transformed to equation 3.2.7, with γ_+ and γ_- formally representing the activity coefficients of the cations and anions respectively. In practice, however, $\gamma_{\pm}$ is inserted.[66]

$$K = \frac{[(M_i CE_n)^{iz+} Y_y^{yv-}]}{Q \cdot \gamma_+ \cdot [M^{z+}]^i \cdot \gamma_- \cdot [Y^{v-}]^y \cdot [CE]^n} \qquad 3.2.7$$

The initial concentrations (indicated by the index “bc”) of the salt $[M_i^{z+}Y_y^{v-}]_{bc}$ and the CE $[CE]_{bc}$ are known, whereas the equilibrium concentrations must be determined. This is accomplished by a calibration that includes the targeted range of salt concentrations. According to Lambert-Beer's law in equation 3.2.8, the absorbance of the UV active anion scales linearly with its concentration, with the absorbance A, the initial light intensity I_0, the intensity of the transmitted light I_1, molar extinction coefficient ε_λ, and the path length d.[85,88]

$$A = \log\left(\frac{I_0}{I_1}\right) = \varepsilon_\lambda \cdot c \cdot d \qquad 3.2.8$$

From the linear equation of calibration, the salt concentration at equilibrium after the extraction (characterized by the index “ac”) $[M_i^{z+}Y_y^{v-}]_{ac}$ can be calculated by measuring the absorbance. The concentration of the UV active counterion corresponds to the concentration of the Li ion by equimolarity. The concentration of the complex $[(M_i CE_n)^{iz+}Y_y^{v-}]_{ac}$ can be determined *via* equation 3.2.9. The equilibrium cation concentration $[M_i^{z+}]_{ac}$, anion concentration $[Y_y^{v-}]_{ac}$, and CE concentration $[CE]_{ac}$ are calculated with equation 3.2.10, 3.2.11, and 3.2.12, respectively.[66]

$$\left[(M_iCE_n)^{iz+}Y_y^{yv-}\right]=[complex]=\left[M_i^{z+}Y_y^{v-}\right]_{bc}-\left[M_i^{z+}Y_y^{v-}\right]_{ac} \quad 3.2.9$$

$$\left[M^{z+}\right]^i=\left[M_i^{z+}Y_y^{v-}\right]_{bc}-i\cdot[complex]^i \quad 3.2.10$$

$$\left[Y^{v-}\right]^y=\frac{y}{i}\cdot\left[M_i^{z+}Y_y^{v-}\right]_{bc}-y\cdot[complex]^y \quad 3.2.11$$

$$[CE]^n=[CE]_{bc}-n\cdot[complex]^n \quad 3.2.12$$

Both the complexation efficiency of the free CEs and the fixed CEs can be defined not only by *K*, but also by the capacity *q*. q_{CE} refers to the amount of Li that is complexed per amount of CE n_{CE} and is calculated using equation 3.2.13 with *V*, the volume of solution. In the presence of a matrix, it is advisable to specify a capacity related to the mass of the material q_{poly} by equation 3.2.14.[89,90] The index “poly” results here from the material used.

$$q_{CE}=\frac{\left(\left[M^{z+}\right]_{bc}-\left[M^{z+}\right]_{ac}\right)V}{n_{CE}} \quad 3.2.13$$

$$q_{poly}=\frac{\left(\left[M^{z+}\right]_{bc}-\left[M^{z+}\right]_{ac}\right)V}{m_{poly}} \quad 3.2.14$$

3.3. COMPUTATIONAL METHODS IN QUANTUM CHEMISTRY

In addition to the previously described experimental methods for assessing complex stability, quantum chemical calculations offer an additional possibility for the systematic evaluation of host-guest complexes. This approach is explained in more detail in the following chapter and especially important for publications 1 and 3. A brief introduction to the basic concepts of quantum chemistry is followed by a description of density functional theory (DFT), which serves as a central tool for calculating electronic structures and analyzing molecular stabilities.[91]

The legitimate question arises as to what advantage a theoretical model offers over experimental methods that accurately represent real systems. This question is easily answered with regard to several aspects: Firstly, compared to experiments, computational chemistry modulations are generally more cost-efficient and significantly less time-consuming. Particularly when modeling novel molecules or materials, computational methods enable a detailed insight into structural and electronic properties without the limitations of synthetic restrictions, molecular instabilities or toxicological risks. In addition, simulated conditions allow specific variation of individual parameters (such as temperature, solvent environment, charge due to pressure), which is only possible to a limited extent experimentally. At the same time, it must always be borne in mind that the calculated results are model-based approximations that do not provide absolute values, but can be very useful for making theoretical predictions and gaining mechanistic insights. The choice of computational chemistry approach depends strongly on the aim of the calculation, the system's size and, in particular, the available computational resources. With a limited amount of time and resources, *semi-empirical* methods offer fast estimation of large molecules at the expense of accuracy, compared to *ab-initio* methods such as Hartree-Fock that offer higher accuracy without the use of empirical parameters. Due to the higher computational effort, these are popular for fundamental research on smaller molecules. DFT has established as an all-round method for numerous chemical systems, with moderate computational effort and high accuracy. However, the accuracy of the result is strongly dependent on the suitability of the selected functional. In fact, DFT is especially suitable for the calculation of CE–cation complexes.[63,92–95]

3.3.1. QUANTUM MECHANICAL BASICS

With the wave function ψ of a quantum mechanical system, all physical properties of this system can be determined as eigenvalues of the corresponding operators. For example, the total energy of the system E is obtained from the Hamiltonian $\hat{H}$. The central equation of quantum mechanics, the Schrödinger Equation (SE), describes how the quantum state of a

physical system changes with time, or, in the case of the time-independent SE as shown in equation 3.3.1, the resulting energy states of the system.[96–99]

$$\hat{H}\psi=E\psi \qquad 3.3.1$$

$\hat{H}$ for a many-body-problem (with the electrons e and the nuclei K) is given in equation 3.3.2. As a physical simplification, the internal structure of the nuclei, made up of protons and neutrons, can be neglected. The electrons and nuclei are therefore approximated as point charges.[96,97,99,100]

$$\hat{H}=-\underbrace{\sum_{i=1}^{N}\frac{\hbar^2}{2m_e}\nabla_i^2}_{\hat{T}_e}-\underbrace{\sum_{I=1}^{K}\frac{\hbar^2}{2M_I}\nabla_I^2}_{\hat{T}_K}+\underbrace{\sum_{i=1}^{N}\sum_{\substack{j=1\\ j>i}}^{N}\frac{e^2}{|r_i-r_j|}}_{\hat{V}_{ee}}+\underbrace{\sum_{I=1}^{K}\sum_{\substack{J=1\\ J>I}}^{K}\frac{e^2Z_IZ_J}{|R_I-R_J|}}_{\hat{V}_{KK}}-\underbrace{\sum_{I=1}^{K}\sum_{i=1}^{N}\frac{e^2Z_I}{|r_i-R_I|}}_{\hat{V}_{eK}} \qquad 3.3.2$$

h (with $\hbar$=h/2π) is the Planck constant, *m* and *M* describe the mass of the electron or nucleus. *N* and *K* are the numbers of electrons and nuclei in the system. *R* and *Z* refer to the coordinates or charges of the nucleus I, and *r* refers to the coordinates of the electron i. The definition of the charge of the electron is redundant. Basically, five terms can be defined separately, the first two of which describe the kinetic energy of the electron T_e or nucleus T_K. The following terms consider the potential energy of the electron-electron interaction V_{ee}, the nucleus-nucleus interaction V_{KK}, and the electron-nucleus V_{eK} interaction. Since protons have a significantly higher mass than electrons, the motion of the nuclei is negligible to a first approximation. The electrons therefore move in a static field of positive point charges. As a result, T_K is omitted and V_{KK} is considered constant. This simplification is known as the Born-Oppenheimer approximation and represents a fundamental approximation of quantum chemistry.[91,97,99,100]

The Born-Oppenheimer approximation leads to the electronic Hamilton operator $\hat{H}_{el}$ according to equation 3.3.3. By applying $\hat{H}_{el}$, the total energy of the system E_{tot} is obtained by adding the constant Coulomb repulsion V_{KK} to the resulting electronic energy E_{el} (equation 3.3.4). This allows a separation into the electronic SE in equation 3.3.5 with the electronic wave function ψ_{el}, and a nuclear SE.[96,97,99]

$$\hat{H}_{el}=\hat{T}_e+\hat{V}_{ee}+\hat{V}_{eK} \qquad 3.3.3$$

$$E_{tot}=E_{el}+V_{KK} \qquad 3.3.4$$

$$(\hat{H}_{el} + \underbrace{\hat{V}_{KK}}_{\text{constant}}) \psi_{el} = E_{tot} \psi_{el} \qquad 3.3.5$$

The electronic SE can be solved as a function of *R* for different molecular conformations of the same molecule. If the resulting energies are represented with respect to *R*, a potential energy hypersurface is obtained.[91,97] As the Born-Oppenheimer approximation is based on the mass gap between electrons and nuclei, the heavier the atoms in the system, the more accurate it becomes. It therefore represents a good simplification of the complex many-body problem, as the electronic Schrödinger equation can be determined for fixed nuclear positions. However, the exact solution of the electronic Schrödinger equation of an *N*-particle system remains computationally very complex. This is particularly the case with an increasing number of electrons, since the wave function generally depends on 3N spatial coordinates.[91,97]

To solve the time-independent SE, *ab initio* methods such as Hartree-Fock theory can be applied. The wave function of the many-body system is approximated by a Slater determinant, which in turn is constructed from several single-electron wave functions. The Slater determinant fulfills the physical requirements for a multi-electron wave function with regard to the Pauli principle and Pauli prohibition. Whereas the exchange interactions are explicitly considered in this approach, the electron correlation term of the energy is neglected. As a result, the calculated energy deviates strongly from the exact ground-state energy of the system. At this point, the density functional theory (DFT) approach provides an alternative approach that incorporates electron correlation effects more effevtively.[91,97,100]

3.3.2. DENSITY FUNCTIONAL THEORY (DFT)

The fundamental idea of density functional theory (DFT) is to determine a system's energy from the electron density, instead of the wave function. This approach enables the electronic properties of many particle systems to be calculated efficiently. The density functional $E[\varrho]$ defines the dependence of E on the electron density ϱ according to equation 3.3.6.

$$E = E[\varrho] \qquad 3.3.6$$

Previously, an *N*-electron system was described using the many-body wave function $\Psi = \Psi(\vec{r}_1,\ldots,\vec{r}_N)$ (with three spatial coordinates $\vec{r}$ for each electron). By introducing the electron density, the *N*-electron problem with $3N$ (or $4N$) [v] spatial variables is reduced to a three-dimensional problem with the variables $\vec{r}$ and $\vec{\varrho}$, thus considerably reducing the complexity of the problem. The electron density determines the probability of finding an electron at a certain

[v] Furthermore, the spin $\vec{s}$ can be considered as a coordinate of the electrons. If this is considered, Ψ depends on $4N$ spatial variables.[96,101]

point $\vec{r}_1$within a volume element $d\vec{r}_1$. This is accomplished by integration over all coordinates, except $\vec{r}_1$, according to equation 3.3.7.[91,96,97,101]

$$\varrho(\vec{r}_1)=N\int|\Psi(\vec{r}_1,\vec{r}_2,\vec{r}_3,\ldots,\vec{r}_N)|^2 d\vec{r}_2, d\vec{r}_3, \ldots, d\vec{r}_N \qquad 3.3.7$$

DFT is based on the Hohenberg-Kohn theorems established by P. Hohenberg and W. Kohn in 1964. These formulate a system of interacting particles in an external potential V_{ext}, resulting from electron-nucleus interactions and any external fields.[102]

Hohenberg-Kohn theorems

The first Hohenberg-Kohn theorem states that, for a given ground state density of a multi-particle system, there is a uniquely determined external potential. Thus, the ground state wave function and all physical properties of the system are clearly given by this density. The ground state electron density therefore contains all the information about the system. There is an unambiguous relationship between the ground state density and the ground state function resp. the external potential according to equation 3.3.8 and 3.3.9.

$$\varrho(\vec{r})\leftrightarrow\Psi=\Psi(\vec{r}_1,\vec{r}_2,\vec{r}_3,\ldots,\vec{r}_N) \qquad 3.3.8$$

$$\varrho(\vec{r})\leftrightarrow V_{ext}(\vec{r}) \qquad 3.3.9$$

The second Hohenberg-Kohn theorem applies the principle of variation (equation 3.3.10): A universal energy functional exists on which the exact ground state energy depends. The universal functional gives energies for test densities that are higher than or equal to the exact ground state energy. The minimum energy is found if the test electron density equals the exact ground state density.[91,97,98]

$$E[\varrho(\vec{r})_{test}]\geq E_0 \qquad 3.3.10$$

The total energy E of the multi-electron system (equation 3.3.11) consists of the kinetic energy of the electrons E_T, the interaction energy of the electrons with the nuclear field E_V, the electron-electron (Coulomb) interaction energy E_J and their exchange energy E_X. E_C denotes the correlation energy resulting from electron correlation that are not captured by the model of the independent particles.[97]

$$E=E_T+E_V+E_J+E_X+E_C \qquad 3.3.11$$

These considerations are valid not only for ideal but also for non-homogeneous (realistic) electron density distributions. In contrast to wave function-based methods, the exact density functional already contains the electron correlation, which in turn leads to significantly more accurate results. The difficulty, however, remains in the fact that the exact form of the functional and the true electron density are unknown. Despite these uncertainties, the high accuracy of DFT results is indisputable.[91,96–98,103] Exact expressions can be defined for the classical potentials, E_V and E_J, whereas this is more challenging for the non-classical terms. The Kohn-Sham (KS) formalism provides suitable approximations for the exact energy functional that relates the energy to the electron density.

Kohn-Sham formalism

$E[\varrho]$ can be separated, as in equation 3.3.12, into a system-dependent part (external potential) and a system-independent part, which includes the kinetic energy of the non-interacting electrons, the classic Coulomb term and the exchange-correlation energy.

$$E[\varrho] = \underbrace{T[\varrho] + V_{ee}[\varrho]}_{\text{system-}\mathbf{in}\text{dependent}} + \int \underbrace{V_{ext}(\vec{r})\varrho(\vec{r})\mathrm{d}\vec{r}}_{\text{system-dependent}} \qquad 3.3.12$$

Suitable expressions must be found to approximate these system-independent parameters. The fundamental premise of the orbital-based KS-DFT introduced by W. Kohn and L. J. Sham in 1965 is the replacement of the real system of N interacting by a virtual system of N non-interacting electrons. However, the ground state electron densities of both systems are identical. The ground state functions of the virtual system can be defined as Slater determinants. These consist of several (N) one-electron equations, the so-called Kohn-Sham-orbitals ψ_k. The system's electron density results from the sum of the electron densities of these KS orbitals according to equation 3.3.13.[97,99,100]

$$\varrho(\vec{r}) = \sum_{k=1}^{N} \mathrm{e}\left|\psi_k(\vec{r})\right|^2 \qquad 3.3.13$$

Therefore, explicit expressions exist for the kinetic energy functional (as an approximation of the exact kinetic energy of the virtual system) and for the Coulomb functional. These can be calculated directly from the KS orbitals or the electron density. However, all contributions to the total energy that cannot be explicitly defined *via* the KS system – for example, the exchange and correlation energies of the electrons, which are present in the real system – are summarized and modeled in the so-called exchange-correlation functional $E_{xc}[\varrho]$.[97,99,100]

3.3.3. EXCHANGE CORRELATION FUNCTIONAL

The KS equations therefore allow an exact description of the system if the exchange-correlation functional was known. The functional of the total energy corresponds to equation 3.3.14.

$$E[\varrho]=T_s[\varrho]+J[\varrho]+E_{XC}[\varrho]+\int \underbrace{V_{ext}(\vec{r})\varrho(\vec{r})d\vec{r}}_{\text{system-dependent}} \qquad 3.3.14$$

$T_s[\varrho]$ describes the functional of the kinetic energy of the virtual system, the functional $J[\varrho]$ contains the coulomb fractions of the electron interactions. $E_{XC}[\varrho]$ contains the small deviation of the kinetic energy of the real system from the reference system. The major part is contributed by the exchange energies (Pauli principle) and the correlation energies of the electron interactions.[97,99]

Based on this expression, the aim is to find the ideal exchange-correlation functional for the description of the system. Various approximations of the exact $E_{XC}[\varrho]$ have been published, all of which differ in accuracy and complexity. A brief estimation of these different levels of approximation, is given in Figure 13. The so-called *Jacob's Ladder* is largely established, although new studies offer a deviation from that estimate. For example, Mardirossian *et al*. published a more exact estimation of around 200 functionals.[104] When considering Jacobs ladder as a conceptual framework for classifying functional complexity, it provides a good assessment.

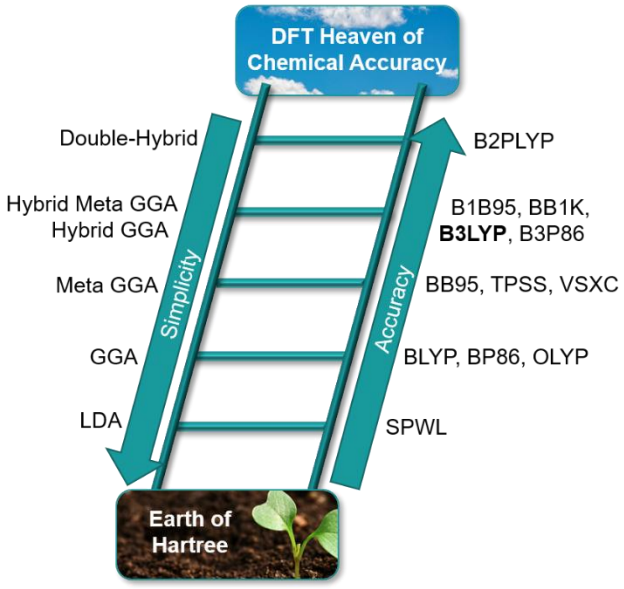

Figure 13: Jacob's ladder, proposed by J. Perdew, illustrating the hierarchy of different generation density functional theory (DFT) functionals. From "Earth of Hartree", the accuracy of the functionals is increasing from simple local density approximation (LDA), the generalized gradient approximation (GGA), the meta GGA), the hybrid GGA and the hybrid meta GGA, and finally the double hybrids. Theoretically, maximum accuracy is achieved at the end of the ladder, the „DFT Heaven of Chemical Accuracy". For each level, example functionals are given. B3LYP is highlighted due to its application in this work (created by the author according to Ref. [96,105,106]).

The Local Density Approximation (LDA), which assumes that the exchange correlation energy is a function of the local electron density, has the highest simplicity. The Generalized Gradient Approximation (GGA) includes both the local density and the density gradient, the meta-GGA extends over the kinetic energy density or the Laplacian. The B3LYP functional approximated by the hybrid GGA (H-GGA) combines GGA functionals (such as Becke and Lee-Yang-Parr) with a fraction of exact Hartree-Fock exchange energy and is one of the most popular approximations for the exact $E_{XC}[\varrho]$. The highest level of accuracy is achieved by double-hybrids, which also take into account virtual orbitals and explicit electron correlation.[96,107–109] Nevertheless, the decision on the $E_{XC}[\varrho]$ depends on the problem under consideration, as there is no generally applicable functional.

In order to find the ground state electron density $\varrho(\vec{r})$, a self-consistent solution cycle (*self-consistent-field* SCF) is applied, shown schematically in Figure 14. In this iterative algorithm, V_{eff} is obtained from an initial, estimated electron density $\varrho^{in}(\vec{r})$. As a result of solving the KS equations, a new electron density $\varrho^{out}(\vec{r})$, is obtained. If the difference between $\varrho^{in}(\vec{r})$ and $\varrho^{out}(\vec{r})$ is found to be significant, the cycle is repeated, otherwise self-consistency is reached.[97,99,100,107]

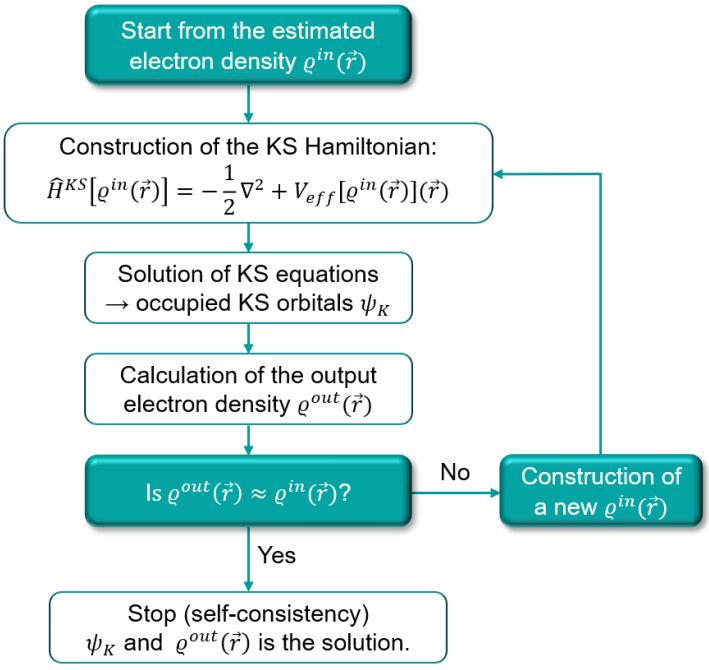

Figure 14: Self-consistent field (SCF) cycle for the solution of the Kohn-Sham equations (created by the author according to Ref. [107]).

The KS orbitals can be approximated by different basis sets. Gaussian-type orbitals (GTOs) are typically used for this purpose, as the combination of several GTOs provides a very good approximation of the exponentially decreasing radial parts of atomic orbitals. Consideration of the problem is also elementary when selecting the basis set, as the suitability depends strongly on the system.[96,110] The basis set of highest complexity used in this work is the def2-TZVP.

Variations in basis sets will be explained in more detail with reference to def2-TZVP. Def2-TZVP is a modernized version of the def basis set developed by Weigend and Ahlrich. It describes the valence orbitals with three functions (Triple-zeta, TZ), with a focus on the accurate description of the valence electrons (V). Additional functions are employed for the consideration of polarization (P) of the orbitals in chemical bonds.[110–112]

3.3.4. GEOMETRY OPTIMIZATIONS

Geometry optimizations are a central step in quantum mechanical calculations for determining the most energetically favorable structure of a molecule in a certain state. As outlined in section 3.3.1, molecular structures can be described based on the BO approximation with fixed nuclear coordinates. A molecule of a certain structure and electronic status has a certain energy. If the structure is varied iteratively (Figure 15), this changes the energy. A potential energy surface (PES) is obtained which formally depends on $3K–6$ (or $3K–5$ in the case of linearity) independent coordinates, corresponding to the number of nuclear degrees of freedom.[97,100]

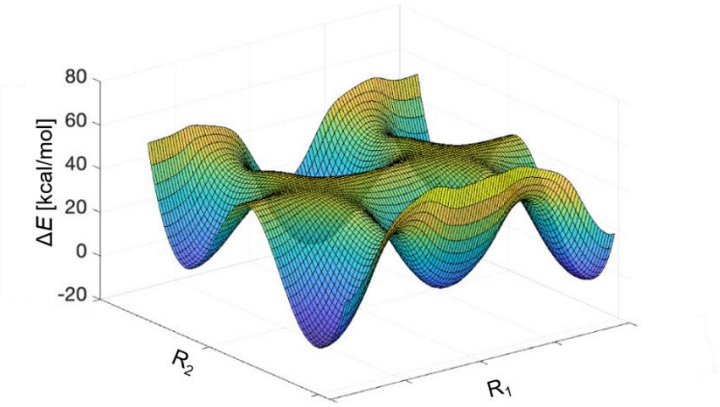

Figure 15: Illustration of a potential energy surface (PES). Several saddle points and local minima are visible. Reprinted and adapted with permission from Ref. [113]. Copyright 2021 American Chemical Society.

The energetic minimum on the PES corresponds to the most stable structure. To ensure that it is a global and not just a local minimum, the absence of imaginary frequencies is confirmed by frequency calculations. For the optimization, gradient methods are used to indicate the direction of the coordinate variation according to the negative gradient of the energy. Newtonian or quasi-Newtonian methods are used as numerical optimization methods for the iterative adjustment of the nuclear coordinates. In both cases, the second derivative of the energy (Hessian) is analyzed. Newtonian methods calculate this explicitly, which makes them accurate but more computationally intensive than quasi-Newtonian methods, which merely approximate the Hessian. In addition to the minimum, other points on the PES are also of interest, such as saddle points, which correspond to transition states, or maxima, which indicate activation energies.[97,114–116]

Unless otherwise defined, geometry optimizations are performed in vacuum. While this approach can be useful for some scenarios, including solvent effects is often essential for obtaining realistic results. Especially when strong interactions with the solvent are present, such as the formation of hydrogen bonds, the consideration of solvent effects becomes more important. Solvent effects can be modeled by incorporating the dielectric constant ε *via* polarizable continuum models (PCM).

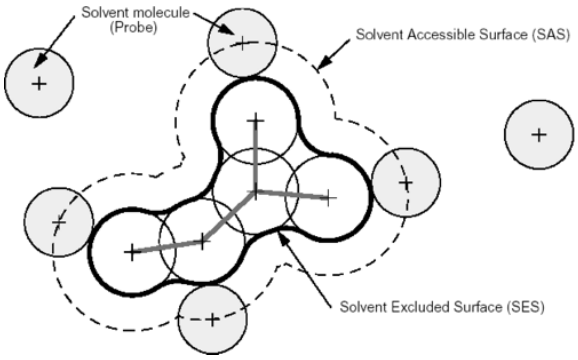

Figure 16: Illustration of the modeling of a solvent *via* a polarizable continuum model (PCM) with the surface accessible to the solvent (SAS) and the non-accessible surface (SES). Reprinted with permission from Ref. [117]. Copyright 2005 American Chemical Society.

The strength of the electrostatic interaction decreases with distance r^{-1}, whereby distance-dependent solvent models are implemented in some cases.[116] By representing the solvent as a continuous dielectric medium (Figure 16), the computational effort compared to explicitly modeling individual solvent molecules is reduced enormously. The polarization of the medium by the charge of the molecule and the effect of the polarization on the molecule are considered by electrostatic interface parameters. Smaller molecules can be successfully modelled with the Integral Equation Formalism (IPCM), larger molecules rather by modelling the solvent as an ideal conductor *via* the conductor like PCM (CPCM)[vi].[117–119]

3.3.5. Population and Orbital Analyses

The distribution of electron density within molecules is particularly interesting with regard to the interpretation of the stability of host-guest complexes. Typically, the concepts of Mulliken[120] or Löwdin[121] can be applied, which divide the electron density on the basis of (orthogonalized) basis functions. However, these methods encounter difficulties since a complete basis set cannot be meaningfully partitioned into atomic subsets. Two methods will be explained below that are relevant to this work: Hirshfeld's population analysis and natural bond orbital (NBO) analysis.[95,110,122]

[vi] Further information and mathematic fundaments regarding solvent models can be found in Ref. [117].

Hirshfeld Population analysis

In order to calculate the charge distribution between the atoms of a molecule, two systems are compared in the Hirshfeld population analysis: The actual molecule and a promolecule.

The actual molecule has the actual electron density $\varrho(\vec{r})$, but the individual atomic electron densities $\varrho_i(\vec{r})$ are unknown. The construction of a promolecule is used to generate a type of distribution key for the electron density within the molecule. The promolecule designates an assembly of atoms analogous to the actual molecule, at the identical spatial positions but excluding interactions between the atoms. The sum of the electron density of these "free" atoms $\varrho_i^{free}(\vec{r})$ gives the total electron density of the promolecule $\varrho^{pro}(\vec{r})$ according to equation 3.3.15.

$$\varrho^{pro}(\vec{r}) = \sum_i \varrho_i^{free}(\vec{r}) \qquad 3.3.15$$

An atom-specific distribution function is provided by equation 3.3.16 with a weighting factor $w_i^{Hirsh}(\vec{r})$, determining the proportion of $\varrho^{pro}(\vec{r})$ accounted for by each atom.

$$w_i^{Hirsh}(\vec{r}) = \frac{\varrho_i^{free}(\vec{r})}{\varrho^{pro}(\vec{r})} \qquad 3.3.16$$

The difference of $\varrho^{pro}(\vec{r})$ and $\varrho(\vec{r})$ is called molecular deformation density $\varrho^{def}(\vec{r})$ and can be calculated by equation 3.3.17. Subsequently, in order to define the atomic deformation density $\varrho_i^{def}(\vec{r})$, equation 3.3.18 can be applied.

$$\varrho^{def}(\vec{r}) = \varrho(\vec{r}) - \varrho^{pro}(\vec{r}) \qquad 3.3.17$$

$$\varrho_i^{def}(\vec{r}) = w_i^{Hirsh}(\vec{r}) \cdot \varrho^{def}(\vec{r}) \qquad 3.3.18$$

The result of the integration over the entire space according to equation 3.3.19 is the desired Hirshfeld charge q_i, i.e. the effective electron number per atom.[110,122–124]

$$q_i = -\int \varrho_i^{def}(\vec{r})\, \mathrm{d}r \qquad 3.3.19$$

Natural Bond Orbital (NBO) analysis

The concept of natural bonding orbitals (NBOs) was introduced by Reed *et al*. and serves to describe electron distribution in molecules through localized orbitals. NBOs represent the closest possible analogy between the representation of the wave function and the Lewis structure with an agreement of up to >99%. Each orbital property is displayed with the maximum possible electron density. This approach enables the description of lone electron pairs, multicenter bonds, as well as σ- and π-bonds.[125,126]

The NBOs are part of a sequence of evolution from simple atomic orbitals (AOs) to canonical molecular orbitals MOs:

$$\text{AOs} \rightarrow \text{NAOs} \rightarrow \text{NHOs} \rightarrow \text{NBOs} \rightarrow \text{NLMOs} \rightarrow \text{MOs}.$$

This sequence includes valence-shell orbitals (natural atomic orbitals, NAOs) optimized for a specific wave function, the resulting orthonormal hybrid orbitals (natural hybrid orbitals, NHOs) and the natural (semi-)localized molecular orbitals (NLMOs).[125–127]

Bonding NBOs σ_{AB} and antibonding NBOs σ^*_{AB} result from equation 3.3.20 and 3.3.21. h_A and h_B represent the NHOs belonging to the atoms A and B and the associated polarization effects c_A and c_B, ranging from $c_A=c_B$ for covalent and $c_A>>c_B$ for ionic bonds.

$$\sigma_{AB}=h_A\cdot c_A+h_B\cdot c_B \qquad 3.3.20$$

$$\sigma^*_{AB}=h_A\cdot c_A-h_B\cdot c_B \qquad 3.3.21$$

σ_{AB} yields “Lewis type” donor NBOs, which have an occupancy close to 2 as an analogy to free electron pairs, and σ^*_{AB} complementary “non- Lewis type” acceptor NBOs with an occupancy close to 0. So, in which way is this useful in the context of this work? In analogy to a cation-CE complex, the stabilization energy $\Delta E^{(2)}_{\sigma\rightarrow\sigma^*}$ can be calculated by $\sigma_{AB} \rightarrow \sigma^*_{AB}$ interaction according to equation 3.3.22. $\hat{F}$ is the Fock operator, ϵ_σ and ϵ_{σ^*} are the energies of the acceptor and donor NBO. The empty acceptor NBO is assigned to the cation, the donor NBO to the heteroatom in the CE. $\Delta E^{(2)}_{\sigma\rightarrow\sigma^*}$ indicates the extent to which the delocalization between the NBOs leads to a more energetically stable structure.[125–127]

$$\Delta E^{(2)}_{\sigma\rightarrow\sigma^*}=-2\cdot\frac{\langle\sigma|\hat{F}|\sigma^*\rangle^2}{\epsilon_{\sigma^*}-\epsilon_\sigma} \qquad 3.3.22$$

3.4. POLYMERS

The high socioeconomic relevance of Li, the fundamental concepts of using CEs to complex Li and the systematic quantum mechanical investigation of these structures have been described so far. The last section of this introduction is dedicated to another, equally important part of this work: polymers. This rather drastic break in topic should be briefly explained. The fundamental aim of this work was to extract Li from seawater. A tool for selective and effective extraction was presented using cation-CE complexes. In order to go beyond theoretical considerations, Liquid-Liquid Extraction (LLE) can be performed. However, this is hardly applicable on an industrial scale, as a large quantity of organic solvent is required as a carrier material. For practical applications, it makes sense to use a different matrix. At this point, polymers can serve as key functional materials. They offer the possibility to attach CEs in different, highly surface-active structures and still leave them accessible for host-guest complexes. Block copolymers exhibit self-assembly properties that are fundamental to this function. The understanding of polymer architectures and self-assembly are fundamental for publication 2 and 3.

3.4.1. POLYMER ARCHITECTURES AND BLOCK COPOLYMERS

Polymers are formed by linking smaller molecules, the monomers, whereby characteristic structures consisting of recurring units are formed. If the system is limited to one type of monomer, it is a homopolymer; if two or more different types are present, it is a copolymer. Copolymers allow an enormous structural variance in the polymer architecture. This is not only by the variation of monomer units, but the particular arrangement of these along the chain. Figure 17 gives an overview of different copolymer topologies.[128–130]

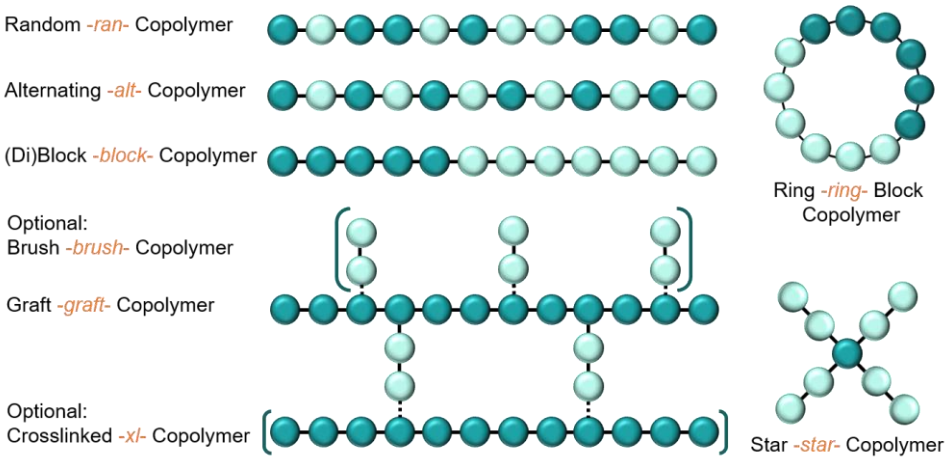

Figure 17: Overview of different polymer sequences and architectures for two types of monomers. The abbreviations for the respective structure type are shown in orange. Created by the author according to Ref. [128–130].

In a random AB copolymer, the monomer units are arranged truly random without preference along the linear chain. Although in some work the term “statistical” is used as a synonym, the

two structural types are not equal. While the random structure type portrays a subcategory of statistical copolymers, the latter describes the arrangement according to statistical laws, like Markovian. Alternating arrangements of A and B monomers result in alternating copolymers. Especially block copolymers are of particular interest for the purpose of this work. These consist of two or more linear blocks each of a certain type of monomer – e.g. AB di-block copolymers, ABA tri-block copolymers, or ABC tri-block copolymer. With the same sequential connection, but a different topological arrangement of the blocks, a vast variety of architectures can be created. If a block is grafted onto a continuous main chain (also known as a backbone), *graft*-copolymers are generated. If these grafted side chains are short and numerous, so-called (*bottle*)*brush*-copolymers can be produced. The connection to an additional main chain forms *crosslinked*-copolymers, suitable for the formation of networks. The designation of the copolymer architectures is often based on optical association, as in the case of circular *ring*-copolymers and *star*-copolymers, representing a number of blocks starting from a core.[128–131]

The monomer distribution within a polymer chain is rarely completely random. It is much more probable that the monomer exhibiting higher reactivity will react slightly in preference. For polymerizations with controlled and sequential chain growth, this leads to the formation of so-called gradient (*grad*-)copolymers. The composition of a copolymer at a certain monomer concentration ratio can be calculated according to the Mayo-Lewis equation (equation 3.4.1.1) for radical polymerizations. Herein [A] and [B] are the concentrations of the monomers A and B, r_1 and r_2 are the reactivity ratios according to equation 3.4.1.2 and 3.4.1.3.

$$\frac{d[A]}{d[B]} = \frac{[A]}{[B]} \cdot \left[\frac{r_1[A]+[B]}{r_2[B]+[A]}\right] \qquad 3.4.1.1$$

If the active, growing chain end is carrying monomer A, the addition of monomer A or B is indicated by the rate constants k_{AA} respectively k_{AB}. Similarly, k_{BB} and k_{BA} describe the addition of monomer B respectively A to a growing chain end of type B.

$$r_1 = \frac{k_{AA}}{k_{AB}} \qquad 3.4.1.2$$

$$r_2 = \frac{k_{BB}}{k_{BA}} \qquad 3.4.1.3$$

With this, a determination of the preferred monomer to be incorporated into the chain at the respective reaction time is enabled. As the concentration ratio of the monomer changes during the reaction, the initial calculated composition is not necessarily the same as the final composition.[129,131] A deeper understanding of the monomer reactivities and their effects

requires a look at the underlying polymerization technique, which is highly relevant in the context of this work: the radical polymerization.

3.4.2. (CONTROLLED) RADICAL POLYMERIZATION

Polymers are accessible by a wide assortment of mechanisms. Polycarbonates or polyesters, for example, are obtainable *via* polycondensations, polyurethanes, for example, *via* polyadditions. Alongside these step growth polymerizations, chain growth reactions are feasible. These chain growth reactions can be cationic, anionic, coordinative, or radical induced, some of which are allow for the synthesis of controlled sequenced copolymers.[130,131]

Free Radical Polymerization

The mechanism of the free radical polymerization starts with the initiation step, which consists of two steps – initiator radical formation and radical addition to the monomer. Typically, initiator molecules can either be cleaved homolytically or undergo single-electron transfer processes. The choice of initiation technique depends strongly on the reaction conditions. For example, peroxides or azo-compounds decompose at elevated temperatures (thermolysis), including the decomposition of dibenzoyl peroxide at 40–90 °C with the formation of two benzoyl radicals or the thermal decomposition of azobis(isobutyronitrile) (AIBN) at 30–80 °C with the elimination of nitrogen and two cyanopropyl radicals, analogous to equation 3.4.2.1.[130,131]

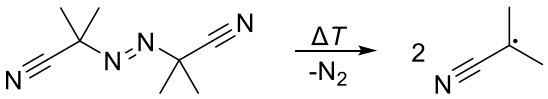

AIBN 3.4.2.1

AIBN can be decomposed not only thermally but also by exposure to UV light, albeit with low efficiency. Photochemical initiators, i.e. initiators whose bond cleavage can take place photolytically, include benzophenone (equation 3.4.2.2) or benzoin alkyl ether. In both cases, a benzoyl radical and either a phenyl or alkoxybenzyl radical are formed. [130,131] One advantage of this method is the excellent and instantaneous control of the external stimulus.

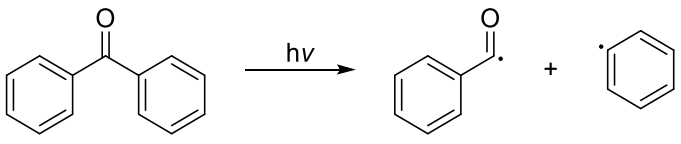

Benzophenone 3.4.2.2

Radicals can also be generated from redox reactions, for example from peroxides and hydroperoxides by using transition metal ions such as iron(II) or cobalt(II). For aqueous systems, a combination of a persulfate ion and a bisulfite ion is suitable, whereby a sulphate

ion, a sulphate radical anion, and a bisulfite are formed.[130] Furthermore, initiation can be achieved by ionizing radiation (γ- or electron irradiation).[131]

In the actual polymerization initiation, the radical adds to the π-system of a monomer, resulting in an active center (shown as an example in equation 3.4.2.3).

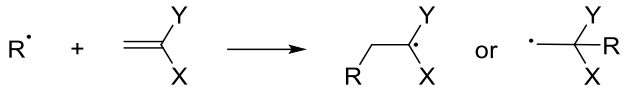

3.4.2.3

Since the radical can add on both sides of the double bond, either a secondary or a primary monomer radical is formed, with the secondary radical being more stable and the reaction being less sterically hindered.[130,131]

The propagation describes the sequential addition of further monomer units to the active center (monomer radical). This addition is also subject to the radical stability of the resulting product and the steric hinderance of the reaction. Theoretically, head-to-tail and head-to-head additions are possible, of which the head-to-tail reaction is generally preferred. Interferences in the sequence are usually very small. The addition takes place according to equation 3.4.2.4, where *n* is the number of added monomers.[130,131]

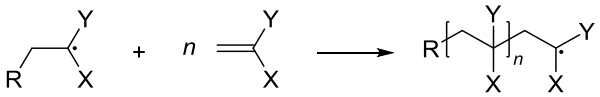

3.4.2.4

Polymerization can be terminated *via* recombination and disproportionation. Recombination (equation 3.4.2.5) involves the combination of two radicals. These can be all radicals which are present in the system, the molecular weight of the dead chain increases accordingly. The disproportionation (equation 3.4.2.6) proceeds while maintaining the molecular weight; a hydrogen is transferred from one growing chain to another, creating a saturated and unsaturated hydrocarbon. Depending on the monomer and polymerization conditions, preference is given to which process occurs.[130,131]

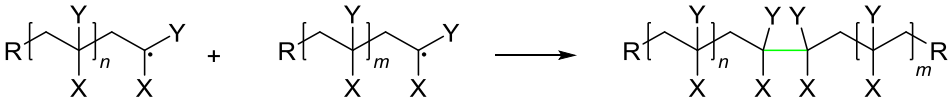

3.4.2.5

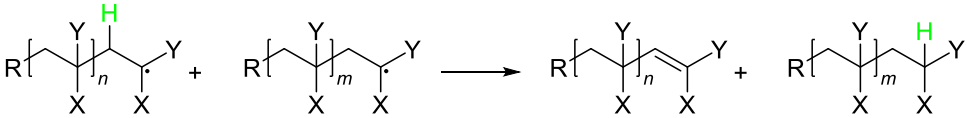

3.4.2.6

Radical polymerizations allow rapid monomer conversion to the polymer due to the highly reactive active centers, but at the expense of molecular weight control. The uncontrollable termination results in polymers with high dispersities. Block copolymers are not accessible with this method, due to uncontrolled nature of the polymerization and differing reactivities of the monomers. A mixture of polymers of different monomer compositions and chain length will most likely be formed.[129,131]

Controlled Radical Polymerization

To meet this challenge while maintaining the simplicity and robustness of the radical polymerization technique, controlled radical polymerization techniques have been developed.[132] These allow for a more precise control of molecular weight and polymer architecture. Thus, *transfer* reagents are utilized. Instead of or in addition to conventional initiators, so-called *inifer* reagents (*ini*tiator trans*fer* agents) can be applied. These generate active and persistent, stable radicals. An equilibrium is formed between small quantities of active radicals and larger quantities of dormant radicals, which is unique depending on the mechanism. The use of transfer reagents not only enables controlled initiation, but also reversible deactivation reactions. The polymerization features are similar to those of ionic living polymerizations, which is why they are often referred to as living radical polymerizations, although the term should not be used synonymously with controlled radical polymerizations. These mechanisms include the common techniques Atom-Transfer Radical Polymerization (ATRP), Nitroxide-Mediated Radical Polymerization (NMP) and Reversible-Addition-Fragmentation Chain-Transfer Radical Polymerization (RAFT), the latter of which is particularly relevant in the context of this work. NMPs are controlled by stable nitroxide radicals formed by thermolytic cleavage of alkoxyamines, which reversibly generate the dormant species with the active chain radicals. ATRP is initiated *via* alkyl halide initiators in combination with transition metal complexes. The reversible atom transfer between the polymer chains and the metal complex forms a dynamic equilibrium between the active and dormant species.[129–131]

3.4.3. RAFT POLYMERIZATION

Compared to other controlled radical polymerizations, RAFT polymerization, developed in 1998 by Le, Moad, Rizzardo and Thang[133], has some remarkable advantages. These include its metal-free nature, which enables a wider range of applications, even in the bio-medical field. Furthermore, RAFT polymerization is significantly more tolerant to functional groups, which expands the suitable monomer spectrum, as well as more tolerant (although still sensitive) to oxygen, which facilitates reaction handling. Depending on the technique, RAFT polymerization is scalable, cost-efficient and allows the design of complex polymer architectures with high polymerization control and predictable end-group functionality.[129,131,133,134]

Mechanism

A thiocarbonylthio compound (e.g. dithioester) serves as a transfer reagent, also named RAFT agent or chain transfer agent (CTA), in RAFT polymerization. The CTA reacts with the conventionally formed radical and establishes a dynamic equilibrium. The mechanism is shown in Figure 18. Similar to classic radical polymerization, the RAFT mechanism begins with the formation of an initiator radical I· in step (1). A conventional initiator as well as a photoiniferter RAFT (PI-RAFT) polymerization, in which the initiator radical is formed from the CTA by photolysis, can be utilized.[130,134,135] In the further course of initiation, I· reacts with a monomer at the preferred position and builds a monomer radical. In step (2), the monomer radical is able to induce a chain reaction with other monomers by growing an oligo- or polymeric chain with a terminal radical function $\cdot P^i$. In the third step, the RAFT mechanism deviates from conventional radical polymerization. The propagating or initiating radical is reversibly coupled to the highly active CTA in an addition-fragmentation step (3). The so-called pre-equilibrium is generated, wherein the stabilities of the polymer radical and the newly formed R· radical from the CTA are of central importance. R· can initiate the chain start in step (4), resulting in the formation of another species of polymer radical $\cdot P^j$. The choice of the Z and R groups of the CTA is crucial for the success of RAFT polymerization and will be further discussed. Once the entire initial CTA has been consumed, the main equilibrium (5) is established by reversible addition of $\cdot P^i$ and $\cdot P^j$ to the dithio species. This equilibrium between the active species (polymer radicals) and the dormant species (dithio radical) is the key point for the vitality of the polymerization and the low dispersity of the resulting polymer mixture. Due to the equal distribution of radicals in this equilibrium, all chains have the same probability of growth.[130,134]

Similar to conventional radical polymerization, termination reactions (6) such as disproportionation and recombination can occur. If a highly active CTA is used and the probability of chain transfer significantly exceeds the probability of the initiation reaction, the addition-fragmentation step is the leading reaction step. Due to the rapid attachment of radicals to the dithio species, there are few active radicals in the system, and dormant species predominate. This has the advantage that bimolecular termination reactions become very improbable. At the same time, the probability of growth is evenly distributed across all chains, resulting in low dispersities.[129,130,134] A special feature of the RAFT process is that bimolecular termination does not lead to a loss of chain end viability, if the chain is bearing a dithioester end group, which can be reactivated. The number of actually “dead” polymer chains can be calculated from the number of initiating radicals.[131,134]

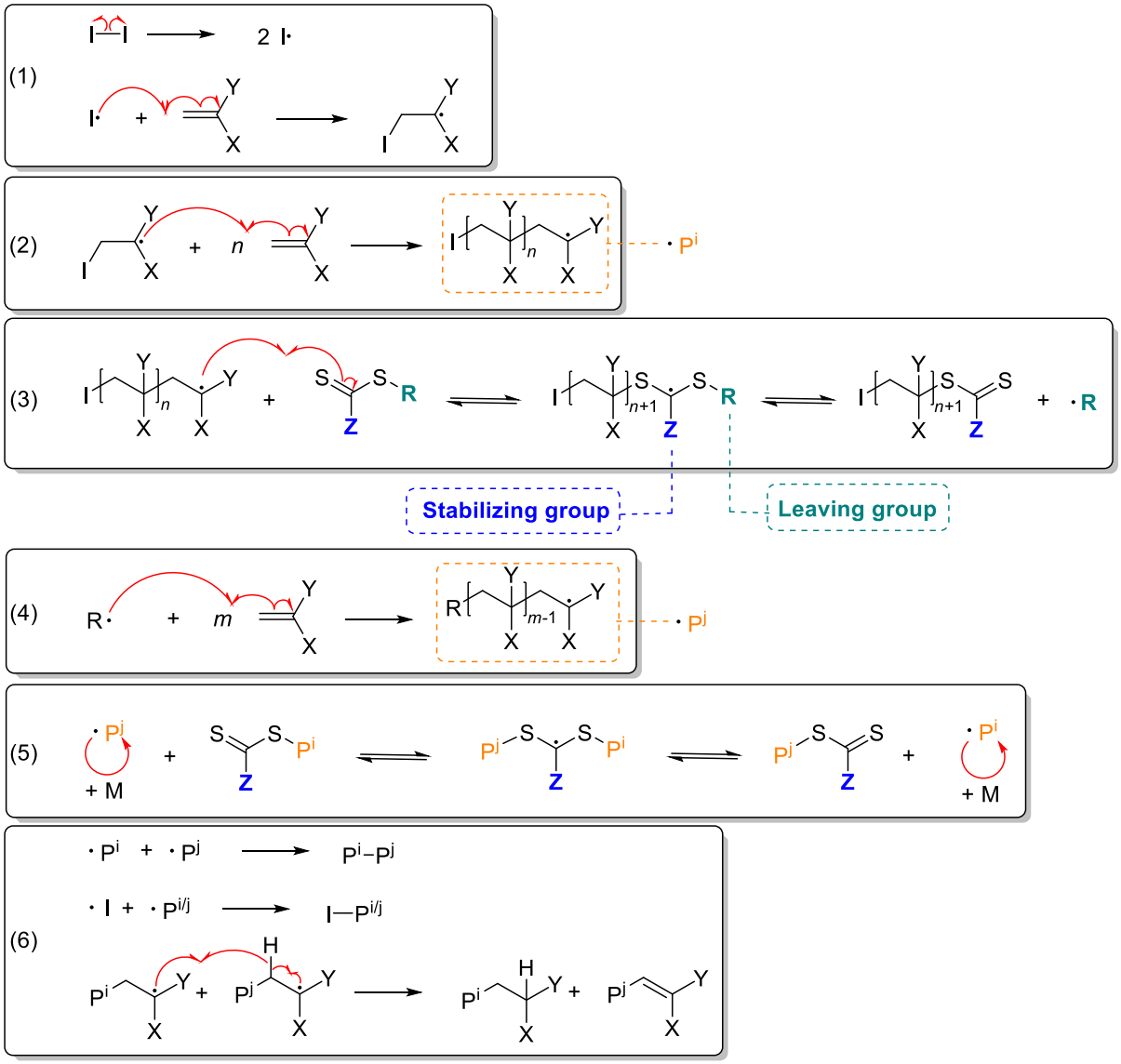

Figure 18: Mechanism of Reversible Addition-Fragmentation Chain Transfer (RAFT) Polymerization. During initiation (1), an initiator radical I· adds to a monomer and forms a polymer radical ·P^{i} during chain growth (2). ·P^{i} adds to the RAFT agent in an equilibrium reaction (3), forming a dormant intermediate radical and releasing a radical ·R, which can add to monomers (4) to form another polymer radical ·P^{j}. After complete conversion of ·R, a main equilibrium (5) is established: two actively growing polymer chains exchange their radical character *via* the RAFT agent, while other chains are temporarily deactivated. As a result, all chains have the same growth probability. Termination (6) occurs through disproportionation or recombination of two active radicals.[129–131,133,134]

Chain Transfer Agent

The choice of the CTA (Figure 18, (3)) is elementary for the course of the reaction. The high monomer compatibility of the process is based on its structural diversity. A suitable CTA contains a C=S bond that is more reactive for radical addition than the monomer alone, ensuring that the reaction must proceed *via* the equilibrium reaction. Monomers can be roughly divided into two classes: more-activated monomers (MAMs) with the vinyl group in conjugation (styrene, acrylate, etc.) and less-activated monomers (LAMs) with the vinyl group next to heteroatoms, or saturated hydrocarbons (vinyl acetate, vinyl chloride, etc.).

The R group must form a good radical (leaving group) and be compatible with the monomer at the same time for an efficient chain start. The polymerization of reactive monomers requires reactive CTAs and vice versa. Although dithiobenzoates (Z=Ph) are the most common structural class for CTAs, trithiocarbonates (Z=SR), dithioalkanoates (Z=alkyl), *N*-pyrrole/*N*-imidazole dithiocarbamates ($Z=NR_2$), xanthates (Z=OR), and dithiodialkylcarbamates ($Z=R_2$, with R=alkyl) are also utilized. The Z group has a direct influence on the stability of the intermediate radical (stabilizing group) and thus on the equilibrium. The phenyl group of the dithiobenzoates stabilizes the intermediate adduct radical (dormant species) through delocalization effects, whereby the addition step is strongly activated.[130,134] More detailed information on the choice of RAFT agent based on the selected monomer can be found in the comprehensive review by S. Perrier.[134]

3.4.4. CE-POLYMER LINKAGE

Following the description of the synthesis of both the polymer matrix and the cation-complexing CEs, the focus now shifts to covalent linking the two building blocks. The CE's connection to a matrix increases manageability, reusability, and adaptation to continuous processes. For this purpose, various strategies are available that are suitable for the immobilization of the CE onto polymers depending on the limitations and possibilities of the system.[77] A brief overview of some common methods is given below, before the method most relevant to this thesis is explained more closely.

One option is the introduction of the CE into the system as part of the polymerization process. The CE can herein be part of the actual polymer chain, as presented by Zhu *et al.* in 2020. They performed a polyaddition reaction between a diaminofunctionalized CE (di(aminobenzo)-14C4) and a difunctional phthalic anhydride (6FDA), yielding a polyimide.[136] Another example was published recently (2025) by Liu *et al*. by the incorporation of Dibenzo-18C6 as part of a polyurethane chain.[137] Additionally, CE-containing monomers can undergo reactions resulting in the CEs being located as side chains on the main polymer chain. For example, Favre-Réguillon *et al*. reported in 1997 the embedding of various (12–24-membered) CEs *via* a polyaddition reaction of diol-functionalized CEs with diisocyanates, as well as the production of (allyloxy)methyl-12C4 from allyl glycidyl ether.[138] As in this example, the CEs can be modified to contain functional or polymerizable groups (e.g., methacrylate, acrylate, or vinyl functionalities). During homopolymerization of these monomers or copolymerization with other monomers, the CE is embedded in the matrix. Liberati *et al.* recently (2025) presented a thermoresponsive *stat*-copolymer based on *N*-isopropylacrylamide (NiPAAm) and 2-(benzo-12C4-ether)ethyl methacrylamide (BCEEM), whereby BCEEM could be obtained *via* two

different reaction pathways. The production of pure P(BCEEM) was also successful.[90] Some of the described procedures are visualized in Figure 19.

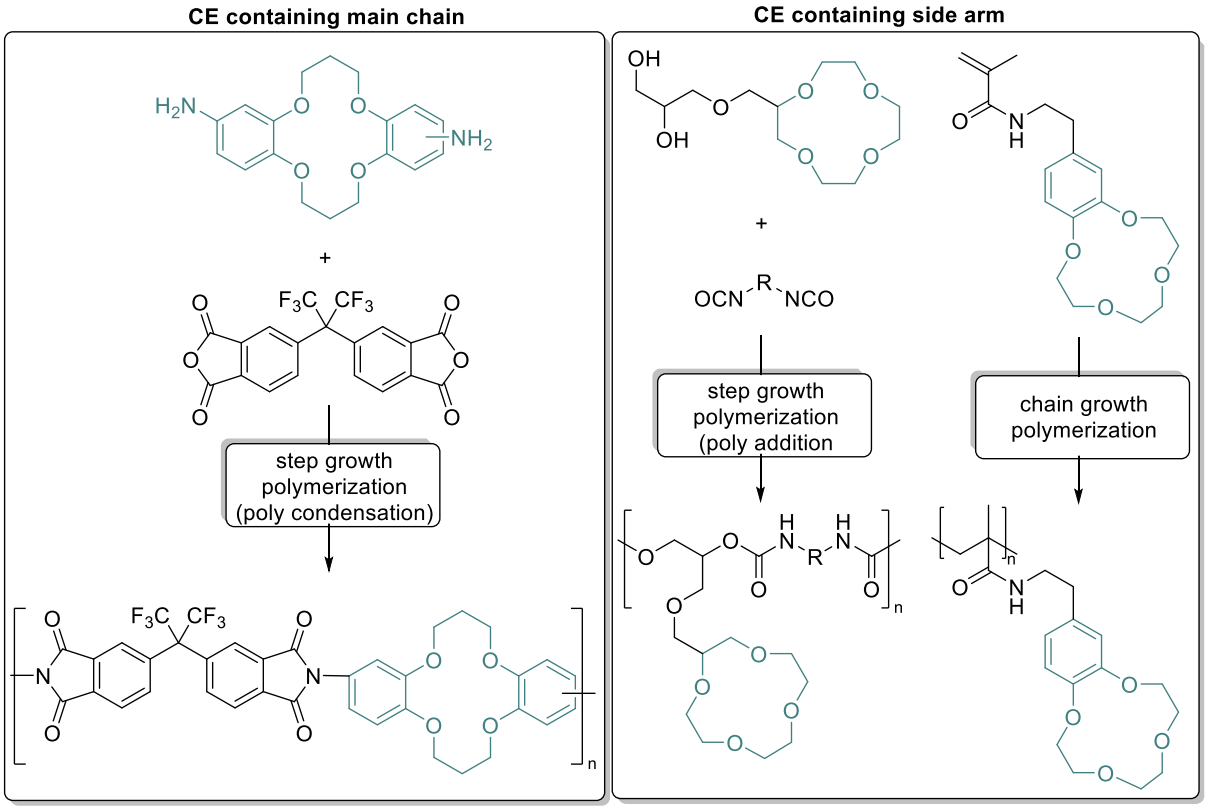

Figure 19: Different approaches for incorporating crown ethers (CEs) into polymers in the main chain or as a side arm during polymerization. The formation of a polyimide (left) from a difunctional phthalic anhydride and a diamine-functionalized, aromatic CE is based on Zhu *et al.* (2020).[136] The formation of the polyurethane (middle) according to Favre-Réguillon *et al.* (1997)[138] from a diisocyanate and a CE-functionalized diol, as well as the chain growth polymerization of a benzo-CE-functionalized methacrylamide (right) according to Liberati *et al.* (2025)[90] leads to the development of a CE side arm on the polymer main chain.

Alternatively, the CEs can be introduced to the system after polymerization is completed, *via* post-modification. Post-modification refers to the targeted functionalization of polymer chains. It is particularly useful when direct functionalization *via* the monomer is not possible, for example, due to limited reactivity, steric hindrance, poor solubility, or incompatible functional groups.[77,139,140] Typical strategies are grafting reactions, which result in functional, oligomeric or polymeric side chains attached to the polymer backbone. However, the polymer backbone must possess specific structural features that enable grafting, depending on the mechanism. As a result of the *grafting-to, grafting-onto,* or *grafting-through* process, side chains of different functionalities are covalently connected to the main chain.[129,139]

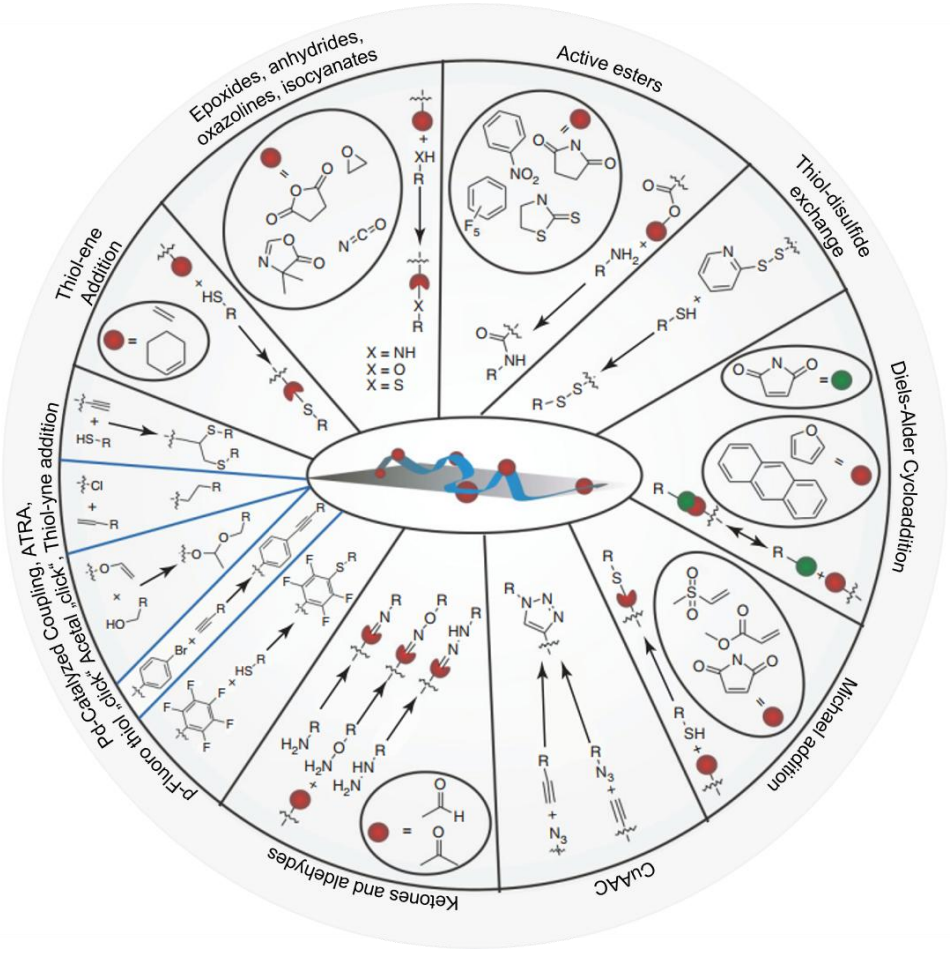

Figure 20: Overview of a variety of different types of reactions that are used for post-polymerization modification. Reprinted and adapted with permission from Ref. [139]. Copyright © 2013 Wiley-VCH Verlag GmbH & Co. KGaA.

Furthermore, especially if only isolated structural features are to be incorporated into the main chain, functional groups within the chain can be modified using classic organic reactions – for example, by esterification of hydroxyl groups or amidation of amine functions. This can be achieved either on functional groups that are intrinsic to the polymer used (e.g., polyvinyl alcohol, polyacrylamide, or polyacrylic acid) or by explicitly incorporating functional groups into the polymer.[77,129,139–141] A number of examples of post-functionalization methods are shown in Figure 20. Owing to the presence of carboxylic acid functionalities, PS-*b*-PMAA (used in this work) offers the possibility of post-modification. The approach of esterification of the MAA unit with a hydroxy-functionalized CE, according to Mitsunobu[142], will be described as shown in Figure 21.

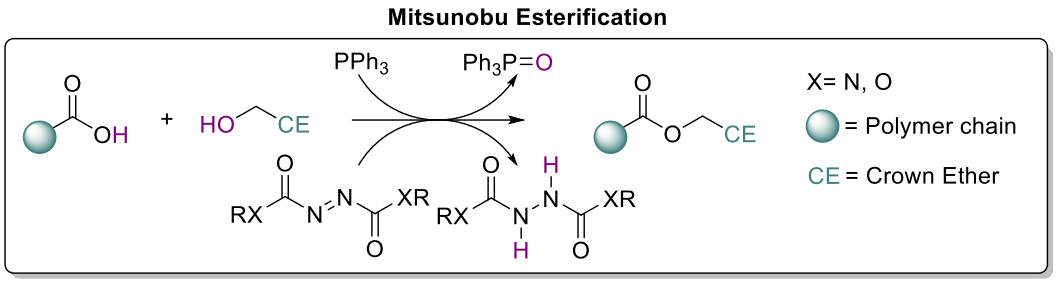

Figure 21: Mitsunobu reaction of carboxylic acid containing polymer and hydroxy functionalized crown ether.[142,143]

The Mitsunobu reaction is a versatile reaction involving the dehydrative coupling of an alcohol with a carboxylic acid. The reaction proceeds *via* the formation of a reactive phosphonium intermediate, which is produced by the reaction of triphenylphosphine and an azodicarboxylic acid derivative. This serves as an activator to convert the alcohol into a good leaving group. Nucleophilic substitution (with inversion of the configuration) takes place. The esterification of carboxylic acids can occur by a variety of mechanisms, the best known of which are the Fischer[144] and Steglich[145] esterification, and carboxylic acid halide reactions[146]. The Mitsunobu reaction takes place under mild conditions, and the range of usable nucleophiles is wide. This enables not only the formation of esters, but also aryl ethers, cyclic ethers, C-C and C-N bonds. With regard to the specific coupling system of CE and MAA, the Mitsunobu reaction proceeds very well in polymer-compatible, comparably harmless solvents and under mild conditions at room temperature. Another major advantage is that the polymer can be easily cleaned of by-products, as these can be removed using solvents that are immiscible with the polymer, making Mitsunobu esterification a time- and resource-efficient choice in this context.[142,143,146]

3.5. POLYMER MANUFACTURING AND SELF-ASSEMBLY

Depending on their composition and environment, copolymers have unique self-organizing properties. An understanding of these is particularly relevant for publication 2 and also publication 3. Fundamental theories for the miscibility and corresponding self-assembly behavior of polymers will henceforth be discussed in more detail in order to establish the reader's knowledge for the following descriptions of membranes, cubosomes, and electrospun fibers.

3.5.1. THERMODYNAMICS OF BLOCK COPOLYMERS

The thermodynamics of polymer mixtures can be described by the Flory-Huggins interaction parameter χ, the degree of polymerization Ni, and the (block) volume fraction φ_i or f_i of the component i. The Flory-Huggins-Staverman theory is an extension of the lattice model for low-molecular substances in solvents, suitable for mixtures of polymers. Figure 22 presents a conceptual diagram of such a lattice.[129,131]

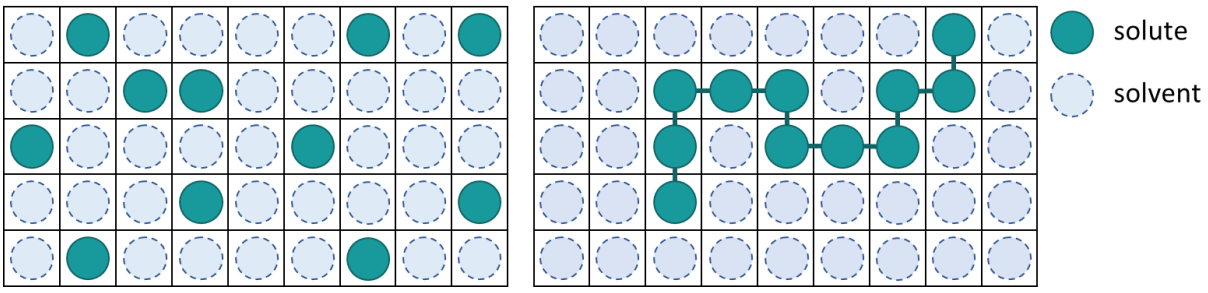

Figure 22: Lattice model describing a dissolved substance in a solvent (left) and a polymer chain in a solvent (right). Created by the author with data from Ref. [129,131].

Several assumptions apply within this lattice: no double occupation of the lattice sites is permitted, nor vacancies, an N-unit polymer chain occupies N lattice sites according to its degree of polymerization, whereby the orientation of the chains is without preference, i.e. entirely coincidental on an adjacent lattice site.[147,148] In order to describe the miscibility of a multi-component system thermodynamically, the free enthalpy of mixing ΔG_{mix} is applied. ΔG_{mix} is the sum of the entropy and enthalpy terms, considering the temperature T (equation 3.5.1.1). If ΔG_{mix} is negative, there is miscibility; if it is positive, the components will segregate.[131]

$$\Delta G_{mix} = \Delta H_{mix} - T\Delta S_{mix} \qquad 3.5.1.1$$

As components are mixed, the entropy of the system increases ($\Delta S_{mix}>0$). In contrast to the process of dissolving low-molecular substances in a solvent, however, ΔS_{mix} increases significantly less with long polymer chains. This is due to the fact, that the pure polymer inherently exhibits a finite entropy, whereas the low-molecular-weight solvent or monomers

can be approximated as entropy-free. As a result, the entropy difference between the pure and mixed states is reduced.[147–150] ΔS_{mix} (for the entire system) results as equation 3.5.1.2, for a binary AB system, with the ideal gas constant R. With increasing *N*, i.e. more bonds between the monomers, the number of potential mixing conformations decreases and consequently ΔS_{mix}.

$$\Delta S_{mix} = -R\left(\frac{\varphi_A}{N_A}\ln\varphi_A + \frac{\varphi_B}{N_B}\ln\varphi_B\right) \qquad 3.5.1.2$$

Miscibility is determined not only by the extent of entropy of mixing but also by the interactions occurring between the components. These are expressed *via* equation 3.5.1.3, the enthalpy of mixing ΔH_{mix} for the system. This is a mean-field description, as the interactions are weighed by the overall volume fractions of the different components. Depending on the system, this relates to the interactions between components A and B, i.e. A-A, B-B, and A-B.[148,150]

$$\Delta H_{mix} = RT\varphi_A\varphi_B\chi_{AB} \qquad 3.5.1.3$$

More precisely, the Flory-Huggins interaction parameter for an AB system χ_{AB} can be defined by the difference between the interaction energies of the pure components (ϵ_{AA} and ϵ_{BB}) and the mixed interaction energies ϵ_{AB} per monomer between the monomers A and B (equation 3.5.1.4). It describes the non-ideal part of the free enthalpy of mixing, i.e. the loss of free energy at the contact between A and B. k_B is the Boltzmann constant, Z_n is the number of nearest neighbors in the postulated lattice. If $\chi_{AB}>0$, the repulsive forces between A and B predominate and the attraction of segments of the same nature prevails. In order to ensure a mixture, however, ΔS_{mix} must be of a compensatory magnitude. $\chi_{AB}<0$ indicates a net attraction and the components A and B are miscible.[131,149]

$$\chi_{AB} = \left(\frac{Z_n}{k_B T}\right)\left(\epsilon_{AB} - \frac{\epsilon_{AA}+\epsilon_{BB}}{2}\right) \qquad 3.5.1.4$$

Generally, especially with polymers of different hydrophilicity, χ_{AB} is positive. A deviation from this phenomenon results, for example, from strong attractive interactions such as hydrogen bonding, charges or a strongly increased temperature, as χ_{AB} is temperature-dependent.[148,149] These relationships result in equation 3.5.1.5 for the systems total ΔG_{mix}.[66,131,148,151] Accordingly, the enthalpy term enhances miscibility when $\chi_{AB}>0$ likewise the entropy term, whereby the influence of the latter, in contrast to classic solution theory, ΔS_{mix} depends strongly on *N*.

$$\frac{\Delta G_{mix}}{RT} = \frac{\varphi_A}{N_A}\ln\varphi_A + \frac{\varphi_B}{N_B}\ln\varphi_B + \varphi_A\varphi_B\chi_{AB} \qquad 3.5.1.5$$

This approach becomes problematic with highly diluted polymer systems [vii], as the intermolecular interactions between polymer chains are drastically reduced.[131,148] Moreover, although the Flory-Huggins-Staverman approach enables the transition from low-molecular systems to high-molecular systems, the behavior of block copolymers is way more complex to describe. The covalent connection of the two blocks with different hydrophilicity leads to a different segregation behavior than with homopolymers, a microphase separation. The entropic proportion of ΔG_{mix} cannot be adequately described by the lattice theory; therefore other theories apply here. These include the SCFT (Self Consistent Field Theory), for example.[152–154] This powerful tool is well suited to describe the self-organization in inhomogeneous systems (such as block copolymers) as a theoretical framework. SCFT reduces the many-body problem for the description of the thermodynamics of block copolymers to a simplified mean-field system. Rather than individually describing all polymer interactions, resulting in an enormous computational effort, a polymer chain (one-body) is thus described in the averaged field (mean field) of other chains. This averaged field is formed in an iterative process as a self-consistent solution to the one-body problem. SCFT reduces the computational effort enormously while maintaining very good agreement between the calculated and the experimentally determined morphologies.[152,155,156]

3.5.2. MICROPHASE SEPARATION OF BLOCK COPOLYMERS

Microphase separation refers to the spontaneous structural compartmentalization of block copolymers of two (or more) incompatible blocks in bulk or in solution. As a result of the covalent bond between the two blocks, no macroscopic phase separation can occur. The generated phase-separated domains range in size from a few nanometers to a few hundred nanometers, thus simplifying the prefix micro (historically as small). The following explanations refer to the consideration of linear diblock copolymers (AB) in providing a basic idea.[149,157]

Depending on the AB block composition, a microphase separation can lead to different structures. Figure 23 shows the phase diagram according to Matsen and Bates for a linear diblock copolymer, using the standard Gaussian chain model according to SCFT.[154] Similar to section 3.5.1, N defines the DP of the polymer, and f_i the proportion of block i in this ($f_i = \frac{N_i}{N}$). Below (or equal to) a critical degree of segregation χN, the system is entropy-determined and lacks an ordered structure. The polymers occur in a random coil structure. With an increase of χN above the critical value, an order-disorder transition (ODT) occurs and enthalpically favored

[vii] Further information on thermodynamics within diluted polymer solutions can be found in Ref. [131] and Ref. [130].

periodic microstructures are formed. For a symmetric diblock copolymer (f_i=0.5) Leibler predicted this ODT at χN=10.5[158], Bates *et al*. at χN=10.4[149]. Interestingly, the smallest structural changes can be sufficient to generate excess free energy contributions that lead to segregation. Even polymer isotopes (PS and deuterated PS) segregate at sufficiently high MWs.

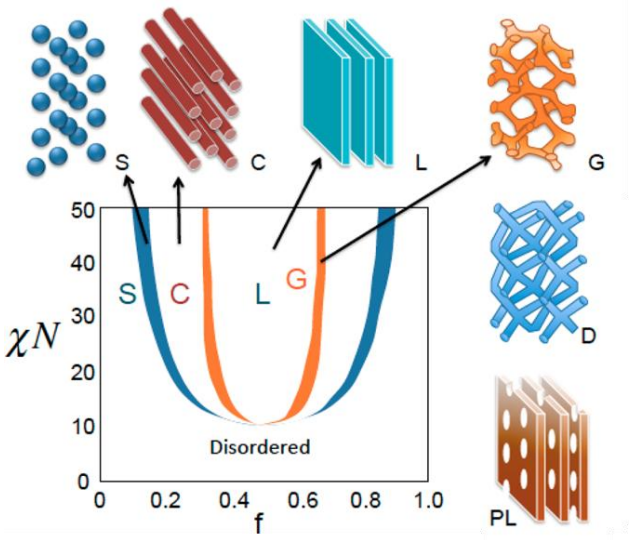

Figure 23: Self-consistent field theory (SCFT) mean-field phase diagram of a linear AB diblock copolymer. Plot of the block composition *f* against the degree of segregation χN. Structures are lamellar L, double-gyroid G, cylindrical C and spherical S. D and PL refer to the metastable double diamond and perforated lamellae structures, respectively. Adapted and reprinted with permission from Ref. [159]. Copyright © 2016 American Chemical Society.

If the AB block composition is close to a value of 0.5, i.e. close to or exactly a symmetrical composition of the two immiscible blocks, an alternating, lamellar structure L exists. The AB blocks can be understood analogously to a head-tail structure. Within the lamellar structure, these arrange themselves as ABBA or BAAB (i.e. head-tail-tail-head or tail-head-head-tail) in an equidistant repeating unit.[149,157,160] With minimal deviation from the equipartition AB (f_i=0.5), a perforated layer structure PL (or catenoid phase) can be formed. However, it was found that PL is only a long-lived transition phase and not thermodynamically stable. The layer structure is traversed by hexagonally packed channels of the majority component.[160] A shift in f_i towards the A or B block can lead, in a narrow range, to the formation of a double-gyroid network G. The minor block forms two interpenetrating threefold coordinated networks. The major block constitutes the surrounding matrix. Changing the block ratio onwards in one direction, the structure approaches that of hexagonally packed cylinders C comprising the minority component, in a matrix of the majority block. Eventually, spherical domains develop with very significant differences in block length. The smaller block characteristically forms a body-centered cubic (bcc) lattice structure in the matrix. However, different cubic arrangements, such as the face-centered (fcc) lattice structure or A15 symmetries, can appear.[160] If the phase diagram is followed alongside different block ratios, the structures are mirrored from the center with interchanged AB markings.[149,157,160,161] The driving force behind these morphological

transitions is the minimization of the free energy of structure formation for a given composition. The increase in interfacial energy is reduced in order to gain the conformational entropy of longer chains (also called chain elasticity).[160,162] The properties of the resultant materials and the practicability of the block copolymers are essentially predicated on the mesoscopic self-assembly in the environment (solid, melt or solution).[149]

Depending on χN, three domains can be defined: the weak segregation limit (WSL), the intermediate segregation regime (ISR) and the strong segregation limit (SSL). The WSL introduced by Leibler[158] and Yerukhimovich[163] describes the phase behavior slightly above the ODT ($10.5 \leq \chi N \leq 15$). The entropic influence is still important in this regime and the incompatibility between the blocks is just strong enough for a microphase separation, whereby the segregation forces are weak and the domains are relatively diffuse and broad compared to the SSL. Semenov[164] extended the theory of phase separation in block copolymers to include the SSL, from which (in contrast to the WSL) the incompatibility between the polymer blocks is very pronounced ($\chi N \geq 100$). The conformational entropy favors a large interfacial area, but is outweighed by the interfacial tension (enthalpic), aiming to minimize interfacial area. As a result, the chains are strongly elongated. The lines between the different phases become far sharper and domain formation is more defined. The intermediate region of WSL and SSL is described by the ISR (Matsen and Bates[154]), in which enthalpic and entropic forces are well-balanced. The enthalpic incompatibility between the blocks is large enough to support an ordered phase separation. Still, the entropic contributions are so significant that no extremely narrow phase boundaries are to be expected.[149,154,158,163–166]

3.5.3. MEMBRANES

Membranes are used for separating substances across different levels. They have numerous applications – e.g., in gas filtration to separate climate-damaging gases from combustion gases, in medical applications for dialysis, or in (drinking) water treatment by separating suspended particles or bacteria (10–0.1 µm), viruses and proteins (0.1–0.01 µm), divalent ions or sub-molecular organic groups (0.01-0.001 µm) up to small monovalent ions (0.001-0.0001 µm) as shown in Figure 24. As in their applicability, membranes are versatile in their membrane geometry, porosity, chemical composition, and surface functionalization, allowing them to be specifically optimized for different separation processes and areas of application. [167–169]

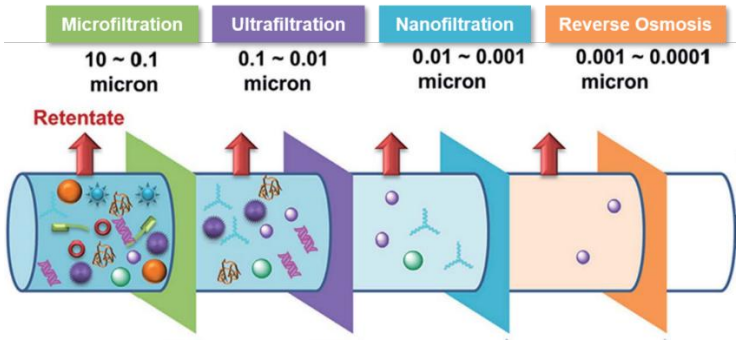

Figure 24: Schematic representation of different orders of magnitude of filtration. Reprinted with permission from Ref. [167]. Copyright © 2017 Elsevier B.V.

An innovative approach to the production of integral asymmetric flat membranes is the SNIPS process, the fundamentals of which will be discussed here and which is important for understanding the unpublished results. The SNIPS process combines the controlled self-organization of block copolymer structures with non-solvent induced phase separation. Through the selection of a suitable solvent (mixture), the minority component forms certain microphase morphologies in a matrix of the majority component, as discussed in the previous section on the self-assembly of block copolymers. The integral asymmetric structure allows for a two-layer structure made from a single material. The fine-pored surface layer is responsible for active separation, while the bottom, coarse-pored layer provides the membrane with high mechanical stability. This also enables high separation performance at high flow rates.[159,168,170,171] Figure 25 shows the membrane casting process *via* SNIPS schematically.

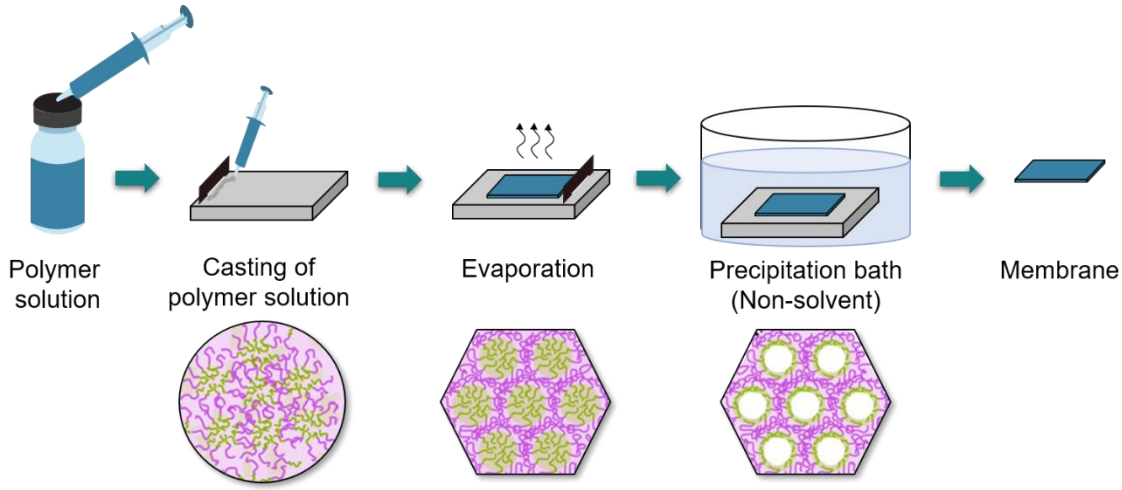

Figure 25: Self-Assembly Nonsolvent-Induced Phase Separation (SNIPS) process. Created by the author according to Ref. [159] with elements (and permission) from Ref. [171,172]. Copyright © The Royal Society of Chemistry 2020.

The block copolymer is dissolved in a suitable solvent mixture and coated onto a substrate to a specific thickness. The substrate can consist, *inter alia*, of non-woven polymers, metallic nets, or ceramics and provides mechanical support with no impairment of the membrane permeability. The minority-selective solvent is low-volatile, while the majority-selective solvent is high-volatile. The time-delayed evaporation creates a concentration gradient perpendicular to the film surface. This has a directing effect on the microphase separation. Transferring the

film to a non-solvent bath in which all solvent and non-solvent components are miscible causes a solvent-non-solvent exchange and sets the structure.[159,168,173]

3.5.4. CUBOSOMES

Cubosomes represent another method of polymer processing utilizing the self-assembly behavior of block copolymers. Cubosomes are self-assembled microparticles with a cubic, open-pored structure. Figure 26 illustrates this structure. Similar to membranes, cubosomes have the advantage of a high surface-to-volume ratio. Although cubosomes are classically formed from unmodified polymers, they also allow for subsequent surface-modification or, as in the case of this work, can be produced from modified amphiphilic block copolymers.

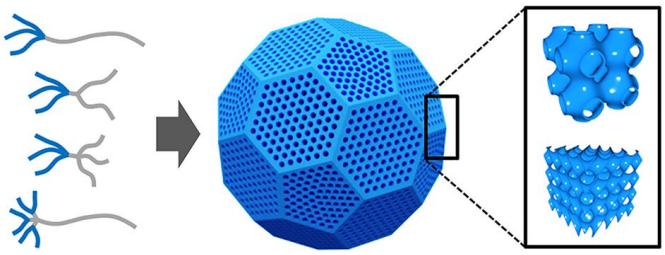

Figure 26: Polymer cubosome structure. Reprinted with permission from Ref. [174]. Copyright © 2020 American Chemical Society.

Applications include catalytic purposes, medical applications (drug release), energy storage, and, *inter alia*, the selective binding (and release) of substances.[175–177] Conceptually, polymeric cubosomes are inspired by lipid cubosomes (based on monolein). Their highly asymmetrical nature, due to the relatively large hydrophobic part with a small hydrophilic head group, results in a large packing parameter.[174,175,177,178] Consequently, self-organization into cubosomes or hexosomes is favored, as shown in Figure 27.

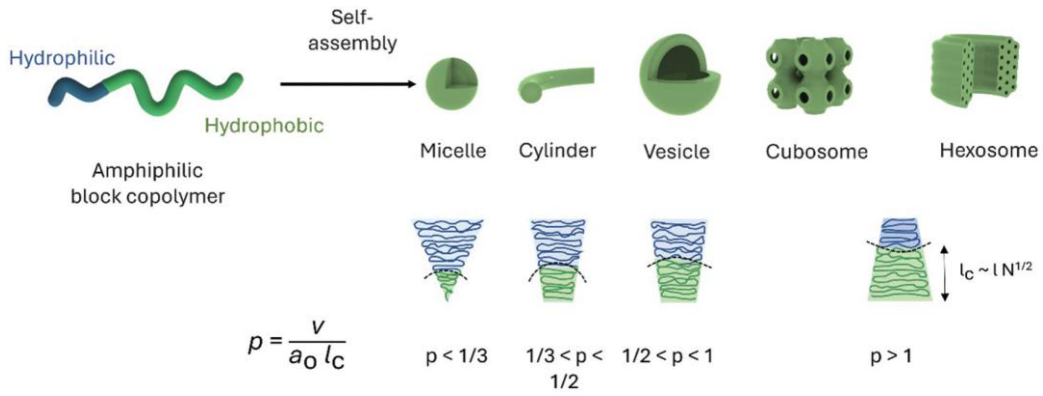

Figure 27: Self-assembled structures of an amphiphilic block copolymer with different packing parameters p. a_0 is the headgroup area, l_c the length of the hydrophobic block, v the volume of the chain. Reprinted with permission from Ref. [177]. Copyright © 2025 Informa UK Limited, trading as Taylor & Francis Group.

Cubosomes can be produced *via* self-assembly induced by solvent evaporation (EISA), solution diffusion evaporation mediation (SDEMS) or in situ polymerization (PISA), or by a

solvent-based approach. These include typical nanoprecipitation, reverse nanoprecipitation and flash nanoprecipitation.

The typical nanoprecipitation of cubosomes follows this pattern: First, the asymmetric block copolymers are dissolved in a suitable solvent (mixture). The polymer blocks start to self-organize in solution into ordered hydrophilic and hydrophobic domains. Typical nanoprecipitation occurs by slowly adding this solution to a selective solvent that can only dissolve one of the two blocks. The structures spontaneously arrange themselves into cubosomes (or hexosomes). The solvent is subsequently removed by dialysis with a non-solvent, which fixes the structure.[175,178,179] In reverse nanoprecipitation, the selective solvent is gradually added to the polymer solution. Flash nanoprecipitation describes the sudden combination of both phases. In either case, a solvent-non-solvent exchange is performed. The system is kept in continuous motion. (Nearly) spherical particles are formed to minimize surface area, but exhibit a long-range cubic internal order. Based on the block copolymer composition, the addition rate of the (non-)solvent, the concentration of the polymer, and the type of (non-)solvent, the mechanical stability, pore size, particle size, lattice constants, etc. of the resulting structures can be adjusted. A closer consideration of the individual production methods can be found in the work of Reyes *et al.*[178]

3.5.5. ELECTROSPINNING

Another way of processing block copolymers from solution (or melt) into structures with a high surface-to-volume ratio is electrospinning. Ultrathin fibers (with diameters in the nm range) can be produced. As the term *electro*spinning implies, spinning is conducted within an electric field. The conceptual setup is shown in Figure 28.[180–182] The polymer, dissolved in a suitable solvent or solvent mixture, is conveyed through a metallic spinneret at a constant flow rate. A high voltage is applied to this spinneret (typically a cannula), which simultaneously serves as an electrode. Facing this is a grounded collector plate. Between the collector plate and the spinneret, an electric field is generated affecting the polymer solution as the solution passes through the spinneret. The assembly can be “bottom-to-top”, “top-to-bottom” or horizontal. A conical deformation of the liquid surface, a so-called Taylor cone, is formed. This is well-known from the electrospray ionization technique applied in mass spectrometry, which involves dispersing it into small droplets as the electric field strength increases. In contrast the field strength in electrospinning is selected to create a stable jet. The polymer solution does not disintegrate, but forms a slender, continuous liquid string moving in the direction of the collector.

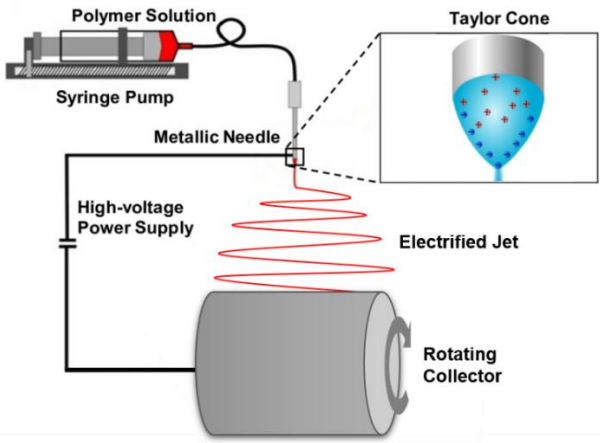

Figure 28: Electrospinning setup with rotating collector. Adapted and reprinted with permission of Ref. [183,184]. Copyright © 2021 IOP Publishing Ltd.

This is due, *inter alia*, to the induced charge in the polymer solution, the suppression of the Rayleigh-Plateau instability and the viscoelasticity of the solution[viii] The Rayleigh-Plateau instability describes the disintegration of a cylindrical body into a series of spherical droplets under volume conservation induced by capillary forces. As the path of the polymer filament increases, the diameter decreases due to the surface tension and the repulsive charge effects on the jet surface as well as the evaporation of the solvent. The jet loses stability with distance, is moved laterally and forms a cone-like swirl facing the collector electrode. With increasing time, it solidifies and hits the collector plate in a swirling motion with a velocity of 40 m s^{-1} (or more).[180,182,185,186] The collector plate can be covered with substrates that serve as a matrix for the electrospun fibers, such as aluminum foil, metal nets or polymer non-woven fabrics. The geometry of the collector plate can vary, which significantly influences the orientation of the fibers. In addition to plates of different sizes, rotating cylinders of different diameters can also be utilized as collector. The latter can be in a cylindrical form or with a flatter side similar to a conveyor belt. With these rotating collectors, the fibers are pushed in a certain direction, depending on the ratio of polymer flow and rotational speed. To illustrate the complexity of electrospinning, the parameters that have a decisive influence on the resulting fibers should be mentioned: Capillary diameter, voltage, tip-to-collector distance, electrode material, electrode arrangement, electric field strength, humidity, temperature, viscosity of the solution, surface tension, solution conductivity and permittivity, molecular weight of the polymer, feed rate, concentration of the solution, solution quality, charge density and chemical composition of the polymer (dispersity, block ratios).[180,186]

[viii] Although electrospinning is a very elegant and easy-to-implement method of polymer processing in terms of the technical application, the theoretical background to the process is very complex. A more detailed description would surpass the scope of this work. However, the physical foundations are described in detail in the literature (Ref. [196]).

With regard to the self-assembly process within a block copolymer, the choice of solvent mixture is decisive in terms of the solvent-block affinity and the vapor pressure of the solvents. Between a homogeneous, continuous nanofiber and the appearance of spherical particles there is an interesting hybrid-formation, the necklace-like *beaded-fibers*. Uniform and beaded-fibers are shown in Figure 29.

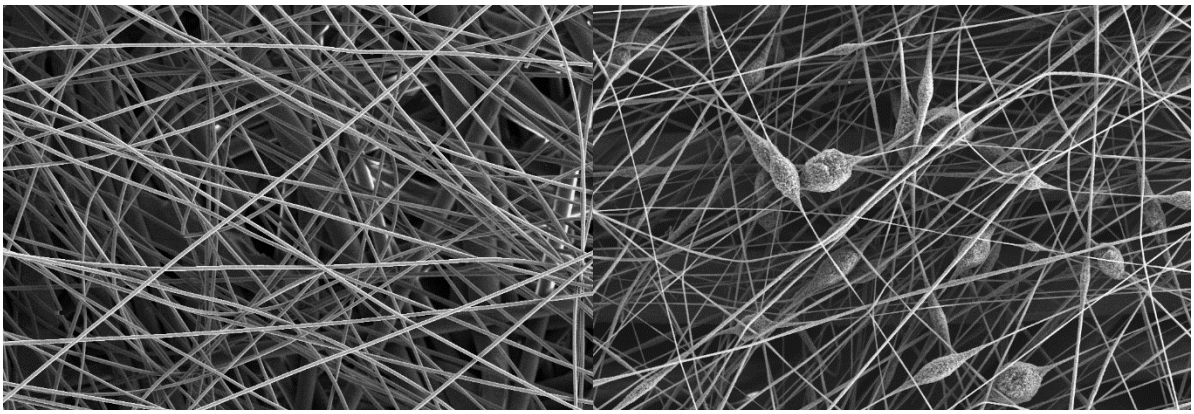

Figure 29: Uniform (left) and beaded (right) fibers of an electrospun PS-*b*-P(MAA-*r*-CE3MA). Pictures taken by electron microscopic service of Helmholtz-Zentrum Hereon.

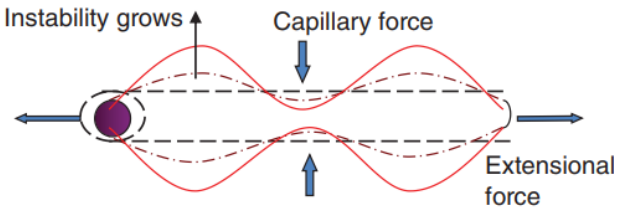

Figure 30: Partial suppression of the Rayleigh-Plateau instability of an electrospun polymer filament in an electric field. Reprinted with permission of Ref. [182]. Copyright © 2012 Elsevier B.V.

This beaded-fiber morphology results from the partial suppression of the Rayleigh-Plateau instability as shown in Figure 30. The capillary forces affect the fluid polymer solution in the electric field. The increasing instability results in the incipient formation of spherical particles. The viscoelastic liquid drains into the developing droplets, causing them to expand, while the extensional force counteracts this deformation, but cannot completely suppress the instability, resulting in the characteristic bead-on-string structure. By adjusting a high viscosity, low surface tension and high surface charge, the process can be urged towards uniform filaments.[180,182,186–188]

4. OBJECTIVES OF THIS WORK

This dissertation is dedicated the development and optimization of an innovative material for the selective extraction of Li from aqueous, low-concentration resources. The goal is to create a system that not only has a high Li capacity and selectivity, but is also suitable for industrial implementation.

Requirements for the system include scalability of the synthesis beyond the laboratory scale, cost-efficient and resource-saving production. This work presents a CE-based approach in which a polymer matrix serves as a functional carrier structure. The centerpiece of this work is the successful transfer of the material into a solid, highly surface-active form. The dissertation is divided into four main thematic sections, which are covered by different publications. A schematic overview is shown in Figure 31.

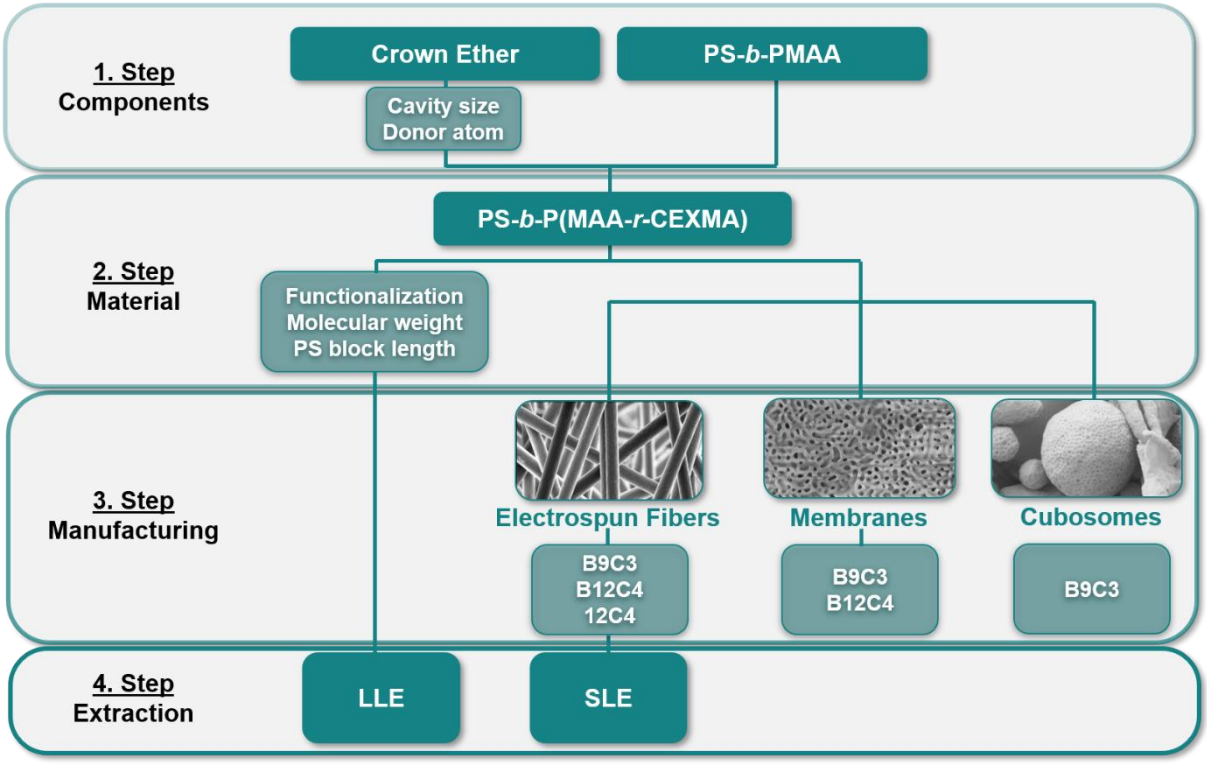

Figure 31: Overview of the concept of this thesis. CEXMA describes the methacrylic acid block functionalized by undefined (X) crown ether, either Benzo-9-crown-3 (B9C3), Benzo-12-crown-4 (B12C4) or 12-crown-4 (12C4). Extractions were performed either in Liquid-Liquid System (LLE) or Solid-Liquid System (SLE).

1. Step: Components

The desired system consists of an active CE component and a functionalizable block copolymer matrix. The selectivity of the system towards different ions is essentially based on the CE's structure. Publication 1 explores the systematic variation of the CE's structure in terms of the number and type of ring atoms. This involved DFT-based structure optimizations, charge distribution analyses, and thermodynamic calculations.

2. Step: Material

The connection with a polymeric matrix offers further possibilities of targeted material design. The total MW of the functionalized block copolymer, the DP of the hydrophobic block, and the functionalization density of the CE have a decisive influence on the material's ability of Li recovery. This is systematically investigated in publication 2.

3. Step: Manufacturing

Block copolymers can be converted into a solid state that is useful for application technology via adjustable precipitation processes. Highly porous structures are accessible by utilizing the tendency of block copolymers to self-organize due to the different solvent affinities of the blocks. In this work, three materials with a high surface-to-volume ratio were produced: electrospun fibers (publication 3), cubosomes, and membranes (unpublished results).

4. Step: Extraction

The thematically final step involves evaluating the systems' efficiency and selectivity. The polymer can act in dissolved form from an organic medium (LLE) and extract Li from an aqueous phase. This is described in publications 1 and 2. Alternatively, Li can be recovered from the aqueous phase using the solid material (SLE) in a more application-oriented manner and without the need for organic solvents, as described in publication 3.

5. CUMULATIVE PART

This section contains reprints of the publications referred to for this cumulative dissertation. Each publication is introduced with a brief foreword explaining its relevance to the overall concept of the thesis. The support provided by coworkers and students for each publication is acknowledged.

5.1. PUBLICATION 1

This publication is reprinted with permission from I. Oral, S. Tamm, C. Herrmann, V. Abetz, Lithium Selectivity of Crown Ethers: The Effect of Heteroatoms and Cavity Size, *Sep. Purif. Technol. 294* (**2022**) 121142 – Copyright 2022 Elsevier B.V.

This work was conducted in close collaboration with Iklima Oral, which contributed equally to this publication. Her input and knowledge played a key role in the success of the project. The project was initiated as my master's thesis and was completed during my doctoral studies under the supervision of Prof. Dr. Volker Abetz and in cooperation with Prof. Dr. Carmen Herrmann. The engagement and expertise of Prof. Herrmann and her working group (especially Dr. Michael Deffner and Dr. Haitao Zhang) were essential for implementing DFT-based calculations in our group and were invaluable for this project.

This publication focused on two aspects: the influence of ring size and heteroatom substitution on the Li complexation of CEs, and the applicability of DFT calculations in this context. Fifteen, twelve-, and nine-membered benzo-CEs were simulated, whereby, in addition to the simulation of purely oxygen containing CEs, one donor atom was replaced by nitrogen or sulfur each. Complex formation with the ions found in high concentrations in seawater (Li^+, Na^+, K^+, Mg^{2+}, and Ca^{2+}) was simulated. In addition to geometry optimizations, Hirshfeld population analyses and NBO analyses were performed. Frequency calculations approximated the system in vacuo and solution. The 15-membered *thio*-CE showed the best Li/Mg selectivity. The estimation of comparability of the simulated data with experimental results led to the extraction of all relevant ions in a dichloromethane/water system of *aza*-15-crown-5. Although smaller absolute values were found, the confirmation of the observed trends showed that computational methods make a valuable contribution to the assessment of CE-cation interactions. These results are particularly useful for reducing complex, time consuming and potentially hazardous CE syntheses and therefore contribute to further development of methods for sustainable Li mining from seawater.

The supplementary information connected to this publication can be found in section 9.2.

Separation and Purification Technology 294 (2022) 121142

Contents lists available at ScienceDirect

Separation and Purification Technology

journal homepage: www.elsevier.com/locate/seppur

Lithium selectivity of crown ethers: The effect of heteroatoms and cavity size

Iklima Oral [a,1], Sabrina Tamm [a,1], Carmen Herrmann [b,*], Volker Abetz [a,c,*]

[a] Universität Hamburg, Institute of Physical Chemistry, Grindelallee 117, 20146 Hamburg, Germany
[b] Universität Hamburg, Institute of Inorganic and Applied Chemistry & The Hamburg Centre for Ultrafast Imaging, HARBOR Blg. 610, Luruper Chaussee 149, 22761 Hamburg, Germany
[c] Institute of Membrane Research, Helmholtz-Zentrum Hereon, Max-Planck-Straße 1, 21502 Geesthacht, Germany

ARTICLE INFO

Keywords:
Crown ether
Density functional theory
Lithium
Natural Bond Orbital analysis
Hirshfeld analysis

ABSTRACT

Lithium is a metal in increasingly high demand due to its use in lithium-ion batteries. However, the extraction from aqueous resources as brines and seawater, which account for a major percentage of worldwide Li^+ reserves, is challenging due to the presence of other interfering metal ions. Crown ethers (CEs) are known to complex metal cations very effectively, but a fundamental understanding of their potential in lithium extraction is still lacking. Therefore, the selective complexation of Li^+ over other alkaline (Na^+, K^+) and alkaline earth metal (Mg^{2+}, Ca^{2+}) ions is investigated by density functional theory (DFT) calculations for 15–, 12–, and 9–membered CEs and their derivatives containing in part nitrogen and sulfur instead of oxygen atoms. Structure optimizations of these CEs are performed in vacuum, and complex stabilities are discussed by evaluating the cavity size, the distances between donor atoms and metal ion, and by performing Hirshfeld charge and Natural Bond Orbital analyses. The qualitative trends obtained from these methods are in good agreement with the complex stabilities, which suggests that they can be used to make simplified predictions of complex stabilities. The selectivity for Li^+ compared to Mg^{2+} in vacuum can be strongly influenced by the ring size, which was the best for B15C5. The general accuracy of DFT is validated by comparing calculations in a polarizable continuum model with the results of a liquid–liquid extraction in a water/dichloromethane mixture using the exemplary extraction of Li^+, Na^+, K^+, Mg^{2+}, and Ca^{2+} by aza–15–crown–5. By doing so, the DFT trends are confirmed (with the stability of the Mg^{2+} complex being overestimated while all others are underestimated), suggesting that DFT is a valuable tool for optimizing CE structures to selectively complex Li^+ or other metal ions. In the context of increasing global lithium demand, the results of this study can serve the further development of selective and sustainable lithium extraction from the largely unexploited resource of seawater.

1. Introduction

Lithium is in growing demand worldwide since it is suitable for various applications, e.g. for ceramics[1], glass[2], pharmaceuticals[3], catalysis[4], grease[5], and rechargeable batteries[6]. The latter is of particular interest in the field of electromobility. The expected growth in this field is approximately estimated at a value of 20 Mt between 2010 and 2100.[7] In the Battery Electric Vehicles (BEVs) industry, lithium is hard to replace due to the low mass and high energy density, enabling small battery dimensions and high recharging efficiency of lithium ion accumulators.[6-9] The limited availability of lithium – being presently extracted from brines, pegmatites, or sedimentary rocks mainly in South America and China – as well as the serious ecological and political problems with conventional production require the development of alternative methods for lithium recovery.[7,10-13] One abundant option would be seawater, in which the lithium concentration is around 0.18 ppm, which gives a total global lithium amount of 230 Bt.[11,12,14] This enormous amount makes the extraction of lithium from seawater indispensable. In addition, the global distribution of the resource would be much more uniform, and time-consuming purification steps, accompanied by conventional extraction, could be prevented if a suitable extraction mechanism was available. Motivated by these

* Corresponding authors.
E-mail addresses: iklima.oral@chemie.uni-hamburg.de (I. Oral), sabrina.tamm@chemie.uni-hamburg.de (S. Tamm), carmen.herrmann@chemie.uni-hamburg.de (C. Herrmann), volker.abetz@hereon.de (V. Abetz).
[1] These authors contributed equally to this work.

https://doi.org/10.1016/j.seppur.2022.121142
Received 27 January 2022; Received in revised form 19 April 2022; Accepted 21 April 2022
Available online 25 April 2022
1383-5866/© 2022 Elsevier B.V. All rights reserved.

evident advantages, several research groups are currently investigating the possibility of lithium extraction from seawater. These include, among others, Li^+–absorbing hydrogen-manganese oxide-modified cellulose films[15] or solar-powered electrolysis with Sodium Super Ionic Conductor (NASICON) solid-state electrolytes.[16].

However, the development of a highly lithium-selective and cost-effective material is still challenging, since the concentration of lithium in seawater is significantly lower than the concentration of competing metal ions like Na^+, K^+, Mg^{2+}, and Ca^{2+}.[12,15,17] In addition, Li^+ and Mg^{2+} show similar ionic radii in aqueous media, which makes the selective complexation of Li^+ rather than Mg^{2+} demanding. One approach to selectively bind lithium is the extraction via crown ethers (CEs).[8,13,18-20] CEs are cyclic ethers with a basic structure usually consisting of ethylene-oxy units (Fig. 1) which are able to complex cations mainly via ion–dipole interactions [8,21-23] (with, depending on the cation, additional stabilizing orbital interactions that represent the charge transfer and polarization and Pauli repulsive orbital interactions).[24-26] The unique properties of CEs allow their use in the fields of phase transfer catalysis[27], chromatography[28,29], substitutes for ionophore antibiotics[30], ion channels[31], sensors [32], and electrodes.[33] Adjustment of the CE ring size and structure can yield a high selectivity towards a specific cation.[8,21,23,34] However, especially the preferential selectivity for Li^+ over Mg^{2+} has rarely been achieved under economically feasible conditions so far. Besides the very similar ionic radii of Li^+ and Mg^{2+}, the latter exhibits a higher electron density and dehydration energy.[8,35,36] Other effects such as the ring strain, the complex stoichiometry, or the favored coordination number of metal ions also play a crucial role for the complex stability, which makes the design of a highly Li^+-selective CE very challenging.[37-39] Compared to other alkali metal ions 14–crown–4 shows the strongest lithium complexation so far, due to its optimal ratio of cavity size to ion radius.[8,13,18,40] However, larger metal ions such as Na^+ or K^+ can form ML_2 sandwich complexes with 14-crown-4 (with M labeling the metal ion and L the ligand). Those complexes are especially stable due to the enthalpy gain caused by the double amount of interaction partners with the complexed metal ion. By incorporating sterically demanding groups into the CE, sandwich complexation can be prevented.[41] However, this CE synthesis is time-consuming and expensive due to chemically complex starting materials and demanding synthetic routes. It is therefore not possible to achieve sufficient selectivity towards Li^+ only via the frequently discussed size relation between CE cavity and metal ion.[23].

A potential route towards lithium selectivity is placing a rigid benzene ring adjacent to the CE to form additionally cation–π interactions and to prevent preorganization effects.[18,42] Recently, our group has developed a promising lithium-selective material based on this idea: Benzo–9–crown–3 (B9C3) was synthesized and bound as a side group to the methacrylic acid units of a poly(methacrylic acid)-*block*-polystyrene (PMAA-*b*-PS) diblock copolymer.[43,44] The detailed synthesis of the block copolymer can be found in Ref. [45]. Due to the small size of the CE ring, lithium ions as well as magnesium ions are complexed as a sandwich, while larger ions, such as sodium or potassium, require more than two CEs and probably cannot be complexed because of the lack of mobility in the polymer. Since we focus on the interactions between the atoms and the influence of the heteroatom substitution in the ring on the complex stability as well as for the evaluation of the correlation between population analysis results and the complexation stability, the focus of this work was consistently set on simple complexes of the form ML. Nevertheless, sandwich complexation is conceivable in some cases, as described below. In fact, CEs incorporated into polymers are very attractive due to their easy separation from solutions and mixtures, especially in the form of membranes, as they have a large surface area, flux, good separation and recovery properties as well as great mechanical stabilities.

In addition to the hard-to-reach Li^+ selectivity compared to Mg^{2+} (achieved by Li et al.[46]), further challenges include the competitive Na^+ complexation in a sandwich type complex as well as the high cost and complexity of existing systems. Nevertheless, the work of Li et al. has given the incentive to consider replacing oxygen with less electronegative heteroatoms (with reduced hardness of the donor atom), such as nitrogen and sulfur, and to study their influence on the complexation of Li^+ and Mg^{2+} in more detail. In order to avoid potentially hazardous and time- and resource-intensive chemical reactions, and for increasing the efficiency and sustainability of CE design, computational chemistry approaches have been considered. Density functional theory (DFT) calculations have provided accurate structures and binding energies for supramolecular structures.[47-49] For example, Sun et al. have investigated the selective complexation of benzo-15-crown-5 (B15C5) towards Li^+ over cobalt, nickel, and manganese at different pH values.[42] In that work, both experimental and theoretical results were consistent with preferential Li^+ complexation at pH = 6 with B15C5. Nevertheless, the ions relevant to seawater-based applications were not considered in that study. Despite the many different publications on CE complexes with metal ions, the search for a suitable CE that favors Li^+ complexation over other alkali as well as alkaline earth metals remains ongoing.

In this work, the complexations of the Li^+, Na^+, K^+, Mg^{2+}, and Ca^{2+} using benzo- 15-, 12-, and 9-membered CEs with different donor atoms are investigated by DFT. The exchange of a single oxygen atom with the less electronegative heteroatoms nitrogen and sulfur with larger radii is chosen to observe a possibly better complexation of Li^+.[35,47] To ensure comparability of the electronic structures, only systems with sp^3-hybridized donor atoms were considered. The different heteroatoms are investigated replacing one oxygen atom in B15C5, benzo–12–crown–4 (B12C4), and B9C3. First, to gain insight into the stability of the

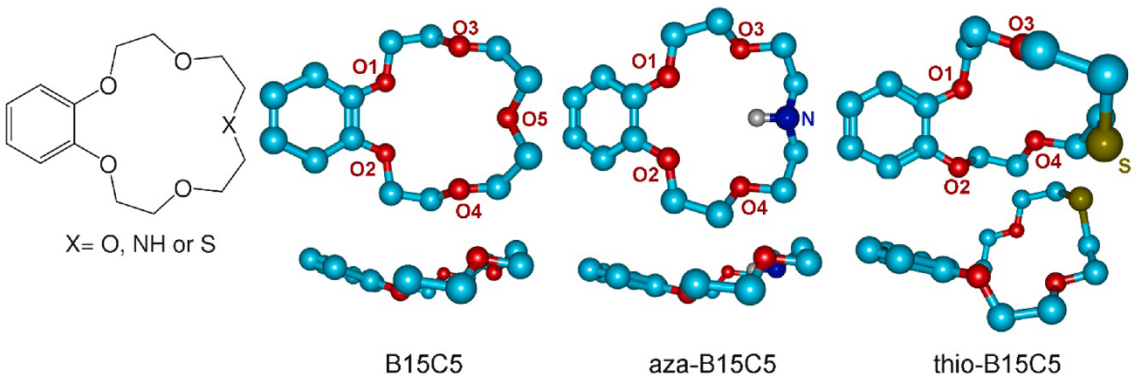

Fig. 1. Lewis structures (left) and energetically optimized ball-and-stick structures of the empty B15C5, aza–B15C5 and thio–B15C5 CEs, the latter shown from two perspectives. The turquoise dots label the carbon atoms, the red dots the oxygen atoms, the blue dots the nitrogen atoms, and the olive–green dots the sulfur atoms. The hydrogen atoms from the C–H bond have been omitted for the sake of clarity.

CE–metal complex and thus to identify factors potentially beneficial to lithium selectivity, DFT is used for calculating the cavity sizes of the CEs, the donor–acceptor distances, the Hirshfeld partial charges, Natural Bond Orbitals (NBO), and the complexes' stability constants K in vacuum. The trends are compared and analyzed with respect to their consistency, in order to assess the suitability of the methods for the design of Li^+-selective CEs.

Furthermore, to estimate the accuracy of DFT stability constants, decisive for the estimation of the complex formation, are evaluated in a continuum solvent model and compared with the experiment. The stability constants are evaluated experimentally for a liquid–liquid extraction of a water/dichloromethane (DCM) mixture using the extraction of Li^+, Na^+, K^+, Mg^{2+}, and Ca^{2+} by the exemplary selected CE aza–15–crown–5 (aza-15C5).

Although no quantitative matching can be expected between the DFT results and the experiment (among others, due to the approximate description of environmental effects and the approximate nature of the exchange–correlation functional), a qualitative assessment of the complexation behavior of different ions under variation of the CE structures is a realistic goal.

2. Experimental and computational methods

2.1. Materials

Aza-15C5 (98 %, TCI, Eschborn, Germany), DCM (99.9 % extra dry, Acros, Schwerte, Germany), lithium–3,5–diiodosalicylic acid (LIS, 100 %, Sigma-Aldrich, Schnelldorf, Germany), sodium ethyl eosin (NaEE, 100 %, Waldeck, Münster, Germany), potassium ethyl eosin (KEE, 100 %, Carl Roth, Karlsruhe, Germany), 8–anilino–1–naphthalenesulfonic acid hemimagnesium salt (MgA, 100 %, TCI, Eschborn, Germany), fuchsin calcium salt (CaF, 100 %, Carl Roth, Karlsruhe, Germany), 15–crown–5 (15C5, 100 %, Alfa Aesar, Kandel, Germany) were used as received. Ultrapure water (MilliQ® quality, resistivity $> 18.2\ M\Omega{\cdot}cm^{-1}$) was obtained from a Millipore (Darmstadt, Germany) MilliQ® water purification system.

2.2. Procedure of the liquid–liquid extraction

For the liquid–liquid extraction, a molar ratio of CE to metal ions ranging from 25:1 to 10:1 was used in a DCM/water system. After phase extraction at 500 rpm for 45 min and phase separation of 30 min at 25 °C, the aqueous phase was characterized by UV/Vis spectroscopy. The formation of the complex $(M_mCE_n)^{mz_+}(X_x)^{xv_-}_{(org)}$ occurred corresponding to the reaction in Equation (1)[43]:

$$mM^{z+}xX^{v-}_{(aq)} + nCE_{(org)} \rightarrow (M_mCE_n)^{mz_+}(X_x)^{xv-}_{(org)} \quad (1)$$

where m and x are the stoichiometric factors of the cation M, of charge z_+, and of the corresponding counterion X (Figure S10), of charge v_-, and n as the equivalents of the CE required for complexation. For all cations, $m = 1$ and $x = 1$, except Mg^{2+} with a value of $x = 2$. A calibration curve of each salt solution was conducted prior to the liquid–liquid extraction to calculate the concentration in the aqueous phase using the Lambert–Beer law. In order to ensure the most accurate values, the calibration was performed shortly before the measurement series and conducted using the same stock solution as for the extraction experiments. The complex constant K of the extraction process was calculated according to Equation (2)[43]:

$$K = \frac{\left[(M_mCE_n)^{mz_+}(X_x)^{xv-}_{(org)}\right]}{(Q{\cdot}(\gamma_+[M^{z-}]^m){\cdot}(\gamma_-[X^{v-}]^x)){\cdot}[CE]^n} \quad (2)$$

with the mean activity coefficients $\gamma_\pm$ and the stoichiometric coefficient Q. More detailed information regarding the calculation of K can be found in the SI.

2.3. UV/Vis spectroscopy

The UV/Vis spectra were recorded with a spectrophotometer UV5 from METTLER TOLEDO at room temperature. The samples were measured from 190 to 1100 nm. The scan time was 10 s.

2.4. DFT calculations

All calculations were performed with the program package *Gaussian 16* (Rev. C.01).[50] The CEs and the corresponding complexes were simulated in *vacuo* (or, in Section 3.4, with solvent approximated by an Integral Equation Formalism Polarizable Continuum Model (IEF–PCM) model with the dielectric constant of DCM) and without symmetry constrains based on DFT. All calculations were employing the B3LYP exchange-correlation functional[51] in combination with Ahlrichs' def–2–TZVP basis set[52], with Grimme's dispersion correction (DFT–D3)[53]. The DFT with pairwise dispersion correction contributes accurate structures of CE structures.[54] The use of other functionals has shown similar property trends for related compounds.[26] However, best results are obtained by using the B3LYP functional.[54] The presence of local minima was ensured by the absence of imaginary frequencies in the computed vibrational spectra. The molecules were visualized and interatomic distances were evaluated using the program *GaussView* 5.0.9.[55] Hirshfeld partial charges were evaluated as implemented in Gaussian 16. The NBO analyses was used as is implemented in Gaussian 16 (*Gaussian NBO version 3.1*).[56] The evaluation of the interatomic distances, and the visualizations of the calculated structures (including the orbitals of the compound) and of the results of the NBO analysis were performed with the program *Chemcraft* 1.8 (build 595b).[57] The change in Gibbs free energy was calculated, as implemented in Gaussian 16, in *vacuo* with a temperature of 298.15 K, as well as in a solvent environment according to the reaction: $CE(CH_2Cl_2) + M^{n+}(H_2O) \rightarrow CE\text{–}M^{n+}(CH_2Cl_2)$.[42] An example input file for a molecular structure optimization of aza-15C5 can be found in the SI.

3. Results and discussion

In this work, different alkali and alkaline earth salts are analyzed in combination with different CEs. First, the optimized structures, the cavity size, and the distances of the metal ions to the respective donor atoms are analyzed, followed by Hirshfeld population and NBO analyses. These data are evaluated based on DFT calculations in vacuum, which allows for comparing the trends of these properties for the different cations, heteroatoms, and ring sizes, and for studying how they correlate with the stability constants K of the different CE complexes. In the last part (Section 3.4), theoretical data in solution is compared with experimental work on liquid–liquid extraction with aza-15C5. In this work, we deal with metal ions only and will use the chemical name of the metal and metal ion interchangeably.

3.1. Optimized molecular structures and cavity sizes

The DFT–optimized structures of the 15–membered B15C5, aza–B15C5, and thio–B15C5 are shown in Fig. 1 (since the property trends for the 12- and 9-membered rings are quite similar to the 15-membered ones, their optimized structures can be found in the SI, **Figure S2 and S6**). In these representations, a structural distortion (relative to a roughly planar ideal CE structure) is observed, which increases with heteroatom size from oxygen over nitrogen and sulfur. Similar observations were made in previous studies.[35,58-60]

The optimized structures of the CEs are investigated for the complexation with Li^+, Na^+, K^+, Mg^{2+}, and Ca^{2+} to verify an influence of the heteroatom substitution on the interaction between donor atom and metal ion (Fig. 2). In the case of K^+ (and to a certain extent also for Ca^{2+}), the cation is pushed out of the ring plane (Fig. 2 (a3), (b3), and (c3), and (a5), (b5) and (c5), respectively), since it exceeds the size of

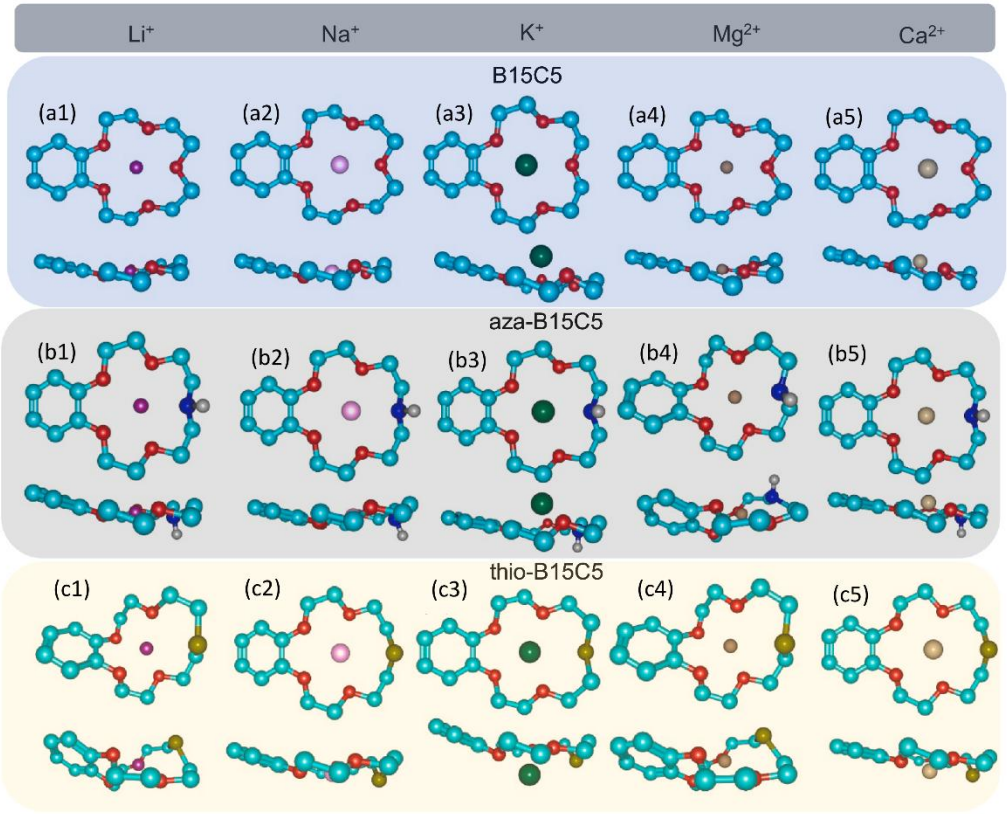

Fig. 2. Optimized structures of the B15C5 (first row), aza–B15C5 (second row), and thio–B15C5 (third row) complexes with Li^+ (violet; a1, b1, and c1), Na^+ (pink; a2, b2, and c2), K^+ (green; a3, b3, and c3), Mg^{2+} (brown; a4, b4, and c4), and Ca^{2+} (beige; a5, b5, and c5), from two perspectives each.

the CE cavity.[43,61,62] As a result, sandwich complexation can be assumed.[63] It is well known that a good size match between CE and cation leads to high complex stabilities[8,23,34,64]. B15C5 with five oxygen atoms shows almost no distortion for all metal–CE complexes (Fig. 2 (a1)–(a5)). In case of the aza–B15C5 and thio–15C5 CE, however, a significant distortion of the CE framework becomes apparent when small cations such as Li^+ and Mg^{2+} are complexed (Fig. 2 (b4), (c1), and (c4)).

The calculated distances between each donor atoms and metal, as well as the cavity size, are listed in **Tab. S1**. In the case of small cations, the distortion is likely caused by the favorable complexation of Li^+ und Mg^{2+} in a tetrahedral or octahedral coordination.[35,37-39] For aza-B15C5-Mg^{2+}, thio-B15C5-Li^+, and thio-B15C5-Mg^{2+}, the distortion is particularly pronounced, presumably resulting from the larger donor atoms (distortion is already observed with empty aza- and thio-B15C5, compare with Fig. 1). The oxygen atoms O1-O4 are located closer to the Li^+ or Mg^{2+} cation (complexation in the tetrahedral coordination) than in the pure-oxygen derivative B15C5 (Fig. 2 (c1), (b4), (c4) and

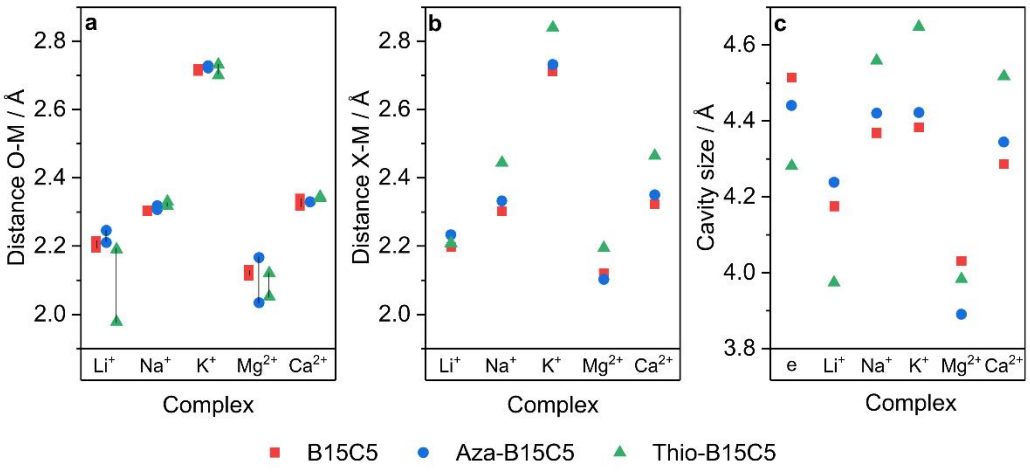

Fig. 3. Distance between the heteroatom X and the metal ion($d^n_{X-M}{}^+$; a) of the CE (B15C5, aza–B15C5, and thio–B15C5) and their complexes with Li^+, Na^+, K^+, Mg^{2+}, and Ca^{2+}, as well as the smallest and largest distance between the oxygen atoms O1–O4 and the metal ion ($d^n_{O-M}{}^+$; b), and the cavity size of the empty CE (e) and the complexes ($d_{CE;}$ c).

Fig. 3**a**), thus increasing the interaction between the donor atoms O1-O4 and the metal ion.[8,35,62] The smallest and largest O-M distances are shown in Fig. 3a. For X = O, N, the smallest and the largest distance increase in the following order: $\mathbf{Mg^{2+} < Li^{+}} < Na^{+} \approx Ca^{2+} < K^{+}$. The same trend is shown for X = S when focusing on the largest O-M distance, while the smallest O-M distance increases in the order $\mathbf{Li^{+}} \approx \mathbf{Mg^{2+}} < Na^{+} \approx Ca^{2+} < K^{+}$. For thio–B15C5-$Li^{+}$, the donor atoms O1-O4 show the shortest distances to the Li^{+} cation compared to B15C5 and aza-B15C5. By comparing the optimized structures of aza-B15C5-Li^{+}/Mg^{2+} (Fig. 2, (b1) and (b4)), a stronger distortion, evidenced by shorter distances between the cation and heteroatoms and a larger variation of O-M distances (see Table S2 and Fig. 3), is observed when Mg^{2+} is complexed with the aza–B15C5, possibly due to the higher charge density and lower hardness of the Mg^{2+} cation.

The distance $d_{X–M}{}^{n+}$ between the heteroatom X and the metal ion increases with larger donor atoms in the following order O < N < S and $\mathbf{Mg^{2+} < Li^{+}} < Na^{+} \approx Ca^{2+} < K^{+}$ (Fig. 3**b**, **Table S2**). In conclusion, the O-M and X-M distances show similar trends for the cations.

The cavity size d_{CE} of the CE can be evaluated as the mean value of the interatomic distances between the donor atoms from the DFT-optimized structures[18,64,65],

$$d_{CE} = \frac{d_{O1-O4} + d_{O1-X} + d_{O2-O3} + d_{O2-X} + d_{O3-O4}}{n} \quad (3)$$

with d labeling the interatomic distance between two donor atoms, n the amount of donor atoms (here: $n = 5$), and X the hetero-donor atom (here: X = O, N, S). An overview of the cavity sizes d_{CE} of the empty CE as well as of the complexes can be found in Fig. 3**c** (for more detailed information, see Table S1). The cavity sizes d_{CE} of the empty CE follow the trend B15C5 > aza–B15C5 > thio–B15C5 (with values of 4.51 Å > 4.44 Å > 4.28 Å). The smaller d_{CE} of the aza or thio–CE can be attributed to the more distorted ring structure. The calculated cavity size d_{CE} for B15C5 corresponds to the theoretically determined values known from the literature (4.118 Å).[42] To the best of our knowledge, no theoretical or experimental data of aza–B15C5 and thio–B15C5 have been reported elsewhere so far.

After complexation, the cavity size for X = O, N is smaller than for the empty CEs, resulting in the order $\mathbf{Mg^{2+} < Li^{+}} < Ca^{2+} < Na^{+} \approx K^{+} <$ empty. For X = S, the cavity size can increase or decrease compared to the empty CE, resulting in the order $\mathbf{Li^{+}} \approx \mathbf{Mg^{2+}} <$ empty $< Ca^{2+} < Na^{+} < K^{+}$. It may be assumed that the smaller cavity size of the Mg^{2+} or Li^{+} complex, in comparison to the Na^{+}, K^{+} and Ca^{2+} complexes, is mainly due to the distortion of the ring and the closer positioning of the four donor atoms due to the favored tetrahedral coordination (O1–O4). The increase in cavity size for X = S with Ca^{2+}, Na^{+}, K^{+} could indicate an unfavorable complexation of CE and cation in a single–ligand complex. Some of these cations have already shown sandwich-type complexes with 15-membered rings.[66-68].

To focus on the comparison between Mg^{2+} und Li^{+} complexation, the cavity sizes d_{CE} of the Li^{+} complexes follow the trend aza–B15C5–Li^{+} > B15C5–Li^{+} > thio–B15C5–Li^{+} with values of 4.24 Å > 4.17 Å > 3.97 Å, while the cavity sizes d_{CE} of the Mg^{2+} complexes follow the trend B15C5–Mg^{2+} > thio–B15C5–Mg^{2+} > aza–B15C5–Mg^{2+}, with values of 4.03 Å > 3.98 Å > 3.89 Å. Thus, it seems that the substitution of oxygen by sulfur leads to a smaller cavity size for Li^{+}, while the exchange with nitrogen leads to a smaller cavity size for Mg^{2+}.

3.2. Hirshfeld- and NBO analysis

To examine the host–guest interactions in more detail, the Hirshfeld population analysis is used, which provides a quantitative description of the local charge distribution.[69,70] In case of complexation, charges are relocated between the entering cation and the negative electrostatic potential region of the CE ring. The latter is based on the presence of the donor atoms X, thus the strongest interaction with the cation occurs here. Complexation–related Hirshfeld charge transfer q_t for an atom X is given as the difference of the Hirshfeld partial charge of X before ($q_{X(CE)}$) and after complexation ($q_{X(CE–M^{n+})}$) by **Equation (4)**[42]:

$$q_{t,X} = q_{X(CE–M^{n+})} - q_{X(CE)} \quad (4)$$

and is summarized graphically in Fig. 4 (numerical values can be found in **Table S3**).

The Mg^{2+} complex exhibits the largest charge transfer in any case, followed by Ca^{2+}, which is likely due to their high charge density. For all complexes, the charge density was mainly transferred from the heteroatoms to the metal ion ($q_{t,O5}$, $q_{t,N5}$, $q_{t,S5}$ (Fig. 4)).

This observation is particularly pronounced for the multivalent metal ions in the aza–B15C5 and thio–B15C5 complexes, while the charge transfer for the monovalent cations is smaller, decreasing in the order $Li^{+} > Na^{+} > K^{+}$. The two oxygen donor atoms attached to the benzene ring (i.e. O1 and O2), show the weakest local charge distribution in almost all cases due to the adjacent electron-withdrawing benzene group.[42] Assuming that a larger charge redistribution (i.e. a higher q_t) correlates with a stronger bond, this would indicate that binding energies follow similar trends. These results are in good agreement with the calculated distances, except for the preferential charge transfer of Ca^{2+} relative to Li^{+} (see Table S2).

NBO analysis was performed to gain further information on the host–guest interactions within the complexes by transformation of the orbitals into a localized, Lewis-like form. The interaction between the Lewis-like donor NBO (with an occupation of 2) and the unoccupied non-Lewis-like acceptor NBO can be determined via second order perturbation theory, in the form of a stabilization energy $E^{(2)}$ (**Equation (5)**):

$$E^{(2)} = b_x \frac{F(X, M^{n+})^2}{\varepsilon_X - \varepsilon_{M^{n+}}} \quad (5)$$

with the occupancy of the donor orbital b_X, the diagonal elements ε and the off diagonal NBO Fock matrix element F(X,M^{n+}).[42,71,72] The larger $E^{(2)}$, the stronger the interaction between the NBOs.[42] The values for $E^{(2)}$ of the donor NBOs, which are the lone pairs of O, N, and S (LP1 and LP2) and the LP* acceptor NBO of the complexed metal ion, are summarized in Fig. 5. The NBO analysis yielded a positive stabilization energy $E^{(2)}$ for each complex (for more detailed data of the NBO analysis, see **Table S4**) and increases for X = O, S in the following order $K^{+} < Na^{+} < Ca^{2+} < \mathbf{Li^{+}} < \mathbf{Mg^{2+}}$.

These results are in good agreement with the calculated distances (see Table S2). However, for X = N, $E^{(2)}$ increases according to the following trend: $K^{+} < Na^{+} < \mathbf{Li^{+}} \approx Ca^{2+} < \mathbf{Mg^{2+}}$, which is in a good agreement with the results from the Hirshfeld analysis.

For the B15C5 complex, the stabilization energies $E^{(2)}$ are similarly high for each donor atom since the ring is hardly distorted and therefore all donor atoms interact similarly strongly with the metal ion, as shown in Fig. 2. Nevertheless, the donor atoms O1 and O2 show slightly lower stabilization energies of 19.71 kJ mol^{-1} compared to the O3 and O4 donor atoms with 22.51 kJ mol^{-1} and O5 with 23.10 kJ mol^{-1} due to the electron density-withdrawing benzene ring, correlating with the results from the Hirshfeld analysis. Similar results were obtained for the aza–B15C5 CE, except for the aza–B15C5–Mg^{2+} complex. In this case, $E^{(2)}_{O1}$ is significantly smaller than the other stabilization energies, while $E^{(2)}_{O3}$, $E^{(2)}_{O4}$ and $E^{(2)}_{N5}$ increase compared to B15C5, which is also due to the observed ring distortion when Mg^{2+} is complexed. A similar trend can be found for the strongly distorted thio-B15C5-Li^{+}/Mg^{2+} complexes, where the values for $E^{(2)}_{O3}$ and $E^{(2)}_{O4}$ differ slightly from one another, while $E^{(2)}_{O1}$ is significantly reduced compared to $E^{(2)}_{O2}$. The decrease of the stabilization energy $E^{(2)}_{O1}$ is particularly striking, considering its direct linkage to the rigid benzene ring and the larger distance between the cation and O1, compared to the other oxygen atoms present in the ring.

As shown with the optimized structures, the cavity sizes as well as the distances between metal ion and donor atoms, the NBO analysis also suggests that Li^{+} complexation increases by putting a sulfide function

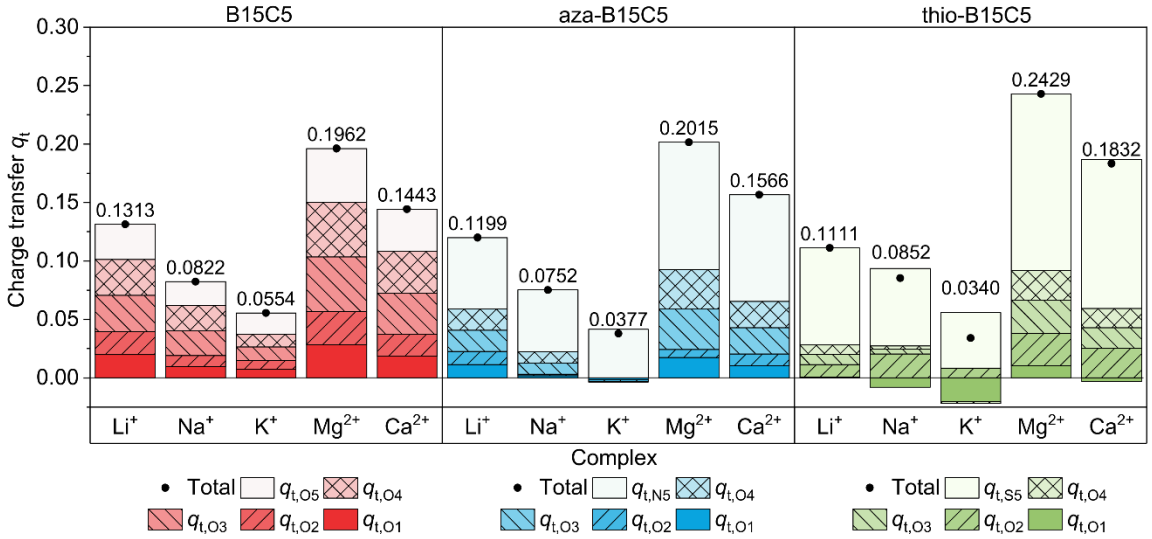

Fig. 4. Hirshfeld charge transfer q_t between the donor atoms (O, N, and S) and Li^+, Na^+, K^+, Mg^{2+}, resp. Ca^{2+} within the complexes with the B15C5, aza–B15C5, and thio–B15C5. The sums of the charge transfers are given above the bars.

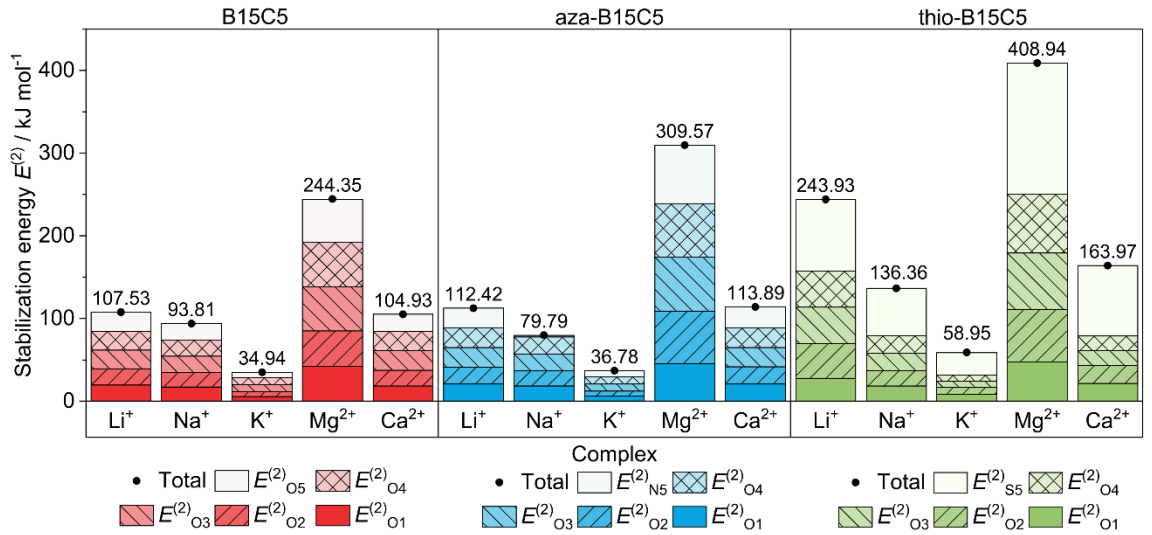

Fig. 5. Stabilization energies $E^{(2)}$ in kJ mol^{-1} within the complexes of the B15C5, aza–B15C5, and thio–B15C5 with Li^+, Na^+, K^+, Mg^{2+}, and Ca^{2+}. The contributions of the lone pair donor NBOs (LP1 and LP2 combined) to the interaction with the acceptor NBOs and the sum of these (above the bars) are given.

into the CE. It is worth mentioning that all systems favor the Mg^{2+} complexation. However, the total stabilization energy of the thio-B15C5-Li^+ complex increases by a factor of 2.27 compared to the B15C5-Li^+ complex, whereas the analogous Mg^{2+} complexes only show an increase by a factor of 1.67, which suggests an enhanced Li^+ selectivity compared to its main competitor Mg^{2+}. The NBOs for thio–B15C5–Li^+ are visualized in Fig. 6. The donor NBOs of the sulfur atom show greater overlap with the LP* of the lithium cation than the donor NBOs of each oxygen as it was determined by the Hirshfeld– and NBO analysis. The previously described strong complexation of the Li^+ and Mg^{2+} cations with aza-B15C5 and thio-B15C5, associated with reduced distances between the metal ion and the four oxygen donor atoms O1-O4 (see Fig. 3), is confirmed by the NBO analysis.

In summary, Mg^{2+} complexation is favored for all systems. However, $E^{(2)}$ increases for nearly all metal ion complexes when an oxygen atom is replaced by nitrogen or sulfur. In case of sulfur, a significant increase in $E^{(2)}$ occurs when Li^+ is coordinated, originating from the better donor abilities compared to oxygen. Moreover, greater selectivities are also observed with respect to the other metal ions.

3.3. Thermodynamic data

In order to consider the effect of the size relation of the CE and the complexed ion in more detail, the following discussion of the 15-membered CEs will be supplemented by analogous discussions of smaller ring sizes (9- and 12-membered CEs). Complex stability can be quantified via the complex constant K. This specifies the thermodynamic direction of a reaction and results from the Gibbs free energy difference ΔG under standard conditions (298.15 K), the temperature T, and the universal gas constant R according to Equations (6) and (7)[42]:

$$\log(K) = -\frac{\Delta G}{2.303RT} \tag{6}$$

$$\Delta G = G_{CE-M^{n+}} - G_{CE} + G_{M^{n+}} \tag{7}$$

with $G_{CE-M}{}^{n+}$, G_{CE}, $G_M{}^{n+}$ being the Gibbs free energy for the complex, CE, and salt, respectively. The entropy contribution to the Gibbs free energy is very small in relation to the enthalpy (more details can be found in Table S10).

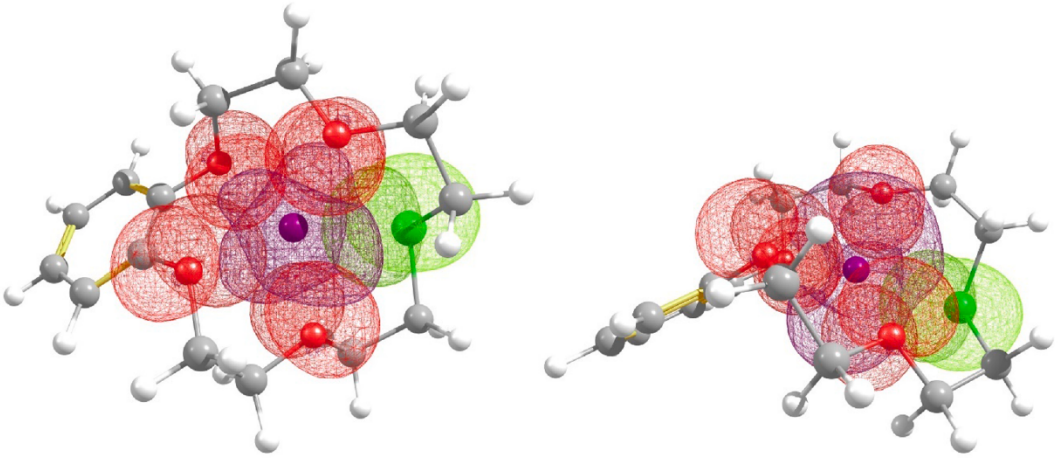

Fig. 6. Representation of the relevant NBOs of the thio–B15C5–Li^+ complex from different perspectives: Donor–NBOs LP1 and LP2 of oxygen (red) and sulfur (green) with an occupancy near 2, as well as acceptor NBO LP* (purple; occupancy = 0.1316) of lithium. Contour value = 0.05.

The complexation constants for the 15-, 12- and 9-membered CEs are compared in Fig. 7 and are summarized, in addition to the Gibbs free energy, in Table S11 – S14. It should be kept in mind that these constants are evaluated in vacuum, and therefore complex stabilities will be strongly overestimated due to charged species in vacuum lacking the stabilization by the solvent as present in the experiment. This effect is especially pronounced for divalent ions. Still, they allow for evaluating the correlation of the chemical concepts discussed above with measurable quantities, and one may expect a reasonable correlation with stability trends in solution (at least if the solvent is not too polar). Complexation constants including the polarizable continuum model (PCM) are given for comparison in the SI (Figure S9). To exclude the additional uncertainty in modeling resulting from the PCM, the thermodynamic calculations in vacuum are the main focus of this manuscript, and will be discussed in the following. This type of calculation is well known also for experimental gas-phase studies of cation complexation by CEs and is suitable for describing host-guest interactions.[73-79] For each complex, the complex constant *K* increases in the following order: $K^+ < Na^+ < \mathbf{Li^+} < Ca^{2+} < \mathbf{Mg^{2+}}$, which is in good agreement with the trends from Hirshfeld and NBO analyses for X = N. The positive values confirm the thermodynamic stability of the complexes (in vacuum). Independent of the ring size, there is a preferential complexation of the divalent alkaline earth metals. For these, as for the alkali metal ions, the complex stability increases with decreasing ionic radius. The heteroatom substitution shows a slight positive effect on the complex stability. For example, the thio-B15C5-Li^+ complex shows a $7{\cdot}10^4$ times higher stability than B15C5-Li^+ (Table S11). The complex stability of the complexes with the 12- and 9-membered CEs benefits more from the introduction of a nitrogen atom into the ring skeleton. Aza-B9C3-Li^+ shows an approximately 10^3 times higher, and aza-B12C4-Li^+ a 10^4 times higher stability than the lithium complexes of the corresponding oxygen-CEs, whereas the thio-CEs only cause a stability increase by a factor of 5 and 20, respectively (see Table S11). In addition, the Mg/Li selectivity decreases for different ring sizes in the following order: B15C5 > B12C4 > B9C3.

Fig. 8 shows a summary of the different methods to evaluate or estimate complex formation for the different CEs with Li^+, Na^+, K^+, Mg^{2+}, and Ca^{2+}, comparing distances, Hirshfeld and NBO analyses, as well as thermodynamic calculations. The values for each method are reported relative to lithium as a reference (with a value of 1). It is evident that all methods yield similar trends, with only slight variations as discussed before, which mostly affect the Ca^{2+} complexes. This suggests that evaluating charge transfer and natural bond orbitals may serve as helpful guides for designing CEs with desired selectivity in future work.

3.4. *DFT data in solution in comparison with experimental results*

To confirm the comparability of the theoretical results to realistic conditions in the laboratory, thermodynamic values are calculated from the just described theoretical models, now including an approximate

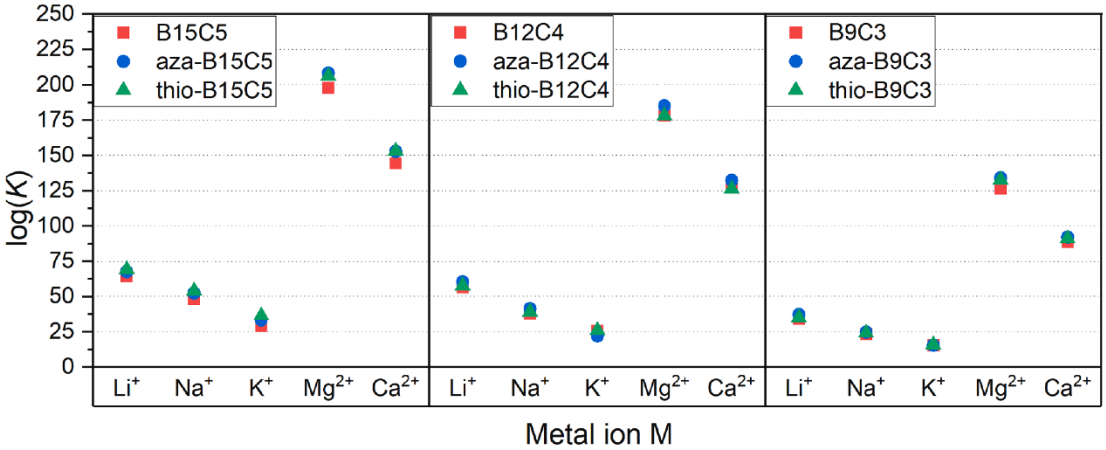

Fig. 7. Logarithm of the equilibrium constant of complex formation of 15-, 12- and 9-membered CEs with different metal ions in vacuum. Values were determined via DFT according to Equations (6) and (7).

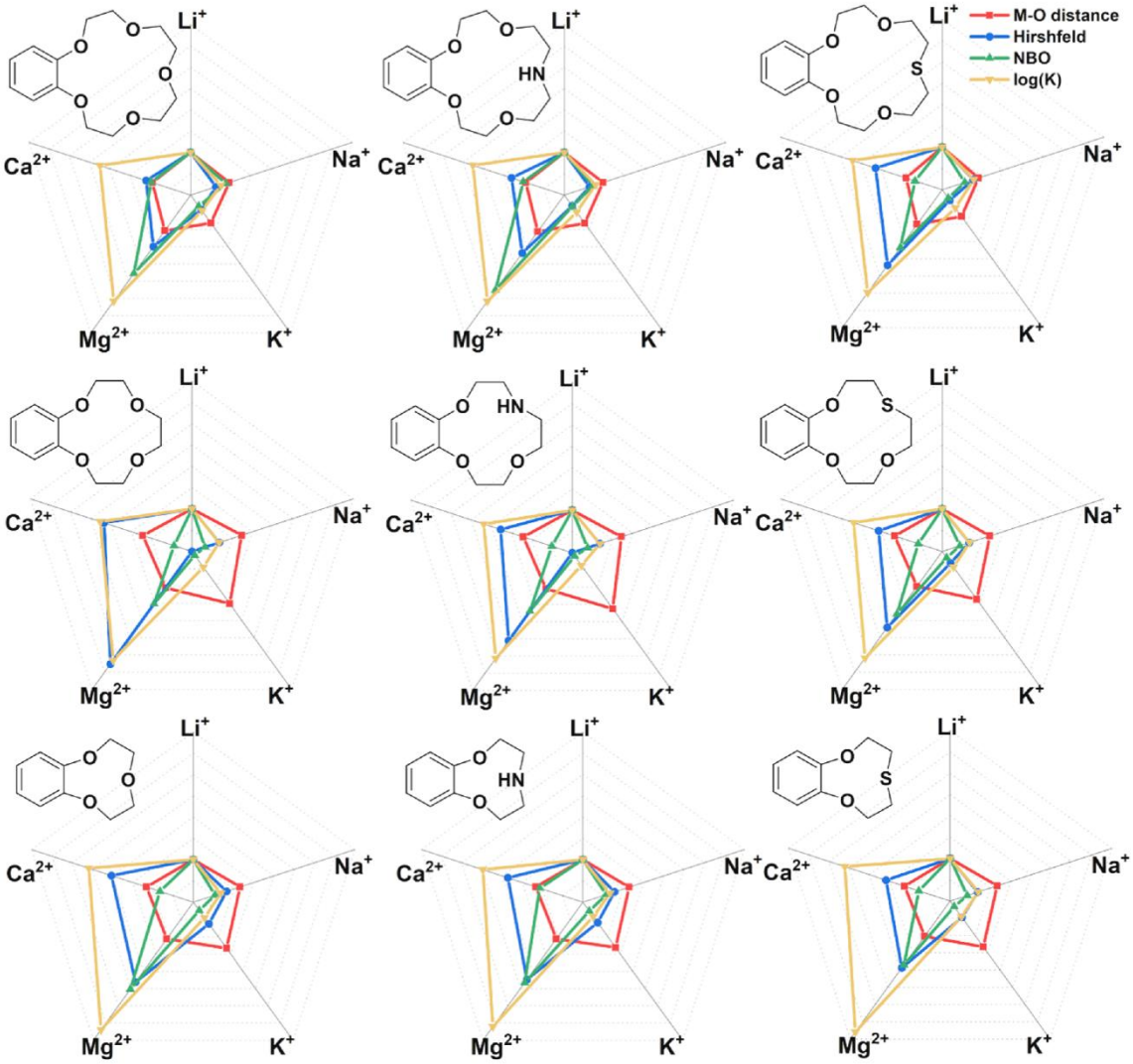

Fig. 8. Comparison of different methods for estimating complex stability within different CE complexes. Lithium is set as a reference point.

model of the solvent via a polarizable continuum model, and compared with experimental data of a liquid–liquid extraction in water/DCM. In this case, however, aza–15C5 (i.e. lacking the attached benzene moiety) is chosen as CE because of its commercial availability.

The structures of the aza–15C5 complexes with the different metal ions were optimized via DFT as shown in Fig. 9. The cavity size and the distances from metal to donor atom were determined, Hirshfeld population and NBO analyses were performed. The results are summarized in **Table S9**. A comparison of the experimental values for log(*K*), shown in Fig. 10, with the geometric and NBO data (showing the consistent trend $Mg^{2+} > Li^{+} > Ca^{2+} > Na^{+} > K^{+}$) and the data of the Hirshfeld population analysis ($Mg^{2+} > Ca^{2+} > Li^{+} > Na^{+} > K^{+}$) indicates a good agreement concerning the predominant Mg^{2+} complexation and rather moderate K^{+} complexation. However, the former is overestimated in relation to the other ions, analogous to the thermodynamic calculations. Although the values are very close to each other, the Na^{+} complexation is computationally estimated to be less favored than Li^{+}, contrary to the experimental trend.

The theoretical values discussed up to this point describe the situation of metal ions in *vacuo*, though this is not the most appropriate

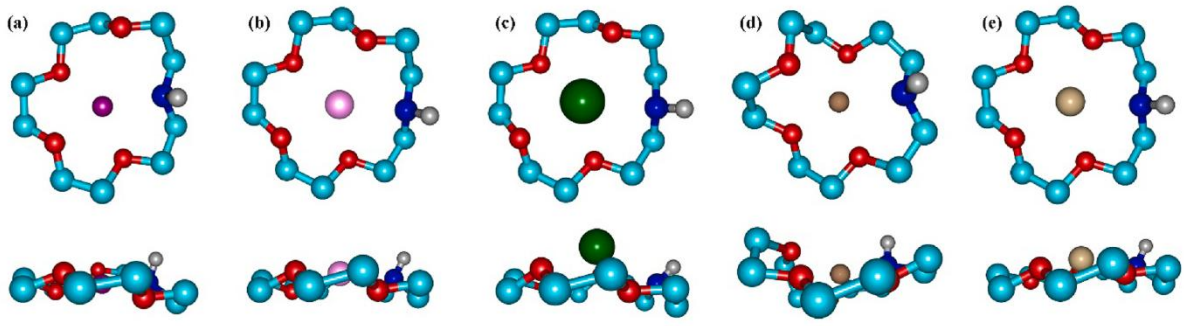

Fig. 9. DFT(PCM)-optimized structures of aza–15C5 complexes with Li^{+} (a), Na^{+} (b), K^{+} (c), Mg^{2+} (d), and Ca^{2+} (e) from two perspectives.

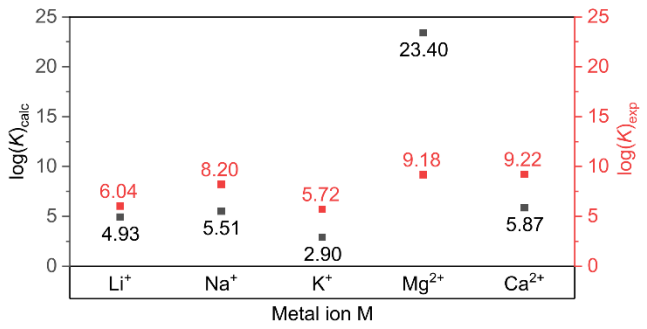

Fig. 10. Comparison of the logarithms of the complex constant *K* of complex formation of aza–15C5 with Li^+, Na^+, K^+, Mg^{2+}, and Ca^{2+}, determined via experimental liquid–liquid extraction (LLE; red) and DFT–based calculations (black). Single-ligand complexes were assumed for all calculations. The corresponding anions of the salts can be found in the SI (**Figure S10**).

description of laboratory conditions for liquid–liquid extraction schemes, as a solvent environment could have significant effects on, e.g., the strength of the host-guest interactions within a complex, on electronic properties of the complex, as well as on the general structure of the CE.[35,64] Metal ions in water create a surroundings hydration shell that must be stripped off before the metal ions can be complexed. [42,76,80] That hydration shell is particularly strong for ions with a high charge density.[81].

To confirm the applicability of the theoretical data to more realistic conditions, the stability of complexation is calculated theoretically and experimentally from liquid–liquid extraction in a DCM/water mixture (considering hydration shells of the metal ions in the aqueous phase and the permittivity of the organic solvent). In such a mixture, the CE is mainly located in the DCM phase and the salt is initially dissolved in the aqueous phase. As a consequence of the immiscibility of both phases, the extraction process takes place at the interface. After successful complexation, the CE–salt complex remains in the DCM phase. The complexation constants *K,* obtained by LLE*,* in comparison with the theoretical data, are shown in Fig. 10, indicating a thermodynamically favored complexation in all cases. The deviation between the experimental and the calculated values is due to factors that were not considered in the theoretical calculations, such as the effect of the anion and its hydration shell [42,76,80], the solubility of CE in DCM or other organic solvents [21,35,82], and the type and stoichiometry of the counterions [83-85], along with unavoidable approximations in the exchange-correlation functional. For cations with radii significantly exceeding the order of magnitude of the CE cavity size, ML_2 complexes are also conceivable. However, to keep things simple these have not been calculated here explicitly. Nevertheless, we obtain a qualitatively consistent picture of the experimental trends.

The experimental and DFT based trends are similar, which confirms the applicability of DFT to qualitatively predict CE complexation for the selected cations. More precisely, the trend of complex stability determined via both methods is $Ca^{2+} > Mg^{2+} > Na^+ > Li^+ > K^+$. In particular, the superiority of the magnesium complexation as well as of the calcium complexation is reproduced by the calculations, which originates from the lower hardness and thus improved interactions in the host–guest system.[86] The absence of the benzene ring and the associated larger structural flexibility of the CE allow a slight distortion of the sodium and calcium complex.[18,87] In absolute terms, however, the complexation of Mg^{2+} is strongly overestimated by DFT, while it is slightly underestimated for the other cations, leading to an overestimation of how much Mg^{2+} complexation is favored. This suggests that a more detailed investigation into appropriate simulation protocols is required if more quantitative predictions shall be made.

4. Conclusion

In this work, the lithium selectivity of three classes of CEs, B15C5, B12C4 and B9C3 (with decreasing ring sizes in that order) was compared with respect to other interfering metal ions as occurring in seawater, such as Na^+, K^+, Mg^{2+}, and Ca^{2+}, using DFT calculations in vacuum. The effects of different donor atoms (O, N, and S) within the CE were analyzed. Based on the theoretically optimized structures, a structural distortion of the CE frameworks was found when O was replaced by N or S, especially when the size relation of the cation and the CE cavity was rather unfavorable. Slightly increased stabilities were achieved when replacing oxygen by nitrogen or sulfur. Hirshfeld- and NBO analysis revealed an improved metal-donor interaction when substituting O by N or S. With only few exceptions, Hirshfeld charge transfer and NBO analyses follow similar trends as the complex stabilities. The best selectivity of Li^+ over Mg^{2+} was achieved by thio-B15C5. It was shown that the relation of the size of CE and the ion is crucial for selectivity as well as the participation of donor atoms. While these calculations in vacuum are not comparable to liquid–liquid extraction experiments in absolute terms, their qualitative trends agree quite well with those obtained exemplarily in solution. These DFT calculations, including DCM or water environments (as used for liquid–liquid extraction) modeled by a polarizable continuum model, showed in almost all cases lower stability constants than in the experiment (except for Mg^{2+}, where they were considerably larger than in the experiment). CE solubility in organic solvents, anion effects, as well as stoichiometry ratios between ion and counter ion were not considered in the calculations. The similar trends observed for the theoretical and experimental data suggest that the combination of geometrical structural optimization, thermodynamic calculation, Hirshfeld population, and NBO analysis could be highly useful for predicting strong interactions between donor atoms and metal ions, with the strong binding of Mg^{2+} presenting a challenge. The systematic study conducted in this work should contribute to the design of host ligands for a stronger complexation of lithium.

Authors contributions

All authors conceived the experiments and calculations. I.O. and S.T. designed and performed all experiments and calculations and wrote the paper, with support by V.A. and C.H. in writing the paper. This work is supported by the Cluster of Excellence 'CUI: Advanced Imaging of Matter' of the Deutsche Forschungsgemeinschaft (DFG) - EXC 2056 - project ID 390715994. All authors analyzed the data.

Declaration of Competing Interest

The authors declare that they have no known competing financial interests or personal relationships that could have appeared to influence the work reported in this paper.

Acknowledgements

The authors thank the High-Performance Computing Center at University of Hamburg for computational resources and Haitao Zhang and Michael Deffner for helpful discussions regarding the DFT calculations.

Appendix A. Supplementary material

Supplementary data to this article can be found online at https://doi.org/10.1016/j.seppur.2022.121142.

References

[1] L.M. Palacios-Romero, H. Pfeiffer, Lithium cuprate (Li2CuO2): a new possible ceramic material for CO2 chemisorption, Chem. Lett. 37 (2008) 862–863, https://doi.org/10.1246/cl.2008.862.

[2] A.R. Kulkarni, H.S. Maiti, A. Paul, Fast ion conducting lithium glasses-Review, Bull. Mater. Sci. 6 (1984) 201–221, https://doi.org/10.1007/BF02743897.

[3] N.C. Patel, M.P. DelBello, H.S. Bryan, C.M. Adler, R.A. Kowatch, K. Stanford, S. M. Strakowski, Open-label lithium for the treatment of adolescents with bipolar depression, J. Am. Acad. Child Adolesc. Psychiatry 45 (2006) 289–297, https://doi.org/10.1097/01.chi.0000194569.70912.a7.

[4] J.W. Makepeace, T.J. Wood, H.M.A. Hunter, M.O. Jones, W.I.F. David, Ammonia decomposition catalysis using non-stoichiometric lithium imide, Chem. Sci. 6 (2015) 3805–3815, https://doi.org/10.1039/c5sc00205b.

[5] B. Lin, I. Rustamov, L. Zhang, J. Luo, X. Wan, Graphene-reinforced lithium grease for antifriction and antiwear, ACS Appl. Nano Mater. 3 (2020) 10508–10521, https://doi.org/10.1021/acsanm.0c02461.

[6] B. Scrosati, J. Garche, Lithium batteries: status, prospects and future, J. Power Sources 195 (2010) 2419–2430, https://doi.org/10.1016/j.jpowsour.2009.11.048.

[7] P.W. Gruber, P.A. Medina, G.A. Keoleian, S.E. Kesler, M.P. Everson, T. J. Wallington, Global lithium availability: a constraint for electric vehicles? J. Ind. Ecol. 15 (2011) 760–775, https://doi.org/10.1111/j.1530-9290.2011.00359.x.

[8] B. Swain, Separation and purification of lithium by solvent extraction and supported liquid membrane, analysis of their mechanism: a review, J. Chem. Technol. Biotechnol. 91 (2016) 2549–2562, https://doi.org/10.1002/jctb.4976.

[9] E.C. Evarts, Lithium batteries: to the limits of lithium, Nature 526 (2015) 93–95, https://doi.org/10.1038/526S93a.

[10] A. Yaksic, J.E. Tilton, Using the cumulative availability curve to assess the threat of mineral depletion: the case of lithium, Resour. Policy 34 (2009) 185–194, https://doi.org/10.1016/j.resourpol.2009.05.002.

[11] X. He, S. Kaur, R. Kostecki, Mining lithium from seawater, Joule 4 (2020) 1357–1358, https://doi.org/10.1016/j.joule.2020.06.015.

[12] P.K. Choubey, K.-S. Chung, M.-S. Kim, J.-C. Lee, R.R. Srivastava, Advance review on the exploitation of the prominent energy-storage element lithium. part II: from sea water and spent lithium ion batteries (LIBs), Miner. Eng. 110 (2017) 104–121.

[13] A. Pálsdóttir, C.A. Alabi, J.W. Tester, Characterization of 14-Crown-4 ethers for the extraction of lithium from natural brines: synthesis, solubility measurements in supercritical carbon dioxide, and thermodynamic modeling, Ind. Eng. Chem. Res. 60 (2021) 7926–7934, https://doi.org/10.1021/acs.iecr.1c00346.

[14] C. Liu, Y. Li, D. Lin, P.C. Hsu, B. Liu, G. Yan, T. Wu, Y. Cui, S. Chu, Lithium extraction from seawater through pulsed electrochemical intercalation, Joule 4 (2020) 1459–1469, https://doi.org/10.1016/j.joule.2020.05.017.

[15] L. Tang, S. Huang, Y. Wang, D. Liang, Y. Li, J. Li, Y. Wang, Y. Xie, W. Wang, Highly efficient, stable, and recyclable hydrogen manganese oxide/cellulose film for the extraction of lithium from seawater, ACS Appl. Mater. Interfaces 12 (2020) 9775–9781, https://doi.org/10.1021/acsami.9b21612.

[16] S. Yang, F. Zhang, H. Ding, P. He, H. Zhou, Lithium metal extraction from seawater, Joule 2 (2018) 1648–1651, https://doi.org/10.1016/j.joule.2018.07.006.

[17] L.S. Balistrieri, J.W. Murray, The influence of the major ions of seawater on the adsorption of simple organic acids by goethite, Geochim. Cosmochim. Acta 51 (1987) 1151–1160, https://doi.org/10.1016/0016-7037(87)90208-0.

[18] R.E.C. Torrejos, G.M. Nisola, H.S. Song, L.A. Limjuco, C.P. Lawagon, K. J. Parohinog, S. Koo, J.W. Han, W.J. Chung, Design of lithium selective crown ethers: synthesis, extraction and theoretical binding studies, Chem. Eng. J. 326 (2017) 921–933, https://doi.org/10.1016/j.cej.2017.06.005.

[19] K. Nishizawa, S.I. Ishino, H. Watanabe, M. Shinagawa, Lithium isotope separation by liquid-liquid extraction using benzo-15-crown-5, J. Nucl. Sci. Technol. 21 (1984) 694–701, https://doi.org/10.1080/18811248.1984.9731102.

[20] X. Bai, J. Dai, Y. Ma, W. Bian, J. Pan, 2-(Allyloxy) methylol-12-crown-4 ether functionalized polymer brushes from porous PolyHIPE using UV-initiated surface polymerization for recognition and recovery of lithium, Chem. Eng. J. 380 (2020) 122386.

[21] R.M. Izatt, J.S. Bradshaw, S.A. Nielsen, J.D. Lamb, J.J. Christensen, D. Sen, Thermodynamic and kinetic data for cation-macrocycle interaction, Chem. Rev. 85 (1985) 271–339, https://doi.org/10.1021/cr00068a003.

[22] C.J. Pedersen, Cyclic polyethers and their complexes with metal salts, J. Am. Chem. Soc. 89 (1967) 7017–7036, https://doi.org/10.1021/ja01002a035.

[23] J.W. Steed, First- and second-sphere coordination chemistry of alkali metal crown ether complexes, Coord. Chem. Rev. 215 (2001) 171–221, https://doi.org/10.1016/S0010-8545(01)00317-4.

[24] A. van der Ham, T. Hansen, G. Lodder, J.D.C. Codée, T.A. Hamlin, D.V. Filippov, Computational and NMR studies on the complexation of lithium ion to 8-Crown-4, ChemPhysChem. 20 (2019) 2103–2109, https://doi.org/10.1002/cphc.201900496.

[25] M. Sarma, T. Chatterjee, S.K. Das, Ammonium-crown ether based host-guest systems: N-H···O hydrogen bond directed guest inclusion featuring N-H donor functionalities in angular geometry, RSC Adv. 2 (2012) 3920–3926, https://doi.org/10.1039/c2ra20109g.

[26] S. Roy, K. Thirumoorthy, U.K. Padidela, P. Vairaprakash, A. Anoop, V. S. Thimmakondu, Organomagnesium crown ethers and their binding affinities with Li+, Na+, K+, Be2+, Mg2+, and Ca2+ ions – a theoretical study, ChemistrySelect 6 (2021) 8782–8790, https://doi.org/10.1002/slct.202102317.

[27] L.J. Mathias, Crown ethers and phase transfer catalysis in polymer chemistry, J. Macromol. Sci. 15 (1981) 853–876, https://doi.org/10.1080/00222338108056772.

[28] S. Chen, H. Yuan, N. Grinberg, A. Dovletoglou, G. Bicker, Enantiomeric separation of trans-2- aminocyclohexanol on a crown ether stationary phase using evaporative light scattering detection S, J. Liq. Chromatogr. Relat. Technol. 26 (2003) 425–442, https://doi.org/10.1081/JLC-120017180.

[29] Y. Kuwahara, H. Nagata, H. Nishi, Y. Tanaka, K. Kakehi, Detection and separation of free amino acid enantiomers by capillary electrophoresis with a chiral crown ether and indirect photometric detection, Chromatographia 62 (2005) 505–510, https://doi.org/10.1365/s10337-005-0658-9.

[30] M. Naumowicz, A.D. Petelska, Z.A. Figaszewski, The effect of the presence of crown ether on ion transport across the lipid bilayer, Cell. Mol. Biol. Lett. 8 (2003) 383–389.

[31] A. Cazacu, C. Tong, A. Van Der Lee, T.M. Fyles, M. Barboiu, Columnar self-assembled ureido crown ethers: an example of ion-channel organization in lipid bilayers, J. Am. Chem. Soc. 128 (2006) 9541–9548, https://doi.org/10.1021/ja061861w.

[32] F. Sannicolò, E. Brenna, T. Benincori, G. Zotti, S. Zecchin, G. Schiavon, T. Pilati, Highly ordered poly(cyclopentabithiophenes) functionalized with crown-ether moieties for lithium-and sodium-sensing electrodes, Chem. Mater. 10 (1998) 2167–2176, https://doi.org/10.1021/cm980067+.

[33] M. Takagi, H. Nakamura, Analytical application of functionalized crown ether - metal complexes, 1986. https://doi.org/10.1080/00958978608075855.

[34] S. De, A. Boda, S.M. Ali, Preferential interaction of charged alkali metal ions (guest) within a narrow cavity of cyclic crown ethers (neutral host): a quantum chemical investigation, J. Mol. Struct. Theochem. 941 (2010) 90–101, https://doi.org/10.1016/j.theochem.2009.11.009.

[35] A. Boda, S. Musharaf Ali, H. Rao, S.K. Ghosh, Ab initio and density functional theoretical design and screening of model crown ether based ligand (host) for extraction of lithium metal ion (guest): effect of donor and electronic induction, J. Mol. Model. 18 (2012) 3507–3522, https://doi.org/10.1007/s00894-011-1348-1.

[36] J. Korchowiec, B. Korchowiec, W. Priebe, E. Rogalska, DFT study on the selectivity of complexation of metal cations with a dioxadithia crown ether ligand, J. Phys. Chem. A 112 (2008) 13633–13640, https://doi.org/10.1021/jp8066052.

[37] G. Donnay, J.W. Gryder, The oxygen coordinations of lithium, J. Chem. Educ. 42 (1965) 223, https://doi.org/10.1021/ed042p223.

[38] M.E. Volipin, Y.N. Novikov, Coordination chemistry of graphite, Pure Appl. Chem. 60 (1988) 1133–1140, https://doi.org/10.1351/pac198860081133.

[39] C.W. Bock, A. Kaufman, J.P. Glusker, Coordination of water to magnesium cations, Inorg. Chem. 33 (1994) 419–427, https://doi.org/10.1021/ic00081a007.

[40] R.A. Bartsch, M.J. Goo, G.D. Christian, X. Wen, B.P. Czech, E. Chapoteau, A. Kumar, Influence of ring substituents and matrix on lithium / sodium selectivity of 14-crown-4 and benzo-13-crown-4-compounds, Anal. Chim. Acta 272 (1993) 285–292, https://doi.org/10.1016/0003-2670(93)80581-5.

[41] K. Kobiro, New class of lithium ion selective crown ethers with bulky decalin subunits, Coord. Chem. Rev. 148 (1996) 135–149, https://doi.org/10.1016/0010-8545(96)01209-X.

[42] Y. Sun, M. Zhu, Y. Yao, H. Wang, B. Tong, Z. Zhao, A novel approach for the selective extraction of Li + from the leaching solution of spent lithium-ion batteries using benzo-15-crown-5 ether as extractant, Sep. Purif. Technol. 237 (2020), 116325, https://doi.org/10.1016/j.seppur.2019.116325.

[43] I. Oral, V. Abetz, A highly selective polymer material using benzo-9-crown-3 for the extraction of lithium in presence of other interfering alkali metal ions, Macromol. Rapid Commun. 42 (2021) 2000746, https://doi.org/10.1002/marc.202000746.

[44] I. Oral, V. Abetz, Improved alkaline metal ion capturing utilizing crown ether-based diblock copolymers in a sandwich-type complexation, Soft Matter (2022), https://doi.org/10.1002/9783527617050.

[45] I. Oral, L. Grossmann, E. Fedorenko, J. Struck, V. Abetz, Synthesis of poly (methacrylic acid)-block-polystyrene diblock copolymers at high solid contents via RAFT emulsion polymerization, Polymers (Basel) 13 (2021) 3675, https://doi.org/10.3390/polym13213675.

[46] E. Li, J. Kang, P. Ye, W. Zhang, F. Cheng, C. Yin, A prospective material for the highly selective extraction of lithium ions based on a photochromic crowned spirobenzopyran, J. Mater. Chem. B 7 (2019) 903–907, https://doi.org/10.1039/c8tb02906g.

[47] K.S. Diao, H.J. Wang, Z.M. Qiu, A DFT study on the metal binding selectivity of 12-crown-4 and its heterocyclic analogs, J. Mol. Struct. Theochem. 901 (2009) 157–162, https://doi.org/10.1016/j.theochem.2009.01.026.

[48] E.R. Dobbs, Transport properties, in: R. Dobbs (Ed.), Helium Three, Oxford University Press, 2001, pp. 275–311.

[49] A.A. Bagatur'yants, A.Y. Freidzon, M.V. Alfimov, E.J. Baerends, J.A.K. Howard, L. G. Kuz'mina, DFT calculations on the electronic and geometrical structure of 18-crown-6 complexes with Ag+, Hg2+, Ag0, Hg+, Hg0, AgNo3, and HgX2 (X = Cl, BR, and I), J. Mol. Struct. Theochem. 588 (1-3) (2002) 55–69.

[50] M.J. Frisch, G.W. Trucks, H.B. Schlegel, G.E. Scuseria, M.A. Robb, J.R. Cheeseman, G. Scalmani, V. Barone, G.A. Petersson, H. Nakatsuji, X. Li, M. Caricato, A. V. Marenich, J. Bloino, B.G. Janesko, R. Gomperts, B. Mennucci, H.P. Hratchian, J. V. Ortiz, A.F. Izmaylov, J.L. Sonnenberg, D. Williams-Young, F. Ding, F. Lipparini, F. Egidi, J. Goings, B. Peng, A. Petrone, T. Henderson, D. Ranasinghe, V.G. Zakrzewski, J. Gao, N. Rega, G. Zheng, W. Liang, M. Hada, M. Ehara, K. Toyota, R. Fukuda, J. Hasegawa, M. Ishida, T. Nakajima, Y. Honda, O. Kitao, H. Nakai, T. Vreven, K. Throssell, J. J. A. Montgomery, J.E. Peralta, F. Ogliaro, M.J. Bearpark, J. J. Heyd, E.N. Brothers, K.N. Kudin, V.N. Staroverov, T.A. Keith, R. Kobayashi, J. Normand, K. Raghavachari, A.P. Rendell, J.C. Burant, S.S. Iyengar, J. Tomasi, M. Cossi, J.M. Millam, M. Klene, C. Adamo, R. Cammi, J.W. Ochterski, R.L. Martin, K. Morokuma, O. Farkas, J.B. Foresman, D.J. Fox, Gaussian 16, Revision C.01, (2019).

[51] A.D. Becke, Density-functional thermochemistry. III. the role of exact exchange, J. Chem. Phys. 98 (7) (1993) 5648–5652.

[52] F. Weigend, R. Ahlrichs, Balanced basis sets of split valence, triple zeta valence and quadruple zeta valence quality for H to Rn: design and assessment of accuracy,

Phys. Chem. Chem. Phys. 7 (2005) 3297–3305, https://doi.org/10.1039/b508541a.
[53] S. Grimme, J. Antony, S. Ehrlich, H. Krieg, A consistent and accurate ab initio parametrization of density functional dispersion correction (DFT-D) for the 94 elements H-Pu, J. Chem. Phys. 132 (15) (2010) 154104.
[54] K.J. Hintze, A. Lützen, T. Bredow, Structure and stability of supramolecular crown ether complexes, J. Comput. Chem. 36 (2015) 1467–1472, https://doi.org/10.1002/jcc.23950.
[55] R.D. Dennington, T.A. Ketith, J.M. Millam, GaussView 5.0.9, (2008).
[56] E.D. Glendening, A.E. Reed, J.E. Carpenter, F. Weinhold, NBO Version 3.1., (n.d.).
[57] G.A. Andrienko, Chemcraft 1.8 (build 595b), (2020).
[58] S.X. Hu, J.J. Liu, J.K. Gibson, J. Li, Periodic trends in actinyl thio-crown ether complexes, Inorg. Chem. 57 (2018) 2899–2997, https://doi.org/10.1021/acs.inorgchem.7b03277.
[59] R. Das, P.K. Chattaraj, Guest-host interaction in an aza crown analog, Int. J. Quantum Chem. 114 (2014) 708–719, https://doi.org/10.1002/qua.24648.
[60] Z. Zhao, H. Tian, M. Zhang, Y. Yang, H. Zhang, Molecular design of macrocyclic compounds for complete removal of thallium(I) from wastewater, Environ. Sci. Pollut. Res. 25 (2018) 34550–34558, https://doi.org/10.1007/s11356-018-3393-0.
[61] N. Alizadeh, A comparison of complexation of Li+ ion with macrocyclic ligands 15-crown-5 and 12-crown-4 in binary nitromethane-acetonitrile mixtures by using lithium-7 NMR technique and ab initio calculation, Spectrochim. Acta - Part A Mol. Biomol. Spectrosc. 78 (2011) 488–493, https://doi.org/10.1016/j.saa.2010.11.014.
[62] C.C. Liou, J.S. Brodbelt, Determination of orders of relative alkali metal ion affinities of crown ethers and acyclic analogs by the kinetic method, J. Am. Soc. Mass Spectrom. 3 (1992) 543–548, https://doi.org/10.1016/1044-0305(92)85031-E.
[63] S.Y. Lin, S.W. Liu, C.M. Lin, C.H. Chen, Recognition of potassium ion in water by 15-crown-5 functionalized gold nanoparticles, Anal. Chem. 74 (2002) 330–335, https://doi.org/10.1021/ac0156316.
[64] A. Boda, S.M. Ali, M.R.K. Shenoi, H. Rao, S.K. Ghosh, DFT modeling on the suitable crown ether architecture for complexation with Cs+ and Sr2+ metal ions, J. Mol. Model. 17 (2011) 1091–1108, https://doi.org/10.1007/s00894-010-0812-7.
[65] R.E.C. Torrejos, G.M. Nisola, S.H. Min, J.W. Han, S. Koo, K.J. Parohinog, S. Lee, H. Kim, W.J. Chung, Aqueous synthesis of 14–15-membered crown ethers with mixed O, N and S heteroatoms: experimental and theoretical binding studies with platinum-group metals, Chempluschem. 84 (2019) 210–221, https://doi.org/10.1002/cplu.201800541.
[66] C.Y. Chen, C.T. Cheng, C.W. Lai, P.W. Wu, K.C. Wu, P.T. Chou, Y.H. Chou, H. T. Chiu, Potassium ion recognition by 15-crown-5 functionalized CdSe/ZnS quantum dots in H2O, Chem. Commun. (2006) 263–265, https://doi.org/10.1039/b512677k.
[67] H.R. Yu, J.Q. Hu, X.H. Lu, X.J. Ju, Z. Liu, R. Xie, W. Wang, L.Y. Chu, Insights into the effects of 2:1 "sandwich-type" crown-ether/metal-ion complexes in responsive host - guest systems, J. Phys. Chem. B. 119 (2015) 1696–1705, https://doi.org/10.1021/jp5079423.
[68] P.D. Beer, S.W. Dent, Potassium cation induced switch in anion selectivity exhibited by heteroditopic ruthenium(II) and rhenium(I) bipyridyl bis(benzo-15-crown-5) ion pair receptors, Chem. Commun. (1998) 825–826, https://doi.org/10.1039/a800356d.
[69] F.L. Hirshfeld, Bonded-atom fragments for describing molecular charge densities, Theor. Claim. Acta. 44 (1977) 129–138, https://doi.org/10.1007/BF00549096.
[70] T. Lu, F. Chen, Multiwfn: a multifunctional wavefunction analyzer, J. Comput. Chem. 33 (2012) 580–592, https://doi.org/10.1002/jcc.22885.
[71] F. Weinhold, C.R. Landis, Natural bond orbitals and extensions of localized bonding concepts, Chem. Educ. Res. Pr. 2 (2001) 91–104, https://doi.org/10.1039/b1rp90011k.
[72] A.E. Reed, L.A. Curtiss, F. Weinhold, Intermolecular interactions from a natural bond orbital, donor-acceptor viewpoint, Chem. Rev. 88 (1988) 899–926, https://doi.org/10.1021/cr00088a005.
[73] S. Maleknia, J. Brodbelt, Gas-phase selectivities of crown ethers for alkali metal ion complexation, J. Am. Chem. Soc. 114 (1992) 4295–4298, https://doi.org/10.1021/ja00037a038.
[74] T. Wulf, T. Heine, Small crown-ether complexes as molecular models for dihydrogen adsorption in undercoordinated extraframework cations in zeolites, J. Phys. Chem. C 124 (2020) 9409–9415, https://doi.org/10.1021/acs.jpcc.0c02815.
[75] J.C. López, C. Pérez, S. Blanco, V.A. Shubert, B. Temelso, G.C. Shields, M. Schnell, Water induces the same crown shapes as Li+ or Na+ in 15-crown-5 ether: a broadband rotational study, Phys. Chem. Chem. Phys. 21 (2019) 2875–2881, https://doi.org/10.1039/c8cp05552a.
[76] Y. Inokuchi, T. Ebata, T.R. Rizzo, UV and IR spectroscopy of transition metal-crown ether complexes in the gas phase: Mn2+(benzo-15-crown-5)(H2O)0–2, J. Phys. Chem. A. 123 (2019) 6781–6786, https://doi.org/10.1021/acs.jpca.9b05706.
[77] F. Gámez, B. Martínez-Haya, S. Blanco, J.C. López, J.L. Alonso, Microwave spectroscopy and quantum chemical investigation of nine low energy conformers of the 15-crown-5 ether, Phys. Chem. Chem. Phys. 14 (2012) 12912–12918, https://doi.org/10.1039/c2cp41635b.
[78] E. Cristina Stanca-Kaposta, D.P. Gamblin, J. Screen, B. Liu, L.C. Snoek, B.G. Davis, J.P. Simons, Carbohydrate molecular recognition: A spectroscopic investigation of carbohydrate-aromatic interactions, Phys. Chem. Chem. Phys. 9 (2007) 4452–4459, https://doi.org/10.1039/b704792d.
[79] V.A. Shubert, W.H. James, T.S. Zwier, Jet-cooled electronic and vibrational spectroscopy of crown ethers: benzo-15-crown-5 ether and 4′-amino-benzo-15-crown-5 ether, J. Phys. Chem. A 113 (28) (2009) 8055–8066.
[80] Y. Tachibana, T. Suzuki, M. Nogami, M. Nomura, T. Kaneshiki, Selective lithium recovery from seawater using crown ether resins, J. Ion Exch. 29 (2018) 90–96, https://doi.org/10.5182/jaie.29.90.
[81] N. Wiberg, Lehrbuch der Anorganischen Chemie, 102nd ed., De Gruyter, Berlin, 2007.
[82] Y. Li, P. Huszthy, I. Móczár, B. Szemenyei, S. Kunsági-Máté, Solvent effect on the complex formation of a crown ether derivative with sodium and potassium ions. thermodynamic background of selectivity, Chem. Phys. Lett. 556 (2013) 94–97, https://doi.org/10.1016/j.cplett.2012.11.056.
[83] U. Olsher, M.G. Hankins, Y.D. Kim, R.A. Bartsch, Anion effect on selectivity in crown ether extraction of alkali metal cations, J. Am. Chem. Soc. 115 (1993) 3370–3371, https://doi.org/10.1021/ja00061a062.
[84] A.F. Danil De Namor, J.C.Y. Ng, M.A. Llosa Tanco, M. Salomon, Thermodynamics of lithium-crown ether (12-crown-4 and 1-benzyl-1-aza-12-crown-4) interactions in acetonitrile and propylene carbonate. the anion effect on the coordination process, J. Phys. Chem. 100 (1996) 14485–14491, https://doi.org/10.1021/jp960519a.
[85] J.D. Lamb, J.J. Christensen, S.R. Izatt, K. Bedke, M.S. Astin, R.M. Izatt, Effects of salt concentration and anion on the rate of carrier-facilitated transport of metal cations through bulk liquid membranes containing crown ethers, J. Am. Chem. Soc. 102 (1980) 3399–3403, https://doi.org/10.1021/ja00530a016.
[86] R.G. Parr, R.G. Pearson, Absolute hardness: companion parameter to absolute electronegativity, J. Am. Chem. Soc. 105 (1983) 7512–7516, https://doi.org/10.1021/ja00364a005.
[87] Z. Talebpour, N. Alizadeh, H.R. Bijanzadeh, M. Shamsipur, Cadmium-113 NMR and theoretical studies of complexation of cadmium ion with 15-crown-5 and benzo-15-crown-5 in acetonitrile and its binary mixtures with water and nitromethane, J. Incl. Phenom. Macrocycl. Chem. 49 (2004) 101–106, https://doi.org/10.1023/B:JIPH.0000031121.36121.52.

5.2. PUBLICATION 2

This publication is reprinted with permission from S. Jaehnke, J. von Chamier Gliszczynski, B. Hankiewicz, V. Abetz, Systematic Investigation of a Crown Ether Functionalized PS-*b*-PMAA Block Copolymer for Optimized Lithium Extraction From Aqueous Media, *J. Polym. Sci*. (**2025**) 1–11. Published by Wiley Periodicals LLC.

Parts of this work were carried out in collaboration with Joachim von Chamier-Gliszczynski as part of his bachelor's thesis, under my supervision and guidance. His great commitment to this project is gratefully acknowledged. The software required for evaluating the DLS measurements was provided by Birgit Hankiewicz, whose expertise contributed significantly to the success of this project.

The material investigated in this thesis comprises two components: the CE and a suitable matrix. Publication 1 explores various CEs with regard to their ability to complex Li. Publication 2 investigates the second component of the material, the polymer matrix, with the objective of maximizing Li extraction. To this end, a series of PS-*b*-PMAA block copolymers were produced and subsequently functionalized *via* Mitsunobu esterification with the 9-membered benzo-CE (B9C3), enabling the formation of ML_2-type sandwich complexes. The influence of the degree of polymerization (DP), the block length of the hydrophobic PS block, and the degree of functionalization of the PMAA block on Li complexation were systematically analyzed.

LLE was performed in a biphasic dichloromethane/water system, the complexation constant was determined, and DLS measurements of the dissolved polymers were conducted before and after complexation. Optimal Li complexation was observed with high-molecular-weight systems (up to 310 kDa), a short length of the hydrophilic block (8wt% PMAA), and high functionalization with CE (72% functionalization of the PMAA units). Furthermore, DLS results showed that intramolecular complexation significantly occurs between the polymer chains.[ix] The combination of the polymer parameters, which found to be ideal, resulted in a system that enabled exceptionally high Li complexation, outperforming all other systems investigated.

The supporting information connected to this publication can be found in section 9.3.

[ix] To investigate this further, studies by J. von Chamier Gliszczynski are already being conducted in our working group.

Check for updates

Journal of Polymer Science

WILEY

JOURNAL OF POLYMER SCIENCE

RESEARCH ARTICLE OPEN ACCESS

Systematic Investigation of a Crown Ether Functionalized PS-*b*-PMAA Block Copolymer for Optimized Lithium Extraction From Aqueous Media

Sabrina Jaehnke[1] | Joachim von Chamier Gliszczynski[1] | Birgit Hankiewicz[1] | Volker Abetz[1,2]

[1]Institute of Physical Chemistry, Universität Hamburg, Hamburg, Germany | [2]Institute of Membrane Research, Helmholtz-Zentrum Hereon, Geesthacht, Germany

Correspondence: Volker Abetz (sabrina.jaehnke@uni-hamburg.de)

Received: 15 January 2025 | **Revised:** 17 February 2025 | **Accepted:** 18 February 2025

Keywords: crown ether | functionalized polymers | liquid–liquid extraction | lithium from aqueous media | lithium recovery | self-assembly

ABSTRACT

Crown ether (CE) functionalized polystyrene-*block*-poly(methacrylic acid) (PS-*b*-PMAA) material (PS-*b*-P(MAA-*r*-CE3MA)) forms lithium-CE sandwich complexes with high selectivity. The complexation strength of PS-*b*-P(MAA-*r*-CE3MA) was determined in a two-phase extraction. A two-step one-pot RAFT polymerization in water was used to synthesize the block copolymers, in which the macro-RAFT agent (PMAA) produced in the first step was polymerized with styrene in an emulsion polymerization in the second step. Subsequently, the MAA block was partially esterified with the functionalized CE. The polymer structure was varied for investigating the influence of the degree of polymerization (DP) of the overall polymer, the DP of the PS, and the functionalization density with regard to increasing the effectiveness of lithium complexation. Based on the observed trends, it was possible to optimize the system toward a significantly improved lithium complexation compared to free CE (by a factor of up to 4×10^8).

1 | Introduction

Lithium's importance to modern society is, particularly, evident in terms of lithium-ion batteries (LIBs), currently accounting for 74% of the lithium global end-use market [1–3]. The predominance of LIBs is attributable to the low-density (0.534 g cm^{-3}) and the low-normal potential (−3.045 V) of the alkali metal, and the high-energy capacity (100–265 Wh kg^{-1}) of LIBs [1, 4–6]. Due to the substantial increase in global lithium demand, the necessity of developing innovative and highly efficient methods of lithium extraction has become indispensable [3, 7–13]. Conventional lithium extraction takes place from primary (minerals, brines, seawater) or secondary resources (wastewater, spent LIBs) in the form of lithium salts, accumulating to a global total of 89 Mt. (2022) [1, 3, 7, 8]. Lithium-rich aqueous resources, which constitute 2/3 of the world's resources, were exploited intensively [1, 2, 7, 9, 14]. The resulting depletion of highly concentrated aqueous resources (i.e., brines, > 50 g L^{-1} Li$^+$) is pushing the industry toward using less concentrated aqueous media, that is, seawater with 0.17 ppm Li$^+$ [1, 15–18]. Although lithium extraction might be more cost- and resource-intensive, the economic feasibility of a process is always a combination of demand, alternatives, and long-term viability. Coupling with desalination plants, in particular, can dramatically reduce the process costs [1, 14, 19].

Innovative methods of lithium extraction from aqueous media include size- or charge-selective membranes, ion sieves, metal-based adorbents, precipitation, supramolecular structures, ionic liquids, and electrochemical processes [13, 19–25]. In addition, the combination of several established lithium extraction methods, known as tandem or coupled technologies, has recently been explored [7]. An example of the latter is selective electrodialysis (S-ED), in which electrodialysis

This is an open access article under the terms of the Creative Commons Attribution License, which permits use, distribution and reproduction in any medium, provided the original work is properly cited.

© 2025 The Author(s). *Journal of Polymer Science* published by Wiley Periodicals LLC.

with an interposed charge-selective membrane separates both ions and neutral molecules as well as differently valent ions [26]. The common denominator for all methods is overcoming general problems associated with lithium extraction from seawater. Besides the high efficiency of the developed systems due to the low percentage of lithium salts in seawater, the presence of significantly higher concentrated, competing ions is challenging [14, 16, 27, 28]. For example, 1.7×10^{-5} wt% Li^+ is found alongside 0.13 wt% Mg^{2+}, 1.8 wt% Na^+, 4×10^{-3} wt% K^+ and Ca^{2+} in the Mediterranean Sea, necessitating highly lithium-selective systems [1, 8]. Specific cation selectivities can be reached by complexation with suitable molecules, typically CEs [29]. In previous work, we have described the synthesis and performance of a highly Li^+ selective, functionalized block copolymer. This PS-*b*-PMAA based system has shown excellent lithium selectivity with respect to other alkali metals [27, 30]. Cation-complexing 9-membered [benzo-9-crown-3 (B9C3)] CEs provide ion selectivity based on the formation of sandwich ($Li(CE)_2$) complexes. To overcome the entropic impediment for complex formation, the immobilization of the CE using a polymer matrix yielded promising results. The liquid–liquid extraction (LLE) data showed several orders of magnitude greater lithium complexation of the polymer-fixed CEs compared to free CEs. These findings were successfully transferred to the complexation of larger ions [30]. Furthermore, the processability of the material in the form of an amphiphilic, water-insoluble polymer is enhanced [27, 31]. The (adapted) polymer synthesis and the formation of $Li(CE)_2$ are presented in Figure 1 [31–33].

In addition to the high lithium selectivity of PS-*b*-P(MAA-*r*-CE3MA), a systematic study of this promising system is essential to optimize its efficiency. High efficiency is of particular interest not only in a scientific context but also from an economic perspective when imagining large-scale applicability. Alongside well-known factors affecting the host-guest relationship, such as the dehydration of the ions and the ion–dipole interactions influenced by the ratio of the cavity/ion radii and the ion charge, this study will focus on the matrix [28, 34–36]. We assume that the structure of the block copolymer is crucial for complexation. Free MAA units, corresponding to varying functionalization density with CEs, can exert a repulsive interaction or even stabilize complex formation with lithium. The self-assembly of amphiphilic block copolymers varies with the block composition [37–40]. As part of the LLE, further factors such as interactions of P(MAA-*r*-CE3MA)–PS, P(MAA-*r*-CE3MA)–solvent A/B, PS–solvent A/B, and solvent A–solvent B decisively influence the thermodynamic equilibrium [41, 42]. Consequently, the process must be studied and understood in more detail to maximize efficiency.

In this study, the influence of different variations in the polymer system on lithium complexation is presented. In total, 15 different polymers were investigated (Figure 2). To this end, we will discuss three main topics: The structure of the polymer was varied with regard to the overall degree of polymerization (DP). The amphiphilic PS-*b*-PMAA was modified with a focus on the DP of the hydrophobic block (PS). Furthermore, the functionalization density (i.e., CE/MAA) is considered important; the presence of intra- and intermolecular sandwich complexes is investigated. The materials synthesis and lithium complexation are investigated using nuclear magnetic resonance (NMR) spectroscopy, dynamic light scattering (DLS), and LLE data via UV/Vis spectroscopy. The comparison of the obtained data gives insight into optimizing and maximizing the lithium complexation ability of the highly selective PS-*b*-P(MAA-*r*-CE3MA), leading to a highly efficient system for lithium extraction from seawater in the future.

2 | Results and Discussion

2.1 | DP

Six polymers with different molecular weights (MWs), ranging from 23 to 310 kDa, were tested. The functionalization density of the MAA units with CE, and the block ratio were kept as constant as possible in order to consider only the influence of the MW. For higher clarity, all polymers have an individual abbreviation according to the series of measurements assigned to them, which are listed in Table 1. For reference: The subscript numbers for the polymer P-MW-23, PS_{151}-*b*-P(MAA_{25}-*r*-$CE3MA_{18}$)[23]

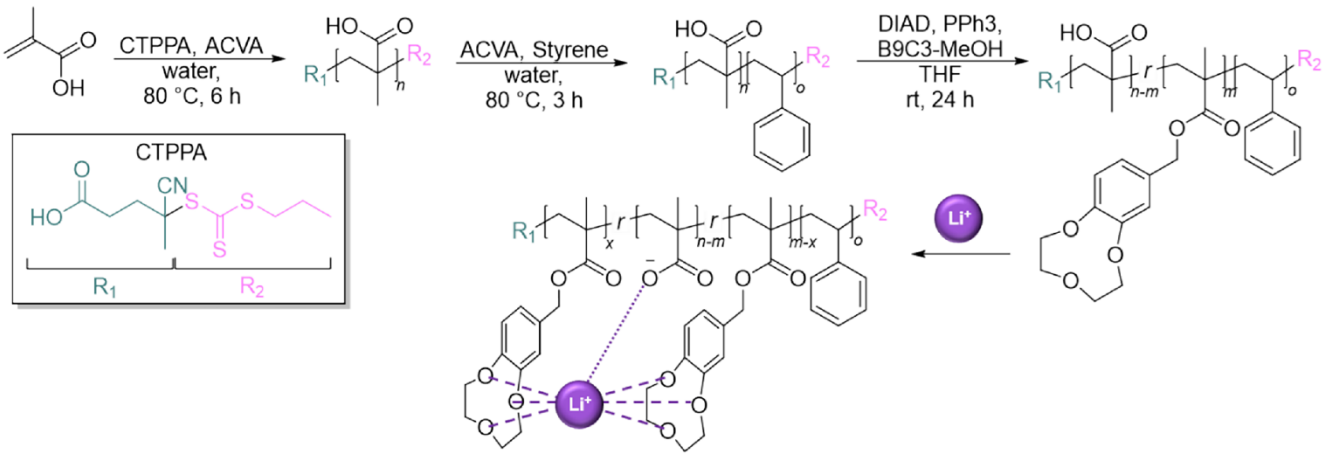

FIGURE 1 | Synthesis of the PMAA macro-RAFT agent, copolymerization with styrene yielding the amphiphilic block copolymer PS-*b*-PMAA, Mitsunobu esterification of the MAA units with hydroxymethyl-benzo-9-crown-3 (B9C3-MeOH) and schematic representation of a potential lithium complexation in sandwich conformation. The free acids can support the complexation.

26424169, 0, Downloaded from https://onlinelibrary.wiley.com/doi/10.1002/pol.20250060 by Universität Hamburg, Wiley Online Library on [02/04/2025]. See the Terms and Conditions (https://onlinelibrary.wiley.com/terms-and-conditions) on Wiley Online Library for rules of use; OA articles are governed by the applicable Creative Commons License

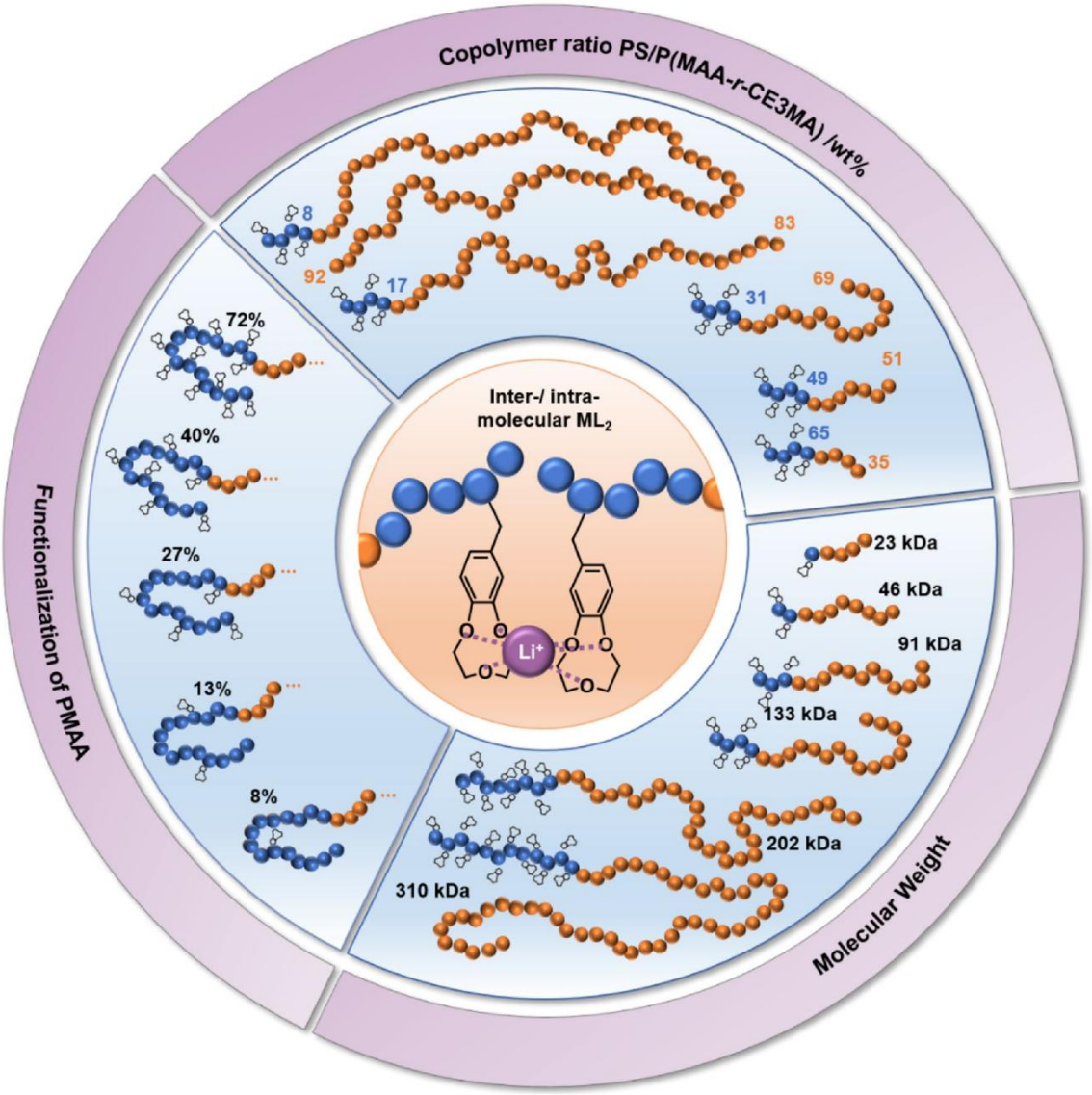

FIGURE 2 | Overview of the analyzed PS-*b*-P(MAA-*r*-CE3MA) polymers. The blue spheres represent MAA, the orange spheres styrene and the purple sphere lithium. The CE is shown schematically in black. The dashed lines indicate the host-guest interaction. Self-assembly of the polymer is coincidental. Intermolecular complexation is shown but is equivalent to the intramolecular depiction.

TABLE 1 | Characteristics of PS-*b*-P(MAA-*r*-CE3MA) copolymers with variation in the degree of polymerization.

Polymer	Sample-ID	Ratio of PS/P(MAA-*r*-CE3MA) (wt%/wt%)	M_n (kDa)	Functionalization of MAA units (%)
PS_{151}-*b*-P(MAA_{26}-*r*-$CE3MA_{17}$)^{23}	P-MW-23	69/31	23	40
PS_{301}-*b*-P(MAA_{56}-*r*-$CE3MA_{35}$)^{46}	P-MW-46	68/32	46	38
PS_{605}-*b*-P(MAA_{113}-*r*-$CE3MA_{70}$)^{91}	P-MW-91	68/32	91	38
PS_{887}-*b*-P(MAA_{173}-*r*-$CE3MA_{101}$)^{133}	P-MW-133	68/32	133	37
PS_{1289}-*b*-P(MAA_{239}-*r*-$CE3MA_{158}$)^{202}	P-MW-202	68/32	202	40
PS_{1998}-*b*-P(MAA_{337}-*r*-$CE3MA_{263}$)^{310}	P-MW-310	67/33	310	44

indicate 151 styrene units in the PS block, 25 MAA units, and 18 MAA units functionalized with B9C3 in the random P(MAA-*r*-CE3MA) block; the superscript number indicates the total number average MW (M_n) in kDa.

These CE functionalized polymers were investigated for their complexation properties within LLE in a two-phase dichloromethane (DCM)–water system. Complex stability can be quantified via the complex constant *K*, which results from

26424169, 0, Downloaded from https://onlinelibrary.wiley.com/doi/10.1002/pol.20250060 by Universitat Hamburg, Wiley Online Library on [02/04/2025]. See the Terms and Conditions (https://onlinelibrary.wiley.com/terms-and-conditions) on Wiley Online Library for rules of use; OA articles are governed by the applicable Creative Commons License

the Gibbs free energy difference ΔG, considering standard conditions (298.15 K). The polymers showed initially different solubility behavior, with the lower MW polymers showing better solubility in DCM. As the amount of polymer used varies with MW or functionalization, the known LLE procedure was slightly modified, as shown in Section 4.2. This adjustment ensures a sufficiently high initial absorbance and accuracy of the system in LLE. A clear solution was finally obtained in each case.

The superiority of the complexation strength of polymer-bound CE over free CE has previously been published [27]. This phenomenon is explained in more detail subsequently by means of the results presented, which also confirm this finding and provide further insights (see Figure 3).

The complexation constants K were calculated assuming the formation of $Li(CE)_2$ complexes. The free B9C3 CE complexes lithium with a log$K$ of only 10.44, which is three orders of magnitude smaller than the polymer with the lowest MW in the series, P-MW-23, with a log$K$ of 13.81 and even six orders of magnitude smaller than P-MW-310, with a log$K$ of 16.31. It is assumed that a lower loss of entropy within the polymer system, compared to free CE, is the key to the much higher complex stability. In earlier work by our group of Bey et al., thermodynamic studies were performed on the cation complexation of free and polymer-bound CEs. Entropy is found to be the driving force of the process, with polymer-bound CEs showing a comparatively lower entropy change upon ML_2 complexation than with free CEs, presumably due to the already limited translational degrees of freedom of the CE, attached to the matrix [30, 43, 44]. The enforced initial spatial proximity of the CE to one another, combined with the limited mobility of the CE, might also contribute to a more probable complex formation. This effect is even more pronounced when the DP is increased while the functionalization and polymer composition remain constant. It should be noted that K, derived from the decline in salt (LIS) concentration within the aqueous phase, pertains to the molar quantity of CE. Figure 3 shows a linear dependence of log$K$ on the MW up to a MW of 202 kDa. A further increase in MW to 310 kDa does not lead to an enhancement of complexation, whereby the slight increase in complex stability is presumably due to the somewhat higher functionalization, as explained in Section 2.3, counterweighted with the tendency of the MW distribution curve (Figure S22) toward smaller MWs compared to the other P-MW polymers. Apparently, a limit value for the optimal MW of the polymer ranges between 133 and 202 kDa, up to which the complexation benefits from an increase in the DP of the polymer.

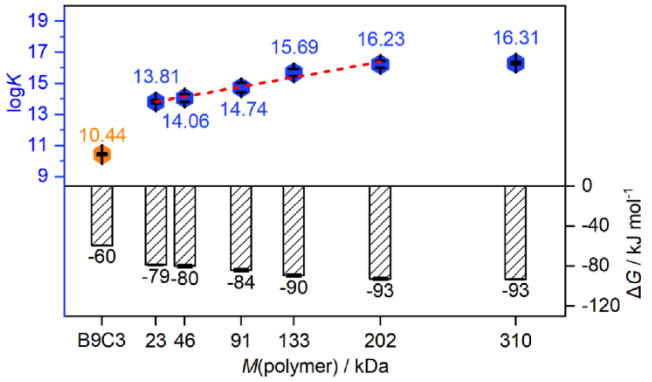

FIGURE 3 | Comparison of complex formation of free B9C3 CE and PS-*b*-P(MAA-*r*-CE3MA) with varying MW. Development of the logarithm of the equilibrium constants and Gibbs free energy with the MW and linear regression.

DLS measurements were performed to assess the nature of the sandwich complexation. On the one hand, intermolecular sandwich complexation is conceivable. Hereby, the CEs forming the $Li(CE)_2$ complex stem from two different polymer chains. On the other hand, intramolecular sandwich complexation corresponds to the formation of a complex of two CE of the same polymer chain, as shown in Figure 4.

The hydrodynamic radius R_h of the polymer chains in DCM increases toward larger MW (Figure 5). The increased deviation

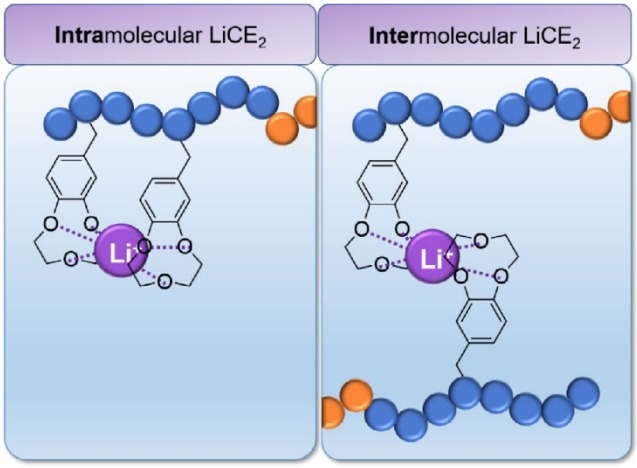

FIGURE 4 | Intra- (left) and intermolecular (right) $Li(CE)_2$ sandwich complexes from polymer bound CE. The blue spheres are MAA, the orange spheres are the (partially visible) styrene units.

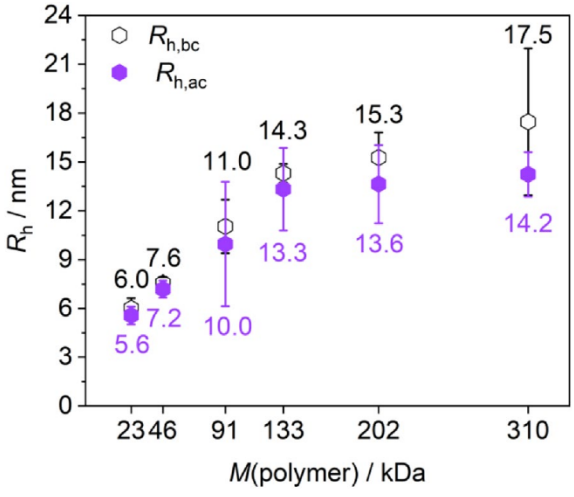

FIGURE 5 | Hydrodynamic radii plotted against the molecular weight of the P-MW polymers in DCM determined via DLS. Measurements were taken before ($R_{h,bc}$) and after complexation ($R_{h,ac}$) with lithium. Shown are the values of the dominant, smaller species, presumably showing intramolecular complexation.

26424169, 0, Downloaded from https://onlinelibrary.wiley.com/doi/10.1002/pol.20250060 by Universitat Hamburg, Wiley Online Library on [02/04/2025]. See the Terms and Conditions (https://onlinelibrary.wiley.com/terms-and-conditions) on Wiley Online Library for rules of use; OA articles are governed by the applicable Creative Commons License

of R_h with MW correlates with the increasing dispersity of the polymers at higher MWs (Table S4). Two species with different radii were identified. The particles with smaller R_h can be related to intramolecular and the ones with larger R_h to intermolecular complexation. The number-weighted ratio of these species was calculated. Interestingly, the ratio is stable at almost 100% intramolecular species both before and after extraction. Therefore, intermolecular complex formation can be neglected when interpreting the DLS data. The small amount of larger particles, present before and after complexation, can also be attributed to the MW distribution of the polymers. The SEC trace of P-MW-23 (Figure S17), for example, shows a peak at twice the MW of the curve's maximum, which suggests a recombinatory termination of the RAFT polymerization. Based on the trends found, it must, therefore, be considered that a slight overestimation of the log$K$ of this sample is possible. However, the trend remains unaffected. Further information can be found in Data S1. During complexation, a slight reduction in the radius can be observed, which presumably results from the complex formation of distant moieties and decreased chain mobility. The reduction in radius for the low MW polymers P-MW-23, P-MW-46, and P-MW-91 is merely 0%–4%. Given the small extent of this effect, it can be assumed that primarily neighboring CEs contribute to the formation of the $Li(CE)_2$ complex. With a 7%–19% decrease in radius, the high MW polymers P-MW-133, P-MW-202, and P-MW-310 are more strongly influenced by complexation. The increased chain mobility of the longer chains may allow the complex formation of non-directly adjacent CE. Even if these effects are considered, there is no evidence for intermolecular complexation. DOSY (diffusion ordered spectroscopy) measurements underline this assumption and are shown in Figures S7–S16. Only one polymer species was found in the DOSY spectra. The diffusion coefficient of this species is lower before extraction, and consequently, the hydrodynamic radius is larger, than after extraction.

The results reveal a significant influence of the DP on the $Li(CE)_2$ complexation strength. This can be attributed to the small entropy loss when forming several complexes with the same chain. The increased chain flexibility at higher MW additionally favors the preferential formation of intramolecular complexes.

2.2 | Length of the PS Block

The influence of the length of the PS block was analyzed in a series of five different CE functionalized polymers (Table 2). The unfunctionalized polymers ranged from 95 to 50 wt% PS, corresponding to the complementary values for PMAA. After functionalization, the values ranged from 92 to 35 wt% PS. In order to investigate the influence of the DP of the PS chain on the complexation solely, the percentage functionalization was kept nearly constant between 36% and 40%. This corresponds to an almost identical number of CE units per chain throughout this series. This is achieved by ensuring the block copolymers are consistently based on the same PMAA-macro-RAFT agent. As a result of the uniform DP of PMAA, as little systematic variance as possible was introduced into the system.

Again, the extraction of LIS with the functionalized block copolymers was analyzed in a two-phase DCM-water system. Elemental analyses were performed to ensure that lithium was not prematurely complexed during the synthesis of the (functionalized) polymer and/or CE. The Li^+ free nature of all CE stages, PS-*b*-PMAA and PS-*b*-P(MAA-*r*-CE3MA) was confirmed. PS-MW-46 is also included in the previous series. For clarity, the designation P-R-69 is used here. The influence of the PS block length on K and ΔG is shown in Figure 6.

With a log$K$ of 16.91 and thus a ΔG of $-96\,kJ\,mol^{-1}$, the polymer P-R-92, with the highest block length of PS within the copolymers, shows the best complexation. Before any interpretations, an interesting and unexpected trend should be pointed out. If the DP of PS is reduced, which is equivalent to an increase in the proportion of PMAA or P(MAA-*r*-CE3MA), log$K$ decreases up to a value of 69% PS. P-R-69, P-R-51, and P-R-35 show hardly any influence of the DP of PS on the complex formation, with a log$K$ of around 14.

The blocks of the amphiphilic copolymer differ in their affinity for the solvents within the LLE. It should be ensured that the hydrophilicity does not falsify the result of the LLE with decreasing PS block length. Hence, the aqueous phases of the LLE were dried before being dissolved in deuterium oxide and analyzed for potentially dissolved polymer using ^{1}H-NMR spectroscopy. Even with the low MW samples P-R-51 and P-R-35, no polymer residues could be found in the aqueous medium (Figures S1–S5).

Considering the MW of the polymer chains, the trend is similar to that for the P-MW series. Contrary to the previous results, this cannot be attributed to the number of complexes per chain. For example, log$K$ is similar for the polymers P-MW-23 and P-R-35 at 13.81 and 13.87 (with 23 and 24 kDa, respectively). The total number of CE3MA units per polymer is significantly different at 17 (P-MW-23) and 36 (P-R-35). Possibly, with increasing DP of

TABLE 2 | Characteristics of PS-*b*-P(MAA-*r*-CE3MA) copolymers with variation of the PS/PMAA ratio.

Polymer	Sample-ID	Ratio of PS/P(MAA-*r*-CE3MA) (wt%/wt%)	M_n (kDa)	Functionalization of MAA units (%)
PS_{1458}-*b*-P(MAA_{56}-*r*-$CE3MA_{35}$)^{167}	P-R-92	92/8	167	39
PS_{695}-*b*-P(MAA_{54}-*r*-$CE3MA_{36}$)^{88}	P-R-83	83/17	88	40
PS_{301}-*b*-P(MAA_{56}-*r*-$CE3MA_{35}$)^{46}	P-R-69[a]	69/31	46	38
PS_{143}-*b*-P(MAA_{58}-*r*-$CE3MA_{33}$)^{29}	P-R-51	51/49	29	36
PS_{78}-*b*-P(MAA_{54}-*r*-$CE3MA_{36}$)^{24}	P-R-35	35/65	24	40

[a]This is the same polymer as P-MW-46 in Table 1.

26424169, 0, Downloaded from https://onlinelibrary.wiley.com/doi/10.1002/pol.20250060 by Universität Hamburg, Wiley Online Library on [02/04/2025]. See the Terms and Conditions (https://onlinelibrary.wiley.com/terms-and-conditions) on Wiley Online Library for rules of use; OA articles are governed by the applicable Creative Commons License

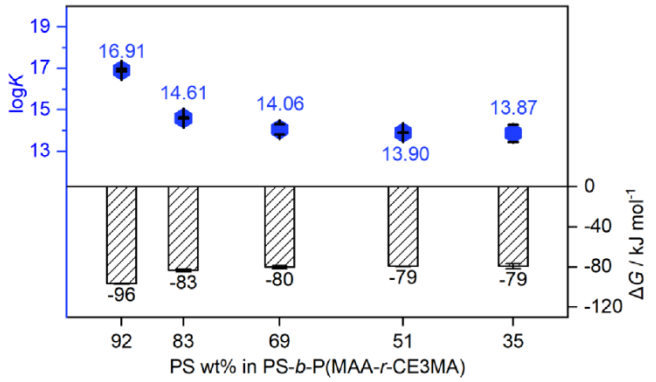

FIGURE 6 | Development of the logarithm of the equilibrium constants and gibbs free energy with increasing PS block length while constant PMAA block length.

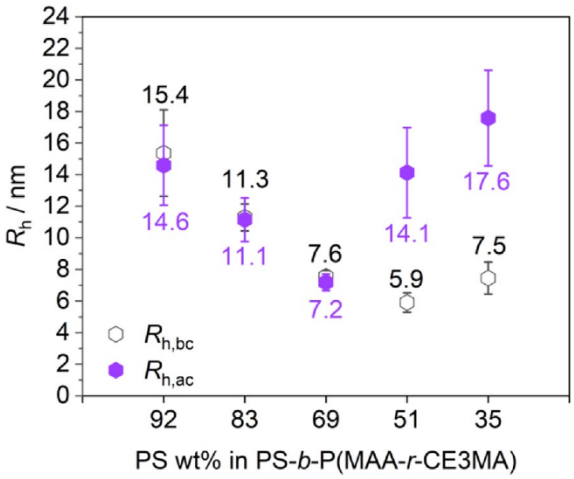

FIGURE 7 | Hydrodynamic radii before ($R_{h,bc}$) and after ($R_{h,ac}$) complexation plotted against the ratio of PS of the P-R polymers (smaller species) in DCM determined via DLS.

PS, the overall flexibility of the chain will remain greater after complexation. Therefore, with a similar number of $Li(CE)_2$, the entropy loss would be less, resulting in higher log$K$. In particular, the increased affinity of PS to DCM compared to PMAA must be noted. The interactions of the polymer units with the solvents were determined using the Hansen solubility parameters (Table S8). Experimental data for the solvents, PS, and PMAA were used; PCE3MA was approximated using the group contribution method (Table S7) [45, 46]. It was found that the hydrophilicity of the PMAA segment decreases considerably after esterification to PCE3MA, significantly influenced by the hydrogen-bonding Hansen solubility parameter δ_{hb}. Polymer–solvent interactions were determined from the Hansen solubility parameters according to Flory and Huggins (Table S9) [45]. The affinity to DCM follows PS>PCE3MA>PMAA and to water PMAA>PC3MA>PS with a higher overall affinity to DCM. The R_h in DCM before and after extraction is shown in Figure 7.

The initial hydrodynamic radii decrease according to the MW of P-R-92 over P-R-83 to P-R-69. With a dominant hydrophilicity, the solubility behavior of P-R-35 is significantly changed compared to the other polymers of the series, causing the elevated $R_{h,bc}$. The two-decay fit results in two distinguishable species. It is noticeable that the behavior of the polymers with low PS contents (P-R-35 and P-R-51) deviates from that of the polymers with higher PS contents. This indicates that the smaller species represent agglomerates of a few chains, rather than forming only intramolecular complexes. Assuming this, the change in R_h in the presence of lithium can be explained as follows. The decrease of 1%–5% (P-R-92, P-R-83 and P-R-69) is due to the intramolecular complexation. The significant increase from $R_{h,bc}$ to $R_{h,ac}$ for P-R-51 and P-R-35 by almost 240% in both cases suggests a (partial) formation of low-molecular agglomerates. In addition, the small DP of PS might create a low steric hindrance for these. With respect to thermodynamic equilibrium, the formation of agglomerates is associated with a higher loss in entropy and a lower log$K$ than for pure intramolecular complexation. The interplay of these factors is reflected in the data of the P-R series, whereby an increasing block length of PS has a beneficial effect on complex formation. It is important to mention that DLS allows estimating the polymer conformation in only one part (here DCM) of the two-phase mixture. Although it was found that no polymer is present in the aqueous phase, the orientations of the chains can be different, especially when varying the amphiphilicity of the polymer at the water-organic interface. Furthermore, despite low dispersity, the SEC trace of P-R-35 shows the occurrence of smaller and larger polymer chains. As already explained, the larger chains are probably due to a recombinatorial termination of the polymerization, while the shorter chains indicate a premature termination of the polymerization due to possible traces of oxygen in the reaction. This minor peak (Figure S23–S26) is present over the P-R series, though the influence decreases with increasing DP of PS. The inclusion of these species could lead to a slight underestimation of log$K$, especially at low PS fractions. However, the presence of longer molecules counteracts this phenomenon due to the MW dependence of the complexation. The DLS results should be interpreted with this in mind.

2.3 | Degree of Functionalization

Five polymers with degrees of functionalization between 8% and 72% were synthesized. P-F-40, the polymer with a degree of functionalization of 40%, is identical to P-MW-202. All polymers in this series (Table 3) were produced from the same initial polymer, ensuring optimum comparability. MWs, therefore, vary only due to CE.

At this point, it should be reiterated that the calculated equilibrium constant refers to the amount of CE. A high functionalization does not automatically necessitate a high value for log$K$. A statistical functionalization of the MAA is assumed.

With increasing functionalization, log$K$ increases (Figure 8). For comparison, log$K$ for P-F-72 has a value of 18.26 and is four orders of magnitude larger than that for P-F-8, with log$K$ of 14.46.

The change in the translational entropies S_T and conformational entropies S_C of the polymers during complexation can be considered in a differentiated manner. The loss in S_T in intramolecular complex formation should vary insignificantly between the polymers. The loss in S_C is estimated to be high when two distant CEs interact. Subsequent complexations result in a lower loss in S_C than initially, as the chain

26424169, 0, Downloaded from https://onlinelibrary.wiley.com/doi/10.1002/pol.20250060 by Universität Hamburg, Wiley Online Library on [02/04/2025]. See the Terms and Conditions (https://onlinelibrary.wiley.com/terms-and-conditions) on Wiley Online Library for rules of use; OA articles are governed by the applicable Creative Commons License

TABLE 3 | Characteristics of PS-*b*-P(MAA-*r*-CE3MA) copolymers with a variation in the degree of functionalization of MAA units.

Polymer	Sample-ID	Ratio of PS/P(MAA-*r*-CE3MA) (wt%/wt%)	M_n (kDa)	Functionalization of MAA units (%)
PS_{1289}-*b*-$P(MAA_{110}$-*r*-$CE3MA_{288})^{224}$	P-F-72	60/40	224	72
PS_{1289}-*b*-$P(MAA_{239}$-*r*-$CE3MA_{158})^{202}$	P-F-40[a]	68/32	202	40
PS_{1289}-*b*-$P(MAA_{291}$-*r*-$CE3MA_{106})^{189}$	P-F-27	84/16	189	27
PS_{1289}-*b*-$P(MAA_{347}$-*r*-$CE3MA_{50})^{178}$	P-F-13	82/18	179	13
PS_{1289}-*b*-$P(MAA_{366}$-*r*-$CE3MA_{31})^{175}$	P-F-8	81/19	175	8

[a]This is the same polymer as P-MW-202.

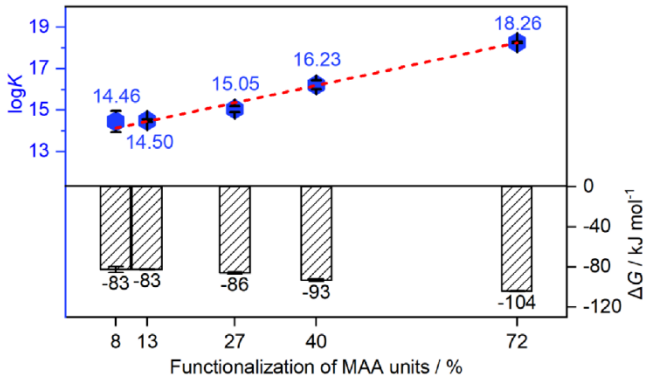

FIGURE 8 | Development of the logarithm of the equilibrium constants and Gibbs free energy with increasing functionalization of MAA as well as linear regression.

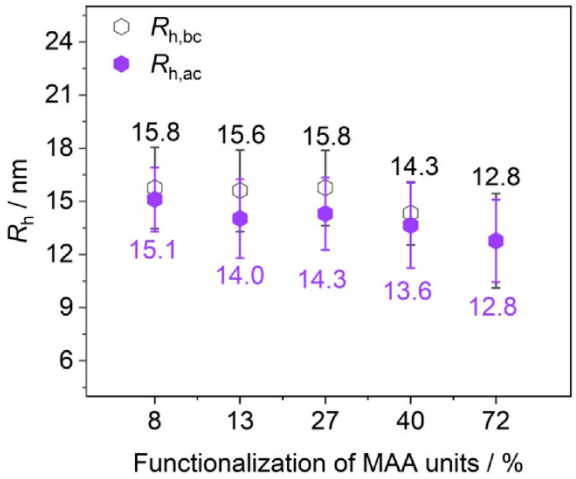

FIGURE 9 | Hydrodynamic radii before ($R_{h,bc}$) and after ($R_{h,ac}$) complexation plotted against the CE functionalization of the P-F polymers in DCM determined via DLS.

flexibility is increasingly restricted. However, the enthalpy decrease of the host-guest interaction, as well as the entropy loss of the ions, accumulates unaffected by the "complexation history" The process is thus increasingly thermodynamically favored, which underpins the excellent efficiency of the system with high functionalization. Additionally, the probability of two CEs to form a $Li(CE)_2$ complex is increased with high functionalization.

The DLS results (Figure 9) reveal a strong preference for intramolecular complexation. This was again confirmed by the number-weighted ratio of the two species resulting from the two decay fits. With MW ranging from 175 to 224 kDa, the formation of low-molecular agglomerates (Section 2) is unlikely.

The R_h of the polymers varies only slightly. Upon esterification, a corresponding number of aromatic CE and thus hydrophobicity is incorporated into the chain. The higher the functionalization (with the same chain length) and thus CE density, the smaller the distance between topologically neighboring CE. The R_h decreases with Li^+ complexation for P-F-8 by 4%, for P-F-13 and P-F-27 by 10% each, for P-F-40 by 5%, and with P-F-72 it does not decrease. In conclusion, the decrease in R_h does not correlate significantly with functionalization. It is assumed that the R_h is more strongly influenced by complexation when the chain still shows high flexibility. With enhanced chain immobilization (sandwich complexation), the conformational flexibility is reduced to a smaller extent with further complexation. Furthermore, rather initially spatially close CEs contribute to complex formation, due to the natural structure of the polymer in the solvent. In contrast to the extraction efficiency, the R_h is not more strongly affected by complexation than with the highly functionalized polymers. The results strikingly reveal the correlation of high functionalization (here 72%) with good complexation.

2.4 | Optimized Conditions According to Trends

Based on the (to some extent linear) relationships between the three properties evaluated (MW, DP of PS, and functionalization) and log*K*, a polymer (P-C) was produced that combines the conditions found to be best in this series: PS_{2634}-*b*-$P(MAA_{43}$-*r*-$CE3MA_{126})^{313}$ with a functionalization of 75%, MW of 313 kDa, and 88 wt% PS. It should be noted that P-C was produced analogously to P-R-92 based on a PS_{95}-*b*-$PMAA_5$ block copolymer. The high functionalization results in a lower value of 88%. With reference to the log*K* values found for P-MW-310 (16.31 ± 0.08), P-R-92 (16.91 ± 0.06), and P-F-72 (18.26 ± 0.04), the new polymer P-C shows improved Li complexation. The actual, experimentally determined value for log*K* is even higher at 19.12 ± 0.28 ($\Delta G = -109 \pm 1.6$ kJ mol^{-1}). The high-complex stability suggests that a positive interference of the influence of the MW, the PS content, and the functionalization occurs. The trends described previously were confirmed in this experiment, and an even more efficient polymer material for lithium extraction was developed.

26424169, 0, Downloaded from https://onlinelibrary.wiley.com/doi/10.1002/pol.20250060 by Universität Hamburg, Wiley Online Library on [02/04/2025]. See the Terms and Conditions (https://onlinelibrary.wiley.com/terms-and-conditions) on Wiley Online Library for rules of use; OA articles are governed by the applicable Creative Commons License

3 | Conclusion

In this work, a number of highly selective crown ether functionalized diblock copolymers were presented. The influence of different structural parameters (MW, DP of the hydrophobic segment, functionalization) was investigated on the lithium complexation from a DCM-water system. Beyond expectations, highly interesting insights were obtained regarding the complexation behavior of the polymers. The objective of optimizing the existing system was accomplished. To conclude, the results showed optimal performance of high MW systems (P-MW-310), low hydrophilic block length (P-R-92) and a functionalization of around 72% (P-F-72). DLS data provided information on the intermolecular host-guest interactions and chain assembly of the polymer before and after extraction. We have shown that the formation of $Li(CE)_2$ complexes leads almost exclusively to the formation of intramolecular complexes. The chain mobility as well as the amphiphilicity of the block copolymers showed a strong influence on the Li^+ complexation in the two-phase system. The combination of these three structural characteristics results in excellent complex-building properties. PS_{2634}-*b*-$P(MAA_{43}$-*r*-$CE3MA_{126})^{313}$, which incorporates the structural trends identified as optimal, demonstrated a log*K* of 19.12, thereby exceeding all other polymers in the series. The obtained more profound understanding of the underlying mechanisms will contribute significantly to the development of further effective lithium-selective extraction processes in the future.

4 | Experimental Section

4.1 | Materials

All reagents purchased from commercial suppliers were used as received unless otherwise noted. Acetonitrile (ACN, 99.95%, VWR, Darmstadt, Germany), aluminium oxide (basic, 98%, Sigma-Aldrich, Schnelldorf, Germany), 4,4-azobis(4-cyanovaleric acid) (ACVA, 98%, Sigma-Aldrich, Schnelldorf, Germany), bis-2-chloroethylether (99%, TCI Chemicals, Eschborn, Germany), catechol (99%, TCI Chemicals, Eschborn, Germany), chloroform-d1 (99.8%, Sigma-Aldrich, Schnelldorf, Germany), deuterium oxide (D_2O, 99.9%, Deutero, Kastellaun, Germany), DCM (99.5%, Grüssing, Filsum, Germany), diisopropyl azodicarboxylate (DIAD, 94%, abcr, Karlsruhe, Deutschland), dimethylformamide (DMF, 99.8%, Fisher Scientific, Schwerte, Germany), heptane (99.7%, Fisher Scientific, Schwerte, Germany), hexamethylenetetramine (99%, TCI Chemicals, Eschborn, Germany), lithium-3,5-diiodosalicylic acid (LIS, 99.9%, Sigma-Aldrich, Schnelldorf, Germany), lithium hydroxide (LiOH, 98%, TCI Chemicals, Eschborn, Germany), magnesium sulfate (99%, Grüssing, Filsum, Germany), methacrylic acid (MAA, ≥99%, stabilized with hydrochinone monomethyl ether, Merck, Darmstadt, Germany), methanol (MeOH, 99.7%, Fisher Scientific, Schwerte, Germany), sodium bicarbonate ($NaHCO_3$, 99%, Grüssing, Filsum, Germany), sodium borohydride (98%, Alfa Aesar, Schwerte, Germany), tetrahydrofuran (THF, 99.7%, Fisher Scientific, Schwerte, Germany), THF-d8 (99.5%, Deutero, Kastellaun, Germany), trifluoroacetic acid (TFA, 99%, Sigma-Aldrich, Schnelldorf, Germany), and triphenylphosphine (TPP, 99%, Merck, Darmstadt, Germany).

Styrene (≥99%, Sigma-Aldrich, Schnelldorf, Germany) was purified by filtration through basic activated alumina to remove the inhibitor (4-tert-butylcatechol). 4-Cyano-4-thioylthiopropyls ulfanyl pentanoic acid (CTPPA) and (2,3,5,6-tetrahydrobenzo[*b*][1,4,7]-trioxonin-9-yl)methanol (B9C3-MeOH) were synthesized according to the literature [47–49]. Ethyl acetate was purified by distillation, and water via a Milli-Q purification system (18.1 MΩ cm at 25°C).

4.2 | LLE

The LLE was modified according to the well-known method described in the literature [28, 30]. The UV/Vis spectra were recorded with a UV–Vis spectrophotometer UV5 from Mettler Toledo. The software used was LabX (11.0.1 build 43). For the systems presented, this ensured a sufficiently high absorbance with a low polymer dosage and high accuracy. Furthermore, the influence of viscosity could be minimized with the adapted procedure shown in Figure 10.

The CE (–functionalized polymer) was dissolved in 2.8 mL DCM and covered with an equal volume of salt solution (CE/LIS ratio: 2/1). Extraction was performed for 45 min at 500 rpm and 25°C. After phase separation (60 min), the aqueous phase was evaporated. The residue was dissolved in 200 µL of water.

The extraction proceeds according to equation [1], with M^{z+} being Li^+, X^{v-} the monovalent 3,5-diiodosalicylate anion, and CE being either the free CE or the CE3MA. Sandwich conformations were assumed for all calculations ($m = 1$, $n = 2$).

$$m\mathrm{M}^{z+}x\mathrm{X}^{v-}_{(\mathrm{aq})} + n\mathrm{CE}_{(\mathrm{org})} \rightarrow \left(\mathrm{M}_m\mathrm{CE}_n\right)^{mz+}X^{xv-}_{x(\mathrm{org})} \quad (1)$$

The salt concentration was determined by UV–Vis spectroscopy measurements. The decrease in Li^+ concentration in the aqueous phase before and after extraction was determined to evaluate the complex formation. In order to obtain information on the lithium concentration, LIS salt with a UV-active counterion was used. The linear correlation (Lambert–Beer law) between the LIS concentration and the measured absorbance is shown by the calibration (Figure 11).

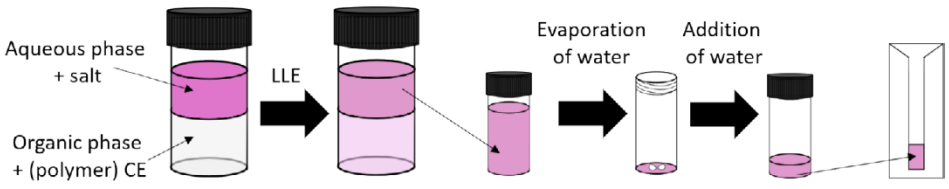

FIGURE 10 | Schematic representation of the LLE procedure.

26424169, 0, Downloaded from https://onlinelibrary.wiley.com/doi/10.1002/pol.20250060 by Universität Hamburg, Wiley Online Library on [02/04/2025]. See the Terms and Conditions (https://onlinelibrary.wiley.com/terms-and-conditions) on Wiley Online Library for rules of use; OA articles are governed by the applicable Creative Commons License

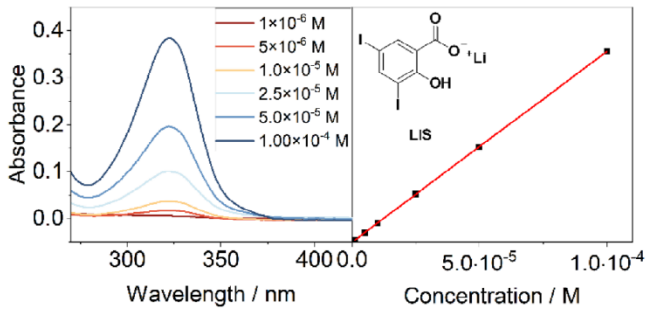

FIGURE 11 | UV–Vis measurements of differently concentrated LIS solutions in water (left) and calibration (absorbance at wavelength of 323 nm; right).

According to the literature [27, 28, 30], the complexation constant K is obtained from equation [2]. The concentrations required for the calculation are taken directly from the UV–Vis measurements. Q corresponds to the stoichiometric factor based on the charges of the cation and anion, and $\gamma+,-$ are the mean activity coefficients. A detailed description of the calculation and resulting data can be found in Data S1.

$$K = \frac{\left[\left(M_m CE_n\right)^{mz+} X_{x(org)}^{xv-}\right]}{\left(Q \bullet \left(\gamma_+ \left[M^{z+}\right]^m\right) \bullet \left(\gamma_- \left[X^{v-}\right]^x\right)\right) \bullet [CE]^n} \quad (2)$$

Furthermore, experiments analogous to the extractions were performed without CE or polymer. These blind samples ensured that the decrease in concentration of LIS in the aqueous phase was attributed to the complex formation solely.

4.3 | DLS

The polymer solutions for the DLS measurements were set up in DCM to a concentration of 0.1 wt% and filtered (PTFE, 0.2 μm), starting from the solid polymer (bc) or the organic phases of the LLE (ac). The measurements were carried out with an ALV/CGS-3 compact goniometer system, an ALV/LSE-5003 multi-tau digital correlator, and a He-Ne laser (633 nm, 35 mW) at measuring angles of 90°–135° (step size of 15°) and a duration of 30 s. Three measurements were carried out for each angle. The temperature was set to 20°C with a toluene bath, controlled using a Julabo F25 thermostat. These data were analyzed using a Matlab R2021a software with a script written by B. Hankiewicz. The fit was performed using two exponential decays. From the linear dependence of the relaxation rate, the inverse relaxation times on the square of the wavevector, the diffusion coefficients were calculated, and via the Stokes–Einstein equation, the hydrodynamic radius R_h was calculated assuming spherical particle geometry. The determined intensity-weighted ratios were recalculated to number-weighted ratios. All three extraction solutions were measured for the ac samples. For the evaluation, mean values were calculated. Polydispersity indices (PDIs) for the two polymeric species can be found in Table S6.

4.4 | NMR Spectroscopy

The ^{1}H-NMR spectra were measured in THF-d_8, $CDCl_3$, and D_2O, and nuclear overhauser and exchange spectroscopy (NOESY) and DOSY spectra in $CDCl_3$ at room temperature using a 300 MHz Bruker FourierHD, a 400 MHz Bruker AVANCE II, or a 600 MHZ Bruker AVANCE III HD spectrometer. The respective solvent signal at $\delta = 7.26$ for $CDCl_3$, $\delta = 3.58$ for THF-d_8, and $\delta = 4.79$ for D_2O provided the reference for the chemical shifts.

4.5 | Size Exclusion Chromatography (SEC)

The MW distributions of the PMAA-*b*-PS diblock copolymers were determined by SEC. The PS-*b*-PMAA solutions were prepared at a concentration of 1 g L^{-1} in THF (5 wt% TFA). Toluene served as an internal reference. The THF-SEC system contained an Agilent 1260 Infinity Series degasser and pump, a combination of three PSS SDV columns (100 Å, 1000 Å, 10000 Å), a refractive index detector, and a UV detector. The measurements were carried out at 30°C with a flow rate of 1.0 mL min^{-1} and an injection volume of 100 μL. Calibration was performed using near-monodisperse PS standards.

4.6 | Elemental Analysis

Elemental Analysis was performed using a Perkin Elmer Analyst 600 AAS Atom Absorption Spectrometer. The sample substances were modified by HNO_3/$HClO_4$ digestion before measurement due to insufficient water solubility.

4.6.1 | One-Pot Process for the Synthesis of the PS-*b*-PMAA Diblock Copolymer

A synthetic method adapted from Chaduc et al. was used [32]. The synthesis is exemplified by the initial polymer for P-MW-23 (PS_{80}-*b*-$PMAA_{20}$)[23]. The exact weights of all reactants and reagents of the polymer syntheses, conversions c, dispersities $Đ$, and SEC traces can be found in Table S4. In the first step, the PMAA block was prepared. CTPPA (0.50 mmol, 0.14 g) was pre-dissolved in MAA (21.5 mmol, 1.85 g). The synthesis of CTPPA is described in Data S1. DMF (3.6 mmol, 0.28 mL) was added as a reference for conversion determination via ^{1}H-NMR. 2.34 mL of a stock solution (0.06 g ACVA, 0.05 g $NaHCO_3$ and 10 mL water) corresponding to 0.05 mmol (0.01 g) ACVA and 0.18 mmol (0.015 g) $NaHCO_3$ was used. A final solids content of 20 wt% was obtained by adding 8.0 mL of water. The solution was stirred at 0°C and purged with nitrogen. After 30 min, a sample corresponding to time $t = 0$ min was taken to determine the conversion. Thereafter, purging was discontinued, and the reaction was initiated at 80°C. After 6 h, the reaction was terminated, and a ^{1}H-NMR (D_2O) sample was taken. The conversion was determined via the ratio between the MAA signal ($\delta = 6.04$) and the DMF signal ($\delta = 7.85$) [27, 31]. c (via ^{1}H-NMR) 99.7%, MW (via ^{1}H-NMR) 3966 g mol^{-1}.

The PS block was formed by adding styrene (76.5 mmol, 7.97 g) to the PMAA-macro-CTA formed in the first step of the one-pot synthesis. 4.67 mL of the stock solution (corresponding to 0.1 mmol [0.03 g] ACVA and 0.35 mmol [0.03 g] $NaHCO_3$) was added as well as a further 31.0 mL of water, corresponding to a solids content of 20 wt%. After 30 min of stirred purging with nitrogen at 0°C, the reaction was initiated at 80°C. After 3 h, the

26424169, 0, Downloaded from https://onlinelibrary.wiley.com/doi/10.1002/pol.20250060 by Universität Hamburg, Wiley Online Library on [02/04/2025]. See the Terms and Conditions (https://onlinelibrary.wiley.com/terms-and-conditions) on Wiley Online Library for rules of use; OA articles are governed by the applicable Creative Commons License

mixture was cooled to room temperature. Following ^{1}H-NMR (THF-d_8) and SEC sampling, the water was removed under reduced pressure. The highly viscous solution formed with THF was precipitated in *n*-heptane. Thereafter, the colorless precipitate was dried, cooled to −196°C, and ground to a powder using a ball mill (30 Hz, 5 min). The conversion was determined via the ratio of the vinyl group of styrene ($\delta = 5.35–5.22$) and the aromatic signals ($\delta = 7.00–6.20$) [27, 31]. *c* (via ^{1}H-NMR) 98.9%, MW (via ^{1}H-NMR) 19,718 g mol^{-1}, $Đ$ (via SEC) 1.2.

4.6.2 | Synthesis of PS-*b*-P(MAA-*r*-CE3MA) via Mitsunobu Esterification

The partial functionalization of the PMAA blocks with the CE was achieved using Mitsunobu's method [33]. The quantities of reagents used are listed in Table S5. The reaction procedure is described exemplarily for P-MW-23. The synthesis of B9C3-MeOH is given in Data S1. $(PS_{80}$-*b*-PMAA$)_{20}$ (2.00 g, 4.75 mmol referred to MAA) and B9C3-MeOH (0.299 g, 1.42 mmol) were dissolved in 50.0 mL THF. At 0°C, the solution was stirred and purged with nitrogen. Meanwhile, TPP (3.73 g, 14.2 mmol) in 20 mL THF and subsequently DIAD (2.89 g, 14.2 mmol) were slowly added via a syringe pump, stirred for 30 min at 0°C, and for 24 h at ambient temperature. After precipitation in cold *n*-heptane, the precipitate was filtered, washed with ACN and MeOH, dried, and ground at −196°C to a fine powder (ball mill, 30 MHz, 5 min). The product was quantitatively verified for successful functionalization by ^{1}H-NMR ($CDCl_3$) and qualitatively by NOESY. The corresponding spectra are shown in Data S1. The quantitative analysis was carried out using the ratio of the $-OCH_2CH_2O-$ ether signal ($\delta = 4.37$) of the CE ring to the meta-protons of the PS ($\delta = 6.82–6.20$) [27]. The PS signal was used as a reference, as it remains constant during the course of the reaction, and there is no interference with other signals. The NOESY coupling appearing after the reaction provides evidence of the CE being covalently bound to the polymer (Figure S6). Coupling is observed over the distance between the polymer backbone ($\delta = 1.33$) and the ether signal ($\delta = 4.37$) as well as the methylene group adjacent to the aromatic system ($\delta = 4.95$). MW (via ^{1}H-NMR) 23,129 g mol^{-1}, functionalization (in reference to MAA) 42%.

Acknowledgments

The authors acknowledge the NMR spectroscopic, mass spectrometric, and elemental analysis division of the Department of Chemistry at the University of Hamburg. We acknowledge Amrei Gouby and Jette Bleicken for synthesizing and measuring the DLS/UV–Vis data and Dr. Thomas Hackl for the support with the interpretation of the DOSY spectra.

References

1. L. Baudino, C. Santos, C. F. Pirri, F. La Mantia, and A. Lamberti, "Recent Advances in the Lithium Recovery From Water Resources: From Passive to Electrochemical Methods," *Advanced Science* 9 (2022): 2201380.

2. Y. Liu, B. Ma, Y. Lü, C. Wang, and Y. Chen, "A Review of Lithium Extraction From Natural Resources," *International Journal of Minerals, Metallurgy, and Materials* 30 (2023): 209–224.

3. J. D. Graham, J. A. Rupp, and E. Brungard, "Lithium in the Green Energy Transition: The Quest for Both Sustainability and Security," *Sustainability* 13 (2021): 11274.

4. P. Lindagato, Y. Li, J. Macháček, et al., "Lithium Metal: The Key to Green Transportation," *Applied Sciences* 13 (2023): 405.

5. H. Zhang, G. Yao, S. Wang, Y. Liu, and H. Luo, "A Chrome-free Conversion Coating for Magnesium-Lithium Alloy by a Phosphate-Permanganate Solution," *Surface and Coatings Technology* 202 (2008): 1825–1830.

6. G. Jiang, F. Li, H. Wang, et al., "Perspective on High-Concentration Electrolytes for Lithium Metal Batteries," *Small Structures* 2 (2021): 1–8.

7. J. Zhang, Z. Cheng, X. Qin, X. Gao, M. Wang, and X. Xiang, "Recent Advances in Lithium Extraction From Salt Lake Brine Using Coupled and Tandem Technologies," *Desalination* 547 (2023): 116225.

8. U.S. Geological Survery, *Mineral Commodity Summaries* (U.S. Geological Survery 2022, 2022).

9. S. Wang, X. Yu, and X. Hu, "Electrochemical Lithium Extraction With Gas Flushing of Porous Electrodes," *Nanomaterials* 13 (2023): 1471.

10. F. Maisel, C. Neef, F. Marscheider-Weidemann, and N. F. Nissen, "A Forecast on Future Raw Material Demand and Recycling Potential of Lithium-Ion Batteries in Electric Vehicles," *Resources, Conservation and Recycling* 192 (2023): 106920.

11. Z. Liang, J. Shen, X. Xu, et al., "Advances in the Development of Single-Atom Catalysts for High-Energy-Density Lithium–Sulfur Batteries," *Advanced Materials* 34 (2022): 1–26.

12. M. V. Reddy, A. Mauger, C. M. Julien, A. Paolella, and K. Zaghib, "Brief History of Early Lithium-Battery Development," *Materials* 13 (2020): 1–9.

13. H. Yu, G. Naidu, C. Zhang, et al., "Metal-Based Adsorbents for Lithium Recovery From Aqueous Resources," *Desalination* 539 (2022): 115951.

14. H. Lee, J. Lim, and J. Kim, "Novel Lithium Production Process Using Desalination Wastewater and Waste Heat From Natural Gas Combined Cycle," *Energy Conversion and Management* 292 (2023): 117396.

15. J. H. T. Luong, C. Tran, and D. Ton-That, "A Paradox Over Electric Vehicles, Mining of Lithium for Car Batteries," *Energies* 15 (2022): 1–25.

16. X. He, S. Kaur, and R. Kostecki, "Mining Lithium From Seawater," *Joule* 4 (2020): 1357–1358.

17. C. Paredes and E. de Rodríguez San Miguel, "Selective Lithium Extraction and Concentration from Diluted Alkaline Aqueous Media by a Polymer Inclusion Membrane and Application to Seawater," *Desalination* 487 (2020): 114500.

18. R. Reich, K. Slunitschek, R. M. Danisi, E. Eiche, and J. Kolb, "Lithium Extraction Techniques and the Application Potential of Different Sorbents for Lithium Recovery From Brines," *Mineral Processing and Extractive Metallurgy Review* 44 (2023): 261–280.

19. S. Raiguel, V. T. Nguyen, I. Reis Rodrigues, C. Deferm, S. Riaño, and K. Binnemans, "Recovery of Lithium from Simulated Nanofiltration-Treated Seawater Desalination Brine Using Solvent Extraction and Selective Precipitation," *Solvent Extraction and Ion Exchange* 41 (2023): 425–448.

20. A. Razmjou, M. Asadnia, E. Hosseini, A. Habibnejad Korayem, and V. Chen, "Design Principles of Ion Selective Nanostructured Membranes for the Extraction of Lithium Ions," *Nature Communications* 10 (2019): 1–15.

21. H. Li, Y. Wang, T. Li, et al., "Nanofiltration Membrane With Crown Ether as Exclusive Li+ Transport Channels Achieving Efficient Extraction of Lithium From Salt Lake Brine," *Chemical Engineering Journal* 438 (2022): 135658.

26424169, 0, Downloaded from https://onlinelibrary.wiley.com/doi/10.1002/pol.20250060 by Universität Hamburg, Wiley Online Library on [02/04/2025]. See the Terms and Conditions (https://onlinelibrary.wiley.com/terms-and-conditions) on Wiley Online Library for rules of use; OA articles are governed by the applicable Creative Commons License

22. T. Hoshino, "Preliminary Studies of Lithium Recovery Technology From Seawater by Electrodialysis Using Ionic Liquid Membrane," *Desalination* 317 (2013): 11–16.

23. Y. Dong, Y. Liu, H. Li, et al., "Crown Ether-Based Tröger's Base Membranes for Efficient Li+/Mg2+ Separation," *Journal of Membrane Science* 665 (2023): 121113.

24. Q. Cheng, Y. Zhang, X. Zheng, et al., "High Specific Surface Crown Ether Modified Chitosan Nanofiber Membrane by Low-Temperature Phase Separation for Efficient Selective Adsorption of Lithium," *Separation and Purification Technology* 262 (2021): 118312.

25. L. Baudino, A. Pedico, S. Bianco, M. Periolatto, C. F. Pirri, and A. Lamberti, "Crown-Ether Functionalized Graphene Oxide Membrane for Lithium Recovery from Water," *Membranes* 12 (2022): 1–12.

26. P. Ji, Z. Ji, Q. Chen, J. Liu, and Y. Zhao, "Effect of Coexisting Ions on Recovering Lithium From High Mg2+/Li+ Ratio Brines by Selective-Electrodialysis," *Separation and Purification Technology* 207 (2018): 1–11.

27. I. Oral and V. Abetz, "A Highly Selective Polymer Material Using Benzo-9-Crown-3 for the Extraction of Lithium in Presence of Other Interfering Alkali Metal Ions," *Macromolecular Rapid Communications* 42, no. 9 (2021): 2000746, https://doi.org/10.1002/marc.202000746.

28. I. Oral, S. Tamm, C. Herrmann, and V. Abetz, "Lithium Selectivity of Crown Ethers: The Effect of Heteroatoms and Cavity Size," *Separation and Purification Technology* 294 (2022): 121142.

29. A. Casadellà, O. Schaetzle, K. Nijmeijer, and K. Loos, "Polymer Inclusion Membranes (PIM) for the Recovery of Potassium in the Presence of Competitive Cations," *Polymers* 8 (2016): 1–14.

30. I. Oral and V. Abetz, "Improved Alkali Metal Ion Capturing Utilizing Crown Ether-Based Diblock Copolymers in a Sandwich-Type Complexation," *Soft Matter* 18, no. 5 (2022): 934–937, https://doi.org/10.1039/d1sm01815a.

31. I. Oral, L. Grossmann, E. Fedorenko, J. Struck, and V. Abetz, "Synthesis of Poly(Methacrylic Acid)-block-Polystyrene Diblock Copolymers at High Solid Contents via RAFT Emulsion Polymerization," *Polymers* 13 (2021): 3675.

32. I. Chaduc, M. Girod, R. Antoine, B. Charleux, F. D'Agosto, and M. Lansalot, "Batch Emulsion Polymerization Mediated by Poly(Methacrylic Acid) MacroRAFT Agents: One-Pot Synthesis of Self-Stabilized Particles," *Macromolecules* 45, no. 15 (2012): 5881–5893, https://doi.org/10.1021/ma300875y.

33. O. Mitsunobu and M. Yamada, "Preparation of Esters of Carboxylic and Phosphoric Acid via Quaternary Phosphonium Salts," *Bulletin of the Chemical Society of Japan* 40 (1967): 2380–2382.

34. Y. Sun, M. Zhu, Y. Yao, H. Wang, B. Tong, and Z. Zhao, "A Novel Approach for the Selective Extraction of Li+ From the Leaching Solution of Spent Lithium-Ion Batteries Using Benzo-15-Crown-5 Ether as Extractant," *Separation and Purification Technology* 237 (2020): 116325.

35. C. Wang, P. Zhang, H. Ju, et al., "Electromigration Separation of Lithium Isotopes: The Multiple Roles of Crown Ethers," *Chemical Physics Letters* 787 (2022): 139265.

36. H. Pei, F. Yan, H. Liu, B. He, and J. Li, "The Selective Complexation of Crown Ethers for Lithium Isotope Separation: A Critical Review," *Separation and Purification Technology* 341 (2024): 126857.

37. C. H. Ko, C. Henschel, G. P. Meledam, et al., "Self-Assembled Micelles From Thermoresponsive Poly(Methyl Methacrylate)-b-Poly(N-Isopropylacrylamide) Diblock Copolymers in Aqueous Solution," *Macromolecules* 54 (2021): 384–397.

38. Y. Li, D. Liu, X. Peng, et al., "Synthesis via Reversible Addition–Fragmentation Chain Transfer Polymerization and Deep Control Property of Amphiphilic Self-Assembled Poly(Ethylene Oxide)-block-Polystyrene," *Energy and Fuels* 38 (2024): 5940–5948.

39. J. G. Werner, Y. Li, and U. Wiesner, "Block-Copolymer-Architected Materials in Electrochemical Energy Storage," *Small Science* 3 (2023): 2300074.

40. M. Stefik, S. Guldin, S. Vignolini, U. Wiesner, and U. Steiner, "Block Copolymer Self-Assembly for Nanophotonics," *Chemical Society Reviews* 44 (2015): 5076–5091.

41. M. Karayianni and S. Pispas, "Block Copolymer Solution Self-Assembly: Recent Advances, Emerging Trends, and Applications," *Journal of Polymer Science* 59 (2021): 1874–1898.

42. Y. Mai and A. Eisenberg, "Self-Assembly of Block Copolymers," *Chemical Society Reviews* 41 (2012): 5969–5985.

43. A. Bey, O. Dreyer, and V. Abetz, "Thermodynamic Analysis of Alkali Metal Complex Formation of Polymer-Bonded Crown Ether," *Physical Chemistry Chemical Physics* 19 (2017): 15924–15932.

44. G. Decher, "Fuzzy Nanoassemblies: Toward Layered Polymeric Multicomposites," *Science* 277 (1997): 1232–1237.

45. C. M. Hansen, *Hansen Solubility Parameters*, vol. 2, 2nd ed. (Taylor & Francis, 2007).

46. E. Stefanis and C. Panayiotou, "Prediction of Hansen Solubility Parameters With a New Group-Contribution Method," *International Journal of Thermophysics* 29 (2008): 568–585.

47. A. Khazaei, S. Saednia, M. K. Borazjani, J. Saien, M. Kiani, and A. Afkhami, "A Novel Covalent Functionalisation of Poly (Styrene-Alt-Maleic Anhydride) With 4-Amino Benzo-9-Crown-3 Ether," *Supramolecular Chemistry* 26 (2014): 88–93.

48. E. Xu, A. E. Smith, S. E. Kirkland, and C. L. McCormick, "Aqueous RAFT Synthesis of pH-Responsive Triblock Copolymer mPEO–PAPMA–PDPAEMA and Formation of Shell Cross-Linked Micelles," *Macromolecules* 41 (2008): 8429–8435.

49. J. Q. Liu, J. J. Yang, J. F. Li, et al., "Catalytic Cross-Coupling Reaction of Aryl Iodides With Triarylbismuths by an N-Heterocyclic Carbene-PdCl2 Based on Benzo-9-Crown-3 Catalyst at Room Temperature," *Molecular Catalysis* 443 (2017): 125–130.

Supporting Information

Additional supporting information can be found online in the Supporting Information section.

26424169, 0, Downloaded from https://onlinelibrary.wiley.com/doi/10.1002/pol.20250060 by Universität Hamburg, Wiley Online Library on [02/04/2025]. See the Terms and Conditions (https://onlinelibrary.wiley.com/terms-and-conditions) on Wiley Online Library for rules of use; OA articles are governed by the applicable Creative Commons License

5.3. PUBLICATION 3

This publication is reprinted with permission from S. Jaehnke, V. Abetz, Electrospun, crown ether functionalized PS-b-PMAA block copolymer fibers for Li extraction from aqueous media, *Desalination* (**2025**) 119343 – Copyright 2025 Elsevier B.V.

This work was done in close collaboration with the Helmholtz-Zentrum Hereon (Geesthacht). Gratitude belongs to Dr. Maryam Radjabian and Joachim Koll for their continuous support and expert technical guidance throughout this project. The EM service (Dr. Martin Held, Anke-Lisa Höhme, Dr. Erik Schneider, and Dr. Evgeni Sperling) should be acknowledged, not only for providing high-quality images, but also for their generous encouragement and valuable contributions to the interpretation of the data.

Publications 1 and 2 systematically investigated the optimal conditions for Li complexation. These studies make a fundamental contribution to a deeper understanding of host-guest processes and enabled the successful optimization of the existing system. At the same time, the use of large quantities of solvents is not practicable on an industrial scale, and integration into existing processes would make much more sense from an ecological and economic perspective. Therefore, the third publication is devoted to converting the system into a solid, solvent-free form using electrospinning.

To ensure high Li absorption in the solid material, thin (diameters of down to 1 µm) continuous fibers with a high surface-to-volume ratio were produced. The transition from the previously optimized system with B9C3 was technically successful, but did not show any significant complexation in solid-liquid extractions (SLE) in aqueous lithium salt solutions. An increase in the CE content led to a slight improvement, but remained below expectations. Analogous systems with 12-membered CEs with and without benzene substituents were produced, which meet an ideal size-fit criterion for lithium complexation. Surprisingly, the competing sodium sandwich formation known in solution did not occur. All systems investigated showed pronounced selectivity towards lithium. Particularly noteworthy is the material based on benzo-12-crown-4 (B12C4), which proved to be the most effective. This exhibited the highest lithium capacities in the series of systems investigated with low CE consumption (14% functionalization of the MAA units). Publication 3 impressively demonstrates the potential of the system for lithium extraction, even for solvent-free applications.

The supporting information connected to this publication can be found in section 9.4.

Several attempts were made in the project to transfer the polymer system to alternative solvent-free forms—membranes and cubosomes—but these were not as successful as the production of electrospun fibers. The results are described in section 6 “Unpublished results”.

Desalination 616 (2025) 119343

Contents lists available at ScienceDirect

Desalination

journal homepage: www.elsevier.com/locate/desal

Electrospun, crown ether functionalized PS-*b*-PMAA block copolymer fibers for Li extraction from aqueous media

Sabrina Jaehnke [a], Volker Abetz [a,b,*]

[a] Universität Hamburg, Institute of Physical Chemistry, Grindelallee 117, 20146 Hamburg, Germany
[b] Institute of Membrane Research, Helmholtz-Zentrum Hereon, Max-Planck-Straße 1, 21502 Geesthacht, Germany

HIGHLIGHTS

- PS-*b*-PMAA-Crown ether fibers form Li^+ complexes in aqueous media.
- Extraction tuned *via* crown ether: Benzo-9-Crown-3, 12-Crown-4, Benzo-12-Crown-4.
- None of studied materials shows uptake of Na^+.
- Benzo-12-Crown-4-based material shows highest Li^+ capacity.
- Solid–liquid extraction shows high selectivity Li^+ *vs.* Na^+.

GRAPHICAL ABSTRACT

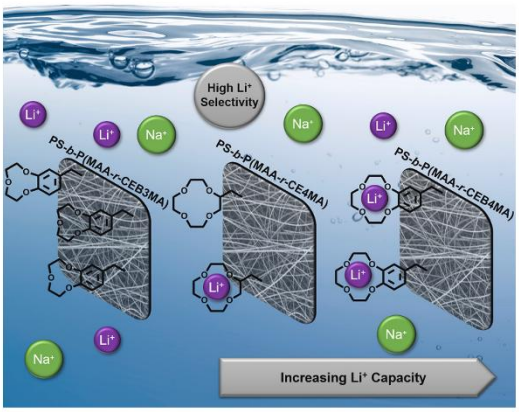

ARTICLE INFO

Keywords:
Crown ether
Functionalized polymers
Electrospun fibers
Li recovery
Li from aqueous media

ABSTRACT

Crown ether-functionalized polystyrene-*block*-poly(methacrylic acid) copolymers form lithium (Li) complexes with ML or ML_2 stoichiometry. The extraction efficiency can be tuned by the choice of crown ether; benzo-9-crown-3, 12-crown-4, and benzo-12-crown-4 were evaluated. To enhance Li uptake in the solid material, electrospun fibers with a high surface-to-volume ratio were fabricated. Li selectivity over sodium and overall uptake performance were assessed *via* solid–liquid extraction. A material based on benzo-12-crown-4 demonstrated the highest Li capacity (up to $1.9{\cdot}10^{-4} \pm 2.4{\cdot}10^{-5}$ mmol Li/g polymer) and excellent selectivity, enabling efficient extraction without the need for organic solvents.

1. Introduction

Due to the high interest in Li-ion batteries (LIBs) for mobile devices and e-mobility, global demand for Li is rising steadily [1–3]. Projections even indicate a twenty-six-fold increase in demand between 2023 and 2050 [1]. The foreseeable under-capacity of conventionally exploited sources, like pegmatites and brines, necessitates the development of efficient Li extraction methods from unconventional sources. With a

* Corresponding author at: Universität Hamburg, Institute of Physical Chemistry, Grindelallee 117, 20146 Hamburg, Germany.
E-mail addresses: sabrina.jaehnke@uni-hamburg.de (S. Jaehnke), volker.abetz@uni-hamburg.de (V. Abetz).

https://doi.org/10.1016/j.desal.2025.119343
Received 30 June 2025; Received in revised form 8 August 2025; Accepted 25 August 2025
Available online 28 August 2025
0011-9164/© 2025 The Authors. Published by Elsevier B.V. This is an open access article under the CC BY license (http://creativecommons.org/licenses/by/4.0/).

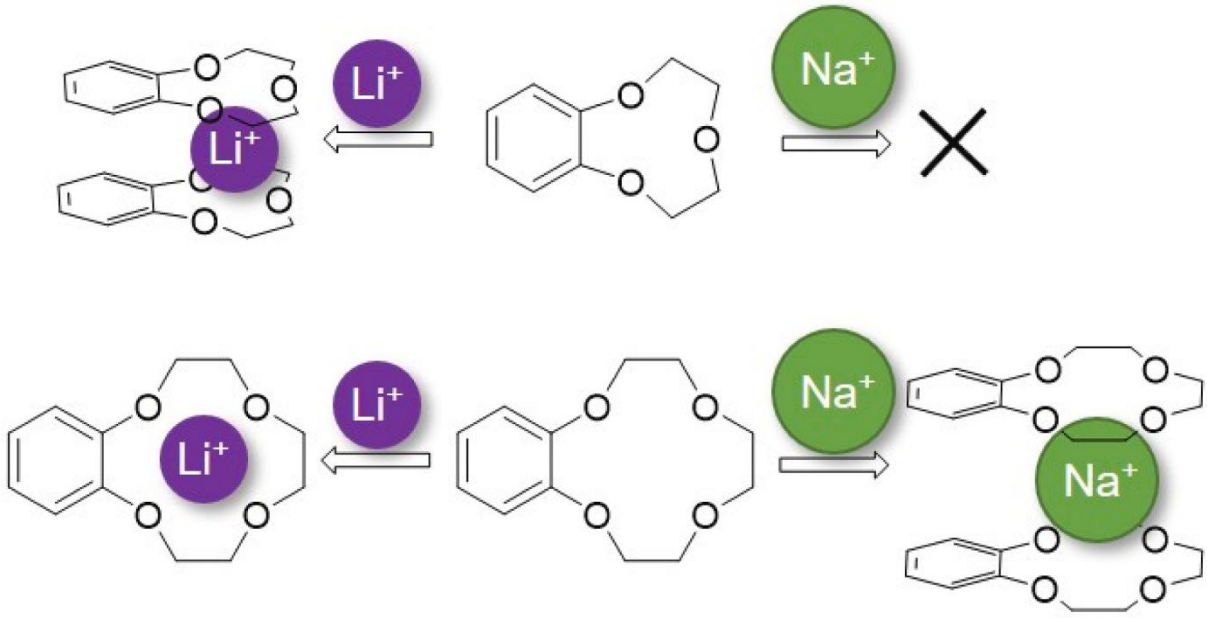

Fig. 1. Illustration of the complex formation of a 9-membered CE (B9C3, top) with Li as ML_2 complex and a 12-membered CE (B12C4, bottom) with Li as ML complex, and sodium as ML_2 complex. With B9C3 there is no complexation in ML or ML_2 conformation with sodium.

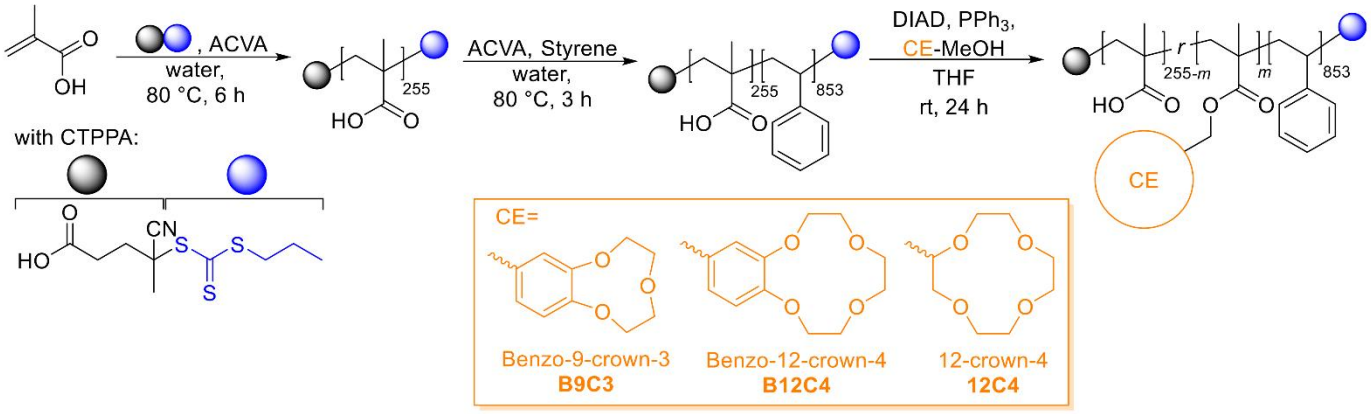

Fig. 2. Schematic representation of the two-step synthesis: thermally initiated one-pot RAFT polymerization for the production of PS-*b*-PMAA, with subsequent partial Mitsunobu esterification of the MAA units with three different methyl-hydroxy-functionalized CEs. (ACVA = 4,4-azobis(4-cyanovaleric acid), CTPPA = 4-cyano-4-thioylthiopropyl-sulfanyl pentanoic acid, DIAD = diisopropyl azodicarboxylate, THF = tetrahydrofuran).

Table 1
Characteristics of the copolymer. The subscript numbers characterize the repeating units of the blocks, superscript numbers represent the total mass of the polymer (in kg/mol). CEXMA denotes the MAA units functionalized with B9C3 (X = B3), B12C4 (X = B4), and 12C4 (X = 4).

Polymer	Sample-ID
PS_{853}-*b*-P(MAA_{101}-*r*-$CEB3MA_{154}$)^{140}	P-B9C3-60
PS_{853}-*b*-P(MAA_{220}-*r*-$CEB3MA_{35}$)^{118}	P-B9C3-14
PS_{853}-*b*-P(MAA_{219}-*r*-$CEB4MA_{36}$)^{119}	P-B12C4-14
PS_{853}-*b*-P(MAA_{220}-*r*-$CE4MA_{35}$)^{118}	P-12C4-14

total quantity of 231 Gigatons of Li, seawater represents a viable alternative Li resource [4,5]. However, low concentrations of Li (0.17 ppm) and the existence of competing ions (Na^+, K^+, Mg^{2+}, and Ca^{2+}) require a high degree of selectivity in the extraction methods [3–9]. Specific cation selectivities can be reached by complexation with crown ethers (CEs) [10–13]. For example, Li et al. designed a 15-Crown-5 based nanofiltration membrane, with exclusive Li^+ transport channels [14].

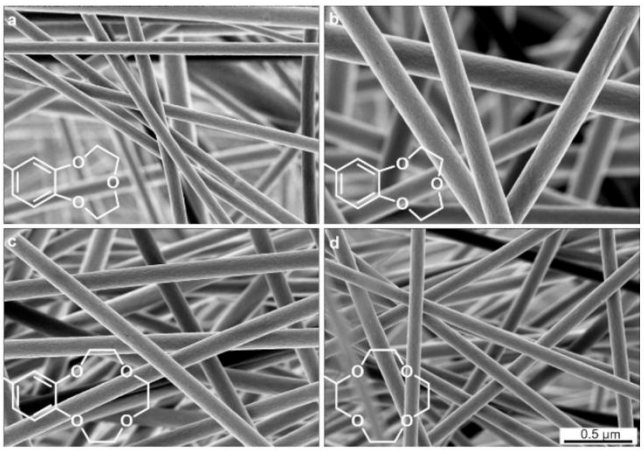

Fig. 3. SEM images of the electrospun fibers of P-B9C3-60 (a), P-B9C3-14 (b), P-B12C4-14 (c), and P-12C4-14 (d).

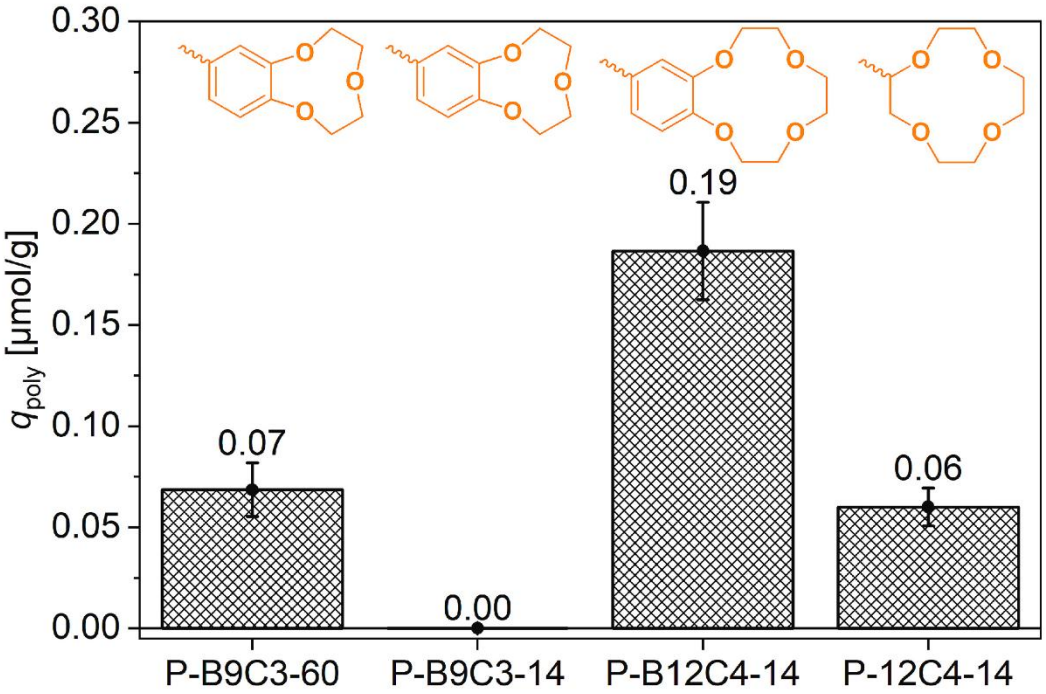

Fig. 4. Data for q_{poly} (µmol/g) from SLE complex formation of electrospun PS-*b*-P(MAA-*r*-CEXMA) block copolymer fibers with 3,5-diiodosalicylate (LIS) in aqueous solution. The error bars represent the standard deviation from the discrete SLE measurements of several samples from the same batch.

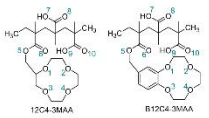

Fig. 5. Schematic representation of 12C4 and B12C4 on a chain of three MAA units.

Yang et al. reported a fluorinated supramolecular nano-container crosslinked hydrogel with high Li^+/Na^+ separation and remarkably high capacity of 122.3 mg/g based on specific Li-F coordination [15]. A cutting-edge CE-based approach was realized by Liberati et al. *via* the development of a thermoresponsive copolymer of *N*-isopropylacrylamide (NiPAAm) and 2-(benzo-12-crown-4-ether)ethyl methacrylamide (BCEEM) with maximum Li^+ capacities of 0.075 mmol/g [16]. In previous work, we introduced a CE functionalized polystyrene (PS)-poly(methacrylic acid) (PMAA) block copolymer for selective Li

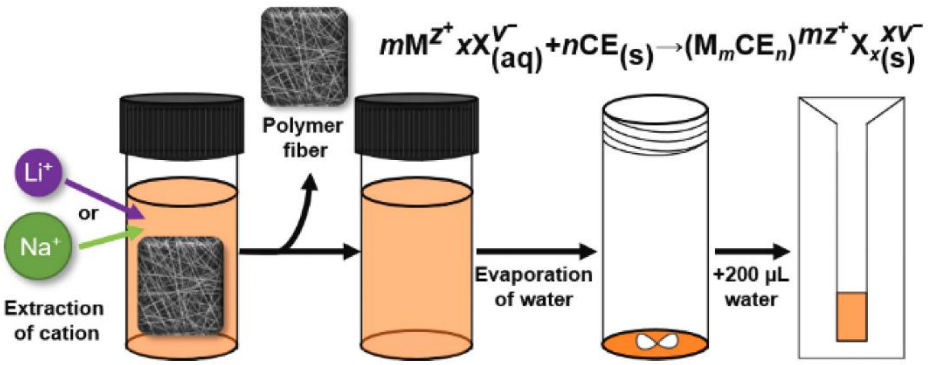

Fig. 6. Process of the SLE. *m* metal ions M of charge z^+ form a host-guest complex (M_mCE_n) with *n* crown ethers CE. Charge equalization is achieved by the presence of *x* anions X of charge v^-.

extraction from aqueous media using benzo-9-crown-3 (B9C3) [17–20]. Due to their structural tunability, CEs can form highly ion specific host-guest complexes (Fig. 1). 12-membered CEs show an ideal cavity size-to-ion diameter ratio for the complexation of Li ions (with cavity size of 120–150 pm and cation diameter of 136 pm) [6,21–23].

For the efficient separation of similarly sized ions like Li^+ and Mg^{2+}, charge-selective membranes, also incorporating CEs, are available [24–26]. The observed Li selectivity of the B9C3-based system in liquid-liquid extractions (LLE) is attributed to the formation of ML_2 (M = metal, L = ligand) complexes, suppressing the complexation of larger ions [17,22,27]. Reduced entropy loss during complexation compared to free CEs likely enhances extraction efficiency [17,20,28]. However, to improve economic viability, organic solvents should be avoided. Instead, inorganic (*e.g.*, ceramics) and organic materials (*e.g.,* polymers) can be employed as water-insoluble carrier materials for the active sites (CE) [4,6,14,21,29]. Decisive for the efficiency of Li extraction using such materials is the area of the active surface. High surface-to-volume structures, such as membranes, porous particles, or fibers improve extraction efficiency [24]. Electrospinning allows diblock copolymers to be processed effectively and conveniently into fibers with diameters in the micro- to nanometer scale [30–32]. Owing to inherent solvent affinities of the blocks and polymer self-assembly, the morphology of the fibers can be adjusted by the solvent choice, allowing surface enrichment with specific blocks [33–35]. Yang et al. published dibenzo 14-crown-4 containing electrospun polyimide nanofibers for Li recovery from LIBs [36]. Pan et al. developed porous polymeric nanosorbent fibers *via* electrospinning, exhibiting high hydrophilicity, efficient Li recovery, and superior mechanical properties [37]. In this work, we present four CE-functionalized PS-*b*-PMAA copolymers (PS-*b*-P(MAA-*r*-CEXMA), with X = B3 for B9C3, X = B4 for B12C4, and X = 4 for 12C4), varying in the type and functionalization density of the CEs. The hydrophilic PMAA block of a PS-*b*-PMAA diblock copolymer derived from a one-pot RAFT polymerization was functionalized with aromatic or non-aromatic CEs (Fig. 2). Electrospun fibers prepared from these polymers were evaluated for Li complexation using UV-active anions. Moreover, the competing complexation of sodium ions was investigated and electronic structure calculations were performed, in order to gain a better understanding of the host-guest complexes. This work presents an innovative approach for lithium extraction from aqueous media, with the possibility of overarching applicability through a high modularity and variability of CE functionalization. The facile RAFT synthesis of water-insoluble carrier materials allows for a scalable and cost-efficient process, owing to the commercial establishment of the monomers. At the same time, the electrospun, highly active fibers do not require organic solvents and thus establish a promising platform for the sustainable, industrial extraction of lithium from seawater.

2. Results and discussion

2.1. Electrospun PS-b-P(MAA-r-CEMA) fibers

Four polymers were synthesized, all based on the same initial polymer PS_{853}-*b*-$PMAA_{255}^{110}$ (Table 1). Two polymers are functionalized with B9C3 (P-B9C3-60, P-B9C3-14; 60 % and 14 % of MAA units esterified with CE, respectively). P-B12C4-14 is functionalized with B12C4 (14 %) and P-12C4-14 with 12C4 (14 %).

Uniform polymer fibers could be produced using a mixture of dimethylformamide (DMF) and dichloromethane (DCM) as a solvent mixture (20–25 wt% DMF/DCM (4/1 *V*/V)) for electrospinning. A polyester-based non-woven fleece was used as a substrate onto which the fibers were spun to increase stability. With every polymer, consistently thick fibers with a continuous structure were obtained. The average fiber diameter was 1.2 ± 0.1 µm for P-B9C3-60, 1.9 ± 0.3 µm for P-B9C3-14, 1.0 ± 0.1 µm and 1.2 ± 0.1 µm for P-B12C4-14 and P-12C4-14, respectively (fiber distribution in Fig. S1). Scanning Electron Microscopy (SEM) images of the fibers at the same magnification are shown in Fig. 3. Both the degree of esterification and the type of CE affect the surface polarity of the polymer, the viscosity of the solution, and consequently, the spinnability. However, fibers of subtly different diameters were obtained, all ranging between 1 and 2 µm and high homogeneity.

2.2. Li Extraction

The ability of the polymer fibers to complex lithium and sodium ions from aqueous media was investigated in a solid-liquid extraction (SLE). The quantitative determination of these ions in an aqueous solution was conducted *via* UV-active anions and UV–Vis spectroscopy, as described in the experimental section. The lithium concentrations were selected according to the concentration of the CE at a constant ratio of salt/CE = 0.5 (ranging in salt concentrations from 1.5 to 12.9 mmol/mL). The pH value of the solution (in Milli-Q water) was measured to be approximately 4.4, which indicates predominantly protonated MAA groups, and was not further adjusted [38,39]. The resulting data for q_{poly} is shown in Fig. 4 and in Table S1. To ensure the presence of an equilibrium and therefore maximum capacity, additional measurements at 30, 60, and 360 min showed equilibrium was nearly reached after 60 min (Table S1, Fig. S6). Additionally, it should be noted that the polymer fibers do not complex with lithium in the absence of CEs. The potential interaction with the free acid groups is insufficient for the purpose, even in an aqueous medium, proven by an SLE with PS-*b*-PMAA fibers (Fig. S2). In our previous work, high Li complexation was demonstrated in an LLE with analogous polymers fully dissolved in DCM [17,20]. At the same time, polymers with 12- to 15-membered CEs showed selectivities for larger ions, presumably due to the formation of ML_2 complexes [19]. Interestingly, the polymer fibers show a completely different behavior in the context of SLE, a technique that is essential for obsoleting organic solvents. The 3,5-diiodosalicylate concentration (from the Li salt LIS) hardly decreased during extraction with the B9C3-providing polymers, especially with low functionalization.

This results in the low values for q_{poly} $6.6{\cdot}10^{-5} \pm 1.3{\cdot}10^{-5}$ mmol/g for the high-functionalized polymer (P-B9C3-60) and $1.2{\cdot}10^{-7} \pm 7.7{\cdot}10^{-8}$ mmol/g for the low-functionalized polymer (P-B9C3-14).

One reason for the low capacity may be the low chain mobility in the solid material. In order to form an ML_2 complex, two CEs are required to be assembled locally. Based on the higher affinity of PMAA (or P(MAA-*r*-CEXMA)) to DMF and of PS to DCM, it is assumed that the PMAA chains are rather located at the surface of the fibers. A statistical distribution of the CEs within the MAA unit is presumed. Chain mobility is provided by the PMAA chains in aqueous solution. A formation of the ML_2 complexes necessary for Li complexation is significantly less probable with a low functionalization (P-B9C3-14) than with a high functionalization with CE (P-B9C3-60). Accordingly, the slightly higher value of q_{poly} for the latter is attributable to the higher probability of locally neighboring CEs. In addition, the smaller fiber diameter *d* and the associated greater active surface area may be a reason for the increased q_{poly} for P-B9C3-60. Comparable, analogous experiments with sodium ethyl eosin (NaEE) showed no complexation of the two polymers with sodium at all, which was to be expected due to the high ionic diameter of sodium (194 pm) [23]. Sodium concentrations were at a constant Na^+/CE ratio of 0.5 (8.7–13.6 mmol/mL).

Furthermore, PS-*b*-PMAA was functionalized with two different 12-membered CEs, with and without an aromatic group. Low degrees of functionalization (14 % of the MAA units) were chosen to suppress possible ML_2 complexation of adjacent CEs with sodium. Unlike the low-functionalized B9C3 polymer, the electrospun polymer fibers of P-B12C4-14 and P-12C4-14 exhibit a very good ability to complex Li, with values of q_{poly} of $1.9{\cdot}10^{-4} \pm 2.4{\cdot}10^{-5}$ mmol/g and $6.0{\cdot}10^{-5} \pm 9.4{\cdot}10^{-6}$ mmol/g, respectively. The q_{poly} values for P-B9C3-60 and P-12C4-14 are quite similar, even though the functionalization of P-B9C3-60 is significantly higher. The effect of the reduced CE requirement for ML compared to ML_2 complexation is evident. Significantly less 12C4 is

required for functionalization to achieve the same total capacity as with B9C3. Additionally, it should be noted that TEM images (Fig. S3) indicate no self-assembled structure, and as the fiber diameters are much larger than the chain size of the block copolymers, therefore some CEs will not be available for complexation on the active surface but will be partially embedded within the fiber. Considering this, the theoretical maximum capacity of the system is even higher. In order to achieve total accessibility of the CEs and supposedly maximize Li complexation, it would be reasonable to functionalize the fibers subsequently. Subsequent surface functionalization, particularly in the presence of carboxyl functionalities, can be achieved through a wide variety of mechanisms [40]. However, due to the solvation of the polymer fibers with common solvents, first results have not been successful and an alternative approach was chosen. Extractions with NaEE were similarly performed with these systems in order to assess possible competition from the highly concentrated Na ion present in seawater. Encouragingly, no complexation of the sodium was found at all. These data demonstrate the ability of the developed system not only to effectively extract Li from aqueous media without the necessity of organic solvents but also to successfully suppress the complexation of the larger Na ion. As discussed, this phenomenon presumably results from the low chain flexibility, which allows single ML complexation of Li by the 12-membered CE, but cannot form ML_2 complexes with sodium. In addition, the low values of Li complexation as ML_2 type (for P-B9C3-60), even at high degrees of functionalization, suggest that the increase of the CE content could lead to a higher efficiency with no or only a slight loss of selectivity. If the functionalization of the CE is performed on the aromatic ring (P-B12C4-14), the system has an even higher capacity to complex Li than the non-aromatic analogue (P-12C4-14).

The higher capacities of P-B12C4-14 compared to P-12C4-14 might be influenced by the slightly smaller *d* of P-B12C4-14 and the resulting greater active surface area. However, the values vary only slightly and are therefore not suitable for the explanation of the more than 3-times higher q_{poly} of P-B12C4-14. For comparison, extraction tests of the CE were carried out in a LLE, using DCM as carrier material, in a volume equivalent to the salt solution. Interestingly, one important conclusion was drawn: The free CEs show no significant difference in their ability to form complexes, with q_{CE} of 28 ± 2 mmol/mol for B12C4 and 29 ± 8 mmol/mol for 12C4 (Table S1). However, total values are not directly comparable to those of the polymer material, the trend, though, is. From the fact that the same polymer was used for all materials, it is concluded that the interaction of CE and polymer strongly influences the materials capacity to uptake Li.

While the exact cause is not yet understood, the result is reproducible. The effect might be attributed to the comparatively milder electron-withdrawing influence of the ester functionality on the aromatic ring, as opposed to direct substitution within the CE ring. This could enhance ion–dipole interactions between the CE and Li ions. Additionally, the lone pairs on the ester group may further stabilize the host–guest complex, as already postulated in earlier works [17,20,28]. Molecular structure optimization and calculation of the Hirshfeld charge distribution, based on density functional theory (DFT), were performed for the unsubstituted CEs and for CEs functionalized with three MAA units (Fig. 5), mimicking the first interacting polymer part of the hydrophilic block (Figs. S9–S16 and Table S2). The structural optimization was performed using the empirical dispersion correction according to Grimme. Solvent effects were considered using a continuum model (*self-consistent reaction field* SCRF; water).

Initially, the Hirshfeld charge distribution in the free CEs is examined. While 12C4 exhibits a nearly symmetrical charge transfer with Li complexation, B12C4 displays pronounced asymmetries. Specifically, the two oxygen atoms adjacent to the aromatic ring (O1 and O3) show differing extents of charge transfer. This disparity is attributed to the reduced conformational flexibility of the macrocyclic cavity caused by the rigid benzene moiety, which facilitates Li ion coordination preferentially from one side. With introducing a short MAA backbone, the data showed no significant influence of the ester (O5 and O6), directly adjacent to the CE, on charge distribution within the CE cavity. Given the actual trends found, it can therefore be assumed that not the existence of the MAA group alone, but its connection to and alignment with the polymer might be of decisive importance for complexation.

The two free acid groups provide further insights into the complexation properties. In particular, the second MAA unit exhibits a noticeable influence on Li coordination. Regardless of the CE, a significant charge transfer occurs from both O7 and O8, whereby the effect is slightly more pronounced with B12C4-3MAA. This indicates a complexation-supporting influence of the polymeric MAA backbone. However, when including the third MAA unit, this effect becomes even more pronounced. While the hydroxy group (O9) only shows a slight (12C4-3MAA) to moderate (B12C4-3MAA) charge transfer upon Li complexation, the carbonyl function (O10) shows a different pattern. A significantly stronger interaction with the Li is observed with the aromatic CE – about two to three times that of 12C4-3MAA. This is a strong indication of the more efficient complexation of B12C4-3MAA and is also apparent visually in the optimized structure (Fig. S16). Li ligation results in a pronounced conformational change in which the MAA units align specifically in the direction of the CE. In contrast, in 12C4-3MAA only the second MAA unit shows a comparable orientation.

3. Conclusion

In this work, four polymers with varying CE types and functionalization densities were synthesized and processed into highly uniform electrospun fibers (1–2 μm). All materials showed strong Li selectivity compared to sodium, while 12-membered CEs also enabled effective Li complexation. With a q_{poly} ($1.9{\cdot}10^{-4}$ ± $2.4{\cdot}10^{-5}$ mmol/g), we expect that the capacity of the system can be significantly increased while maintaining the same selectivity, provided that the CE/polymer ratio is adjusted, although this is of secondary importance due to the cost-efficiency of the matrix. Indeed, P-B12C4-14 is a promising candidate for selective Li extraction from aqueous media — without the use of organic solvents.

4. Experimental section

The parameters of the methods for analysis and processing are described in detail in the SI. The solid liquid extractions (SLE) were performed according to Fig. 6. The exact process is described in the SI.

The polymer fibers were shaken in aqueous solutions of Li and Na salts for 6 h, the salt solution was separated. In order to obtain a sufficiently large signal, the solution was evaporated, if necessary, and replenished by adding a small volume of water. Applying Lambert-Beer law, the salt concentration (Fig. S5) and consequently the equilibrium absorption capacity per CE q_{CE} (Eq. (1)) with c_{bc} the Li-concentration before and c_{ac} after the SLE, the volume of solution *V,* and the amount of CE in the sample (n_{CE}) or per 1 g polymer q_{poly} was calculated.

$$q_{CE} = \frac{(c_{bc} - c_{ac})V}{n_{CE}} \quad (1)$$

CRediT authorship contribution statement

Sabrina Jaehnke: Writing – review & editing, Writing – original draft, Investigation, Formal analysis, Data curation, Conceptualization. **Volker Abetz:** Writing – review & editing, Writing – original draft, Supervision, Resources, Methodology, Conceptualization.

Declaration of competing interest

The authors declare that they have no known competing financial interests or personal relationships that could have appeared to influence the work reported in this paper.

Acknowledgements

The authors would like to thank the NMR spectroscopic, mass spectrometric, elemental analysis, and electron microscopy service of the Department of Chemistry at the University of Hamburg. Furthermore, the authors would like to acknowledge collaborators from Helmholtz-Zentrum Hereon, especially Maryam Radjabian and Joachim Koll for the introduction and support in the production of electrospun fibers, and Martin Held, Erik Schneider, and Anke-Lisa Höhme for measuring and analyzing the SEM and TEM images. For this work the HPC-cluster Hummel-2 at University of Hamburg was used. The cluster was funded by Deutsche Forschungsgemeinschaft (DFG, German Research Foundation) – 498394658. Grateful thanks to Gloria Signorato and Patrick Schütz for proofreading and insightful feedback.

Appendix A. Supplementary data

Supplementary data to this article can be found online at https://doi.org/10.1016/j.desal.2025.119343.

Data availability

Data will be made available on request.

References

[1] Y. Wu, Q. Yuan, M. Yang, M. Zhai, G. Hu, Y. Gu, Impact of circular economy on the long-term allocation structure of primary and secondary lithium, Commun. Earth Environ. 5 (2024) 503, https://doi.org/10.1038/s43247-024-01667-2.
[2] U.S.G. U.S. Department of the InteriorSurvey, Mineral commodities summary 2024. http://pubs.er.usgs.gov/publication/mcs2023, 2023.
[3] P. Lindagato, Y. Li, J. Machăcek, G. Yang, I. Mungwarakarama, A. Ndahimana, H.P. K. Ntwali, Lithium metal: the key to green transportation, Appl. Sci. 13 (2023) 405.
[4] L. Baudino, C. Santos, C.F. Pirri, F. La Mantia, A. Lamberti, Recent advances in the lithium recovery from water resources: from passive to electrochemical methods, Adv. Sci. 9 (2022) 2201380, https://doi.org/10.1002/advs.202201380.
[5] X. He, S. Kaur, R. Kostecki, Mining lithium from seawater, Joule 4 (2020) 1357–1358, https://doi.org/10.1016/j.joule.2020.06.015.
[6] P.W. Fritz, T. Ashirov, A. Coskun, Porous organic polymers with heterocyclic crown ethers for selective lithium-ion capture, Chem 10 (2024) 2207–2219, https://doi.org/10.1016/j.chempr.2024.03.014.
[7] H. Yu, G. Naidu, C. Zhang, C. Wang, A. Razmjou, D.S. Han, T. He, H. Shon, Metal-based adsorbents for lithium recovery from aqueous resources, Desalination 539 (2022) 115951, https://doi.org/10.1016/j.desal.2022.115951.
[8] C. Paredes, E. Rodríguez de San Miguel, Selective lithium extraction and concentration from diluted alkaline aqueous media by a polymer inclusion membrane and application to seawater, Desalination 487 (2020) 114500, https://doi.org/10.1016/j.desal.2020.114500.
[9] T. Ye, H. Gao, Q. Li, N. Liu, X. Liu, L. Jiang, J. Gao, Highly selective lithium transport through crown ether pillared angstrom channels, Angew. Chem. 136 (2024), https://doi.org/10.1002/ange.202316161.
[10] A. Casadellà, O. Schaetzle, K. Nijmeijer, K. Loos, Polymer inclusion membranes (PIM) for the recovery of potassium in the presence of competitive cations, Polymers (Basel) 8 (2016) 1–14, https://doi.org/10.3390/polym8030076.
[11] H. Nikkhah, D. Ipekçi, W. Xiang, Z. Stoll, P. Xu, B. Li, J.R. McCutcheon, B. Beykal, Challenges and opportunities of recovering lithium from seawater, produced water, geothermal brines, and salt lakes using conventional and emerging technologies, Chem. Eng. J. 498 (2024) 155349, https://doi.org/10.1016/j.cej.2024.155349.
[12] S. Katsuta, K. Maeda, Extraction spectrophotometry using a lithium-ion selective metallacrown: temperature effect on extraction reaction and application to determination of lithium in serum and seawater, Anal. Sci. 40 (2024) 1373–1379, https://doi.org/10.1007/s44211-024-00569-9.
[13] K. Liu, Y. Xia, X. Chen, X. Li, K. Zhou, Y. Zeng, G. Zeng, X. Cheng, Z. Luo, S. Yi, Bilayer crown ether-engineered nanofiltration membranes with dual Li^+ transport channels for ultra-high Mg^{2+}/Li^+ separation from saline lake brines, Water Res. 284 (2025) 123924, https://doi.org/10.1016/j.watres.2025.123924.
[14] H. Li, Y. Wang, T. Li, X.K. Ren, J. Wang, Z. Wang, S. Zhao, Nanofiltration membrane with crown ether as exclusive Li^+ transport channels achieving efficient extraction of lithium from salt lake brine, Chem. Eng. J. 438 (2022) 135658, https://doi.org/10.1016/j.cej.2022.135658.
[15] L. Yang, Y. Tu, H. Li, W. Zhan, H. Hu, Y. Wei, C. Chen, K. Liu, P. Shao, M. Li, G. Yang, X. Luo, Fluorine-rich supramolecular nano-container crosslinked hydrogel for lithium extraction with super-high capacity and extreme selectivity, Angew. Chem. 135 (2023), https://doi.org/10.1002/ange.202308702.
[16] A.F. Liberati, A. Geneste, B. Prelot, J.P. Mericq, C. Faur, S. Monge, Synthesis, characterization and Li adsorption study of a new thermoresponsive crown-ether bearing copolymer, Sep. Purif. Technol. 354 (2025) 129123, https://doi.org/10.1016/j.seppur.2024.129123.
[17] I. Oral, V. Abetz, A highly selective polymer material using benzo-9-crown-3 for the extraction of lithium in presence of other interfering alkali metal ions, Macromol. Rapid Commun. 42 (2021) 2000746, https://doi.org/10.1002/marc.202000746.
[18] I. Oral, S. Tamm, C. Herrmann, V. Abetz, Lithium selectivity of crown ethers: the effect of heteroatoms and cavity size, Sep. Purif. Technol. 294 (2022) 121142, https://doi.org/10.2139/ssrn.4021934.
[19] I. Oral, V. Abetz, Improved alkali metal ion capturing utilizing crown ether-based diblock copolymers in a sandwich-type complexation, Soft Matter 18 (2022) 934–937, https://doi.org/10.1039/D1SM01815A.
[20] S. Jaehnke, J. von Chamier Gliszczynski, B. Hankiewicz, V. Abetz, Systematic investigation of a crown ether functionalized PS-b-PMAA block copolymer for optimized lithium extraction from aqueous media, J. Polym. Sci. (2025) 1–11, https://doi.org/10.1002/pol.20250060.
[21] L. Baudino, A. Pedico, S. Bianco, M. Periolatto, C.F. Pirri, A. Lamberti, Crown-ether functionalized graphene oxide membrane for lithium recovery from water, Membranes (Basel) 12 (2022) 1–12, https://doi.org/10.3390/membranes12020233.
[22] C.C. Liou, J.S. Brodbelt, Determination of orders of relative alkali metal ion affinities of crown ethers and acyclic analogs by the kinetic method, J. Am. Soc. Mass Spectrom. 3 (1992) 543–548, https://doi.org/10.1016/1044-0305(92)85031-E.
[23] E. Weber, Crown ethers, in: Ullmann's Encycl. Ind. Chem, Wiley-VCH Verlag GmbH & Co. KGaA, Weinheim, Germany, 2007, pp. 471–478, https://doi.org/10.1002/14356007.a08_091.pub2.
[24] M. Ge, C. Wei, T. Fang, X. Liu, Molecular insight into the separation mechanism of crown ether-based channels for lithium extraction, Sep. Purif. Technol. 338 (2024) 126415, https://doi.org/10.1016/j.seppur.2024.126415.
[25] Y. Dong, Y. Liu, H. Li, Q. Zhu, M. Luo, H. Zhang, B. Ye, Z. Yang, T. Xu, Crown ether-based Tröger's base membranes for efficient Li^+/Mg^{2+} separation, J. Membr. Sci. 665 (2023) 121113, https://doi.org/10.1016/j.memsci.2022.121113.
[26] L. Zheng, X. Song, J. Liu, H. Jiang, A. Toghan, Crown ether regulated nanocomposite membrane with lithium channels for highly selective Li^+/Mg^{2+} separation, Desalination 592 (2024) 118121, https://doi.org/10.1016/j.desal.2024.118121.
[27] H.R. Yu, J.Q. Hu, X.H. Lu, X.J. Ju, Z. Liu, R. Xie, W. Wang, L.Y. Chu, Insights into the effects of 2:1 "sandwich-type" crown-ether/metal-ion complexes in responsive host - guest systems, J. Phys. Chem. B 119 (2015) 1696–1705, https://doi.org/10.1021/jp5079423.
[28] A. Bey, O. Dreyer, V. Abetz, Thermodynamic analysis of alkali metal complex formation of polymer-bonded crown ether, Phys. Chem. Chem. Phys. 19 (2017) 15924–15932, https://doi.org/10.1039/c7cp02651j.
[29] J. Hua, J. He, H. Pei, X. Ma, S.R. Wickramasinghe, J. Li, Supported ionic liquid membrane contactor with crown ether functionalized polyimide membrane for high-efficient Li^+/Mg^{2+} selective separation, J. Membr. Sci. 687 (2023) 122038, https://doi.org/10.1016/j.memsci.2023.122038.
[30] H. Yu, Z. Tan, Introduction to Electrospinning and Nanofiber, Springer Nature Switzerland, Cham, 2025, https://doi.org/10.1007/978-3-031-74310-8.
[31] A. Greiner, J.H. Wendorff, Electrospinning: a fascinating method for the preparation of ultrathin fibers, Angew. Chem. Int. Ed. 46 (2007) 5670–5703, https://doi.org/10.1002/anie.200604646.
[32] M. Ma, G.C. Rutledge, 7.10 - nanostructured electrospun fibers, Polym. Sci. a Compr. Ref. 1-10 (1–10) (2012) 187–210, https://doi.org/10.1016/B978-0-444-53349-4.00191-6.
[33] J.G. Werner, Y. Li, U. Wiesner, Block-copolymer-architected materials in electrochemical energy storage, Small Sci. 3 (2023) 2300074, https://doi.org/10.1002/smsc.202300074.
[34] V. Abetz, P.F.W. Simon, Phase behaviour and morphologies of block copolymers, in: Block Copolym. I, Springer-Verlag, Berlin/Heidelberg, 2005, pp. 125–212, https://doi.org/10.1007/12_004.
[35] K. Foroutani, S.M. Ghasemi, How does micro- and macro-phase separation of block copolymers affect the formation of integral asymmetric isoporous membranes? A review on effective factors, Macromol. Mater. Eng. 307 (2022) 1–23, https://doi.org/10.1002/mame.202200084.
[36] F. Yang, L. Li, J. Hua, J. He, X. Ma, J. Li, Electrospun nanofiber membrane of dibenzo 14-crown-4-ether polyimide for efficient selective lithium recovery from discarded lithium-ion batteries, Sep. Purif. Technol. 334 (2024) 126018, https://doi.org/10.1016/j.seppur.2023.126018.
[37] Y. Pan, Y. Zhang, C. Thompson, G. Liu, W. Zhang, Electrospun lithium porous nanosorbent fibers for enhanced lithium adsorption and sustainable applications, ACS Appl. Mater. Interfaces 16 (2024) 54259–54271, https://doi.org/10.1021/acsami.4c13253.
[38] C. Fernyhough, A.J. Ryan, G. Battaglia, pH controlled assembly of a polybutadiene–poly(methacrylic acid) copolymer in water: packing considerations and kinetic limitations, Soft Matter 5 (2009) 1674, https://doi.org/10.1039/b817218h.
[39] S. Kawaguchi, A. Yekta, M.A. Winnik, Surface characterization and dissociation properties of carboxylic acid core–shell latex particle by potentiometric and conductometric titration, J. Colloid Interface Sci. 176 (1995) 362–369, https://doi.org/10.1006/jcis.1995.9956.
[40] S. Zhong, T. Wang, J. Xu, Y. Su, J.R. Hoffman, B. Su, A. Li, A. Atassi, M.J. Webber, R. Guo, W.A. Phillip, Designing phenolphthalein-based adsorptive membranes for the high-affinity, high-capacity capture of contaminants from water, ACS Appl. Mater. Interfaces 16 (2024) 68262–68272, https://doi.org/10.1021/acsami.4c13901.

6. UNPUBLISHED RESULTS

6.1. MEMBRANE PREPARATION

This section is devoted to membrane development through the SNIPS process. The results presented here were carried out as preliminary work for the development of a solvent-free system from the block copolymers described. The transformation of the polymer system into a membrane form using the SNIPS process promises, with optimized parameters, to produce a material with a high surface/volume ratio, that can be manufactured on an industrial size, is scalable, energy-efficient and cost-efficient, and could be reused over several cycles with possible non-destructive decomplexation of Li.

The work in this section was accomplished with the valuable support of students Andja Çela, Amrei Gouby, and Joel Senador Hauptvogel. Dr. Andreas Meyer, Amrei Gouby, and Joel Senador Hauptvogel contributed significantly to the AFM data acquisition. Dr. Zhenzhen Zhang provided essential insight and implementation support through her introduction to the fundamental processes of membrane fabrication. The excellent SEM and TEM images were produced by the EM Service at the Helmholtz-Zentrum Hereon (Dr. Martin Held, Anke-Lisa Höhme, Dr. Erik Schneider, and Dr. Evgeni Sperling) and form a key basis for the imaging analysis.

6.1.1. PS-*b*-PMAA MEMBRANE

As a first step toward developing a Li-selective polymer membrane, membranes were produced from the unfunctionalized block copolymer. The aim was to characterize the basic self-assembly behavior of the polymer in various solvents in order to generate decisive information for subsequent processing. Modification of the polymer changes the solvent affinity according to the selected CE and its degree of functionalization. Based on the findings obtained in this chapter, subsequent processing should be facilitated by assessing the solvent affinities. To support this assessment, solubility parameters were calculated as part of this work, but also from preliminary work by Andres Castro Villavicencio (under the supervision of Dr. Iklima Oral), which are (partially) transferable to the system used here. These are introduced at an appropriate point. The synthesis of a non-functionalized membrane also serves as a starting point for potential post-modification, in which functionalization with CE takes place after the block copolymer's self-assembly into an ordered structure. However, this alternative approach should not be the focus here and will be addressed in section 7.4.

To guarantee a high level of environmental compatibility for the system, water ought to be used as the precipitation bath. This is suitable for this application since the polymer is not water-

soluble before and after functionalization due to its desired applicability in seawater. At the same time, the non-solvent bath represents the largest amount of liquid in the SNIPS process and therefore offers the greatest potential for an environmentally friendly and sustainable manufacturing process, even though it still has to be purified before disposal.

The solvent chosen for the polymer must be miscible in the precipitation bath, i.e., it must be water-soluble. Based on initial research results by I. Oral[66] and K. Foroutani *et al.*[189], 1,4-dioxane (DOX) was initially selected as the solvent. DOX is a selective solvent for the PS block, which is also confirmed by the calculated Flory-Huggins-Staverman parameters being $\chi_{PS\text{-}DOX}$=0.15 and $\chi_{PMAA\text{-}DOX}$ =1.03. Moreover, attention should be paid to the potential solubility of PMAA in water. In the supporting information for publication 2 (section 9.3), the interaction parameters $\chi_{PS\text{-}water}$ and $\chi_{PMAA\text{-}water}$ were determined to be 1.83 and 0.78, respectively. In order to reduce possible solvation of the PMAA block, the precipitation was carried out at low temperatures (<4°C).

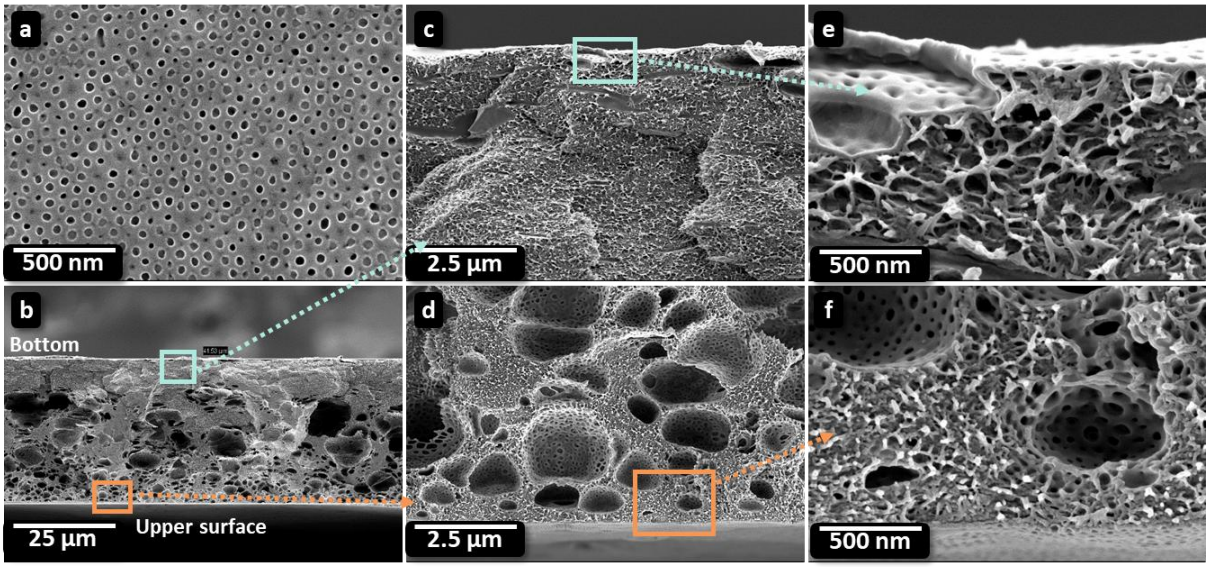

Figure 32: Scanning electron microscopy images of PS_{80}-*b*-$PMAA_{20}^{170}$ diblock copolymer (*Đ*=1.5; 20wt% in 1,4-dioxane (DOX), evaporation *t*=60 s, non-solvent *T*=2.2 °C, humidity=33%, r.t.= 16°C). Sputter coated with 1-1.5 nm Pt. Acceleration voltage of 1.5 – 3kV. Shown are top view (**a**, mag=50 000x), cross-section (**b**, mag= 1000x), bottom (**c**, mag=10 000x and **e**, mag=50 000x) and upper surface (**d**, mag=10 000x and **f**, mag= 50 000x). Data by Helmholtz-Zentrum Hereon.

Figure 32 shows a top view and cross-section of the polymer film produced from a solution of PS_{80}-*b*-$PMAA_{20}^{170}$ in DOX (20wt%; with 80 wt% PS, 20 wt% PMAA and a MW of 170 kDa). The film was free-standing on a glass substrate with a drying time of 60 seconds, at an environmental temperature of 16°C, humidity of 33%, and a non-solvent bath temperature of 2.2°C. In the top view (Figure 32, a), an orderly and isoporous surface structure appears evident. Thus, self-assembly of the block copolymer occurred in DOX. Considering the system, the increased affinity of PS to the low-volatility DOX suggests micelle formation consisting of PMAA blocks within a PS matrix. The apparent interaction of PMAA with the non-solvent

enhances the localization of the hydrophilic blocks at the pore walls. The surface structure indicates the formation of spherical and standing cylindrical pores with an average pore diameter of 41.4 ± 10 nm (measured over 50 pores). The presence of spherical morphology can be assumed, as the pores only partially exhibit optical depth and opening in both the cross-sections and the top view. The asymmetric structure of the membrane is evident in cross-section (Figure 32, b–f), which shows increasing porosity up to a dense bottom surface. Flow measurements would be reasonable to perform, in order to verify the optical assessment of the pore porosity. However, since the focus of this work was on the formation of functional membranes, preferably on already functionalized polymer material, film preparations were performed with the variously functionalized PS-*b*-PMAA copolymer based on the results of the unfunctionalized polymer.

6.1.2. B9C3-MEMBRANE

In the LLE, the polymers functionalized with B9C3 proved to be highly Li-selective. This is presumably due to the formation of ML_2 complexes. For this reason, it is advisable not to reduce the functionalization density of the polymers too much in order to enable a predetermined spatial proximity of the CEs. This is particularly important in solvent-free systems, in which the mobility of the chains is additionally restricted. This section describes the initial results for two B9C3-functionalized PS-*b*-PMAA block copolymers, PS_{74}-*b*-P(MAA_{15}-*r*-CEB9MA_{11})[121] and PS_{67}-*b*-P(MAA_{10}-*r*-CEB9MA_{22})[199] with a functionalization of 20% and 40% respectively.

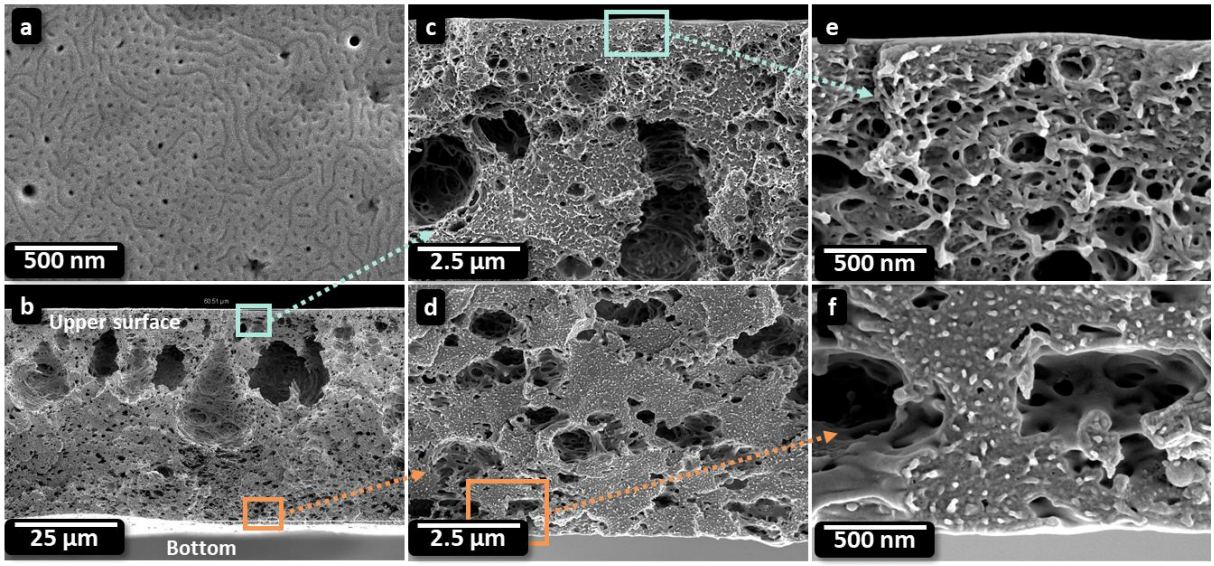

Figure 33: Scanning electron microscopy images of PS_{74}-*b*-P(MAA_{15}-*r*-CEB9MA_{11})[121] (*Đ*=1.4; 27wt% in 1,4-dioxane, evaporation *t*=90 s, non-solvent *T*=1.9 °C, humidity=46%, r.t.= 15°C). Sputter coated with 1-1.5 nm Pt. Acceleration voltage of 1.5 – 3kV. Shown are top view (**a**, mag=50 000x), cross-section (**b**, mag= 1000x), bottom (**c**, mag=10 000x and **e**, mag=50 000x) and upper surface (**d**, mag=10 000x and **f**, mag= 50 000x). Data by Helmholtz-Zentrum Hereon.

Figure 33 illustrates SEM images of PS_{74}-*b*-P(MAA_{15}-*r*-CEB9MA_{11})[121]. The surface shows hardly any open pores, which is also confirmed by the cross-sectional images. Instead, worm-like morphologies are visible on the film surface, as well as spherical indentations. This may be due to the long evaporation time. However, films drawn at shorter evaporation times did not exhibit any visible self-assembly. The cross-sectional images reveal a relatively compact polymer matrix interspersed in places with large pore domains. Similar surface structures are visible for the polymer PS_{67}-*b*-P(MAA_{10}-*r*-CEB9MA_{22})[199] in Figure 34. In this case, exclusively worm-like, closed structures are recognizable. At 30 s, the evaporation time is significantly reduced compared to the previous sample, while the concentration of the solution (20wt%) corresponds to that of the unfunctionalized polymer.

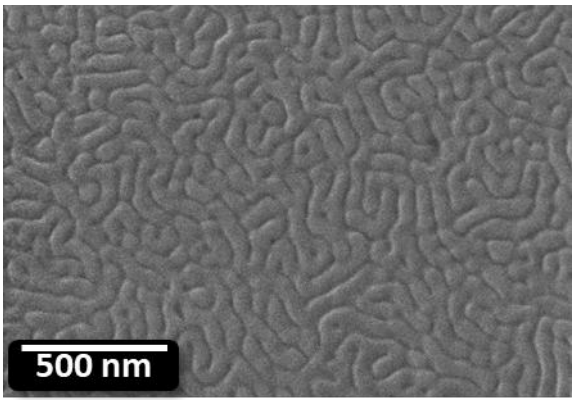

Figure 34: Scanning electron microscopy image of the surface of PS_{67}-*b*-P(MAA_{10}-*r*-CEB9MA_{22})[199] (*Đ*=1.5; 20wt% in 1,4-dioxane, evaporation *t*=30 s, non-solvent *T*=1.5 °C, humidity=41%, r.t.= 17°C). Sputter coated with 1-1.5 nm Pt. Acceleration voltage of 3kV. Magnitude= 50 000x. Data by Helmholtz-Zentrum Hereon.

The structures indicate disturbed self-organization of the polymer with CE functionalization of the hydrophilic block. With Flory-Huggins-Staverman parameters of the functionalized MAA block of $\chi_{B9C3MA\text{-}DOX}$=0.84, the affinity of the solvent to the pore-forming block is significantly increased with functionalization. Furthermore, the mass of the hydrophilic block increases during functionalization, shifting the weight ratio of the blocks toward P(MAA-*r*-CEB3MA). The "worm-like" structures could indicate cylindrical morphologies perpendicular to the film surface. At the same time, if the evaporation time is too long, it is possible that the pores will collapse due to increasing structural instability (especially if the proportion of the matrix-forming block is low). Additives can be added to the polymer solution to adjust the membrane morphology, as described in the following section.

6.1.3. ADDITIVES FOR MEMBRANE FORMATION

The membrane morphology can be adjusted by additives such as *γ*-butyrolactone (GBL)[190], polyethylene glycol[191], or salts (silver, zinc, or copper salts)[192]. By adding the low-volatility GBL, the solvent evaporates more slowly and the block copolymer has more time for efficient self-organization. At the same time, GBL changes the miscibility with the non-solvent

water, which can have a direct influence on pore formation. In work by Clodt *et al.*[190], the addition of GBL to an amphiphilic block copolymer of PS and poly-4-vinylpyridine (P4VP) led to a lower required polymer concentration and, consequently, the formation of a more open substructure. Similarly, membranes were produced from functionalized PS_{67}-*b*-P(MAA_{10}-*r*-CEB9MA_{22})[199] and non-functionalized PS_{80}-*b*-$PMAA_{20}$[170] with the addition of GBL to the polymer solvent. Another approach was chosen by adding low-molecular-weight polyacrylic acid (PAA). PAA was intended to support self-assembly *via* non-covalent interactions with the free carboxylic acid groups of P(MAA-*r*-CEB3MA). Subsequently, the low-molecular-weight PAA would be washed out by the precipitation bath, leaving behind a more defined pore structure. The results for the film preparation with addition of GBL or PAA are summarized in Figure 35.

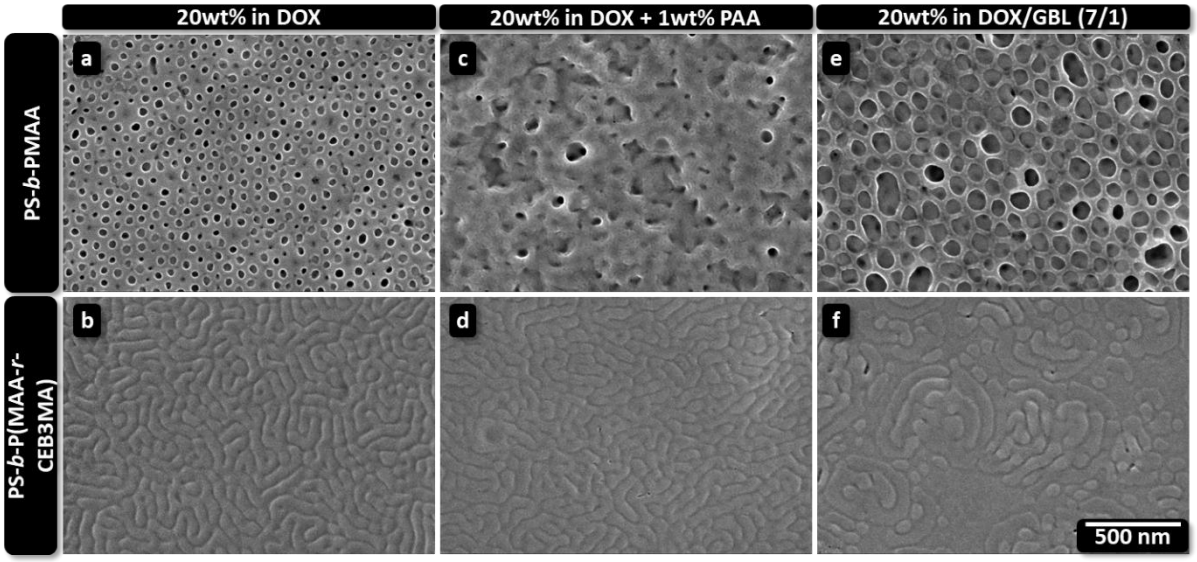

Figure 35: Scanning electron microscopy image of the surface of PS_{80}-*b*-$PMAA_{20}$[170] (**a**, 20wt% in 1,4-dioxane (DOX); **c**, 20wt% in DOX + 1wt% poly(acrylic acid) (PAA; 2100 Da), evaporation *t*=30 s, non-solvent *T*=1.5 °C, humidity=50%, r.t.= 18°C; **e**, 20wt% in DOX/ γ-butyro lactone (GBL; 70wt%/10wt%), evaporation *t*=30 s, non-solvent *T*=1.6 °C, humidity=50%, r.t.= 18°C) and PS_{67}-*b*-P(MAA_{10}-*r*-CEB9MA_{22})[202] (**b**, 20wt% in DOX; **d**, 20wt% in DOX + 1wt% PAA (2100 Da), evaporation *t*=30 s, non-solvent *T*=1.5 °C, humidity=41%, r.t.= 17°C; **f**, 20wt% in DOX/GBL (70wt%/10wt%), evaporation *t*=30 s, non-solvent *T*=1.0 °C, humidity=41%, r.t.= 17°C). Sputter coated with 1-1.5 nm Pt. Acceleration voltage of 3kV. Magnitude= 50 000x. Data by Helmholtz-Zentrum Hereon.

The addition of PAA to PS-*b*-PMAA causes significantly smaller and less defined pores. It appears as if swelling occurs during the process. This could indicate a possible morphological distortion due to the simultaneous interaction of PMAA and PAA as well as PAA and water. The addition of PAA has little effect on the functionalized polymer. The addition of GBL, on the other hand, leads to significantly larger pore formation in the unfunctionalized block copolymer. However, this behavior cannot be transferred to the polymer functionalized with B9C3. In order to improve self-organization, polymers with B12C4 and with lower functionalization were investigated in various solvent mixtures. With regard to the results from section 5.3, these polymers are of particular interest as they yielded good results in the production of electrospun fibers.

6.1.4. B12C4-MEMBRANE

Films were also produced using the SNIPS process from the B12C4-functionalized polymer PS_{75}-*b*-P(MAA_{16}-*r*-$CEB12MA_8$)[118]. Solutions of the Polymer in DOX were prepared, as in the previous experiments, as well as in a mixture of DMF and THF. THF is a selective solvent for the PS block ($\chi_{PS\text{-}THF}$=0.19, $\chi_{PMAA\text{-}THF}$=0.55)[66], DMF for the PMAA block ($\chi_{PS\text{-}DMF}$=0.75, $\chi_{PMAA\text{-}DMF}$=0.11)[66].

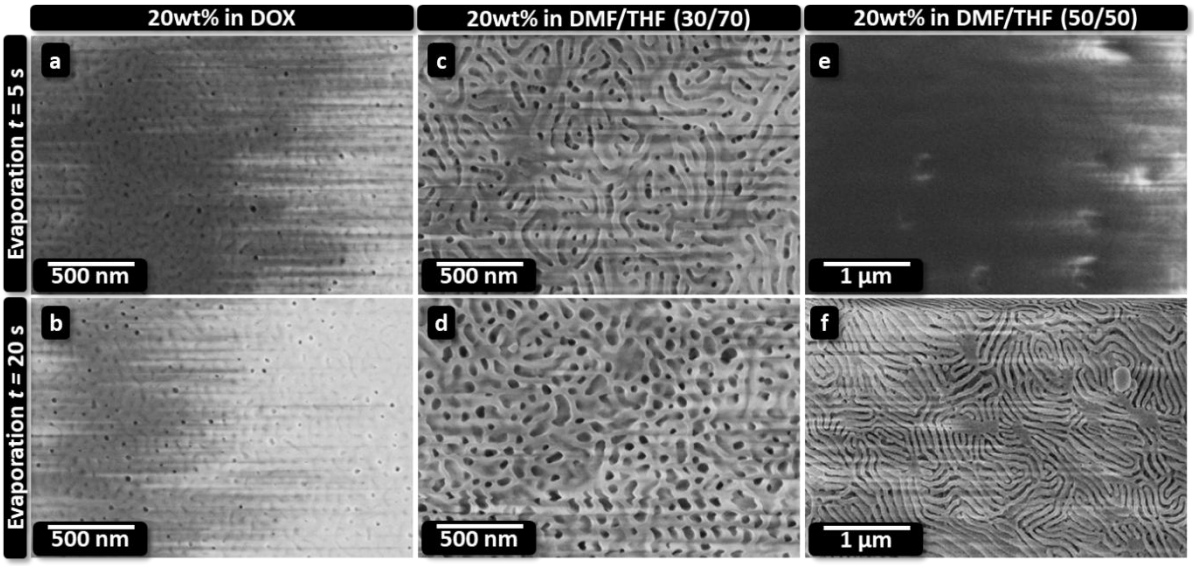

Figure 36: Scanning electron microscopy images of the surface of PS_{75}-*b*-P(MAA_{16}-*r*-$CEB12MA_8$)[118] (*Đ*=1.5; **a** and **b**, 20wt% in 1,4-dioxane, evaporation *t*=5 s and 20 s, non-solvent *T*=1.5–1.7 °C, humidity=32%, r.t.= 18°C; **c** and **d**, 25wt% in *N,N'*-dimethylformamide (DMF)/ tetrahydrofuran (THF) 30/70 (*V*/*V*), evaporation *t*=5 s and 20 s, non-solvent *T*=1.7 °C, humidity=42%, r.t.= 18°C; **e** and **f**, 25wt% in DMF/THF 50/50 (*V*/*V*), evaporation *t*=5 s and 20 s, non-solvent *T*=1.6–1.9 °C, humidity=44%, r.t.= 18°C). Data by UHH. EHT= 1 kV. Mag (a–d)=50 000x, Mag (e,f)= 25 000x.

The films, produced from a DOX solution, show a worm-like appearance and a few small spherical openings (Figure 36 a,b). Here as well, self-assembly appears to be disrupted by the presence of CE. The evaporation time was reduced to 5 s and 20 s. However, since no difference in morphology can be detected between these time intervals, it is assumed that varying this factor will not produce any improvement. At 118 kDa, the molar mass of the polymer is reduced compared to the polymer described in the previous section (PS_{67}-*b*-P(MAA_{10}-*r*-$CEB9MA_{22}$)[199]), and the functionalization is lower at only 10% of the MAA units. This could contribute to improved self-organization. The results of the DMF/THF mixture are given in Figure 36 c-f. With equivalent volumes, no self-assembly occurred after 5 s, but after 20 s pronounced worm-like indentations appeared in the surface. With an excess volume of the more volatile THF (30/70 DMF/THF), horizontal cylinders with a few spherical openings initially formed after 5 s. After 20 s, this structure appeared to be even more pronounced. Self-assembly into a structure with spherical openings perpendicular to the surface (double gyroid or cylindrical) seemed to have developed. Cross-sectional images and flow measurements could provide more detailed information about the membrane properties and porosity.

However, since these were only preliminary tests, the promising topic of membrane production from block copolymers was not pursued further. In particular, the B12C4-based polymer, which also yielded good results in electrospinning, formed the most interesting surface structures so far. Due to the ML single complexation of B12C4 with Li, it is reasonable to keep the functionalization low in order to avoid ML_2 complexation with the competing sodium ion. Low functionalization is apparently also beneficial to the membrane structure.

6.1.5. EXPERIMENTAL SECTION

In the following, the experimental setup and reagents used for the film preparation according to the SNIPS process will be mentioned.

Materials

All chemicals were used as received unless otherwise noted. The polymers were synthesized according to known literature and publications 2 and 3. Functionalizations with the hydroxy functionalized CEs were performed also according to Publications 2 and 3, *via* Mitsunobu esterification. THF (99.7%, Fisher Scientific, Hampton), DMF (99.8%, Fisher Scientific, Hampton), DOX (99%, Grüssing, Filsum), GBL (99.7%, TH. Geyer, Renningen), PAA (2100 g/mol; 99%, Aldrich, Steinheim). Water was purified *via* a Milli-Q purification system (18.1 MΩcm at 25 °C).

SNIPS Procedure

The casting solutions were prepared and mixed for at least 12 hours at 40°C and 300 rpm until they appeared homogenous. Afterwards, solutions were transferred into a syringe and casted on a glass plate with a thickness of 200 µm, using a metal doctor blade. After the evaporation time, the glass plates were transferred into a precooled water bath (volume of 1 L). After 4 h, the detached polymer films were put on a silicon mat and dried in vacuum (40°C) for 24 h.

Scanning electron microscopy

Scanning electron microscopy (SEM) characterization was performed with an Merlin SEM (Zeiss, Oberkochen, Germany) or with a LEO GEMINI 1550 (Zeiss, Oberkochen, Germany). The polymer samples were dried for 72 h (vacuum, 60 °C) before measurement. Afterwards the samples were sputter-coated at Helmholtz-Zentrum Hereon (platinum, 1–1.5 nm) with a CCU-010 coating device (Safematic, Switzerland) or at UHH without further coating. The pore diameters were determined by analyzing 50 data points, using the software ImageJ (version 1.51f).

6.2. CUBOSOME PREPARATION

This section is focused on the conversion of the described block copolymers into cubosomes. As outlined in section 3.5.4, cubosomes are porous, spherical particles on a nano- to micrometer size scale. The transition of the described amphiphilic polymer material into a cubic phase promises, with targeted optimization of the process parameters, the creation of stable and highly organized particles with a large internal surface area, resulting in a high capacity for active surface processes (such as Li complexation) and the potential for targeted (Li) release. Cubosomes show promising application potential in selective ion separation. On the one hand, they can be used in a similar way to chromatographic column materials, whereby Li ions can be specifically filtered out of aqueous media. On the other hand, it is possible to use the particles in larger, but spatially isolated aqueous volumes for complexation. Compared to other nanoscale structures such as micelles, cubosomes offer the decisive advantage that they can be specifically separated by sedimentation. This process can be accelerated by centrifugation if necessary. This property facilitates the recovery and reusability of the particles and makes them particularly attractive for resource-saving Li extraction from water.

This project was realized in valued collaboration with the research group of Prof. Dr. André Gröschel (University of Bayreuth). Following collaborative conceptualization, the B9C3-functionalized diblock copolymers PS-b-P(MAA-r-CEB3MA) produced at the University of Hamburg were processed into cubosomes by Marcel Schumacher (University of Münster) and analyzed as such. We greatly appreciated the collegial cooperation and professional dialogue. Polymers, carefully synthesized by Joachim von Chamier Gliszczynski and Erika Werner during their internships under my supervision, were used for this project.

6.2.1. B9C3 CUBOSOMES

The cubosomes were produced from the B9C3-modified block copolymers. Cubosomes are typically produced from block copolymers with large discrepancies in block lengths ($f \geq 0.9$).[174,175,179] In this work, PS_{90}-*b*-$PMAA_{10}$ (MW=80 kDa, $Đ$=1.32) and PS_{95}-*b*-$PMAA_5$ (MW=160 kDa, $Đ$=1.58) were used as starting points. After CE functionalization, the polymers PS_{83}-*b*-P(MAA_5-*r*-$CEB3MA_{12}$)[87] and PS_{94}-*b*-P(MAA_4-*r*-$CEB3MA_2$)[162] were obtained. It should be noted that the hydrophilic block increases considerably in weight due to the bulky CE after functionalization.

For optimizing the parameters, various solvent mixtures consisting of DMF and DOX were used, as well as various precipitation baths of methanol (MeOH) or water (ranging in pH values from 4 to 10). Figure 37 shows the results for the polymer PS_{94}-*b*-P(MAA_4-*r*-$CEB3MA_2$)[162].

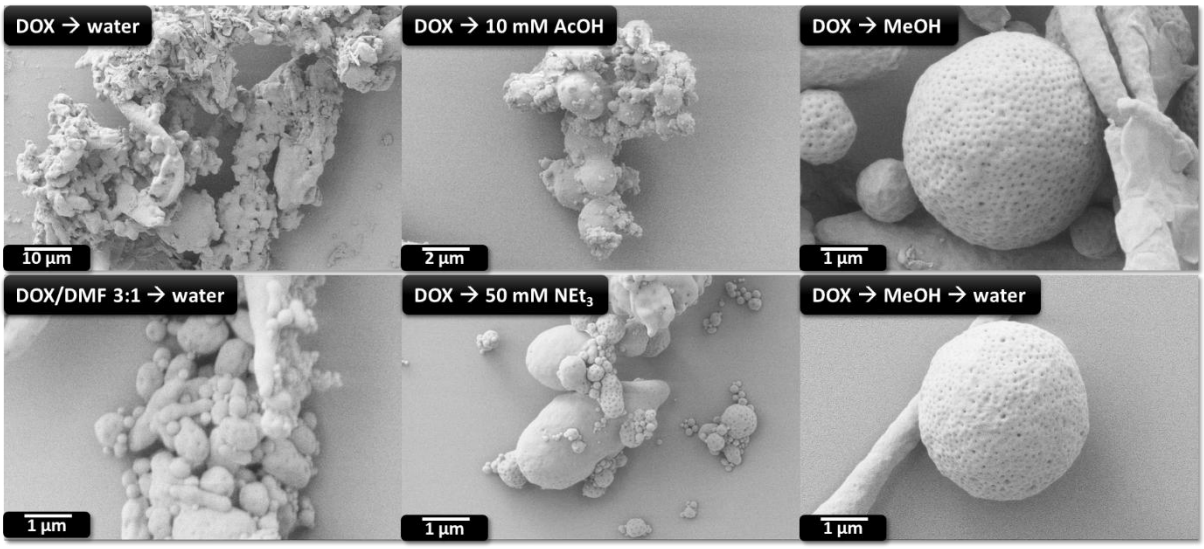

Figure 37: Scanning electron microscopy data of nano-precipitated PS_{94}-*b*-$P(MAA_4$-*r*-$CEB3MA_2)^{162}$. 1,4-dioxane (DOX) or DOX/*N,N'*-dimethylformamide (DMF) was used as solvent (mixture), water (pure or with additional Acetic acid (AcOH) or triethylamine (NEt_3)) or methanol (MeOH) were used as non-solvent. Data was received from M. Schumacher (University of Münster). EHT= 2 kV. Mag=3440 – 26690x.

The production of cubosomes via nanoprecipitation was partially successful. The precipitation of PS_{94}-*b*-$P(MAA_4$-*r*-$CEB3MA_2)^{162}$ (functionalization of the PMAA of 14%) from DOX in MeOH proved to be most promising. In contrast, the precipitation of the polymer from DOX in water was not successful; no spherical structures emerged, reflecting the non-solvent dependence of the morphology. DOX exhibits greater selectivity for the PS block. By adding DMF, which has a higher affinity for the PMAA block, it was possible to approximate the structure of a sphere more closely. However, no porosity was achieved.

Since PMAA acts as a pH-sensitive block, it can be assumed that the acidity of the precipitation bath has a direct influence on self-assembly. By adding acetic acid (AcOH, *pH*=4), the free MAA units are largely protonated, reducing the repulsive interactions within the hydrophilic segment. a_0 is decreased and *p* is increased, which favors the formation of cubosome-like structures. However, an improvement in spherical porosity could not be achieved in this case. If the pH value of the precipitation bath is increased, for example by the addition of triethylamine (NEt_3, *pH*=10), the MAA units are predominantly deprotonated. Thus, more electrostatic repulsion occurs and *p* decreases. In fact, more pronounced porosity can be observed, but no spherical structures. When the polymer was precipitated from DOX to MeOH, spherical particles with porous surface formed. Unlike in an aqueous medium, the PMAA block swells less strongly in MeOH. The resulting lower a_0 leads to a larger *p* and to the obviously more effective formation of inverse structures in a spherical shape. Due to the existing fixation, subsequent dialysis has no effect on the particle's structure.

SEM data of the nano-precipitated PS_{83}-*b*-P(MAA_5-*r*-CEB3MA_{12})[87] (functionalization of the PMAA of 40%) is summarized in Figure 38. Nanoprecipitation was performed in MeOH or water from polymer solutions in DOX/DMF or pure DMF.

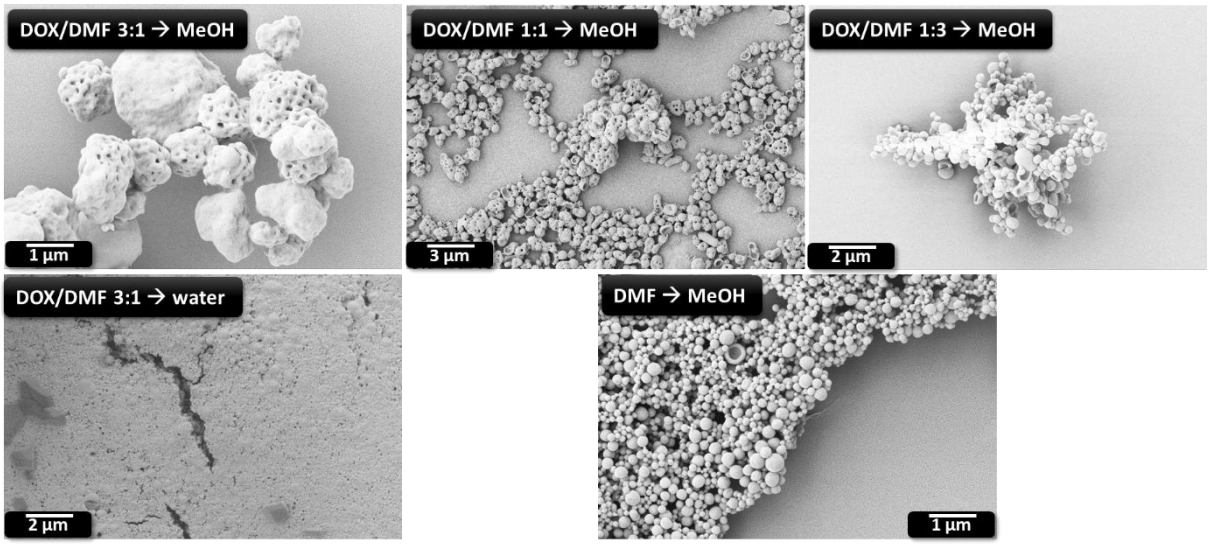

Figure 38: Scanning electron microscopy data of nano-precipitated PS_{83}-*b*-P(MAA_5-*r*-CEB3MA_{12})[87]. *N,N'*-dimethylformamide (DMF) or 1,4-dioxane (DOX)/DMF was used as solvent (mixture), water or methanol (MeOH) were used as non-solvent. Data was received from M. Schumacher (University of Münster). EHT= 2 kV. Mag=6560 – 23070x.

While initial nanoprecipitation attempts in MeOH from DOX solution showed promise, repeating the results proved challenging due to different solubility behaviors of the polymers. Pure DOX did not yield a stable solution, highlighting the need for a tailored solvent combination. For this reason, various proportions of DMF were added (from 25 to 100% DMF). Initially, a precipitation from DOX/DMF (3/1 V/V) was carried out in MeOH and water as a non-solvent. Significant differences in the developed morphology were observed. Although precipitation in water proved ineffective, MeOH enabled the successful formation of porous, isolated particles. With a decreasing proportion of DMF in the solution the particles are less vesicle-shaped and the size and porosity of the resulting particles increases considerably.

Increasing the DMF content results in more selective solvation of the PMAA block. This results in a larger a_0, thereby reducing *p* – self-organization shifts toward vesicular, micellar structures. Conversely, the application of more DOX results in a compaction of the hydrophilic segment, a smaller a_0, and thus a larger value for *p*. Consequently, cubosome-like structures with negative curvature form despite the comparatively large weight fraction of the hydrophilic segment. It was possible to produce cubosomes from the highly functionalized polymer by specifically selecting a suitable solvent mixture that compresses the hydrophilic part but remains above the solubility limit in combination with a suitable precipitation bath. This is particularly interesting as the polymer's Li complexing capacity is largely determined by the CE functionalization in the corona, which are kept high at 16.9wt% with the developed method. Further optimizations could lead to an even higher CE content and a more spherical shape.

While particle yield in the upscaled approach (up to 200 mg) remains modest, the successful demonstration of cubosome formation marks a significant milestone. The findings form a solid basis for further investigations into the functional capacity and applicability of the structures.

6.2.2. EXPERIMENTAL SECTION

In the following, the experimental setup and reagents used for the cubosome preparation *via* nanoprecipitation process will be mentioned.

Materials

The polymers were synthesized according to known literature and publication 2. Functionalization with the hydroxy functionalized CE was performed also according to publication 2, *via* Mitsunobu esterification. Further information on the purity of the solvents used for nanoprecipitation is not available, as this was carried out by a cooperation partner.

Nanoprecipitation Procedure

Nanoprecipitation was performed at the University of Münster. Water was used Milli-Q grade. Dialysis tubes had a molecular weight cutoff of 3500 g/mol. The solutions were prepared in DOX/DMF or pure solvent until they appeared homogenous in concentrations ranging from 0.01 – 10wt%. The solution was gently stirred during self-assembly. 1 mL of selective solvent (water, aqueous solution or MeOH) was added within 1 h to 1 mL of polymer solution. The needle was thereby submerged in the assembly solution. After nanoprecipitation, the solutions were dialyzed against water with 5 bath changes every min. 4 h. The particles were stored in aqueous solutions.

Scanning electron microscopy

The data was provided by Marcel Schumacher from the University of Münster.

7. DISCUSSION

This chapter is intended to emphasize the red thread of this work, by summarizing the outcomes of the published and unpublished results presented before. Therefore, each chapter will be recapped in an adequate place and the importance in the context of this thesis will be outlined.

7.1. COMPUTATIONAL MODELING OF CES

The system developed for selective Li extraction from aqueous environments combines two components: a functionalizable polymer matrix and an active CE component. Preliminary work by I. Oral revealed a strong correlation between the efficiency and selectivity of CE-Li binding and the size, i.e., the size of the CE, its hydrophobicity, and the donor atoms included.[62,66] Publication 1 takes up this finding and goes one step further. Targeted structural modifications are discussed with the aim of improving Li complexation, particularly with regard to the highly competitive magnesium ion. To recap: With a similar ionic radius but a divalent charge, the electron density of the magnesium ion is higher than that of the Li ion and thus the strength of the electrostatic interactions with classical CEs.

The synthesis of CEs can be time-consuming and resource-intensive. This is especially the case when no synthesis protocols have been developed so far. In addition, the lack of toxicological characterization of CEs makes it difficult to assess potential hazards. This is particularly concerning given that a potential benefit for Li extraction does not necessarily arise. Molecular structure calculations provide a valuable opportunity to evaluate molecular properties theoretically in advance without the need for tedious synthesis procedures. Moreover, these enable deep insight into structure-function relationships, charge distributions, thermodynamic parameters, spectroscopic and other properties. In publication 1, molecular structure optimizations were performed based on density functional theory.

As part of these calculations, benzo-CEs of various sizes (9-, 12-, and 15-membered) were modeled. In addition to fully oxygen-containing CEs, one donor atom was specifically replaced by nitrogen or sulfur in each case to determine the electronic and structural effects of this substitution. Based on the HSAB principle, donor atoms with a larger radius and polarizability (O < N < S) represent softer Lewis bases, resulting in a more favorable interaction with softer Lewis acids. The structures are shown in Figure 39.

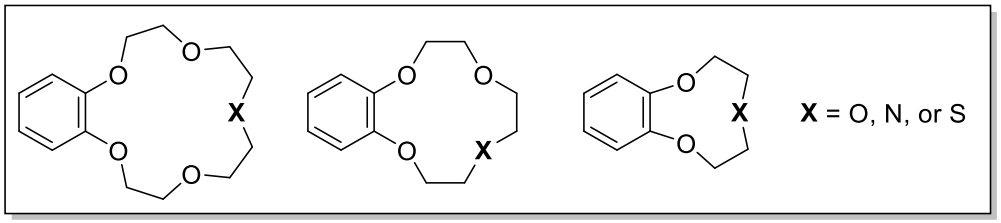

Figure 39: Overview of crown ether structures with different donor atoms and cavity sizes.

The complex formation of the modeled CEs with ions typical for seawater (Li^+, Na^+, K^+, Mg^{2+}, and Ca^{2+}) was systematically investigated. The charge distribution within the complexes was estimated by Hirshfeld population analysis and NBO analysis. These were supplemented by frequency calculations of the systems in vacuum and solution. Of special interest is the 15-membered *thio*-CE, which exhibited increased selectivity towards Li compared to magnesium. To validate the theoretical results, an extraction experiment with *aza*-15-crown-5 in a DCM/water mixture was performed, confirming the applicability of DFT studies in this context. The results showed promising predictions by computer-assisted simulations as a strategic tool for reducing experimental effort in CE synthesis. These findings become relevant further in publication 3 as a supporting tool in the explanation of the different complexation behaviors of CEs.

Publication 1 focused on ML type complexation, ML_2 complexes were not investigated at this stage. However, this was changed in publications 2 and 3 and is notably relevant in the application of a polymer matrix.

7.2. CE-POLYMERS IN SOLUTION

Within the context of application technology, the use of a matrix for immobilizing the CEs in solution is essential to ensure manageability and recovery of the complexes that are formed. In this work, an amphiphilic block copolymer (PS-*b*-PMAA) was utilized, whose hydrophilic block offers the possibility of functionalization. In previous work, a PS-*b*-P(MAA-*r*-CEXMA) with X as B9C3 was employed, which showed excellent Li selectivity over other alkali metal ions. In fact, Li complexation was increased by several orders of magnitude compared to free CEs. This was attributed to the initially reduced degrees of freedom of the matrix-bound CE and the associated lower entropy decrease during complex formation in an ML_2 type.

Publication 2 further increases the efficiency of the system—not only scientifically, but also in terms of large-scale applicability. In this publication, a systematic variation of the polymer-CE system was carried out and the influences of these variations were quantified. The focus was on three parameters: the total degree of polymerization (i.e., the molecular weight of the polymer), the length of the hydrophobic PS segment with a constant hydrophilic block, and the

density of the CE functionalization. Analogous to the preliminary work, the behavior of the polymers was examined in a two-phase mixture of DCM and aqueous salt solution.

The key findings of this section are as follows: A high molecular weight (up to 310 kDa), a low proportion of the hydrophilic block (8wt% PMAA), and a high functionalization of the PMAA block with the CE (72%) were beneficial for the Li uptake of the material. DLS measurements and DOSY-NMR measurements also revealed a strong preference for intramolecular interactions between the chains. Li complexation improves with increasing molecular weight, as the entropy loss during the formation of ML_2 complexes decreases relatively for longer chains. In addition, the increased flexibility of the longer chains enables a more efficient intramolecular approximation of distant CEs. The high complex stability based on small PS blocks can be attributed to the different solubility behavior of the blocks in DCM. PS exhibits an increased affinity to DCM, while PMAA exhibits an increased affinity to water. With increasing PS content, the solubility changes accordingly, particularly at the decisive phase interface. With high functionalization, complex formation increases, firstly because the probability of spatial proximity between two CEs is higher and secondly because the loss of conformational entropy (with constant enthalpy gain and loss in translational entropy) per newly formed ML_2 becomes relatively smaller. This effect becomes increasingly pronounced with increasing functionalization.

In combination with these optimized parameters, the material exhibited exceptionally high Li complexation, which outperformed all previously compared materials.

7.3. CE-POLYMERS IN SOLID-STATE

Since the use of large quantities of organic solvents is not feasible on an industrial scale, it was necessary to shift the material's application range from solution to solid-state. This type of system requires a large active surface area to ensure efficient interaction between the material and its environment. For this purpose, three processing forms with a large surface-to-volume ratio were considered: membranes, cubosomes, and electrospun fibers. The starting point for these three methods is a solution of the polymer in an organic solvent, whose block affinities are intended to contribute to the efficient self-assembly of the block copolymer.

The production of membranes using the SNIPS process and the production of cubosomes via nanoprecipitation have several similarities. Nanostructured materials are produced through controlled self-assembly and subsequent phase separation. Both processes are based on a bottom-up approach to the production of nanostructures without mechanical comminution. The resulting structure is fixed by solvent-non-solvent exchange. In this work, cubosomes were successfully produced from B9C3-functionalized polymers, with the yield still having potential

at a maximum of 200 mg cubosomes per batch. Following the successful production of PS-b-PMAA membranes, the production of B9C3 or B12C4 functionalized membranes still presents a challenge – self-assembly appears to be significantly disrupted by the introduction of aromatic CEs.

The most promising and successful approach in this work was reported in publication 3, the production of electrospun fibers from functionalized polymers. The implementation of B9C3, B12C4, and 12C4-functionalized polymers was straightforward and feasible on a large scale. The fine fibers (approx. 1000 nm) produced from a polymer solution spun in a high-voltage field additionally demonstrated the ability to complex Li. In particular, the B12C4-based polymer exhibited a high Li capacity with optimal selectivity towards sodium. This leads to the conclusion that ML-type complexation is clearly preferred over ML_2 complexation in the solid state. It was therefore possible to enable effective Li complexation in the presence of competing sodium ions in a form relevant to application technology—electrospun fibers. In addition, the suitability of 12-membered CEs in this context was demonstrated, a very interesting deviation from the behavior in solution, in which both free and matrix-bound ML_2 complexes are primarily formed.

These promising results open up prospects for further research approaches, which are outlined in the next section.

7.4. OUTLOOK

The amphiphilic diblock copolymer presented in this work showed promising results as a matrix for the CE-based system for Li extraction from seawater. At the same time, it is conceivable that this matrix could be further optimized.

One possibility for this could be the substitution of the MAA block with a polymeric amine, such as polyallylamine. This would enable subsequent conversion with an acid-functionalized CE—which has already been successfully produced by Marc Weber in his bachelor's thesis under my guidance—to form an amide group. Compared to esters, amides have the advantage of increased temperature and hydrolysis resistance. This would significantly increase the range of applications for the material.

Furthermore, the polymer backbone could be varied to such an extent that the self-assembly of the blocks in solution is less restricted. One way of achieving this would be to produce PS-*b*-PMCEXMA-*b*-PMAA triblock copolymers. For this purpose, the MAA monomer could be functionalized prior to polymerization. Subsequent sequential polymerization would result in a triblock copolymer with defined blocks. An advantage of this system would be the gradual increase in the hydrophilicity of the system along the chain, which could support self-assembly.

Another possibility for supportive self-organization is the synthesis of so-called asymmetric bottle-brush polymers. These structures are known to promote slow self-assembly, especially at high molecular weights, by counteracting strong tangling due to the side chains.[193,194] Here, the PS block could be present as a long unbranched block—thus representing the “grip” of the brushes—whereas the hydrophilic, active part occurs as an accumulation of short-chain dense side chains—analogous to the "brushes". The self-assembly of such a polymer has been described in works by Liberman *et al.*[193] and is schematically represented in Figure 40.

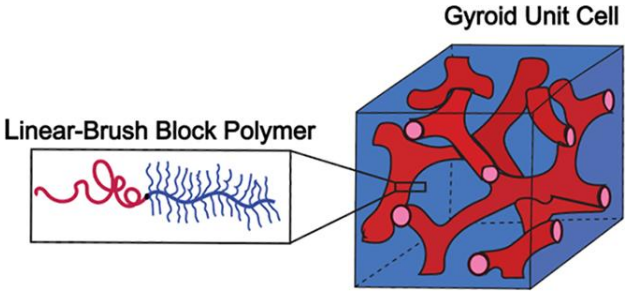

Figure 40: Formation of a gyroid structure by self-assembly of a linear bottle-brush polymer. Reprinted with permission from Ref. [193]. Copyright 2022 American Chemical Society.

The membrane formation of the unfunctionalized diblock polymers was successful. In order to circumvent the challenge of the disturbed self-organization of functionalized polymers, a post-modification approach could also be chosen. Since the membrane structure remains stable in aqueous solution, post-modification could take place using an esterification method that is feasible in water (e.g., Steglich esterification). A prerequisite for this would be the use of water-soluble CEs such as hydroxy-functionalized 12-crown-4.

Another interesting area of research would be the formation of a CE-based hydrogel. Hydrogels are three-dimensional, water-rich polymer networks. The formation of network points could be achieved by targeted modification of the polymer matrix, for example by introducing graft polymers. Polymers such as P(NIPAM) or chitosan are known for the formation of hydrogels and therefore represent a potential starting point for the development of (stimulus-responsive) systems. In fact, the ongoing research by Amrei Gouby (from our working group) is targeting this aspect. Furthermore, network formation might also be controlled via CE complexes. For example, ML_2 complexes with targeted complexation of Li could function as reversible cross-linking units. In such a system, the water-soluble polymer would transition to a gel-like state once Li ions are present, whereby the chains would be interconnected via the formation of CE-Li complexes. The gel could subsequently be recovered from the aqueous medium.

The controlled release of Li ions from the complex system is another relevant aspect of future research. Photochemical, thermal, or charge-induced stimuli appear promising for targeted decomplexation. Of particular interest in this context is the possible integration of an *aza*-CE, whose structure allows for phase-dependent charge modulation. Targeted protonation within

the ring system could induce a positive charge, destabilizing the Li bond and thus enabling its release.

Overall, despite the already highly satisfactory and encouraging results, the subject addressed in this work opens up a wide range of further intriguing questions that can serve as a starting point for additional research.

8. REFERENCES

1. Meyer, H.-J. *Allgemeine Und Anorganische Chemie*. *Allgemeine und Anorganische Chemie* (Walter de Gruyter GmbH, Berlin/Boston, 2024, p. 8, 63, 27–248). doi:10.3813/9783777632797.

2. Balaram, V., Santosh, M., Satyanarayanan, M., Srinivas, N. & Gupta, H. Lithium: A review of applications, occurrence, exploration, extraction, recycling, analysis, and environmental impact. *Geosci. Front.* **15**, 101868 (2024).

3. Reich, R., Slunitschek, K., Danisi, R. M., Eiche, E. & Kolb, J. Lithium Extraction Techniques and the Application Potential of Different Sorbents for Lithium Recovery from Brines. *Miner. Process. Extr. Metall. Rev.* **44**, 261–280 (2023).

4. Jose, S. A. *et al.* Critical Review of Lithium Recovery Methods: Advancements, Challenges, and Future Directions. *Processes* **12**, 2203 (2024).

5. Luong, J. H. T., Tran, C. & Ton-That, D. A Paradox over Electric Vehicles, Mining of Lithium for Car Batteries. *Energies* **15**, 1–25 (2022).

6. Cheng, Q. *et al.* High specific surface crown ether modified chitosan nanofiber membrane by low-temperature phase separation for efficient selective adsorption of lithium. *Sep. Purif. Technol.* **262**, 118312 (2021).

7. Lindagato, P. *et al.* applied sciences Lithium Metal : The Key to Green Transportation. *Appl. Sci.* **13**, 405 (2023).

8. Baudino, L., Santos, C., Pirri, C. F., La Mantia, F. & Lamberti, A. Recent Advances in the Lithium Recovery from Water Resources: From Passive to Electrochemical Methods. *Adv. Sci.* **9**, 2201380 (2022).

9. U.S. Geological Survey. *Mineral Commodities Summaries 2024*. *U.S. Government Publishing Office: U.S. Geological Survey* http://pubs.er.usgs.gov/publication/mcs2023 (2023).

10. U.S. Geological Survey. *Mineral Commodity Summaries 2022*. *U.S. Government Publishing Office: U.S. Geological Survey* https://pubs.usgs.gov/periodicals/mcs2022/mcs2022-zeolites.pdf (2022).

11. Tabelin, C. B. *et al.* Towards a low-carbon society: A review of lithium resource availability, challenges and innovations in mining, extraction and recycling, and future perspectives. *Miner. Eng.* **163**, 106743 (2021).

12. Yang, S., Zhang, F., Ding, H., He, P. & Zhou, H. Lithium Metal Extraction from Seawater. *Joule* **2**, 1648–1651 (2018).

13. Krishnan, R. & Gopan, G. A comprehensive review of lithium extraction: From historical perspectives to emerging technologies, storage, and environmental considerations. *Clean. Eng. Technol.* **20**, 100749 (2024).

14. Hahn, T. & Behruzi, M. Lithium-Aluminium-Silikate und -Germanate. in *Kristallchemie, Strukturen und Phasenumwandlungen von Silikaten, Germanaten und Boraten* 5–29 (VS Verlag für Sozialwissenschaften, Wiesbaden, 1981). doi:10.1007/978-3-322-87525-9_2.

15. Lin, B., Rustamov, I., Zhang, L., Luo, J. & Wan, X. Graphene-reinforced lithium grease for antifriction and antiwear. *ACS Appl. Nano Mater.* **3**, 10508–10521 (2020).

16. Åkröm, H. & Höglund, E. Rheological properties of lithium, lithium complex, and sodium greases. *J. Synth. Lubr.* **10**, 225–236 (1993).

17. Adhvaryu, A., Sung, C. & Erhan, S. Z. Fatty acids and antioxidant effects on grease microstructures. *Ind. Crops Prod.* **21**, 285–291 (2005).

18. Wen, X. *et al.* A novel strategy for promoting corrosion and wear resistance of Mg-Li alloys: Gradient eutectic high-entropy alloy coating induced by in-situ bidirectional diffusion. *J. Magnes. Alloy.* 1–16 (2023) doi:10.1016/j.jma.2023.09.019.

19. Ochoa, E. L. M. Lithium as a Neuroprotective Agent for Bipolar Disorder: An Overview. *Cell. Mol. Neurobiol.* **42**, 85–97 (2022).

20. Patel, N. C. *et al.* Open-label lithium for the treatment of adolescents with bipolar depression. *J. Am. Acad. Child Adolesc. Psychiatry* **45**, 289–297 (2006).

21. Riedel, E. & Meyer, H.-J. *Allgemeine Und Anorganische Chemie*. (De Gruyter, Berlin, Boston, 2019, p. 74–76, 166, 199–200).

22. Teng, F.-Z. *et al.* Lithium isotopic composition and concentration of the upper continental crust. *Geochim. Cosmochim. Acta* **68**, 4167–4178 (2004).

23. Vega-muratalla, V. O. Review of Lithium as a Strategic Resource for Electric Vehicle Battery Production : Availability , Extraction , and Future Prospects. *Resources* **13**, 148 (2024).

24. Rentier, E. S., Hoorn, C. & Seijmonsbergen, A. C. Lithium brine mining affects geodiversity and Sustainable Development Goals. *Renew. Sustain. Energy Rev.* **202**, 114642 (2024).

25. Wu, Y. *et al.* Impact of circular economy on the long-term allocation structure of primary and secondary lithium. *Commun. Earth Environ.* **5**, 503 (2024).

26. Graham, J. D., Rupp, J. A. & Brungard, E. Lithium in the green energy transition: The quest for both sustainability and security. *Sustain.* **13**, 11274 (2021).

27. Sahoo, S. K. *et al.* Beneficiation of lithium bearing pegmatite rock: a review. *Miner. Process. Extr. Metall. Rev.* **45**, 1–27 (2024).

28. Khakmardan, S., Werner, T. T., Crawford, R. & Li, W. Reevaluating the Land Use Impact of a Li-ion Battery Related Mining Project, A Case Study of Greenbushes Mine. *Procedia CIRP* **122**, 1030–1035 (2024).

29. Kesler, S. E. *et al.* Global lithium resources: Relative importance of pegmatite, brine and other deposits. *Ore Geol. Rev.* **48**, 55–69 (2012).

30. Dessemond, C., Lajoie-Leroux, F., Soucy, G., Laroche, N. & Magnan, J.-F. Spodumene: The Lithium Market, Resources and Processes. *Minerals* **9**, 334 (2019).

31. Liu, Y., Ma, B., Lü, Y., Wang, C. & Chen, Y. A review of lithium extraction from natural resources. *Int. J. Miner. Metall. Mater.* **30**, 209–224 (2023).

32. Rabe, B. A., Ravenelle, R. M. & Leblanc, R. US 2022/0220578 A1. (2022).

33. Swain, B. Separation and purification of lithium by solvent extraction and supported liquid membrane, analysis of their mechanism: a review. *J. Chem. Technol. Biotechnol.* **91**, 2549–2562 (2016).

34. Maisel, F., Neef, C., Marscheider-Weidemann, F. & Nissen, N. F. A forecast on future raw material demand and recycling potential of lithium-ion batteries in electric vehicles. *Resour. Conserv. Recycl.* **192**, 106920 (2023).

35. Zeng, X., Li, J. & Singh, N. Recycling of Spent Lithium-Ion Battery: A Critical Review. *Crit. Rev. Environ. Sci. Technol.* **44**, 1129–1165 (2014).

36. Yu, H. *et al.* Metal-based adsorbents for lithium recovery from aqueous resources.

Desalination **539**, 115951 (2022).

37. Zhao, J., Fan, R., Xiang, S., Hu, J. & Zheng, X. Preparation and Lithium-Ion Separation Property of ZIF-8 Membrane with Excellent Flexibility. *Membranes (Basel).* **13**, 500 (2023).

38. Long, F. *et al.* Performance of functionalized UIO-66 and HKUST-1 for Li+ absorption and separation from aqueous solutions with Li+. *Inorg. Chem. Commun.* **181**, 115169 (2025).

39. Pei, H. *et al.* In situ one-pot formation of crown ether functionalized polysulfone membranes for highly efficient lithium isotope adsorptive separation. *Eur. Polym. J.* **109**, 288–296 (2018).

40. Huang, W., Liu, S., Liu, J., Zhang, W. & Pan, J. 2-Methylol-12-crown-4 ether immobilized PolyHIPEs toward recovery of lithium(I). *New J. Chem.* **42**, 16814–16822 (2018).

41. Qi, D. *et al.* Synthesis of lithium ion-imprinted polymers for selective recovery of lithium ions from salt lake brines. *Sep. Purif. Technol.* **340**, 126661 (2024).

42. Liu, S. *et al.* In-situ pH regulation of biomass-based hydrogel composite: A green approach to efficient lithium ion capture from salt lake brine. *Chem. Eng. J.* **523**, 168426 (2025).

43. Vögtle, F. *Supramolekulare Chemie*. (Teubner Studienbücher Chemie, Stuttgart, 1992, p. 33, 45–54, 57- 64,179). doi:10.1007/978-3-322-94013-1.

44. Pedersen, C. J. Cyclic Polyethers and Their Complexes with Metal Salts. *J. Am. Chem. Soc.* **89**, 7017–7036 (1967).

45. Paul D. Beer, Barendt, T. A. & Lim, J. Y. C. *Supramolecular Chemistry*. (Oxford University Press, Oxford, 2022, p. 1–12).

46. Gokel, G. W. *Cation Binding by Crown Ethers*. *Comprehensive Supramolecular Chemistry II* (Elsevier, 2013, p. 203–216). doi:10.1016/B978-0-12-409547-2.05615-8.

47. Weber, E. *Crown Ethers*. *Ullmann's Encyclopedia of Industrial Chemistry* (Wiley-VCH Verlag GmbH & Co. KGaA, Weinheim, Germany, 2007, p. 471–478). doi:10.1002/14356007.a08_091.pub2.

48. Izatt, R. M. *et al.* Thermodynamic and Kinetic Data for Cation-Macrocycle Interaction. *Chem. Rev.* **85**, 271–339 (1985).

49. Mathias, L. J. Crown Ethers and Phase Transfer Catalysis in Polymer Chemistry. *J. Macromol. Sci.* **15**, 853–876 (1981).

50. Pei, H., Yan, F., Liu, H., He, B. & Li, J. The selective complexation of crown ethers for lithium isotope separation: A critical review. *Sep. Purif. Technol.* **341**, 126857 (2024).

51. Chen, S., Yuan, H., Grinberg, N., Dovletoglou, A. & Bicker, G. Enantiomeric Separation of trans-2- Aminocyclohexanol on a Crown Ether Stationary Phase Using Evaporative Light Scattering Detection S. *J. Liq. Chromatogr. Relat. Technol.* **26**, 425–442 (2003).

52. Pyta, K., Przybylski, P. & Bartl, F. Regioselective Long-Range Proton Transfer in New Rifamycin Antibiotics: A Process in which Crown Ethers Act as Stronger Brønsted Bases than Amines. *ChemPhysChem* **16**, 938–942 (2015).

53. Kralj, M., Tušek-Božić, L. & Frkanec, L. Biomedical Potentials of Crown Ethers: Prospective Antitumor Agents. *ChemMedChem* **3**, 1478–1492 (2008).

54. Cazacu, A., Tong, C., Van Der Lee, A., Fyles, T. M. & Barboiu, M. Columnar self-

assembled ureido crown ethers: An example of ion-channel organization in lipid bilayers. *J. Am. Chem. Soc.* **128**, 9541–9548 (2006).

55. Liu, J. *et al.* Ion-Selective Micropipette Sensor for In Vivo Monitoring of Sodium Ion with Crown Ether-Encapsulated Metal-Organic Framework Subnanopores. *Anal. Chem.* **96**, 2651–2657 (2024).

56. Ranno, L. *et al.* Crown ether decorated silicon photonics for safeguarding against lead poisoning. *Nat. Commun.* **15**, 3820 (2024).

57. Takagi, M. & Nakamura, H. *Analytical Application of Functionalized Crown Ether - Metal Complexes*. *Journal of Coordination Chemistry* vol. 15 (1986, p. 53–82).

58. Ge, M., Wei, C., Fang, T. & Liu, X. Molecular insight into the separation mechanism of crown Ether-Based channels for lithium Extraction. *Sep. Purif. Technol.* **338**, 126415 (2024).

59. Baudino, L. *et al.* Crown-Ether Functionalized Graphene Oxide Membrane for Lithium Recovery from Water. *Membranes (Basel).* **12**, 1–12 (2022).

60. Muñoz, S. *et al.* Ultrathin Monolayer Lipid Membranes from a New Family of Crown Ether-Based Bola-Amphiphiles. *J. Am. Chem. Soc.* **115**, 1705–1711 (1993).

61. Oral, I., Tamm, S., Herrmann, C. & Abetz, V. Lithium Selectivity of Crown Ethers: The Effect of Heteroatoms and Cavity Size. *Sep. Purif. Technol.* **294**, 121142 (2022).

62. Oral, I. & Abetz, V. Improved alkali metal ion capturing utilizing crown ether-based diblock copolymers in a sandwich-type complexation. *Soft Matter* **18**, 934–937 (2022).

63. Boda, A., Ali, S. M., Shenoi, M. R. K., Rao, H. & Ghosh, S. K. DFT modeling on the suitable crown ether architecture for complexation with Cs+ and Sr2+ metal ions. *J. Mol. Model.* **17**, 1091–1108 (2011).

64. Behjatmanesh-Ardakani, R. DFT-B3LYP and SMD study on the interactions between aza-, diaza-, and triaza-12-crown-4 (A n -12-crown-4, n = 1, 2, 3) with Na+ in the gas phase and acetonitrile solution. *Struct. Chem.* **25**, 919–929 (2014).

65. Steed, J. W. First- and second-sphere coordination chemistry of alkali metal crown ether complexes. *Coord. Chem. Rev.* **215**, 171–221 (2001).

66. Oral, I. Dissertation Iklima Oral. (University of Hamburg, 2022).

67. Shamov, G. A. & Schreckenbach, G. The role of peripheral alkyl substituents: A theoretical study of substituted and unsubstituted uranyl isoamethyrin complexes. *Inorg. Chem.* **47**, 805–811 (2008).

68. Bartsch, R. A. *et al.* Influence of ring substituents and matrix on lithium / sodium selectivity of 14-crown-4 and benzo-13-crown-4-compounds. *Anal. Chim. Acta* **272**, 285–292 (1993).

69. Torrejos, R. E. C. *et al.* Design of lithium selective crown ethers: Synthesis, extraction and theoretical binding studies. *Chem. Eng. J.* **326**, 921–933 (2017).

70. Kobiro, K. New class of lithium ion selective crown ethers with bulky decalin subunits. *Coord. Chem. Rev.* **148**, 135–149 (1996).

71. Oral, I. & Abetz, V. A Highly Selective Polymer Material using Benzo-9-Crown-3 for the Extraction of Lithium in Presence of Other Interfering Alkali Metal Ions. *Macromol. Rapid Commun.* **42**, 2000746 (2021).

72. Kim, J., Shamsipur, M., Huang, S. Z., Huang, R. H. & Dye, J. L. Sandwich and Mixed Sandwich Complexes of the Cesium Ion with Crown Ethers in Nitromethane. *J. Phys. Chem. A* **103**, 5615–5620 (1999).

73. Shannon, R. D. Revised effective ionic radii and systematic studies of interatomic distances in halides and chalcogenides. *Acta Crystallogr. Sect. A* **32**, 751–767 (1976).

74. Measures, C. I. & Edmond, J. M. Determination of beryllium in natural waters in real time using electron capture detection gas chromatography. *Anal. Chem.* **58**, 2065–2069 (1986).

75. Jabbari, A. & Shamsipur, M. Spectroscopic study of some alkali and alkaline earth complexes with benzo crown ethers in ethanol solution. *Spectrosc. Lett.* **26**, 1715–1724 (1993).

76. Torrejos, R. E. C. *et al.* Aqueous Synthesis of 14-15-Membered Crown Ethers with Mixed O, N and S Heteroatoms: Experimental and Theoretical Binding Studies with Platinum-Group Metals. *Chempluschem* **84**, 210–221 (2019).

77. Alexandratos, S. D. & Stine, C. L. Synthesis of ion-selective polymer-supported crown ethers: a review. *React. Funct. Polym.* **60**, 3–16 (2004).

78. Olsher, U., Hankins, M. G., Kim, Y. D. & Bartsch, R. A. Anion Effect on Selectivity in Crown Ether Extraction of Alkali Metal Cations. *J. Am. Chem. Soc.* **115**, 3370–3371 (1993).

79. Schultz, R. A., White, B. D., Dishong, D. M., Arnold, K. A. & Gokel, G. W. 12-, 15-, and 18-Membered-ring nitrogen-pivot lariat ethers: syntheses, properties, and sodium and ammonium cation binding properties. *J. Am. Chem. Soc.* **107**, 6659–6668 (1985).

80. Wakita, R., Yonetani, M., Nakatsuji, Y. & Okahara, M. C-pivot lariat ethers bearing an electron-donating side arm as lithium cation selective extractants. *J. Org. Chem.* **55**, 2752–2756 (1990).

81. Gokel, G. W. Complexation by Crowns and Cryptands. in *Crown Ethers and Cryptands* (ed. J. F. Stoddart) 64–98 (The Royal Society of Chemistry, 1991). doi:10.1039/9781788010917-00064.

82. Wang, Q., Wang, X. & Li, L. Density functional theory study on a fluorescent chemosensor device of aza-crown ether. *J. Phys. Org. Chem.* **27**, 546–554 (2014).

83. Kanagasundaram, T., Murphy, O., Haji, M. N. & Wilson, J. J. The recovery and separation of lithium by using solvent extraction methods. *Coord. Chem. Rev.* **509**, 215727 (2024).

84. Bey, A., Dreyer, O. & Abetz, V. Thermodynamic analysis of alkali metal complex formation of polymer-bonded crown ether. *Phys. Chem. Chem. Phys.* **19**, 15924–15932 (2017).

85. Bechmann, W. & Bald, I. *Einstieg in Die Physikalische Chemie Für Naturwissenschaftler*. (Springer Spektrum, Berlin, Heidelberg, 2020, p. 140, 164). doi:10.1007/978-3-662-62034-2.

86. Job, G. & Rüffler, R. *Physikalische Chemie*. (Springer Spektrum, Hamburg, 2021, p. 525).

87. Solomon, T. The Definition and Unit of Ionic Strength. *J. Chem. Educ.* **78**, 1691 (2001).

88. Lechner, M. D. *Einführung in Die Quantenchemie*. (Springer, Berlin, Heidelberg, 2017, p. 85).

89. Bai, X., Dai, J., Ma, Y., Bian, W. & Pan, J. 2-(Allyloxy) methylol-12-crown-4 ether functionalized polymer brushes from porous PolyHIPE using UV-initiated surface polymerization for recognition and recovery of lithium. *Chem. Eng. J.* **380**, 122386 (2020).

90. Liberati, A. F. *et al.* Synthesis, characterization and Li adsorption study of a new thermoresponsive crown-ether bearing copolymer. *Sep. Purif. Technol.* **354**, 129123 (2025).

91. Zülicke, L. *Molekulare Theoretische Chemie*. *Molekulare Theoretische Chemie* (Springer Fachmedien Wiesbaden, Wiesbaden, 2015, p. 6,154-156, 167–169, 386–405, 421, 444–449, 836–838). doi:10.1007/978-3-658-00489-7.

92. Alizadeh, N. A comparison of complexation of Li+ ion with macrocyclic ligands 15-crown-5 and 12-crown-4 in binary nitromethane-acetonitrile mixtures by using lithium-7 NMR technique and ab initio calculation. *Spectrochim. Acta - Part A Mol. Biomol. Spectrosc.* **78**, 488–493 (2011).

93. Arif, A. M., Yousaf, A., Xu, H. liang & Su, Z. M. N-(O-methoxyphenyl)aza-15-crown-5-ether derivatives: Highly efficient and wide range nonlinear optical response based cation recognition. *J. Mol. Liq.* **301**, 22–24 (2020).

94. Martínez-Haya, B. *et al.* Emergence of symmetry and chirality in crown ether complexes with alkali metal cations. *J. Phys. Chem. A* **114**, 7048–7054 (2010).

95. Sun, Y. *et al.* A novel approach for the selective extraction of Li + from the leaching solution of spent lithium-ion batteries using benzo-15-crown-5 ether as extractant. *Sep. Purif. Technol.* **237**, 116325 (2020).

96. Püschner, D. *Quantitative Rechenverfahren Der Theoretischen Chemie*. (Springer Spektrum, Wiesbaden, 2017, p. 1–3, 13–16, 43–53).

97. Reinhold, J. *Quantentheorie Der Moleküle*. (Springer Spektrum, Wiesbaden, 2013, p. 42, 51–52, 59–62, 79–80, 119–121, 223–225, 233–235).

98. Lewars, E. G. *Computational Chemistry*. (Springer International Publishing, Cham, 2024, p. 493, 497–499). doi:10.1007/978-3-031-51443-2.

99. Koch, W. & Holthausen, M. C. *A Chemist 's Guide to Density Functional Theory*. (WILEY-VCH, Weinheim, 2001, p. 43–47).

100. Kohanoff, J. & Gidopoulos, N. I. Density Functional Theory: Basics, New Trends and Applications. in *Handbook of Molecular Physics and Quantum Chemistry* vol. 2 532–568 (John Wiley & Sons, Ltd, Chichester, 2003).

101. Jacob, C. R. & Reiher, M. Spin in density-functional theory. *Int. J. Quantum Chem.* **112**, 3661–3684 (2012).

102. Hohenberg, P. & Kohn, W. Inhomogeneous Electron Gas. *Phys. Rev.* **136**, 864–871 (1964).

103. Kunz, R. W. *Molecular Modelling Für Anwender*. (Teubner Studienbücher Chemie, Stuttgart, 1997, p. 16–17, 52–55, 58–60, 65, 198).

104. Mardirossian, N. & Head-Gordon, M. Thirty years of density functional theory in computational chemistry: an overview and extensive assessment of 200 density functionals. *Mol. Phys.* **115**, 2315–2372 (2017).

105. Sousa, S. F., Fernandes, P. A. & Ramos, M. J. General Performance of Density Functionals. *J. Phys. Chem. A* **111**, 10439–10452 (2007).

106. Perdew, J. P. Jacob's ladder of density functional approximations for the exchange-correlation energy. in *AIP Conference Proceedings* vol. 577 1–20 (AIP, 2001).

107. Woods, N. On the Nature of Self-Consistency in Density Functional Theory. *PhD thesis* (Clare College, 2018, p. 15,16).

108. Gomes, J. R. B. *et al.* Density functional treatment of interactions and chemical

reactions at interfaces. *Density Funct. Theory Princ. Appl. Anal.* 1–58 (2013).

109. Becke, A. D. Perspective: Fifty years of density-functional theory in chemical physics. *J. Chem. Phys.* **140**, 18A301 (2014).

110. Jensen, F. *Introduction to Computational Chemistry*. (John Wiley & Sons, Chichester, Hoboken, 2017, p. 88–89, 189–204, 233–236, 284, 323–328, 333–337).

111. Weigend, F. Accurate Coulomb-fitting basis sets for H to Rn w. *Phys. Chem. Chem. Phys.* **8**, 1057–1065 (2006).

112. Weigend, F. & Ahlrichs, R. Balanced basis sets of split valence, triple zeta valence and quadruple zeta valence quality for H to Rn: Design and assessment of accuracy. *Phys. Chem. Chem. Phys.* **7**, 3297–3305 (2005).

113. Morrow, Z., Kwon, H.-Y., Kelley, C. T. & Jakubikova, E. Efficient Approximation of Potential Energy Surfaces with Mixed-Basis Interpolation. *J. Chem. Theory Comput.* **17**, 5673–5683 (2021).

114. Schlegel, H. B. Geometry optimization. *Wiley Interdiscip. Rev. Comput. Mol. Sci.* **1**, 790–809 (2011).

115. Reveles, J. U. & Köster, A. M. Geometry optimization in density functional methods. *J. Comput. Chem.* **25**, 1109–1116 (2004).

116. Höltje, H.-D., Sippl, W., Rognan, D. & Folkers, G. *Molecular Modeling*. (Wiley-VCH Verlag GmbH & Co. KGaA, Weinheim, Germany, 2003, p. 18–22).

117. Tomasi, J., Mennucci, B. & Cammi, R. Quantum Mechanical Continuum Solvation Models. *Chem. Rev.* **105**, 2999–3093 (2005).

118. Cossi, M. *et al.* Molecules in Solution with the C-PCM Solvation Model. *J. Comput. Chem.* **24**, 670–681 (2003).

119. Lange, A. W. & Herbert, J. M. A simple polarizable continuum solvation model for electrolyte solutions. *J. Chem. Phys.* **134**, 204110 (2011).

120. Mulliken, R. S. Electronic population analysis on LCAO-MO molecular wave functions. I. *J. Chem. Phys.* **23**, 1833–1840 (1955).

121. Löwdin, P.-O. On the Non-Orthogonality Problem Connected with the Use of Atomic Wave Functions in the Theory of Molecules and Crystals. *J. Chem. Phys.* **18**, 365–375 (1950).

122. Davidson, E. R. & Chakravorty, S. A test of the Hirshfeld definition of atomic charges and moments. *Theor. Chim. Acta* **83**, 319–330 (1992).

123. Hirshfeld, F. L. Bonded-Atom Fragments for Describing Molecular Charge Densities. *Theor. Claim. Acta* **44**, 129–138 (1977).

124. Zhou, X. Y., Rong, C. Y., Lu, T. & Liu, S. Bin. Hirshfeld Charge as a Quantitative Measure of Electrophilicity and Nucleophilicity: nucleophilicity: Nitrogen-Containing Systems. *Wuli Huaxue Xuebao/ Acta Phys. - Chim. Sin.* **30**, 2055–2062 (2014).

125. Reed, A. E., Curtiss, L. A. & Weinhold, F. Intermolecular Interactions from a Natural Bond Orbital , Donor-Acceptor Viewpoint. *Chem. Rev.* **88**, 899–926 (1988).

126. Weinhold, F. & Landis, C. R. Natural Bond Orbitals and Extensions of Localized Bonding Concepts. *Chem. Educ. Res. Pr.* **2**, 91–104 (2001).

127. Raupach, M. Quantenchemische Untersuchungen zur chemischen Bindung an Oberflächen. (Philipps-Universität Marburg, 2015, p. 2, 23–24).

128. Larder, R. Synthesis and Application of P4VP Based Block Copolymers from Supercritical CO 2. (University of Nottingham, 2021).

129. Koltzenburg. *Synthese, Eigenschaften Und Anwendungen Koltzenburg. 2014. Polymere* -. (Springer, Berlin, Heidelberg, 2012, p. 31–45, 66, 243–251, 277–279, 397–401, 424–429).

130. Young, R. J. & Lovell, P. A. *Introduction to Polymers*. (Taylor & Francis Group, Boca Raton, 2011, p. 6–9, 15–30, 91–118, 220–223, 237–245).

131. Tieke, B. *Makromolekulare Chemie - Eine Einführung*. (WILEY-VCH, Weinheim, 2014, p. 60–86, 157–159, 257–267).

132. Hawker, C. J. “Living” Free Radical Polymerization: A Unique Technique for the Preparation of Controlled Macromolecular Architectures. *Acc. Chem. Res.* **30**, 373–382 (1997).

133. Chiefari, J. *et al.* Living Free-Radical Polymerization by Reversible Addition-Fragmentation Chain Transfer: The RAFT Process. *Macromolecules* **31**, 5559–5562 (1998).

134. Perrier, S. 50th Anniversary Perspective: RAFT Polymerization - A User Guide. *Macromolecules* **50**, 7433–7447 (2017).

135. Beres, M. A., Rho, J. Y., Kerr, A., Smith, T. & Perrier, S. Photoiniferter-RAFT polymerization mediated by bis(trithiocarbonate) disulfides. *Polym. Chem.* **15**, 522–533 (2024).

136. Zhu, Q. *et al.* A highly-efficient lithium adsorptive separation membrane derived from a polyimide-containing dibenzo-14-crown-4 moiety. *Sep. Purif. Technol.* **247**, 116940 (2020).

137. Liu, X., Lu, S. & Zhang, W. A crown-ether-based polyurethane with enhanced energy dissipation via sacrificing host-guest complex structures. *Polymer (Guildf).* **333**, 128681 (2025).

138. Favre-Réguillon, A., Dumont, N., Dunjic, B. & Lemaire, M. Polymeric and immobilized crown compounds, material for ion separation. *Tetrahedron* **53**, 1343–1360 (1997).

139. Theato, P. & Klok, H. *Functional Polymers by Post-Polymerization Modification*. (Wiley-VCH Verlag GmbH & Co. KGaA, Weinheim, Germany, 2013, p. 1–5, 268).

140. Gauthier, M. A., Gibson, M. I. & Klok, H. Synthesis of Functional Polymers by Post-Polymerization Modification. *Angew. Chemie Int. Ed.* **48**, 48–58 (2009).

141. Fu, Y., Huang, X., Zhong, S., Yi, W.-J. & Li, L.-J. A new chloromethylation method based on polystyrene–divinylbenzene. *Chem. Pap.* **73**, 2183–2188 (2019).

142. Mitsunobu, O. & Yamada, M. Preparation of Esters of Carboxylic and Phosphoric Acid via Quaternary Phosphonium Salts . *Bull. Chem. Soc. Jpn.* **40**, 2380–2382 (1967).

143. But, T. Y. S. & Toy, P. H. The Mitsunobu Reaction: Origin, Mechanism, Improvements, and Applications. *Chem. Asian J.* **2**, 1340–1355 (2007).

144. Fischer, E. & Speier, A. Darstellung der Ester. *Berichte der Dtsch. Chem. Gesellschaft* **28**, 3252–3258 (1895).

145. Neises, B. & Steglich, W. Einfaches Verfahren zur Veresterung von Carbonsäuren. *Angew. Chemie* **90**, 556–557 (1978).

146. Kürti, L. & Czakó, B. *Strategic Applications of Named Reactions in Organic Synthesis: Background and Detailed Mechanisms*. *Choice Reviews Online* vol. 44 (Elsevier Academic Press, Burlington, 2006, p. 294, 398).

147. Teraoka, I. *Polymer Solutions: An Introduction to Physical Properties*. vol. 3 (John Wiley & Sons, Inc., New York, 2002, p. 71–72).

148. Timothy P. Lodge. *Polymer Chemistry*. (Taylor & Francis Group, Routledge, 2020, p. 278–283, 302–310).

149. Bates, F. S. & Fredrickson, G. H. Block Copolymers—Designer Soft Materials. *Phys. Today* **52**, 32–38 (1999).

150. Tambasco, M., Lipson, J. E. G. & Higgins, J. S. Blend miscibility and the Flory-Huggins interaction parameter: A critical examination. *Macromolecules* **39**, 4860–4868 (2006).

151. Beaucage, G., Stein, R. S. & Koningsveld, R. Tacticity Effects on Polymer Blend Miscibility. 1. Flory-Huggins-Staverman Analysis. *Macromolecules* **26**, 1603–1608 (1993).

152. Whitmore, M. D. & Vavasour, J. D. Self-consistent field theory of block copolymers and block copolymer blends. *Acta Polym.* **46**, 341–360 (1995).

153. Matsen, M. W. The standard Gaussian model for block copolymer melts. *J. Phys. Condens. Matter* **14**, 21–47 (2002).

154. Matsen, M. W. & Bates, F. S. Block copolymer microstructures in the intermediate-segregation regime. *J. Chem. Phys.* **106**, 2436–2448 (1997).

155. Arora, A. *et al.* Broadly Accessible Self-Consistent Field Theory for Block Polymer Materials Discovery. *Macromolecules* **49**, 4675–4690 (2016).

156. Shi, A. *Self-Consistent Field Theory*. *Encyclopedia of Polymeric Nanomaterials* (Springer Berlin Heidelberg, Berlin, Heidelberg, 2013, p. 1–6). doi:10.1007/978-3-642-36199-9.

157. Matsushita, Y. Microphase Separation (of Block Copolymers). in *Encyclopedia of Polymeric Nanomaterials* 1–6 (Springer Berlin Heidelberg, Berlin, Heidelberg, 2014). doi:10.1007/978-3-642-36199-9_149-1.

158. Leibler, L. Theory of Microphase Separation in Block Copolymers. *Macromolecules* **13**, 1602–1617 (1980).

159. Nunes, S. P. Block Copolymer Membranes for Aqueous Solution Applications. *Macromolecules* **49**, 2905–2916 (2016).

160. Abetz, V. & Simon, P. F. W. Phase Behaviour and Morphologies of Block Copolymers. in *Block Copolymers I* vol. 189 125–212 (Springer-Verlag, Berlin/Heidelberg, 2005).

161. Xiang, L. *et al.* Block Copolymer Self-Assembly Directed Synthesis of Porous Materials with Ordered Bicontinuous Structures and Their Potential Applications. *Adv. Mater.* **35**, 1–28 (2023).

162. Bates, F. S. BLOCK COPOLYMER: Theory and Experiment. *Annu. Rev. Phys. Chem.* **41**, 525–557 (1990).

163. Yerukhimovich, I. Y. Fluctuations and the formation of domain structure in heteropolymers. *Polym. Sci. U.S.S.R.* **24**, 2223–2232 (1982).

164. Semenov, A. N. Contribution to the theory of microphase layering in block-copolymer melts. *Zh. Eksp. Teor. Fiz* **88**, 1242–1256 (1985).

165. Zhenzhen Zhang. Isoporous Block Copolymer Membranes with Charged Nanochannels. (University of Hamburg, 2020).

166. Matsen, M. W. Strong-segregation limit of the self-consistent field theory for diblock

copolymer melts. *Eur. Phys. J. E* **33**, 297–306 (2010).

167. Selatile, M. K., Ray, S. S., Ojijo, V. & Sadiku, R. Recent developments in polymeric electrospun nanofibrous membranes for seawater desalination. *RSC Adv.* **8**, 37915–37938 (2018).

168. Abetz, V. Filtrationsmembranen und spezifische Adsorber auf der Basis von maßgeschneiderten selbst-organiserenden Blockcopolymeren. *Chemie Ing. Tech.* **95**, 1361–1371 (2023).

169. Purkait, M. K., Sinha, M. K., Mondal, P. & Singh, R. Introduction to Membranes. in *Interface Science and Technology* vol. 25 1–37 (Elsevier Ltd, 2018).

170. Rahman, M. M. Selective Swelling and Functionalization of Integral Asymmetric Isoporous Block Copolymer Membranes. *Macromol. Rapid Commun.* **42**, 1–12 (2021).

171. Zhang, Z., Rahman, M. M., Abetz, C. & Abetz, V. High-performance asymmetric isoporous nanocomposite membranes with chemically-tailored amphiphilic nanochannels. *J. Mater. Chem. A* **8**, 9554–9566 (2020).

172. Yi, Z. *et al.* Advanced functional membranes based on amphiphilic copolymers. *Prog. Polym. Sci.* **159**, 101907 (2024).

173. Peinemann, K.-V., Abetz, V. & Simon, P. F. W. Asymmetric superstructure formed in a block copolymer via phase separation. *Nat. Mater.* **6**, 992–996 (2007).

174. Ha, S., La, Y. & Kim, K. T. Polymer Cubosomes: Infinite Cubic Mazes and Possibilities. *Acc. Chem. Res.* **53**, 620–631 (2020).

175. Schumacher, M. *et al.* Poly(4-Vinylpyridine)-Based Cubosomes: Synthesis, Assembly, and Loading Capabilities. *Small Sci.* **4**, 1–8 (2024).

176. Palma, A. S., Casadei, B. R., Lotierzo, M. C., de Castro, R. D. & Barbosa, L. R. S. A short review on the applicability and use of cubosomes as nanocarriers. *Biophys. Rev.* **15**, 553–567 (2023).

177. Wurm, F. R. Polyphosphoester cubosomes: introducing a novel drug delivery system. *Expert Opin. Drug Deliv.* **22**, 609–613 (2025).

178. Grandes Reyes, C. F., Ha, S. & Kim, K. T. Synthesis and applications of polymer cubosomes and hexosomes. *J. Polym. Sci.* **61**, 1196–1213 (2023).

179. Chen, H. *et al.* Photocleavable Polymer Cubosomes: Synthesis, Self-Assembly, and Photorelease. *J. Am. Chem. Soc.* **146**, 14776–14784 (2024).

180. Yu, H. & Tan, Z. *Introduction to Electrospinning and Nanofiber*. *Electrospinning for Tissue Regeneration* (Springer Nature Switzerland, Cham, 2025, p. 8–10). doi:10.1007/978-3-031-74310-8.

181. Werner, J. G., Li, Y. & Wiesner, U. Block-Copolymer-Architected Materials in Electrochemical Energy Storage. *Small Sci.* **3**, (2023).

182. Ma, M. & Rutledge, G. C. 7.10 - Nanostructured Electrospun Fibers. *Polym. Sci. a Compr. Ref. Vol. 1-10* **1**–**10**, 187–210 (2012).

183. Nakagawa, Y., Nagao, K. & Tochikubo, F. Interaction between negative corona discharge and droplet emission from liquid Taylor cone. *J. Phys. D. Appl. Phys.* **54**, 305201 (2021).

184. Nalbandian, M. Development and Optimization of Chemically-Active Electrospun Nanofibers for Treatment of Impaired Water Sources. *Dissertation* (University of California Riverside, 2014, p. 21).

185. Molares, M. E. T., Balogh, A. G., Cornelius, T. W., Neumann, R. & Trautmann, C. Fragmentation of nanowires driven by Rayleigh instability. *Appl. Phys. Lett.* **85**, 5337–5339 (2004).

186. Greiner, A. & Wendorff, J. H. Electrospinning: A fascinating method for the preparation of ultrathin fibers. *Angew. Chemie - Int. Ed.* **46**, 5670–5703 (2007).

187. Jaeger, R., Schönherr, H. & Vancso, G. J. Chain packing in electro-spun poly(ethylene oxide) visualized by atomic force microscopy. *Macromolecules* **29**, 7634–7636 (1996).

188. Fong, H., Chun, I. & Reneker, D. H. Beaded nanofibers formed during electrospinning. *Polymer (Guildf).* **40**, 4585–4592 (1999).

189. Foroutani, K., Ghasemi, S. M. & Pourabbas, B. Molecular tailoring of polystyrene-block-poly (acrylic acid) block copolymer toward additive-free asymmetric isoporous membranes via SNIPS. *J. Memb. Sci.* **623**, 119099 (2021).

190. Clodt, J. I. *et al.* Performance study of isoporous membranes with tailored pore sizes. *J. Memb. Sci.* **495**, 334–340 (2015).

191. Yang, C. *et al.* Tailoring the pore size and permeability of isoporous membranes through blending with poly(ethylene glycol): Toward the balance of macro- and microphase separation. *J. Memb. Sci.* **598**, 117755 (2020).

192. Cheng, J. *et al.* Metal ions ‘sewing’ isoporous membranes with polystyrene-block-poly (acrylic acid) block copolymer. *J. Memb. Sci.* **587**, 117086 (2019).

193. Liberman, L., Coughlin, M. L., Weigand, S., Bates, F. S. & Lodge, T. P. Phase Behavior of Linear-Bottlebrush Block Polymers. *Macromolecules* **55**, 2821–2831 (2022).

194. Jiang, L., Nykypanchuk, D., Pastore, V. J. & Rzayev, J. Morphological Behavior of Compositionally Gradient Polystyrene–Polylactide Bottlebrush Copolymers. *Macromolecules* **52**, 8217–8226 (2019).

195. Gokel, G. W. *Crown Ethers and Cryptands*. (The Royal Society of Chemistry, Cambridge, 1991, p. 74).

196. Xue, J., Wu, T., Dai, Y. & Xia, Y. Electrospinning and Electrospun Nanofibers: Methods, Materials, and Applications. *Chem. Rev.* **119**, 5298–5415 (2019).

9. APPENDIX

9.1. AUTHOR CONTRIBUTIONS

In the following, the contributions of the authors to the publications 1–3 will be assigned.

1) Lithium Selectivity of Crown Ethers: The Effect of Heteroatoms and Cavity Size
   Iklima Oral*, Sabrina Tamm*, Carmen Herrmann, Volker Abetz
   *: Both authors contributed equally to this project.
   Separation and Purification Technology **2022**, *294*, 121142.
   doi.org/10.1016/j.seppur.2022.121142

All authors conceived the experiments and calculations. Iklima Oral and Sabrina Tamm designed and performed all experiments and calculations and wrote the paper, with support by Volker Abetz and Carmen Herrmann in writing the paper. This work is supported by the Cluster of Excellence 'CUI: Advanced Imaging of Matter' of the Deutsche Forschungsgemeinschaft (DFG) - EXC 2056 - 390715994. All authors analyzed the data.

2) Systematic Investigation of a Crown Ether Functionalized PS-*b*-PMAA Block Copolymer for Optimized Lithium Extraction from Aqueous Media
   Sabrina Jaehnke, Joachim von Chamier Gliszczynski, Birgit Hankiewicz, Volker Abetz
   Journal of Polymer Science **2025**; n/a.
   doi.org/10.1002/pol.20250060

Sabrina Jaehnke and Volker Abetz conceived the experiments, interpreted the data and wrote the manuscript. Sabrina Jaehnke and Joachim von Chamier Gliszczynski conducted and analyzed the experiments. DLS analyses were performed by Sabrina Jaehnke, Birgit Hankiewicz and Joachim von Chamier Gliszczynski.

3) Electrospun, Crown Ether Functionalized PS-b-PMAA Block Copolymer Fibers for Li Extraction from Aqueous Media
   Sabrina Jaehnke, Volker Abetz
   Desalination **2025**, 616, 119343.
   doi.org/10.1016/j.desal.2025.119343

Sabrina Jaehnke and Volker Abetz conceptualized the experiments, formally analyzed and validated the data, and wrote the manuscript. S. Jaehnke visualized the data, and designed and accomplished the experiments. For this work the HPC-cluster Hummel-2 at University of Hamburg was used. The cluster was funded by Deutsche Forschungsgemeinschaft (DFG, German Research Foundation) – 498394658.

9.2. SUPPORTING INFORMATION FOR PUBLICATION 1

The supporting information are reprinted with permission from I. Oral, S. Tamm, C. Herrmann, V. Abetz, Lithium Selectivity of Crown Ethers: The Effect of Heteroatoms and Cavity Size, *Sep. Purif. Technol. 294* (**2022**) 121142. – Copyright 2022 Elsevier B.V.

Lithium Selectivity of Crown Ethers: The Effect of Heteroatoms and Cavity Size – Supporting Information

Iklima Oral, Sabrina Tamm, Carmen Herrmann, Volker Abetz

1. 15-membered Rings

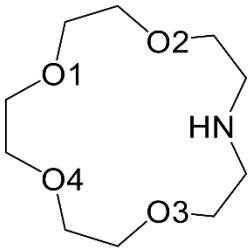

Figure S1: Lewis structure of aza-15C5.

1.1. Cavity Size d_{CE}

Table S1: The distances between the heteroatoms opposing each other as well as the cavity sizes d_{CE} of the empty CE (B15C5, aza-B15C5, thio-B15C5, and aza-15C5) and their complexes with Li^+, Na^+, K^+, Mg^{2+}, and Ca^{2+}.

	Distance / Å					
Complex	**O1-O4**	**O1-X**	**O2-O3**	**O2-X**	**O3-O4**	**cavity size d_{CE}**
B15C5	4.4991	4.4497	4.4984	4.4492	4.6768	**4.5146**
B15C5-Li^+	4.1656	4.1738	4.1658	4.1739	4.1956	**4.1749**
B15C5-Na^+	4.3506	4.3830	4.3507	4.3831	4.3719	**4.3678**
B15C5-K^+	4.4246	4.1946	4.4249	4.1948	4.6769	**4.3831**
B15C5-Mg^{2+}	4.0344	4.0354	4.0344	4.0354	4.0160	**4.0311**
B15C5-Ca^{2+}	4.2927	4.2320	4.2929	4.2320	4.3787	**4.2857**
aza-B15C5	4.4958	4.2307	4.4958	4.2307	4.7499	**4.4406**
aza-B15C5-Li^+	4.1905	4.2831	4.1905	4.2831	4.2448	**4.2384**
aza-B15C5-Na^+	4.3557	4.4911	4.3556	4.4911	4.4074	**4.4202**
aza-B15C5-K^+	4.4514	4.2366	4.4515	4.2367	4.7337	**4.4220**
aza-B15C5-Mg^{2+}	3.6803	4.2199	3.7446	3.8615	3.9441	**3.8901**
aza-B15C5-Ca^{2+}	4.3086	4.3403	4.3086	4.3403	4.4230	**4.3441**
thio-B15C5	3.1569	4.9271	4.6851	4.9124	3.7239	**4.2811**
thio-B15C5-Li^+	3.4803	4.7346	3.8329	4.0794	3.7419	**3.9738**
thio-B15C5-Na^+	4.3465	4.8801	4.3465	4.8801	4.3404	**4.5587**
thio-B15C5-K^+	4.3371	5.2288	4.3371	5.2279	4.1099	**4.6481**
thio-B15C5-Mg^{2+}	3.5442	4.5671	3.8701	4.0614	3.8734	**3.9832**
thio-B15C5-Ca^{2+}	4.2858	4.9215	4.2858	4.9215	4.1733	**4.5176**
aza-15C5	4.7790	4.1060	4.7890	4.5980	4.1500	**4.4844**
aza-15C5-Li^+	3.9690	3.8700	4.5470	4.1550	4.6840	**4.2450**
aza-15C5-Na^+	4.2030	4.4450	4.5200	4.5610	4.4710	**4.4400**
aza-15C5-K^+	4.0290	4.4340	4.7760	4.8300	4.5560	**4.5250**
aza-15C5-Mg^{2+}	3.9760	3.7690	3.6080	4.0930	3.8240	**3.8540**
aza-15C5-Ca^{2+}	4.1940	4.4490	4.3760	4.5500	4.3170	**4.3772**

1.2. Metal Heteroatom Distance $d_{X\text{-}M}{}^{n+}$

Table S2: The distances and average distances between the heteroatoms of the CE (B15C5, aza-B15C5, thio-B15C5, and aza-15C5) and the complexed cations (Li^+, Na^+, K^+, Mg^{2+}, and Ca^{2+}).

	Distance / Å					
Complex	**O1-M**	**O2-M**	**O3-M**	**O4-M**	**X-M**	**Average distance**
B15C5-Li^+	2.2154	2.2154	2.1946	2.1945	2.1652	**2.1970**
B15C5-Na^+	2.3034	2.3034	2.3046	2.3045	2.2980	**2.3028**
B15C5-K^+	2.7125	2.7125	2.7194	2.7193	2.6920	**2.7111**
B15C5-Mg^{2+}	2.1315	2.1315	2.1132	2.1132	2.1119	**2.1202**
B15C5-Ca^{2+}	2.3170	2.3170	2.3388	2.3388	2.3044	**2.3232**
aza-B15C5-Li^+	2.2455	2.2455	2.2102	2.2102	2.2554	**2.2334**
aza-B15C5-Na^+	2.3179	2.3179	2.3075	2.3075	2.4110	**2.3324**
aza-B15C5-K^+	2.7282	2.7281	2.7218	2.7219	2.7600	**2.7320**
aza-B15C5-Mg^{2+}	2.1667	2.0713	2.0558	2.0338	2.1848	**2.1025**
aza-B15C5-Ca^{2+}	2.3294	2.3294	2.3291	2.3291	2.4349	**2.3504**
thio-B15C5-Li^+	2.1902	2.0544	1.9778	2.0439	2.6207	**2.1774**
thio-B15C5-Na^+	2.3179	2.3179	2.3309	2.3309	2.7945	**2.4184**
thio-B15C5-K^+	2.7004	2.7003	2.7315	2.7315	3.1959	**2.8119**
thio-B15C5-Mg^{2+}	2.1209	2.0650	2.0519	2.0688	2.5375	**2.1688**
thio-B15C5-Ca^{2+}	2.3446	2.3446	2.3396	2.3396	2.8338	**2.4404**
aza-15C5-Li^+	2.0680	2.8060	2.1040	2.1930	2.0940	**2.2530**
aza-15C5-Na^+	2.3230	2.3590	2.3510	2.4390	2.3300	**2.3604**
aza-15C5-K^+	2.7000	2.6920	2.7240	2.8490	2.7030	**2.7336**
aza-15C5-Mg^{2+}	2.1080	2.0650	2.0340	2.1720	2.0660	**2.0890**
aza-15C5-Ca^{2+}	2.3300	2.3120	2.3520	2.4840	2.3060	**2.3568**

1.3. Hirshfeld Partial Charges

Table S3: Hirshfeld charge transfer between the oxygen, nitrogen, resp. sulfur atoms of B15C5, aza-B15C5, thio-B15C5, and aza-15C5 and the complexed cations (Li^+, Na^+, K^+, Mg^{2+}, and Ca^{2+}), based on the difference in Hirshfeld partial charges between the empty CE and the coronates.

	Charge transfer					
Complex	**O1-M**	**O2-M**	**O3-M**	**O4-M**	**X-M**	**Total**
B15C5-Li^+	0.0198	0.0198	0.0309	0.0309	0.0299	**0.1313**
B15C5-Na^+	0.0095	0.0095	0.0214	0.0214	0.0203	**0.0822**
B15C5-K^+	0.0075	0.0075	0.0113	0.0113	0.0179	**0.0554**
B15C5-Mg^{2+}	0.0285	0.0285	0.0465	0.0465	0.0463	**0.1962**
B15C5-Ca^{2+}	0.0185	0.0185	0.0355	0.0355	0.0364	**0.1443**
aza-B15C5-Li^+	0.0113	0.0113	0.0182	0.0182	0.0609	**0.1199**
aza-B15C5-Na^+	0.0016	0.0016	0.0095	0.0095	0.0531	**0.0752**
aza-B15C5-K^+	-0.0015	-0.0015	-0.0004	-0.0004	0.0414	**0.0377**
aza-B15C5-Mg^{2+}	0.0174	0.0069	0.0344	0.0340	0.1088	**0.2015**
aza-B15C5-Ca^{2+}	0.0101	0.0102	0.0225	0.0225	0.0913	**0.1566**
thio-B15C5-Li^+	0.0007	0.0108	0.0085	0.0080	0.0831	**0.1111**
thio-B15C5-Na^+	-0.0082	0.0204	0.0040	0.0028	0.0662	**0.0852**
thio-B15C5-K^+	-0.0201	0.0085	-0.0003	-0.0014	0.0473	**0.0340**
thio-B15C5-Mg^{2+}	0.0101	0.0281	0.0283	0.0253	0.1511	**0.2429**
thio-B15C5-Ca^{2+}	-0.0034	0.0252	0.0176	0.0164	0.1273	**0.1832**
aza-15C5-Li^+	0.0203	0.0174	0.0136	0.0177	0.0593	**0.1283**
aza-15C5-Na^+	0.0114	0.0105	0.0106	0.0127	0.0528	**0.0979**
aza-15C5-K^+	0.0022	0.0056	0.0014	0.0077	0.0392	**0.0561**
aza-15C5-Mg^{2+}	0.0381	0.0348	0.0389	0.0353	0.1109	**0.2580**
aza-15C5-Ca^{2+}	0.0257	0.0235	0.0242	0.0275	0.0909	**0.1918**

1.4. NBO Analysis

Table S4: Stabilization energies $E^{(2)}$ (in kJ mol^{-1}) between the acceptor NBO of the complexed metal (Li^+, Na^+, K^+, Mg^{2+}, and Ca^{2+}) and the donor NBOs of B15C5, aza-B15C5, thio-B15C5, and aza-15C5. LP1 and LP2 represent the donor NBOs corresponding to the free electron pairs of the heteroatoms.

	Stabilization energy / kJ mol^{-1}										
	O1		**O2**		**O3**		**O4**		**X**		
Complex	**LP1**	**LP2**	**LP1**	**LP2**	**LP1**	**LP2**	**LP1**	**LP2**	**LP1**	**LP2**	**Sum**
B15C5-Li^+	19.71	0.00	19.71	0.00	20.96	1.55	20.96	1.55	21.80	1.30	107.53
B15C5-Na^+	17.36	0.00	17.36	0.00	17.28	2.26	17.28	2.26	17.91	2.09	93.81
B15C5-K^+	5.82	0.00	5.82	0.00	8.45	0.00	8.45	0.00	6.15	0.25	34.94
B15C5-Mg^{2+}	40.58	1.88	40.58	1.88	33.64	19.83	33.64	19.83	35.52	16.95	244.35
B15C5-Ca^{2+}	17.57	1.00	17.57	1.00	20.00	3.81	20.00	3.81	14.39	5.77	104.93
aza-B15C5-Li^+	20.67	0.00	20.67	0.00	22.26	1.46	22.26	1.46	23.64	-	112.42
aza-B15C5-Na^+	18.28	0.00	18.28	0.00	18.54	2.05	18.54	2.05	2.05	-	79.79
aza-B15C5-K^+	6.02	0.00	6.02	0.00	8.79	0.00	8.79	0.00	7.15	-	36.78
aza-B15C5-Mg^{2+}	40.79	4.48	19.92	44.02	42.89	22.09	47.86	16.61	70.92	-	264.30
aza-B15C5-Ca^{2+}	19.50	1.26	19.50	1.26	20.42	3.10	20.42	3.10	25.36	-	113.89
thio-B15C5-Li^+	27.87	0.00	24.56	17.53	41.00	2.68	37.66	6.11	31.67	54.85	243.93
thio-B15C5-Na^+	18.54	0.00	18.54	0.00	18.49	2.51	18.49	2.51	20.71	36.57	136.36
thio-B15C5-K^+	7.82	0.54	7.82	0.54	6.86	0.59	6.86	0.59	14.90	12.43	58.95
thio-B15C5-Mg^{2+}	41.80	5.56	18.83	44.69	43.18	25.15	39.46	31.59	24.98	133.72	408.94
thio-B15C5-Ca^{2+}	21.55	0.00	21.55	0.00	14.43	3.51	14.43	3.51	20.38	64.60	163.97
aza-15C5-Li^+	28.91	0.75	9.62	2.22	24.77	0.96	25.02	1.00	26.02	-	119.29
aza-15C5-Na^+	18.16	2.09	18.07	2.55	17.49	1.97	19.20	1.38	20.96	-	101.88
aza-15C5-K^+	7.57	0.42	9.16	0.29	7.03	0.38	9.25	0.00	8.87	-	42.97
aza-15C5-Mg^{2+}	38.28	27.03	34.31	32.64	37.40	26.94	48.66	14.27	76.32	-	335.85
aza-15C5-Ca^{2+}	16.32	5.73	19.46	2.34	15.86	3.89	21.63	3.22	27.82	-	116.27

2. 12-membered Rings

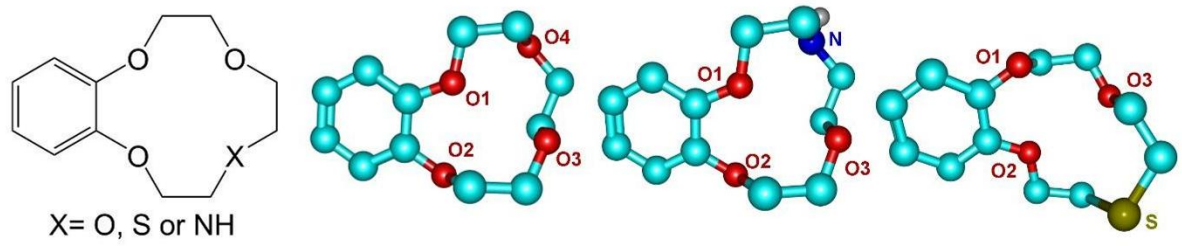

Figure S1: Lewis structure representation (left) and optimized structures of the empty crown ethers B12C4, aza-B12C4 and thio-B12C4 (from left to right).

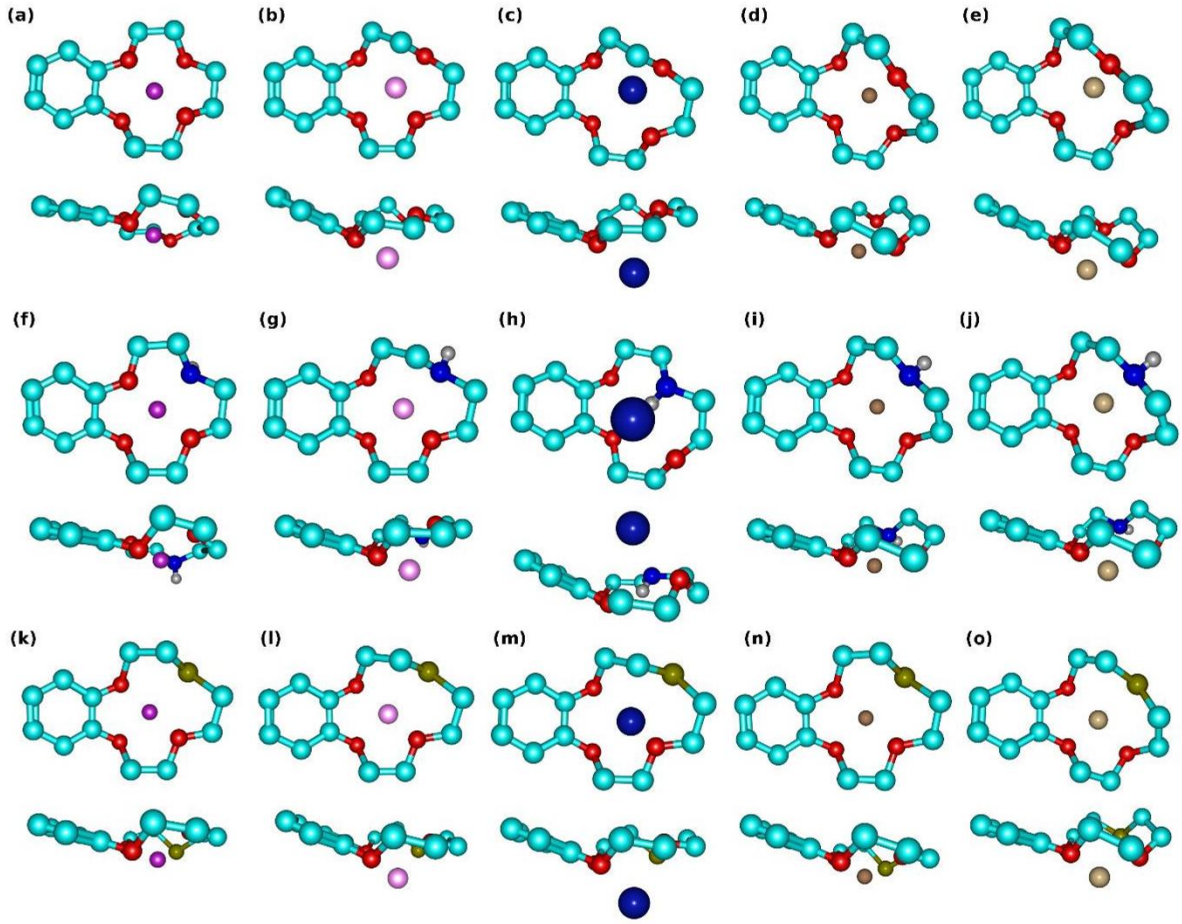

Figure S2: Optimized structures of the B12C4 (first row), aza-B12C4 (second row) and thio-B12C4 (third row) complexes with Li^+ (violet; a, f, k), Na^+ (pink; b, g, l), K^+ (dark blue; c, h, m), Mg^{2+} (brown; d, i, n), and Ca^{2+} (beige; e, j, o), from two perspectives each.

2.1. Cavity Size d_{CE}

Table S5: The distances between the heteroatoms opposing each other as well as the cavity sizes d_{CE} of the empty CE (B12C4, aza-B12C4, and thio-B12C4) and their complexes with Li^+, Na^+, K^+, Mg^{2+}, and Ca^{2+}.

Distance / Å			
Complex	**O1-X**	**O2-O3**	**cavity size d_{CE}**
B12C4	3.0255	4.6405	3.8330
B12C4-Li^+	3.2267	3.8388	3.5327
B12C4-Na^+	3.7123	3.9695	3.8409
B12C4-K^+	4.0347	3.7944	3.9145
B12C4-Mg^{2+}	3.9100	3.3572	3.6336
B12C4-Ca^{2+}	4.1428	3.2566	3.6997
aza-B12C4	3.0279	4.6922	3.8601
aza-B12C4-Li^+	3.1846	3.9996	3.5921
aza-B12C4-Na^+	3.6782	4.1036	3.8909
aza-B12C4-K^+	4.4422	3.0966	3.7694
aza-B12C4-Mg^{2+}	3.9150	3.5730	3.7440
aza-B12C4-Ca^{2+}	4.1412	3.4748	3.8080
thio-B12C4	3.0639	5.0078	4.0358
thio-B12C4-Li^+	3.3844	4.4042	3.8943
thio-B12C4-Na^+	3.5718	4.5372	4.0545
thio-B12C4-K^+	3.6282	4.5808	4.1045
thio-B12C4-Mg^{2+}	3.5207	4.3551	3.9379
thio-B12C4-Ca^{2+}	4.0554	4.0654	4.0604

2.2. Metal-Heteroatom Distance $d_{X\text{-}M}{}^{n+}$

Table S6: The distances and average distances between the heteroatoms of the CE (B12C4, aza-B12C4, and thio-B12C4) and the complexed cations (Li^+, Na^+, K^+, Mg^{2+}, and Ca^{2+}).

	Distance / Å				
Complex	**O1-M**	**O2-M**	**O3-M**	**X-M**	**Average distance**
B12C4-Li^+	1.88276	1.93689	1.90707	1.88562	1.9031
B12C4-Na^+	2.25056	2.32322	2.33354	2.48729	2.3487
B12C4-K^+	2.63358	2.75425	2.72497	3.3917	2.8761
B12C4-Mg^{2+}	2.01429	1.99333	1.99924	1.99691	2.0009
B12C4-Ca^{2+}	2.3165	2.3117	2.32801	2.30168	2.3145
aza-B12C4-Li^+	1.87088	1.97566	2.03397	1.88438	1.9412
aza-B12C4-Na^+	2.25933	2.32952	2.41851	2.44828	2.3639
aza-B12C4-K^+	3.93576	3.15176	2.73397	2.78264	3.1510
aza-B12C4-Mg^{2+}	2.015	1.998	1.999	2.105	2.0293
aza-B12C4-Ca^{2+}	2.31307	2.30893	2.47131	2.29894	2.3481
thio-B12C4-Li^+	1.89609	1.98914	1.93381	2.48055	2.0749
thio-B12C4-Na^+	2.27169	2.32707	2.39736	2.78747	2.4459
thio-B12C4-K^+	2.67233	2.71239	2.94127	3.196	2.8805
thio-B12C4-Mg^{2+}	1.96279	2.01405	1.9642	2.4574	2.0996
thio-B12C4-Ca^{2+}	2.33247	2.31118	2.31433	2.81501	2.4432

2.3. Hirshfeld Partial Charges

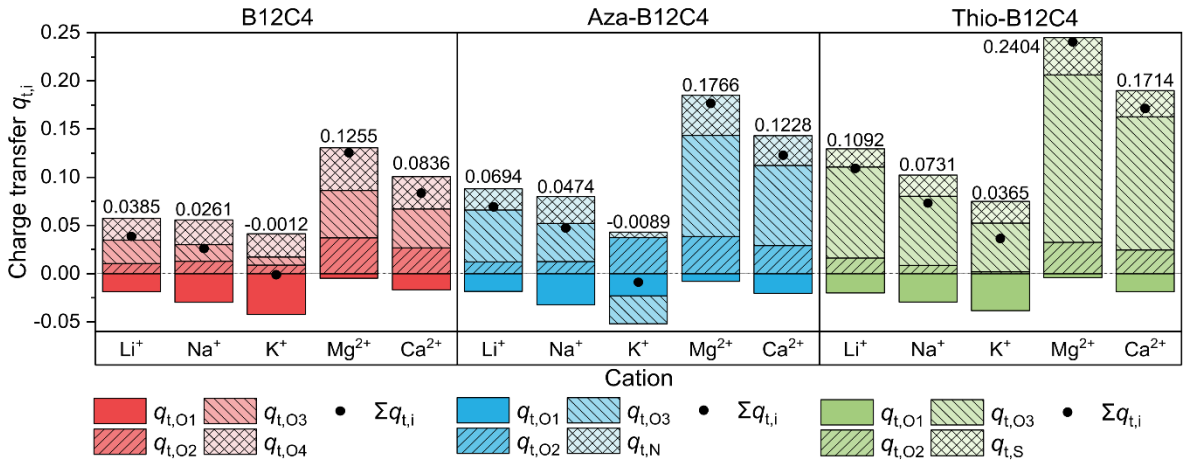

Figure S3: Hirshfeld charge transfer q_t between the donor atoms (O, S, and N) and Li^+, Na^+, K^+, Mg^{2+}, resp. Ca^{2+} within the complexes with the B12C4, aza-B12C4 and thio-B12C4CE. The sums of the charge transfers are given above the bars.

2.4. NBO Analysis

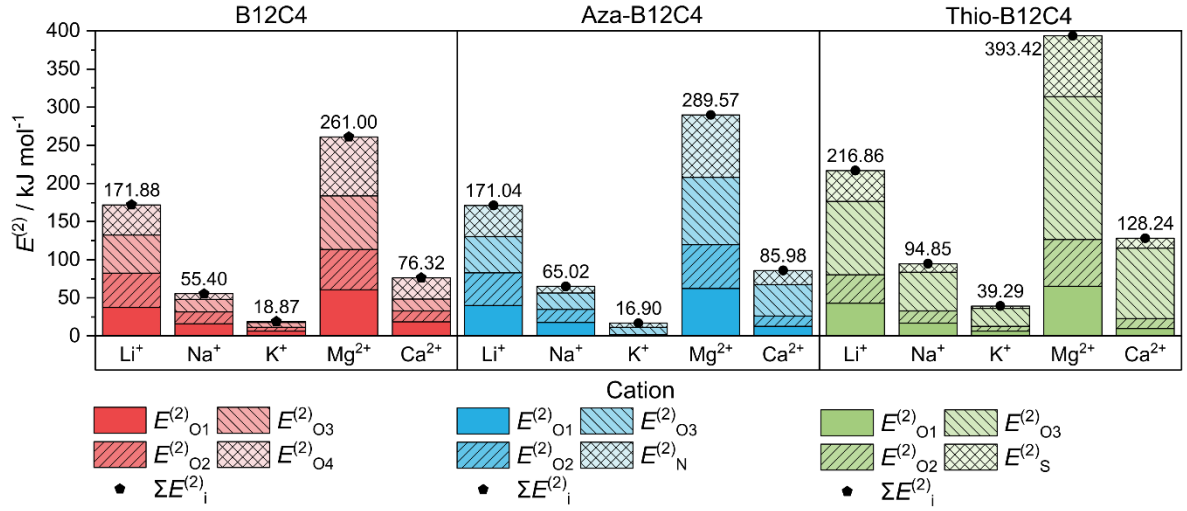

Figure S4: Stabilization energies $E^{(2)}$ within the complexes of the B12C4, aza-B12C4 and thio-B12C4 CEs with Li^+, Na^+, K^+, Mg^{2+}, and Ca^{2+}. The contributions of the lone pair donor NBOs (LP1 and LP2 combined) to the interaction with the acceptor NBOs and the sum of these, above the bars, are given.

3. 9-membered Rings

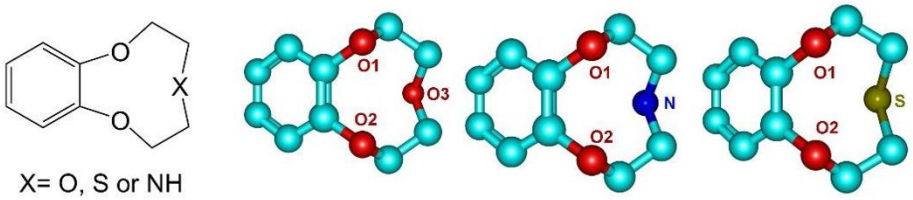

Figure S5: Lewis structure representation (left) and optimized structures of the empty crown ethers B9C3, aza-B9C3 and thio-B9C3(from left to right).

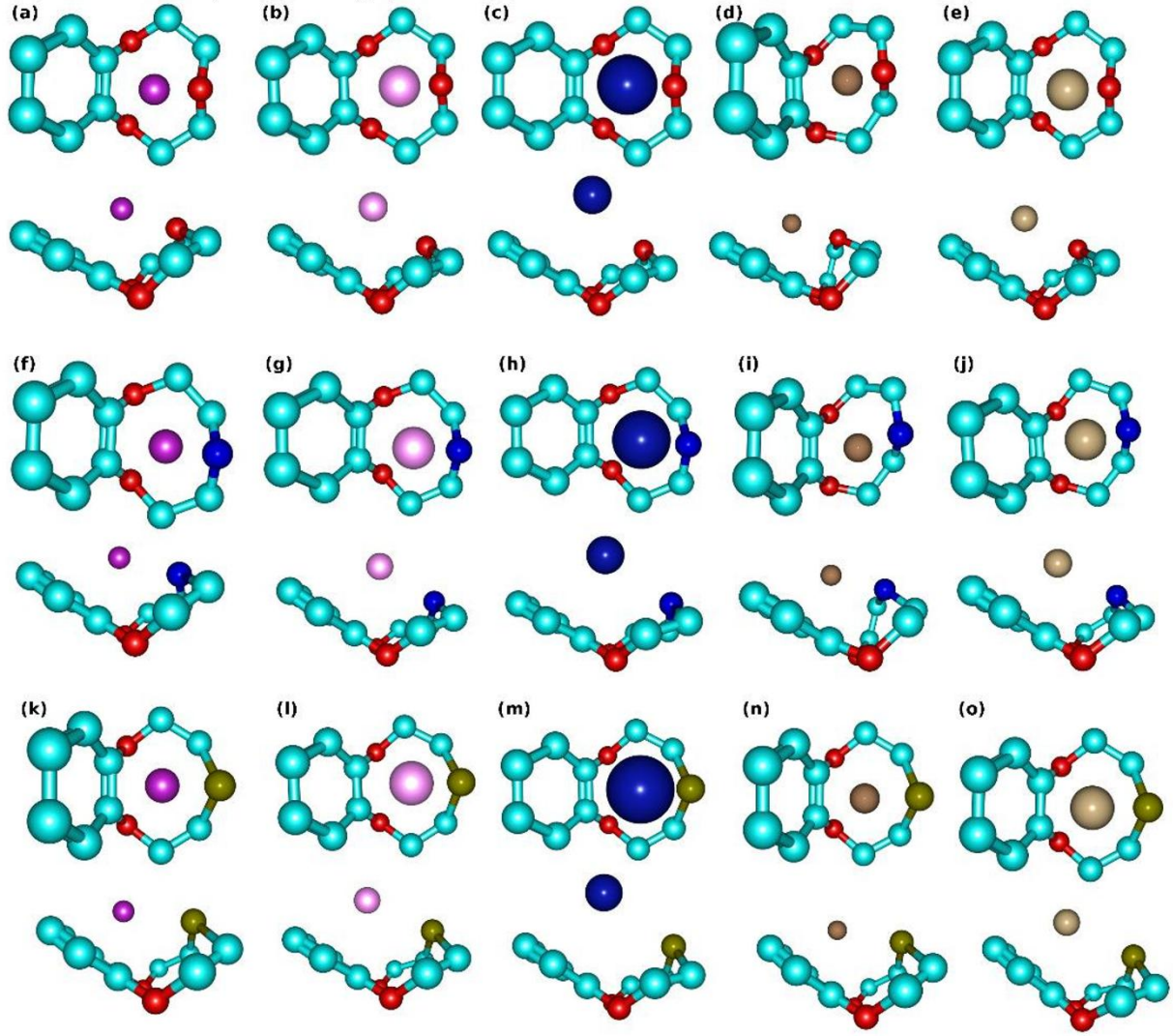

Figure S6: Optimized structures of the B9C3 (first row), aza-B9C3 (second row) and thio-B9C3 (third row) complexes with Li^+ (violet; a, f, k), Na^+ (pink; b, g, l), K^+ (dark blue; c, h, m), Mg^{2+} (brown; d, i, n), and Ca^{2+} (beige; e, j, o), from two perspectives each.

3.1. Cavity Size d_{CE}

Table S7: The distances between the heteroatoms opposing each other as well as the cavity sizes d_{CE} of the empty CE (B9C3, aza-B9C3, and thio-B9C3) and their complexes with Li^+, Na^+, K^+, Mg^{2+}, and Ca^{2+}.

	Distance / Å			
Complex	**O1-O2**	**O1-X**	**O2-X**	**cavity size d_{CE}**
B9C3	2.7619	2.9516	2.9518	2.9517
B9C3-Li^+	2.7599	2.8265	2.8265	2.8265
B9C3-Na^+	2.7554	2.8565	2.8564	2.8564
B9C3-K^+	2.7517	2.8793	2.8791	2.8792
B9C3-Mg^{2+}	2.6673	3.0147	2.6719	2.8433
B9C3-Ca^{2+}	2.7251	2.8200	2.8200	2.8200
aza-B9C3	2.7453	3.0029	3.0031	3.0030
aza-B9C3-Li^+	2.7362	2.8485	3.1312	2.9898
aza-B9C3-Na^+	2.7275	2.8903	3.1850	3.0376
aza-B9C3-K^+	2.7263	2.8632	3.2438	3.0535
aza-B9C3-Mg^{2+}	2.6455	3.2238	2.8452	3.0345
aza-B9C3-Ca^{2+}	2.7091	3.1877	2.8194	3.0036
thio-B9C3	2.7144	3.3362	3.3362	3.3362
thio-B9C3-Li^+	2.6959	3.2706	3.2704	3.2705
thio-B9C3-Na^+	2.6957	3.3104	3.3104	3.3104
thio-B9C3-K^+	2.6939	3.3169	3.3142	3.3156
thio-B9C3-Mg^{2+}	2.6580	3.2959	3.2959	3.2959
thio-B9C3-Ca^{2+}	2.6544	3.2475	3.2475	3.2475

3.2. Metal-Heteroatom Distance $d_{X\text{-}M}{}^{n+}$

Table S8: The distances and average distances between the heteroatoms of the CE (B9C3, aza-B9C3, and thio-B9C3) and the complexed cations (Li^+, Na^+, K^+, Mg^{2+}, and Ca^{2+}).

	Distance / Å			
Complex	**O1-M**	**O2-M**	**X-M**	**Average distance**
B9C3-Li^+	3.03717	3.0372	1.90168	2.6587
B9C3-Na^+	3.48023	3.48044	2.29895	3.0865
B9C3-K^+	3.96879	3.96868	2.70061	3.5460
B9C3-Mg^{2+}	3.23355	3.24632	1.97804	2.8193
B9C3-Ca^{2+}	3.46233	3.46233	2.30701	3.0772
aza-B9C3-Li^+	2.98015	3.07539	2.04977	2.7018
aza-B9C3-Na^+	3.38056	3.44922	2.44694	3.0922
aza-B9C3-K^+	3.82026	3.90454	2.90715	3.5440
aza-B9C3-Mg^{2+}	3.22019	3.27441	2.09757	2.8641
aza-B9C3-Ca^{2+}	3.4907	3.45066	2.47986	3.1404
thio-B9C3-Li^+	3.23056	3.23053	2.48556	2.9822
thio-B9C3-Na^+	3.7947	3.79472	2.79966	3.4630
thio-B9C3-K^+	4.33251	4.33238	3.22413	3.9630
thio-B9C3-Mg^{2+}	3.32405	3.32405	2.47001	3.0394
thio-B9C3-Ca^{2+}	3.63854	3.63854	2.80637	3.3612

3.3. Hirshfeld Partial Charges

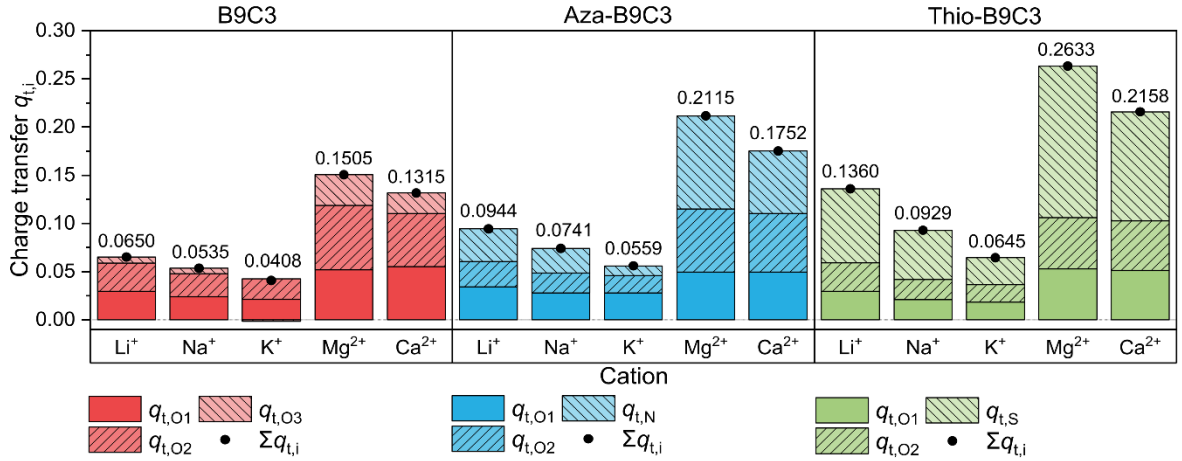

Figure S7: Hirshfeld charge transfer q_t between the donor atoms (O, S, and N) and Li^+, Na^+, K^+, Mg^{2+}, resp. Ca^{2+} within the complexes with the B9C3, aza-B9C3 and thio-B9C3 CE. The sums of the charge transfers are given above the bars.

3.4. NBO Analysis

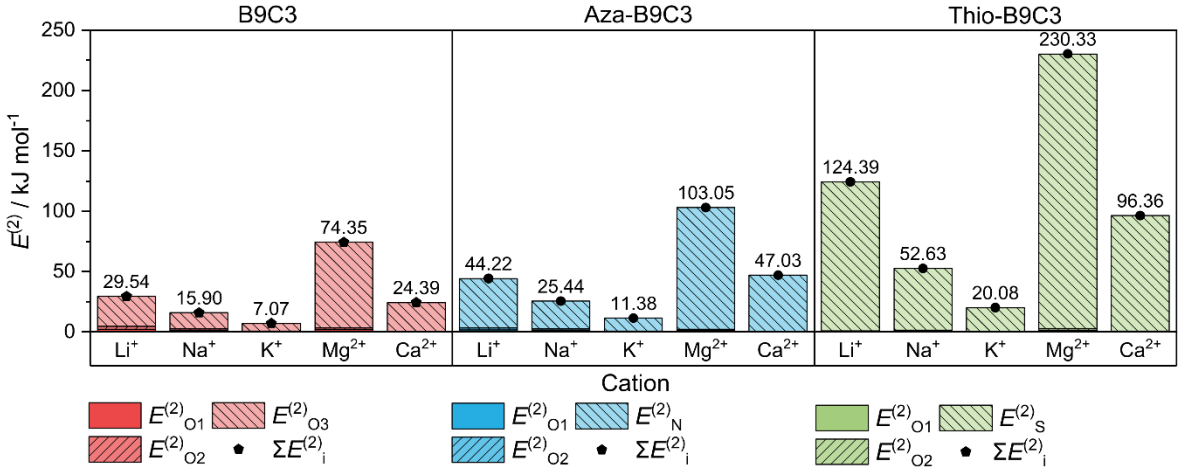

Figure S8: Stabilization energies $E^{(2)}$ within the complexes of the B9C3, aza-B9C3 and thio-B9C3 CEs with Li^+, Na^+, K^+, Mg^{2+}, and Ca^{2+}. The contributions of the lone pair donor NBOs (LP1 and LP2 combined) to the interaction with the acceptor NBOs and the sum of these, above the bars, are given.

4. Aza-15-crown-5

Table S9: Cavity size, metal–donor atom distance, Hirshfeld charge transfer, and NBO stabilization energy $E^{(2)}$ calculated via DFT for complexes of aza-15C5 with Li^+, Na^+, K^+, Mg^{2+}, and Ca^{2+}.

Complex	Cavity size		Hirshfeld partial charge	NBO
Aza-15C5-M	d_{CE} / Å	$d_{X\text{-}M^{n+}}$ / Å	q_t	$E^{(2)}$ / kJ mol^{-1}
M^{n+} = none	4.48	-	-	-
$M^{n+} = Li^+$	4.25	2.25	0.13	119.29
$M^{n+} = Na^+$	4.44	2.36	0.10	101.88
$M^{n+} = K^+$	4.53	2.73	0.06	42.97
$M^{n+} = Mg^{2+}$	3.85	2.09	0.26	335.85
$M^{n+} = Ca^{2+}$	4.38	2.36	0.19	116.27

5. Thermodynamic Calculations

5.1. Entropy and Enthalpy

Table S10: Changes in enthalpy H and entropy S for the complexation of Li^+, Na^+, K^+, Mg^{2+} and Ca^{2+} with aza-15-crown-5, simulated in vacuum and solvent environment as modeled by a polarizable continuum model.

Complex	Vacuum		DCM	
Aza-15C5-M	**ΔS [kJ mol^{-1}K^{-1}]**	**ΔH [kJ mol^{-1}]**	**ΔS [kJ mol^{-1}K^{-1}]**	**ΔH [kJ mol^{-1}]**
$M^{n+} = Li^+$	-0.13	-433.04	-0.14	-68.95
$M^{n+} = Na^+$	-0.14	-349.72	-0.13	-71.27
$M^{n+} = K^+$	-0.13	-244.29	-0.14	-57.42
$M^{n+} = Mg^{2+}$	-0.15	-1247.75	-0.16	-181.85
$M^{n+} = Ca^{2+}$	-0.15	-932.80	-0.17	-83.59

5.2. Equilibrium Constant and Gibbs Free Energy

Table S11: Equilibrium constants K for the complexation of Li^+, Na^+, K^+, Mg^{2+} and Ca^{2+} with aza-15-crown-5, benzo-15-crown-5, aza-benzo-15-crown-5 and thio-benzo-15-crown-5, simulated in vacuum.

Complex	B15C5	aza-B15C5	thio-B15C5	aza-15C5
$M^{n+} = Li^+$	$1.9\cdot10^{64}$	$4.1\cdot10^{67}$	$1.4\cdot10^{69}$	$9.8\cdot10^{68}$
$M^{n+} = Na^+$	$1.8\cdot10^{48}$	$2.8\cdot10^{52}$	$9.5\cdot10^{53}$	$1.5\cdot10^{54}$
$M^{n+} = K^+$	$1.2\cdot10^{29}$	$2.3\cdot10^{33}$	$3.6\cdot10^{36}$	$7.0\cdot10^{35}$
$M^{n+} = Mg^{2+}$	$7.9\cdot10^{197}$	$1.6\cdot10^{208}$	$2.0\cdot10^{206}$	$4.0\cdot10^{210}$
$M^{n+} = Ca^{2+}$	$1.6\cdot10^{144}$	$6.3\cdot10^{152}$	$1.3\cdot10^{153}$	$4.3\cdot10^{155}$
Complex	**B12C4**	**aza-B12C4**	**thio-B12C4**	
$M^{n+} = Li^+$	$2.7\cdot10^{56}$	$2.7\cdot10^{60}$	$4.9\cdot10^{57}$	
$M^{n+} = Na^+$	$9.2\cdot10^{37}$	$3.0\cdot10^{41}$	$1.3\cdot10^{39}$	
$M^{n+} = K^+$	$5.0\cdot10^{25}$	$1.4\cdot10^{22}$	$1.3\cdot10^{26}$	
$M^{n+} = Mg^{2+}$	$1.1\cdot10^{178}$	$1.1\cdot10^{185}$	$1.7\cdot10^{178}$	
$M^{n+} = Ca^{2+}$	$1.0\cdot10^{128}$	$1.5\cdot10^{132}$	$1.5\cdot10^{126}$	
Complex	**B9C3**	**aza-B9C3**	**thio-B9C3**	
$M^{n+} = Li^+$	$1.82\cdot10^{34}$	$1.6\cdot10^{37}$	$9.5\cdot10^{34}$	
$M^{n+} = Na^+$	$2.18\cdot10^{23}$	$7.6\cdot10^{24}$	$2.4\cdot10^{24}$	
$M^{n+} = K^+$	$2.48\cdot10^{15}$	$2.8\cdot10^{15}$	$7.5\cdot10^{15}$	
$M^{n+} = Mg^{2+}$	$3.12\cdot10^{126}$	$1.0\cdot10^{134}$	$5.1\cdot10^{132}$	
$M^{n+} = Ca^{2+}$	$3.18\cdot10^{88}$	$1.1\cdot10^{92}$	$1.2\cdot10^{91}$	

Table S12: Equilibrium constants *K* for the complexation of Li^+, Na^+, K^+, Mg^{2+} and Ca^{2+} (non-complexed simulated in H_2O) with aza-15-crown-5, benzo-15-crown-5, aza-benzo-15-crown-5 and thio-benzo-15-crown-5, simulated in DCM as modeled by a polarizable continuum model. No convergence of SCF runs could be achieved for B9C3-Ca^{2+}.

Complex	**B15C5**	**aza-B15C5**	**thio-B15C5**	**aza-15C5**
$M^{n+} = Li^+$	$2.87 \cdot 10^{5}$	$1.02 \cdot 10^{4}$	$2.51 \cdot 10^{2}$	$8.48 \cdot 10^{4}$
$M^{n+} = Na^+$	$5.61 \cdot 10^{4}$	$2.46 \cdot 10^{3}$	$3.98 \cdot 10^{5}$	$3.26 \cdot 10^{5}$
$M^{n+} = K^+$	$1.53 \cdot 10^{3}$	$2.87 \cdot 10^{1}$	$6.02 \cdot 10^{2}$	$7.87 \cdot 10^{2}$
$M^{n+} = Mg^{2+}$	$1.45 \cdot 10^{19}$	$5.93 \cdot 10^{18}$	$2.62 \cdot 10^{15}$	$2.52 \cdot 10^{23}$
$M^{n+} = Ca^{2+}$	$1.33 \cdot 10^{1}$	$4.98 \cdot 10^{1}$	2.00	$7.43 \cdot 10^{5}$
Complex	**B12C4**	**aza-B12C4**		**thio-B12C4**
$M^{n+} = Li^+$	$5.26 \cdot 10^{-3}$	7.78		$1.25 \cdot 10^{-2}$
$M^{n+} = Na^+$	$5.33 \cdot 10^{-3}$	$2.58 \cdot 10^{-1}$		$2.76 \cdot 10^{-3}$
$M^{n+} = K^+$	$1.83 \cdot 10^{-1}$	1.62		$2.09 \cdot 10^{-2}$
$M^{n+} = Mg^{2+}$	$1.76 \cdot 10^{7}$	$2.16 \cdot 10^{10}$		$1.76 \cdot 10^{4}$
$M^{n+} = Ca^{2+}$	$2.26 \cdot 10^{-6}$	$6.12 \cdot 10^{-6}$		$2.26 \cdot 10^{-9}$
Complex	**B9C3**	**aza-B9C3**		**thio-B9C3**
$M^{n+} = Li^+$	$4.69 \cdot 10^{-11}$	$4.67 \cdot 10^{-11}$		$3.70 \cdot 10^{-9}$
$M^{n+} = Na^+$	$1.59 \cdot 10^{-8}$	$2.15 \cdot 10^{-8}$		$2.45 \cdot 10^{-9}$
$M^{n+} = K^+$	$4.09 \cdot 10^{-6}$	$2.15 \cdot 10^{-7}$		$3.64 \cdot 10^{-7}$
$M^{n+} = Mg^{2+}$	$3.40 \cdot 10^{-30}$	$2.36 \cdot 10^{-26}$		$9.27 \cdot 10^{-27}$
$M^{n+} = Ca^{2+}$		$4.96 \cdot 10^{-29}$		$4.06 \cdot 10^{-31}$

Table S13: Change in Gibbs free energy [kJ mol^{-1}] for the complexation of Li^+, Na^+, K^+, Mg^{2+} and Ca^{2+} with aza-15-crown-5, benzo-15-crown-5, aza-benzo-15-crown-5 and thio-benzo-15-crown-5, simulated in vacuum.

Complex	**B15C5**	**aza-B15C5**	**thio-B15C5**	**aza-15C5**
$M^{n+} = Li^+$	-366.967931	-385.918522	-394.651777	-393.807461
$M^{n+} = Na^+$	-275.411458	-299.385098	-308.118353	-3.09E+02
$M^{n+} = K^+$	-165.988916	-190.476277	-208.684827	-204.605988
$M^{n+} = Mg^{2+}$	-1129.61508	-1188.40758	-1177.56236	-1202.09562
$M^{n+} = Ca^{2+}$	-823.09497	-872.183852	-873.896255	-888.348062
Complex	**B12C4**	**aza-B12C4**		**thio-B12C4**
$M^{n+} = Li^+$	-322.088187	-344.965297		-329.275511
$M^{n+} = Na^+$	-216.682853	-236.711809		-223.284796
$M^{n+} = K^+$	-146.689133	-126.423925		-149.012282
$M^{n+} = Mg^{2+}$	-1016.28182	-1056.22949		-1017.37384
$M^{n+} = Ca^{2+}$	-730.657888	-754.514133		-720.220781
Complex	**B9C3**	**aza-B9C3**		**thio-B9C3**
$M^{n+} = Li^+$	-195.561522	-212.322998		-199.650356
$M^{n+} = Na^+$	-133.213664	-142.014262		-139.174031
$M^{n+} = K^+$	-87.8715131	-88.1651408		-90.6184412
$M^{n+} = Mg^{2+}$	-722.033206	-764.91108		-757.477086
$M^{n+} = Ca^{2+}$	-505.171328	-525.398708		-519.91034

Table S14: Change in Gibbs free energy [kJ mol^{-1}] for the complexation of Li^+, Na^+, K^+, Mg^{2+} and Ca^{2+} (non-complexed simulated in H_2O) with aza-15-crown-5, benzo-15-crown-5, aza-benzo-15-crown-5 and thio-benzo-15-crown-5, simulated in DCM as modeled by a polarizable continuum model. No convergence of SCF runs could be achieved for B9C3-Ca^{2+}.

Complex	**B15C5**	**aza-B15C5**	**thio-B15C5**	**aza-15C5**
M^{n+} = Li^+	-31.1511765	-22.8745056	-13.6973962	-28.1322325
M^{n+} = Na^+	-27.1060243	-19.3569447	-31.9623417	-31.4666175
M^{n+} = K^+	-18.1809235	-8.32393318	-15.8656407	-16.530148
M^{n+} = Mg^{2+}	-109.376992	-107.15886	-88.0119127	-133.572312
M^{n+} = Ca^{2+}	-6.42082573	-9.68894657	-1.72199231	-33.511882
Complex	**B12C4**	**aza-B12C4**		**thio-B12C4**
M^{n+} = Li^+	13.00701249	-5.08469486		10.8623421
M^{n+} = Na^+	12.97550428	3.36264548		14.6109061
M^{n+} = K^+	4.205318921	-1.20227804		9.59185333
M^{n+} = Mg^{2+}	-41.3599515	-58.9843441		-24.2316419
M^{n+} = Ca^{2+}	32.22747873	29.7572805		49.3531055
Complex	**B9C3**	**aza-B9C3**		**thio-B9C3**
M^{n+} = Li^+	58.95546155	58.9693891		48.129879
M^{n+} = Na^+	44.52047632	43.7621102		49.1483592
M^{n+} = K^+	30.75743796	38.0531303		36.753017
M^{n+} = Mg^{2+}	168.206478	146.283669		148.594899
M^{n+} = Ca^{2+}		161.560871		173.474914

5.3. Solvent Simulation for 9-, 12- and 15-membered Crown Ethers

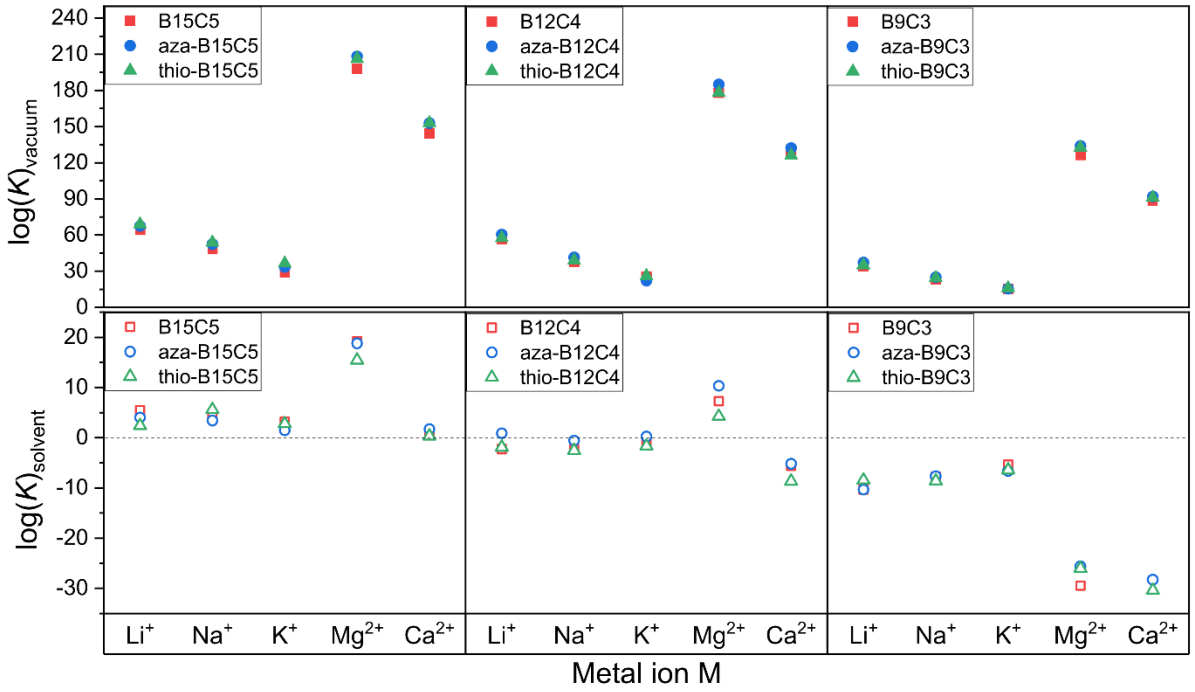

Figure S9: Logarithm of the equilibrium constant of complex formation of 15-, 12- and 9-membered CEs with different metal ions in vacuum (top) and with solvent simulation (bottom, Polarizable Continuum Model). No convergence of SCF runs could be achieved for B9C3-Ca^{2+}. Values were determined via DFT according to Equations 6 and 7. The dotted line illustrates $\log(K)_{solvent}=0$.

Compared to the results obtained in vacuum, the solvent-based complexation constants are significantly lower, due to the charged species in vacuum lacking the stabilization by the solvent as present in the experiment. In analogy to the observations in vacuum, a loss of stability of the complexes with decreasing ring size is evident. Negative values for $\log(K)$ indicate unfavorable formation of 9-membered complexes, 12-membered complexes with larger cations (Na^+, K^+, and Ca^{2+}) as well as (thio-)B12C4-Li^+. This might be due to the unfavorable size-relation between CE cavity and cation radius, possibly resulting in a ML_2 (sandwich) type complex. Based on this behavior, the complexation of Na^+, K^+, and Ca^{2+} can be selectively avoided. Independent of the heteroatom, a preferential complexation of Mg^{2+} for 15- and 12-membered CEs is present. Only for the 9-membered CEs, both divalent cations are complexed less than Li^+, Na^+ and K^+. In solvent environment, the trend for the alkali metal ions is less pronounced compared to vacuum. Similarly, however, the dimensions do not differ decisively. For B15C5, aza-B15C5 and B12C4, Li^+ complexation is favored, whereas thio-B15C5 appears to complex Na^+ preferentially. In fact, for nitrogen and sulfur analogs of B12C4, very small deviations are observed, and no clear trend can be identified. B12C4, along with the 9-membered CEs, exhibits the following trend: $K^+ > Na^+ > Li^+$, noticeably with a narrow variation.

Dependent on the type of complex, heteroatom substitution can lead to an improvement in complex stability. The presence of a sulfur atom in the CE ring leads in all cases (except for thio-B15C5-Na^+ and thio-B9C3-Li^+) to a reduced stability of the complexes, compared to the oxygen and nitrogen containing CEs. Although no significant influence of the substitution of an oxygen atom in the 15-membered system (with the exception of a slight improvement for thio-B15C5-Na^+) on the complex stability can be observed, the 12-membered CEs indicate a positive effect of the introduction of a nitrogen atom as a donor atom. Interestingly, the presence

of nitrogen in aza-B12C4 enables lithium to be complexed in the first place. The Mg/Li ratio, which is particularly interesting for selective lithium extraction from seawater, changes for the stable complexes as follows: aza-B12C4 < thio-B15C5 < aza-B15C5 < B15C5, with the most stable Li^+ incorporation into B15C5.

5.4. Calculation of the complex constant *K* from the liquid-liquid extraction

The following equations present more detailed information on the calculation of the equilibrium constant *K* from the experimental data. Due to the electroneutrality condition, only the activity, representing the deviation between the ideal and the real response of a salt in solution, of the entire system can be determined. Therefore, the mean activity coefficient $\gamma_{(+,-)}$ is applied for γ_+ and γ_-. According to Eq. **Fehler! Verweisquelle konnte nicht gefunden werden.**), $\gamma_{(+,-)}$ is calculated from the ionic charges z_+ and ν_-, a dimensionless factor A (literature values, here: 0.5019) and the ionic strength I_a (Eq. **Fehler! Verweisquelle konnte nicht gefunden werden.**)). The stoichiometric coefficient Q can be calculated by Eq. **Fehler! Verweisquelle konnte nicht gefunden werden.**) based on the stoichiometric factors of the cation and anion, *m* and *x*.

$$log(\gamma_{+,-}) = |z_+ \nu_-| \cdot A \cdot \sqrt{I_a} \quad (1)$$

$$I_a = \frac{1}{2}\sum_i c_i \cdot z_i^2 \quad (2)$$

$$Q = (m^m \cdot x^x)^{\frac{1}{m+x}} \quad (3)$$

The concentration of the salt $[M_m^{z+}X_x^{\nu-}]$ and the CE before complexation $[CE]_{bc}$ are known. The amount of the CE-metal complex can be determined by the salts of the aqueous phase. The indices *bc* and *ac* refer to the situation *before* and *after complexation*. The concentration of the complex $[(M_mCE_n)^{mz+}(X_x)^{x\nu-}_{(org)}]$ can be calculated from Eq. (4). The concentrations of cations and anions after the complexation are determined as shown in Eq. (5) and Eq. (6), with *m* and *x* being the stoichiometric factors of the metal ion and the corresponding anion. The concentration of the free CE after the complexation process is calculated from Eq. (7).

$$[(M_mCE_n)^{mz+}(X_x)^{x\nu-}_{(org)}] = [complex] = [M_m^{z+}X_x^{\nu-}]_{bc} - [M_m^{z+}X_x^{\nu-}]_{ac} \quad (4)$$

$$[M^{z+}]^m = [M_m^{z+}X_x^{\nu-}]_{bc} - (m \cdot [complex]^m) \quad (5)$$

$$[X^{\nu-}]^x = \frac{x}{m}[M_m^{z+}X_x^{\nu-}]_{bc} - (x \cdot [complex]^x) \quad (6)$$

$$[CE]^n = [CE]_{bc} - (n \cdot [complex]^n) \quad (7)$$

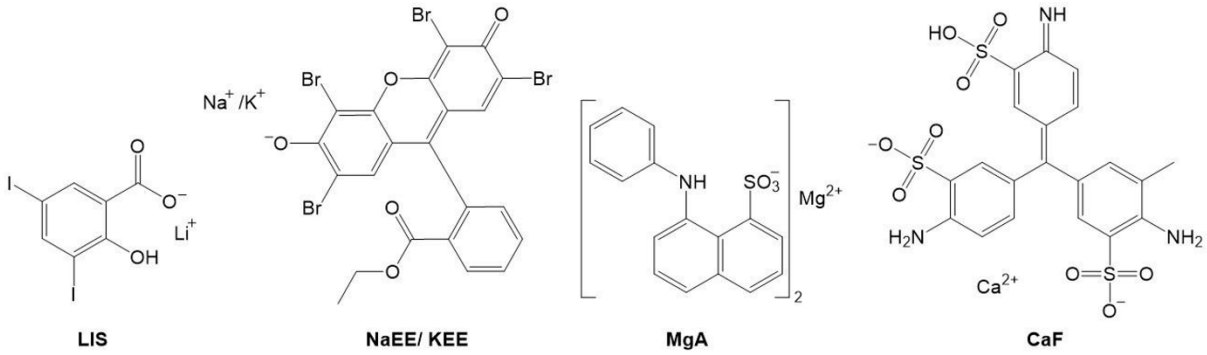

Figure S10: Salts used for LLE.

6. Input file for optimization of aza-15C5 in vacuum

```
%nprocshared = 32
%mem = 56GB
%Chk=aza-15c5_optfreqC.chk
#p opt=tight int=ultrafine freq b3lyp/def2tzvp geom=connectivity
empiricaldispersion=gd3bj

aza-15C5

0 1
 C                  1.50651492   -2.59255480    0.29029936
 C                  2.50326811   -1.46811358    0.33640907
 O                  0.20629625   -2.01868596    0.43898998
 H                  1.69523453   -3.31641665    1.08809791
 H                  1.57080198   -3.10180208   -0.67586402
 O                  2.14506904   -0.57898581   -0.71537429
 H                  3.51618205   -1.85531717    0.18821047
 H                  2.46435589   -0.96404534    1.30891925
 C                  2.95010820    0.59057235   -0.81644058
 C                  2.48770787    1.64217882    0.17076442
 H                  2.81383405    0.95534821   -1.83387050
 H                  4.00806831    0.35648045   -0.66749646
 H                  2.96433236    2.60127161   -0.05302052
 H                  2.72546045    1.37581821    1.20640756
 C                  0.44494361    2.81880549    0.67971992
 C                 -0.95491994    2.88691736    0.12523841
 H                  0.97455193    3.75542632    0.48552540
 H                  0.43612842    2.63508282    1.75932401
 O                 -1.49628330    1.57649699    0.24786410
 H                 -0.92801925    3.17863168   -0.93006478
 H                 -1.56030560    3.61104153    0.67837327
 C                 -2.71150190    1.36612425   -0.46422334
 C                 -3.14262941   -0.04043589   -0.14481834
 H                 -2.53739688    1.49513559   -1.53843626
 H                 -3.48056843    2.07649519   -0.14675870
 O                 -2.03151662   -0.89426852   -0.41340376
 H                 -4.00766069   -0.32979657   -0.74832146
 H                 -3.40882712   -0.11552377    0.91420091
 C                 -2.14052412   -2.17103524    0.21112221
 C                 -0.83669802   -2.88696875   -0.00459218
 H                 -2.96357538   -2.74779581   -0.22161096
 H                 -2.33079646   -2.03558562    1.28113511
 H                 -0.68889351   -3.11612721   -1.06507766
 H                 -0.82671654   -3.82293322    0.56179965
 N                  1.07620022    1.73338780    0.00578402
 H                  1.47032481    2.58888077   -0.76265393

 1 2 1.0 3 1.0 4 1.0 5 1.0
 2 6 1.0 7 1.0 8 1.0
 3 30 1.0
 4
 5
 6 9 1.0
 7
```

```
 8
 9 10 1.0 11 1.0 12 1.0
 10 13 1.0 14 1.0 35 1.0
 11
 12
 13
 14
 15 16 1.0 17 1.0 18 1.0 35 1.0
 16 19 1.0 20 1.0 21 1.0
 17
 18
 19 22 1.0
 20
 21
 22 23 1.0 24 1.0 25 1.0
 23 26 1.0 27 1.0 28 1.0
 24
 25
 26 29 1.0
 27
 28
 29 30 1.0 31 1.0 32 1.0
 30 33 1.0 34 1.0
 31
 32
 33
 34
 35 36 1.0
 36
```

Input file for optimization of aza-15C5 in DCM (based on optimization in vacuum):

```
%nprocshared = 32
%mem = 56GB
%Chk=aza-15c5_optfreqC.chk
#p opt freq b3lyp/def2tzvp geom=allcheck scrf=(solvent=dichloromethane)
empiricaldispersion=gd3bj formcheck
```

Input file for Hirshfeld analysis of aza-15C5 (based on optimization in vacuum):

```
%nprocshared = 32
%mem = 56GB
%Chk=aza-15c5_Hirshfeld.chk
#p SP b3lyp/def2tzvp geom=allcheck Pop=hirshfeld
```

Input file for NBO analysis of aza-15C5 (based on optimization in vacuum):

```
%nprocshared = 32
%mem = 56GB
%Chk= Li_azab15c5_NBO.chk
#p SP b3lyp/def2tzvp geom=allcheck Pop=(FULL,NBOread,savenbos) formcheck

$NBO PLOT FILE= NAME $END
```

9.3. SUPPORTING INFORMATION FOR PUBLICATION 2

The supporting information are reprinted with permission from S. Jaehnke, J. von Chamier Gliszczynski, B. Hankiewicz, V. Abetz, Systematic Investigation of a Crown Ether Functionalized PS-*b*-PMAA Block Copolymer for Optimized Lithium Extraction From Aqueous Media, *J. Polym. Sci*. (**2025**) 1–11. Published by Wiley Periodicals LLC.

Supporting Information

Systematic Investigation of a Crown Ether Functionalized PS-*b*-PMAA Block Copolymer for Optimized Lithium Extraction from Aqueous Media

Sabrina Jaehnke, Joachim von Chamier Gliszczynski, Birgit Hankiewicz, Volker Abetz*

Calculation of the complex constant *K* from the liquid-liquid extraction

The following equations offer a more detailed explanation of how the equilibrium constant *K* is calculated from the LLE data. Because of the electroneutrality condition, it is only possible to determine the mean activity coefficient $\gamma_{(+,-)}$, which illustrates the deviation between the ideal and real behavior of a salt in solution. Consequently $\gamma_{(+,-)}$ is applied for γ_+ and γ_-.

According to Eq. (1), $\gamma_{(+,-)}$ is calculated from the ionic charges z_+ and ν_-, a dimensionless factor *A* (literature values, in this case: 0.5019) and the ionic strength I_a (Eq. (2)). *Q*, the stoichiometric coefficient, can be derived from Eq. (3) using the stoichiometric factors of the cation M^{z+} and anion X^{v-}, *m* and *x*.

$$\log\left(\gamma_{+,-}\right) = |z_+ \nu_-| \cdot A \cdot \sqrt{I_a} \qquad \text{Eq. (1)}$$

$$I_a = \frac{1}{2}\sum_i c_i \cdot z_i^2 \qquad \text{Eq. (2)}$$

$$Q = \left(m^m \cdot x^x\right)^{\frac{1}{m+x}} \qquad \text{Eq. (3)}$$

The salt concentration $\left[M_m^{z+}X_x^{v-}\right]$ and the concentration of the CE (before complexation) $[CE]_{bc}$ are known. The complex concentration $[(M_mCE_n)^{mz+}(X_x)^{xv-}_{(org)}]$ simplified as [complex], can be calculated from the salt concentration before and after complexation (bc and ac) (Eq. (4)). The concentrations of cations and anions after the complexation are determined as shown in Eq. (5) and Eq. (6), with *m* and *x* being the stoichiometric factors of the metal ion and the anion. The concentration of the free CE, not present in a complex after the complexation process, is calculated from Eq. (7).

$$[(M_mCE_n)^{mz+}(X_x)^{xv-}_{(org)}] = [\text{complex}] = \left[M_m^{z+}X_x^{v-}\right]_{bc} - \left[M_m^{z+}X_x^{v-}\right]_{ac} \qquad \text{Eq. (4)}$$

$$\left[M^{z+}\right] = \left[M_m^{z+}X_x^{v-}\right]_{bc} - (m \cdot [\text{complex}]) \qquad \text{Eq. (5)}$$

$$\left[X^{v-}\right] = \frac{x}{m}\left[M_m^{z+}X_x^{v-}\right]_{bc} - (x \cdot [\text{complex}]) \qquad \text{Eq. (6)}$$

$$[CE] = [CE]_{bc} - (n \cdot [\text{complex}]) \qquad \text{Eq. (7)}$$

UV Vis measurements

Table S 1: Data of the UV-Vis measurements of the different PS-*b*-P(MAA-*r*-CE3MA) polymers and B9C3. Shown are the complexation constants *K* of the three independent measurements as well as the logarithm of the mean value and the standard deviation.

Sample-ID	*K* 1	*K* 2	*K* 3	Average log*K*	Standard deviation
P-MW-23	9.16E+13	5.29E+13	5.64E+13	13.81	0.11
P-MW-46	7.09E+13	8.14E+13	2.61E+14	14.06	0.25
P-MW-91	1.07E+15	2.19E+14	6.98E+14	14.74	0.29
P-MW-133	2.75E+16	2.75E+16	3.97E+15	15.69	0.22
P-MW-202	2.10E+16	8.38E+15	2.75E+16	16.23	0.22
P-MW-310	2.54E+16	1.61E+16	2.06E+16	16.31	0.08
P-R-92	8.42E+16	6.73E+16	5.53E+17	16.91	0.06
P-R-83	9.01E+14	2.30E+14	3.47E+14	14.62	0.25
P-R-69	7.09E+13	8.14E+13	2.61E+14	14.06	0.25
P-R-51	8.19E+13	8.17E+13	7.69E+13	13.90	0.01
P-R-35	2.65E+14	2.58E+13	6.04E+13	13.87	0.42
P-F-72	1.60E+18	8.11E+19	1.26E+18	18.26	0.04
P-F-40	2.10E+16	8.38E+15	2.75E+16	16.23	0.22
P-F-27	1.75E+15	1.05E+15	7.79E+14	15.05	0.15
P-F-13	3.52E+14	2.55E+14	3.42E+14	14.50	0.06
P-F-8	9.05E+14	4.56E+14	5.75E+13	14.46	0.51
P-C	2.59E+19	5.49E+18	1.63E+19	19.12	0.28
B9C3	2.52E+10	3.26E+10	2.57E+10	10.44	0.05

DLS measurements

Table S 2: DLS data. From the two exponential decay fit the hydrodynamic radii of the smaller polymer species before and after LLE. The extraction was three times repeated (A, B, and C). The averaged hydrodynamic radius and its averaged standard deviation are shown. All polymer solutions are measured at concentrations of 0.1 wt% in DCM.

	Before extraction	After extraction				
Sample-ID	**R_h 1 /nm**	**R_h A /nm**	**R_h B /nm**	**R_h C /nm**	**Average R_h /nm**	**Standard deviation**
P-MW-23	6.0	4.9	5.6	6.2	5.6	0.5
P-MW-46	7.6	7.1	7.2	7.3	7.2	0.1
P-MW-91	11.1	10.0	8.8	11.0	10.0	0.9
P-MW-133	14.3	14.3	13.0	12.7	13.3	0.7
P-MW-202	15.3	13.5	13.8	13.7	13.6	0.2
P-MW-310	17.5	14.7	14.0	14.1	14.2	0.3
P-R-92	15.4	14.7	14.1	15.0	8.7	0.4
P-R-83	11.3	10.7	9.8	12.9	11.1	1.3
P-R-69	7.6	7.1	7.2	7.3	7.2	0.1
P-R-51	5.9	14.0	14.6	13.7	14.1	0.4
P-R-35	7.5	15.4	18.9	18.4	17.6	1.5
P-F-72	15.8	14.0	15.1	16.2	15.1	0.9
P-F-40	14.3	13.5	13.8	13.7	13.6	0.2
P-F-27	15.8	14.8	13.8	-	14.3	0.5
P-F-13	15.6	13.8	13.7	14.6	14.0	0.4
P-F-8	15.8	14.0	15.1	16.2	15.1	0.9

Table S 3: DLS data. From the two exponential decay fit the hydrodynamic radii of the larger polymer species before and after LLE. The extraction was three times repeated (A, B, and C). The averaged hydrodynamic radius and its averaged standard deviation are shown. All polymer solutions are measured at concentrations of 0.1 wt% in DCM.

	Before extraction	After extraction				
Sample-ID	**R_h 1 /nm**	**R_h A /nm**	**R_h B /nm**	**R_h C /nm**	**Average R_h /nm**	**Standard deviation**
P-MW-23	64.5	36.6	55.2	60.2	50.7	10.2
P-MW-46	69.4	57.7	58.7	64.9	60.4	3.2
P-MW-91	20.1	14.3	11.2	14.0	13.2	1.4
P-MW-133	49.6	35.4	27.0	32.9	31.8	3.5
P-MW-202	46.9	43.6	43.7	42.5	43.3	0.6
P-MW-310	66.6	76.6	73.0	72.3	74.0	1.9
P-R-92	67.9	10.6	66.6	75.5	70.9	3.6
P-R-83	33.5	27.6	19.7	50.8	32.7	13.2
P-R-69	69.4	57.7	58.7	64.9	60.4	3.2
P-R-51	53.2	49.7	56.5	50.9	52.4	3.0
P-R-35	66.5	108.0	129.3	98.2	111.8	13.0
P-F-72	90.5	93.6	78.5	93.7	88.6	7.1
P-F-40	54.5	43.6	43.7	42.5	43.3	0.6
P-F-27	32.8	54.5	55.9	-	77.4	31.5
P-F-13	83.7	43.7	42.5	52.8	46.3	4.6
P-F-8	84.1	103.5	93.1	98.0	98.2	4.2

Synthesis of CTPPA

The synthesis was carried out according to Xu *et al*. but slightly modified.[1] In the first step of the two-step synthesis, propanethiol (55.2 mmol, 4.20 g) was slowly dripped into a solution of KOH (69.2 mmol, 3.88 g) in water (20 mL). Carbon disulfide (55.2 mmol, 4.20 g) was added and stirred for 30 minutes at room temperature. *p*-Tosyl chloride (28.1 mmol, 5.35 g) was dissolved in 28 mL acetone and slowly dripped into the reaction mixture at -5°C. After 2 h, the reaction was terminated, the acetone removed and extracted with DCM. The organic phase, washed with water and dried over magnesium sulphate, was dried. Bis (propylsulfanylthiocarbonyl) disulfide was obtained as red oil (6.29 g, 74%). In the second step, bis (propylsulfanylthiocarbonyl) disulfide (19.9 mmol, 6.02 g) and 4,4′-azobis(4-cyanovaleric

acid) (ACVA, 40.2 mmol, 11.3 g) were dissolved in ethyl acetate (150 mL). After reacting at 85 °C for 24 h, the solvent was removed and the product was purified by column chromatography (silica gel, ethyl acetate/cyclohexane (1/3 *V*/*V*)+1% acetic acid). An orange solid was obtained (6.13 g, 50%). ^{1}H NMR (300 MHz, $CDCl_3$, 296 K): δ [ppm] = 3.33 (t, ^{3}J = 6 Hz, 2H, -S-CH2-CH2-CH3), 2.75–2.32 (m, 4H, COOH-CH2-CH2-C-), 1.89 (s, 3H, -C-CH3), 1.73 (dt, ^{3}J =15 Hz, 2H, -S-CH2-CH2-CH3), and 1.03 (t, ^{3}J = 7 Hz, 3H, -S-CH2-CH2-CH3).

Synthesis of (2,3,5,6-tetrahydrobenzo[*b*][1,4,7]trioxonin-9-yl)methanol

Benzo-9-crown-3 (B9C3) was synthesized according to Khazaei *et al.*[2] The synthesis was carried out in the absence of oxygen. A solution of lithium hydroxide (0.925 mol, 22.2 g), catechol (0.462 mol, 50.9 g) and water (1800 mL) was purged with nitrogen for one hour. Bis-2-chloroethyl ether (0.462 mol, 66.1 g) was added dropwise with vigorous stirring. After room temperature for 30 minutes, the reaction was heated to reflux for 72 hours. Purification was performed by steam distillation, B9C3 was obtained as colorless crystals (15.0 g, 18%). The functionalization of B9C3 was carried out according to an adapted procedure by Liu *et al.* and Smith *et al.*[3,4] The synthesis was carried out in the absence of oxygen. In the first step, 2,3,5,6-tetrahydrobenzo[*b*][1,4,7]trioxonine-9-carbaldehyde (B9C3-CHO) was produced. B9C3 (88.1 mmol, 15.87 g) and hexamethylenetetramine (88.1 mmol, 12.34 g) were dissolved in trifluoroacetic acid (TFA, 75 mL). The reaction was performed at 90 °C for a total of 5.5 h. After 4 h, 150 mL of water was added. Neutralization was done with sodium bicarbonate. The mixture was extracted with DCM, the organic phases were washed with water and then dried over magnesium sulphate. After removal of the solvent, the product was purified by column chromatography (silica gel, dry-load, ethyl acetate/heptane (3/1 V/V)). B9C3-CHO was obtained as a slightly yellowish liquid (7.12 g, 39%). To reduce the aldehyde to (2,3,5,6-tetrahydrobenzo[*b*][1,4,7]trioxonin-9-yl)methanol (B9C3-MeOH), B9C3-CHO (24.5 mmol, 5.10 g) was dissolved in methanol (75 mL). Sodium borohydride (51.5 mmol, 1.95 g) was added at 0 °C. After 2 h, water (100 mL) was added. The mixture was extracted with DCM and the combined organic phases were dried over magnesium sulphate. After removal of the solvent, B9C3-MeOH was obtained as a yellowish, highly viscous liquid (5.10 g, 99%). ^{1}H-NMR (500 MHz, CDCl3, 296 K): δ [ppm] = 7.06–6.90 (m, 3H, -Ph-H), 4.59 (m, 2H, -CH_2-OH), 4.47–4.26 (m, 4H, Ph-O-CH_2-), 3.98–3.87 (m, 4H, Ph-O-CH_2-CH_2-). Elemental analysis (%): *calcd*. for $C_{11}H_{14}O_4$, C 62.85, H 6.71, N 0.00, S 0.00, O 30.44 *found,* C 60.79, H 6.84, N 0.00, S 0.00, O 30.95. MS (ESI): m/z *calcd*. for $C_{11}H_{14}O_4$ $[M+Na]^+$ 233.0784, *found* 233.0793.

Polymer synthesis and functionalization

Table S 4: Weighing of MAA, CTPAA, styrene, ACVA and sodium hydrogen carbonate for the polymer syntheses. Dispersities determined via SEC (via RI detector).

Sample-ID	***n* MAA /mmol**	***n* CTPPA /mmol**	***n* styrene /mmol**	***n* ACVA /mmol**	***n* $NaHCO_3$ /mmol**	***Đ* (SEC, IR)**
P-MW-23	21.5	0.500	76.5	0.150	0.525	1.2
P-MW-46/ P-R-69	27.3	0.300	93.6	0.090	0.315	1.2
P-MW-91	22.0	0.120	73.8	0.036	0.126	1.4
P-MW-133	33.0	0.120	111	0.036	0.126	1.5
P-MW-202	60.0	0.150	195	0.045	0.158	1.5
P-MW-310	18.5	0.030	61.5	0.003	0.011	1.7
P-F-72	60.0	0.150	195	0.045	0.158	1.5
P-F-40						
P-F-27						
P-F-13						
P-F-8						
PMAA macro-CTA	109	1.2	-	0.120	0.42	-
P-C	2.565	0.015	41.1	0.002	0.00525	1.7
Sample-ID	***n* PMAA macro-CTA /mmol**		***n* styrene /mmol**	***n* ACVA /mmol**	***n* $NaHCO_3$ /mmol**	***Đ* (SEC, IR)**
P-R-92	0.040		60.000	0.008	0.028	1.6
P-R-83	0.080		56.000	0.016	0.056	1.6
P-R-51	0.250		36.000	0.050	0.175	1.2
P-R-35	0.350		27.300	0.070	0.245	1.2

Table S 5: Weighing of CE, Polymer, TPP, and DIAD for the polymer functionalization.

Sample-ID	***n* CE /mmol**	***n* polymer /mmol**	***n* TPP /mmol**	***n* DIAD /mmol**
P-MW-23	4.674	9.348	28.04	28.04
P-MW-46	2.383	4.767	14.30	14.30
P-MW-91	3.187	6.375	19.12	19.12
P-MW-133	4.772	9.545	28.63	28.63
P-MW-202	4.983	9.966	29.90	29.90
P-MW-310	0.929	1.859	5.570	5.570
P-R-92	0.246	0.587	1.760	1.760
P-R-83	1.743	3.486	10.46	10.46
P-R-69	2.383	4.767	14.30	14.30
P-R-51	6.100	12.20	36.60	36.60
P-R-35	4.648	9.296	27.89	27.89
P-F-72	0.925	1.186	3.356	3.356
P-F-40	4.983	9.966	29.90	29.90
P-F-27	0.8306	2.373	7.120	7.120
P-F-13	0.3204	2.373	7.120	7.120
P-F-8	0.4747	4.747	14.24	14.24
P-C	0.4759	0.4759	1.428	1.428

NMR data

It was to be ensured that no polymer was transferred to the aqueous phase during extraction. The aqueous phases were dried and dissolved in deuterium oxide. ^{1}H NMR spectra were measured (Figure S 1 - Figure S 5).

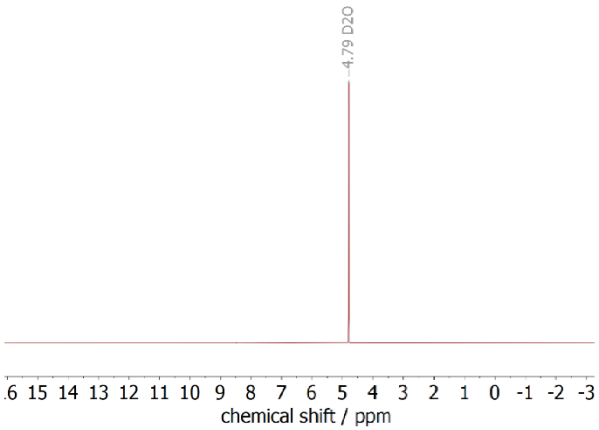

Figure S 1: ^{1}H-NMR Spectrum of P-R-92 (400 MHz, D_2O, 299.5 K).

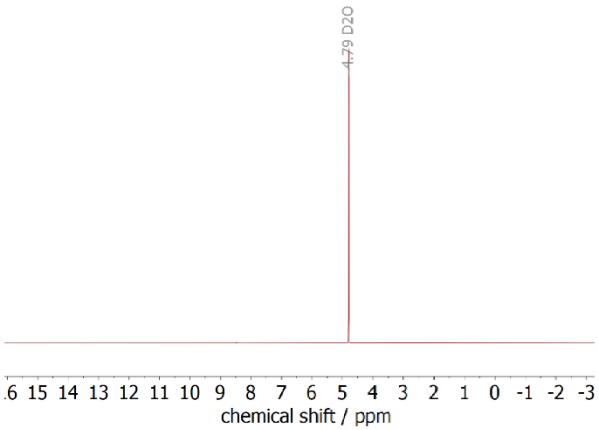

Figure S 2: ^{1}H-NMR Spectrum of P-R-83 (400 MHz, D_2O, 299.5 K).

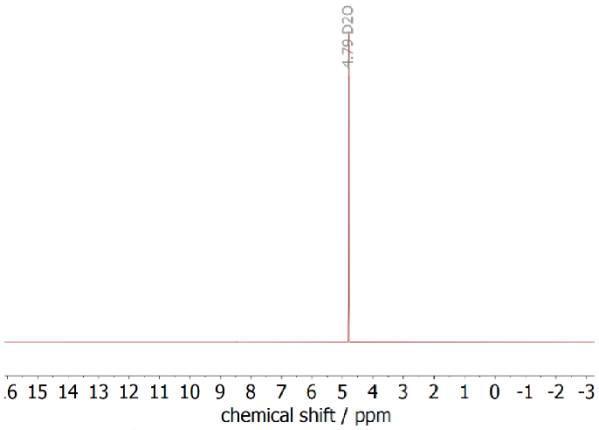

Figure S 3: ^{1}H-NMR Spectrum of P-R-69 (400 MHz , D_2O, 299.5 K).

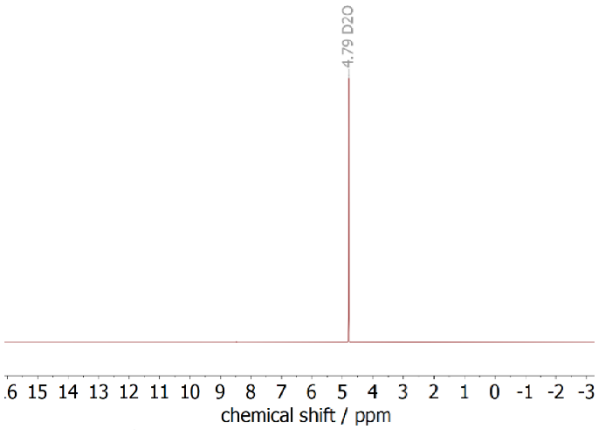

Figure S 4: ^{1}H-NMR Spectrum of P-R-51 (400 MHz, D_2O, 299.5 K).

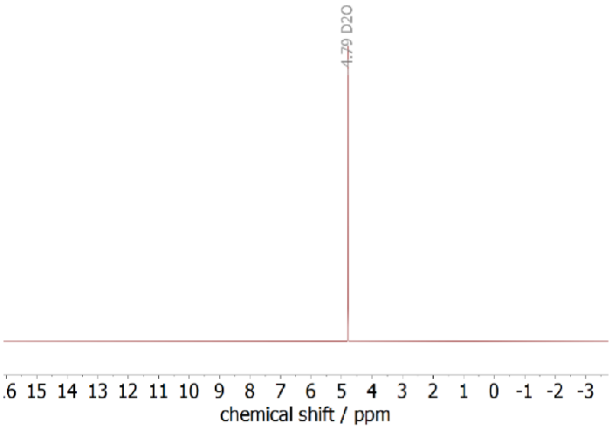

Figure S 5: ^{1}H-NMR Spectrum of P-R-35 (400 MHz, D_2O, 299.5 K).

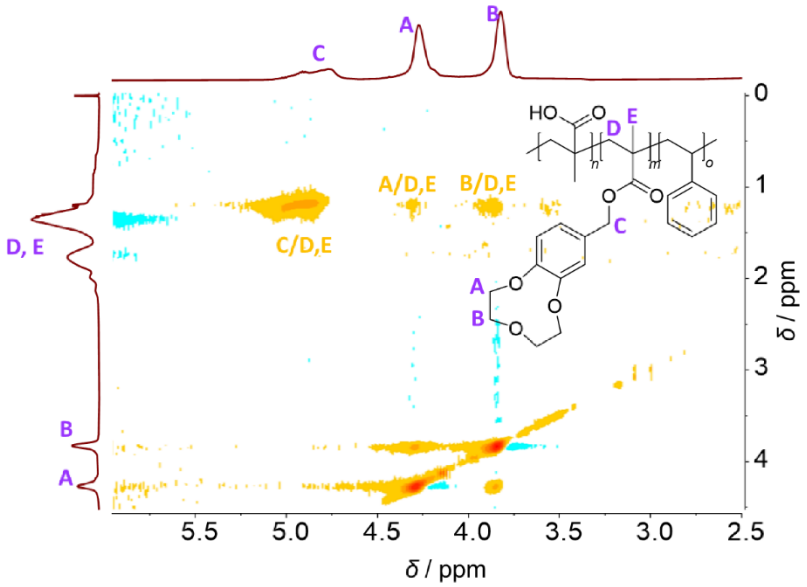

Figure S 6: Illustration of PS-*b*-P(MAA-*r*-CE3MA) and NOESY spectrum of P-MW-23 (400 MHz, $CDCl_3$, 295 K). The region in which the coupling of the CE and backbone signals can be seen is shown explicitly.

DOSY NMR

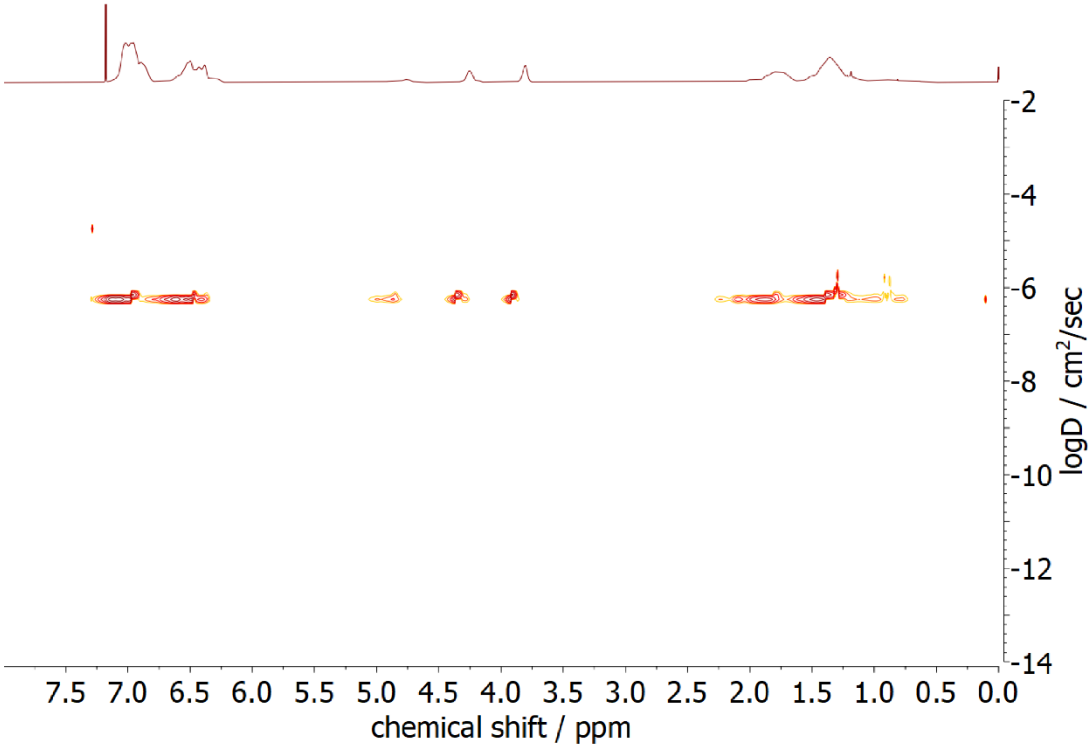

Figure S 7: DOSY spectrum of P-MW-23 (600 MHz, $CDCl_3$, 298 K) before extraction. The chemical shift in ppm is shown on the horizontal axis and the logarithm of the diffusion coefficient on the vertical axis.

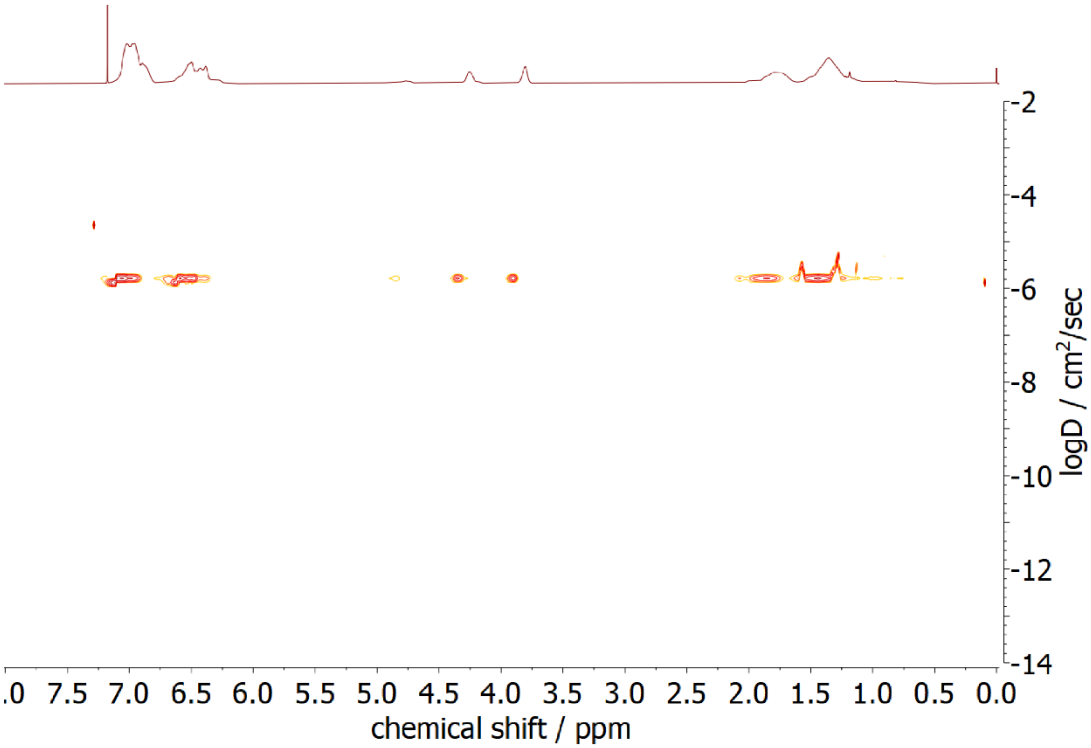

Figure S 8: DOSY spectrum of P-MW-23 (600 MHz, $CDCl_3$, 298 K) after extraction. The chemical shift in ppm is shown on the horizontal axis and the logarithm of the diffusion coefficient on the vertical axis.

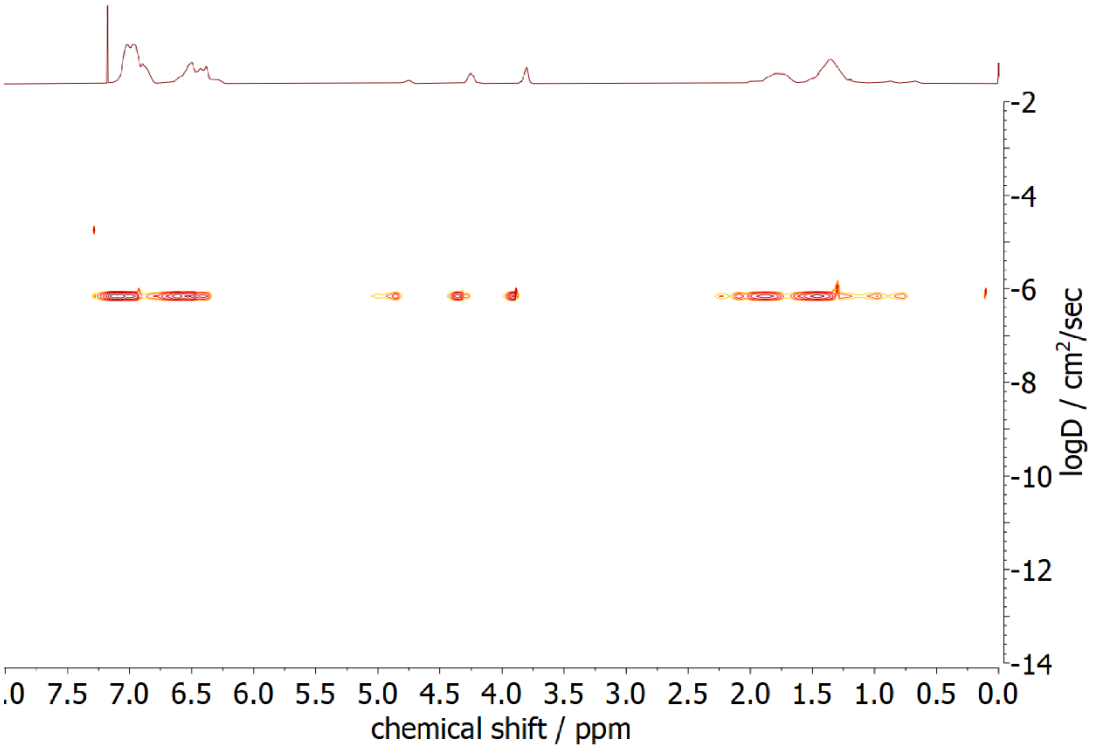

Figure S 9: DOSY spectrum of P-MW-46 (600 MHz, $CDCl_3$, 298 K) before extraction. The chemical shift in ppm is shown on the horizontal axis and the logarithm of the diffusion coefficient on the vertical axis.

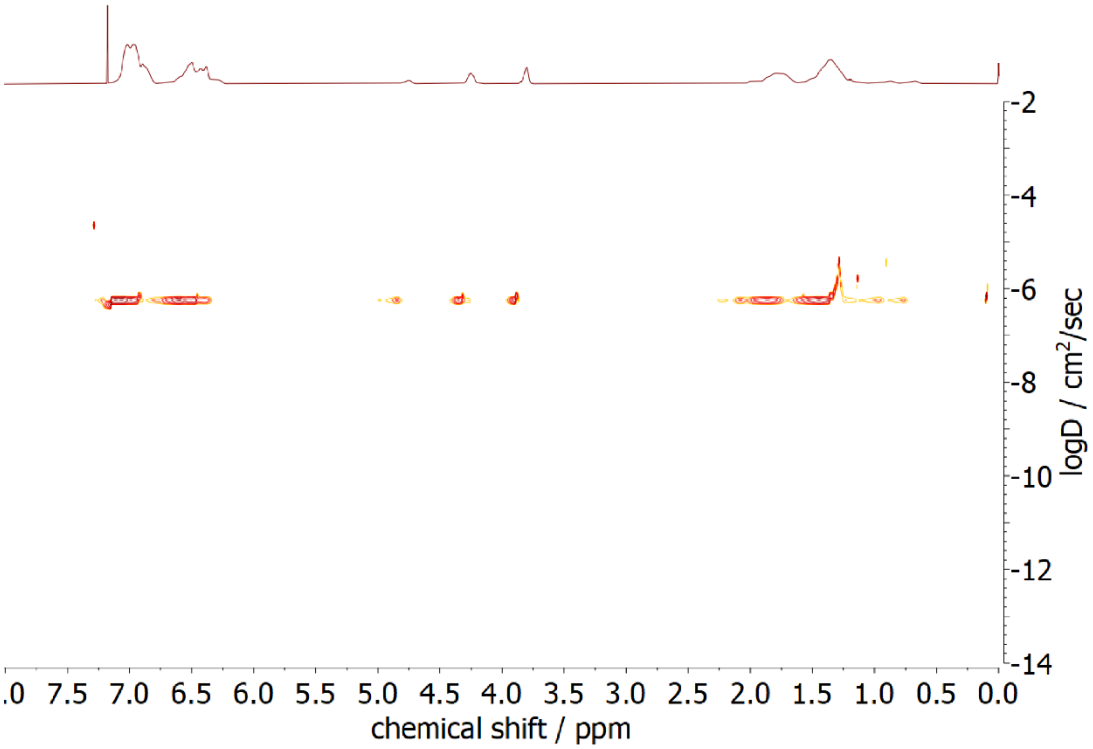

Figure S 10: DOSY spectrum of P-MW-46 (600 MHz, $CDCl_3$, 298 K) after extraction. The chemical shift in ppm is shown on the horizontal axis and the logarithm of the diffusion coefficient on the vertical axis.

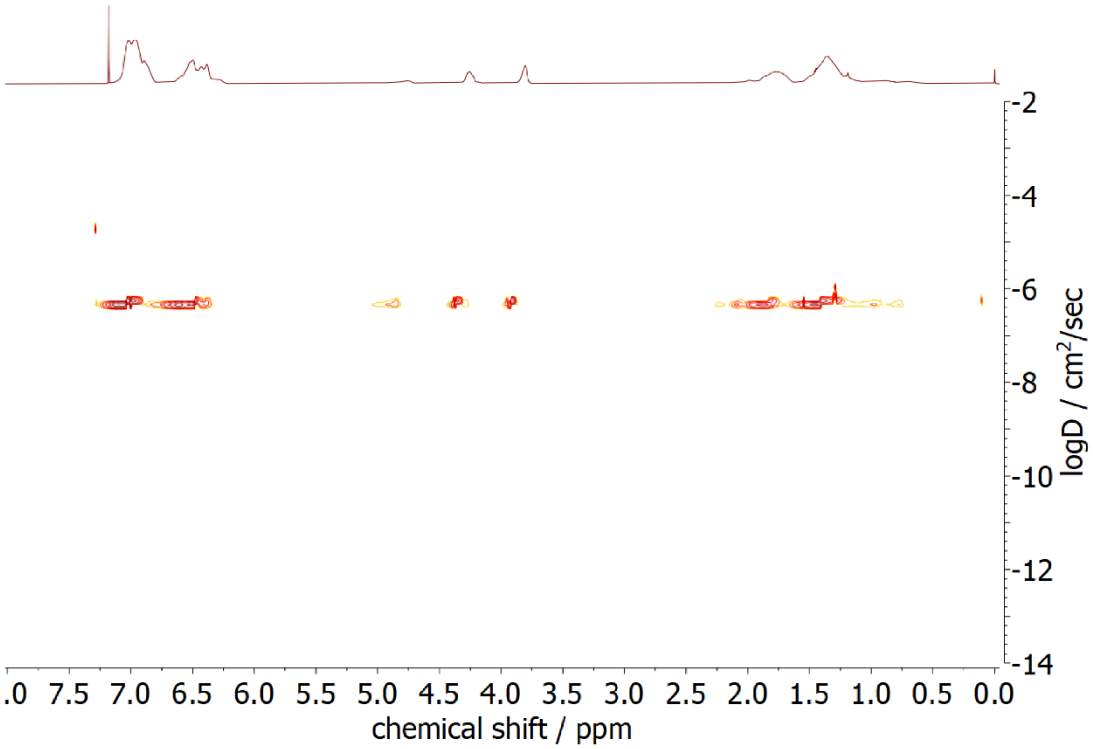

Figure S 11: DOSY spectrum of P-MW-91 (600 MHz, $CDCl_3$, 298 K) before extraction. The chemical shift in ppm is shown on the horizontal axis and the logarithm of the diffusion coefficient on the vertical axis.

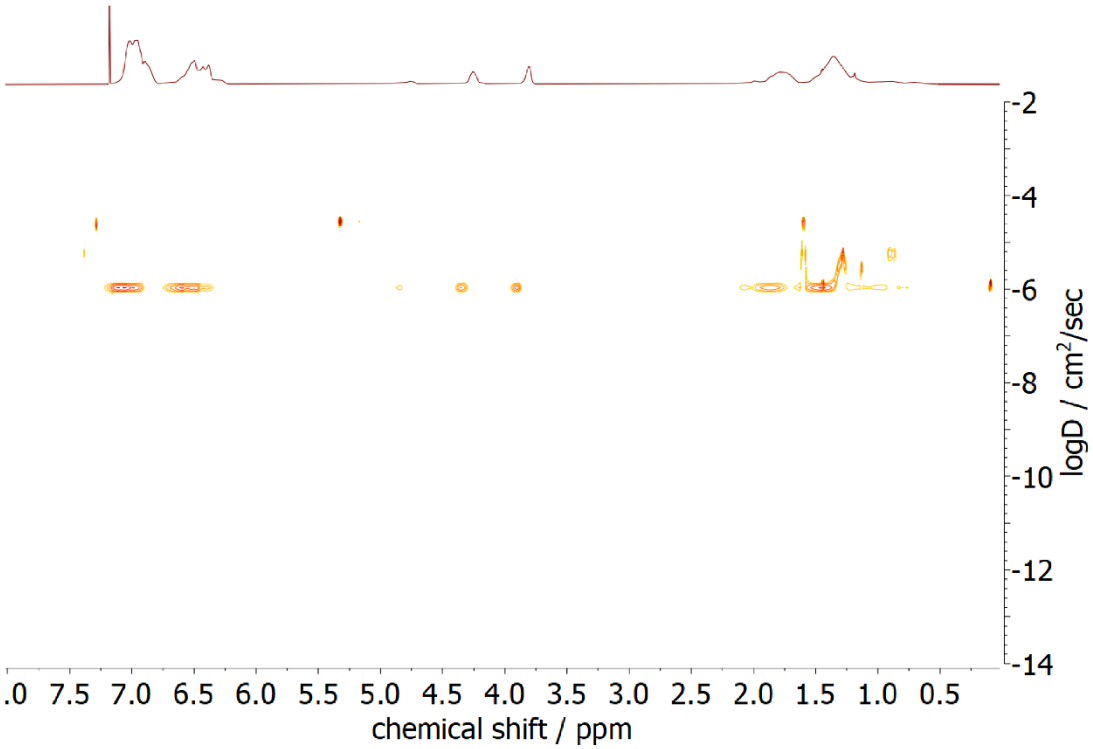

Figure S 12: DOSY spectrum of P-MW-91 (600 MHz, $CDCl_3$, 298 K) after extraction. The chemical shift in ppm is shown on the horizontal axis and the logarithm of the diffusion coefficient on the vertical axis.

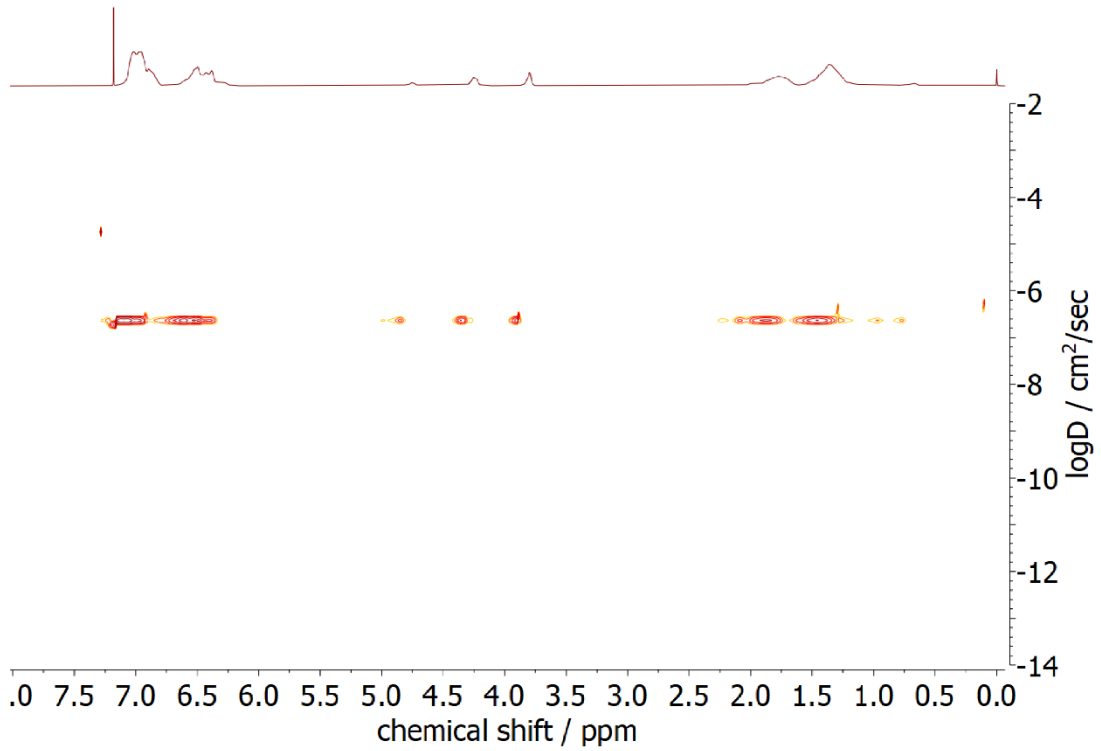

Figure S 13: DOSY spectrum of P-MW-133 (600 MHz, $CDCl_3$, 298 K) before extraction. The chemical shift in ppm is shown on the horizontal axis and the logarithm of the diffusion coefficient on the vertical axis.

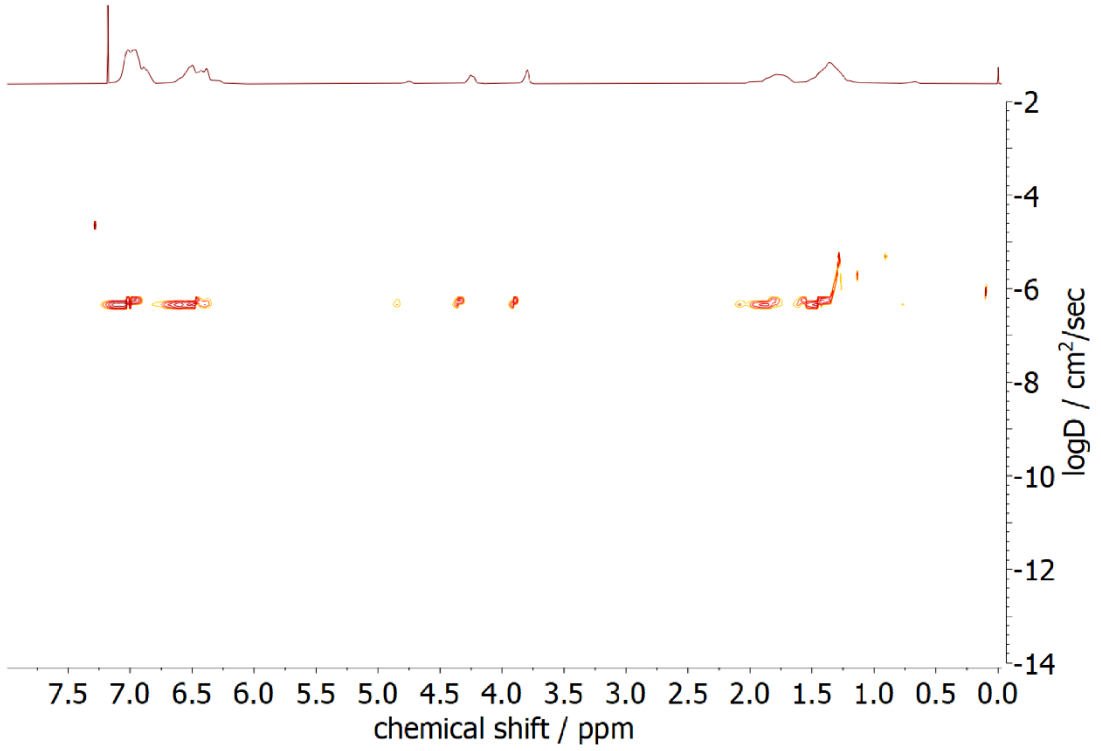

Figure S 14: DOSY spectrum of P-MW-133 (600 MHz, $CDCl_3$, 298 K) after extraction. The chemical shift in ppm is shown on the horizontal axis and the logarithm of the diffusion coefficient on the vertical axis.

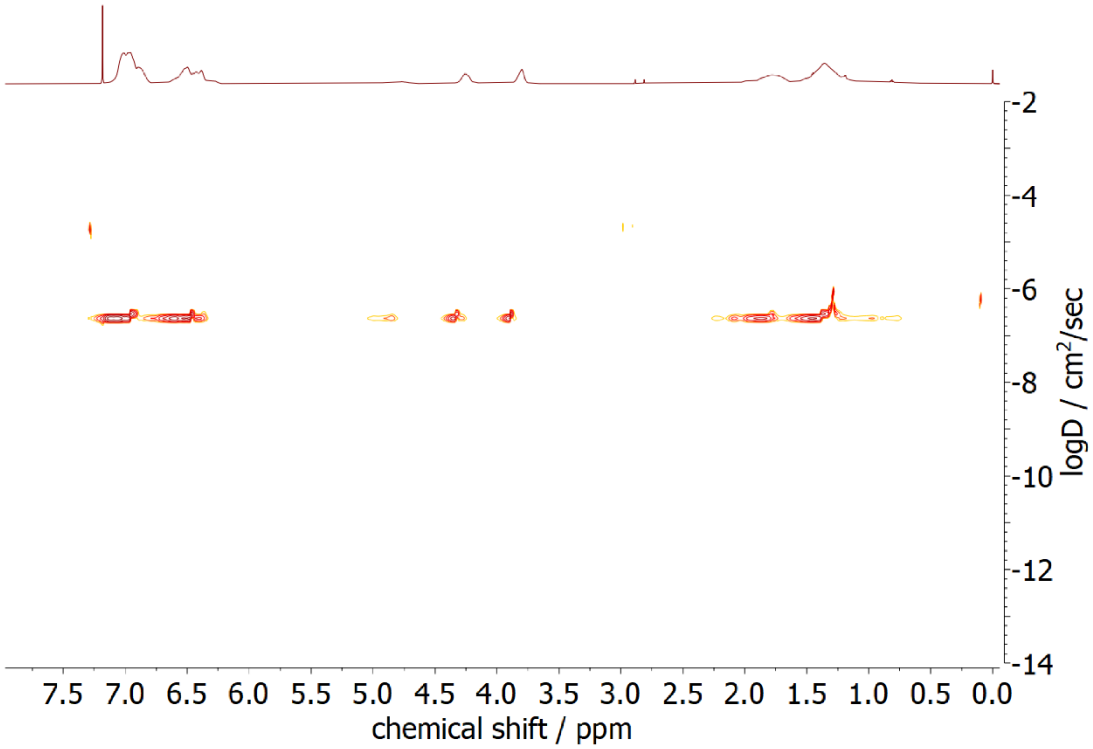

Figure S 15: DOSY spectrum of P-MW-202 (600 MHz, $CDCl_3$, 298 K) before extraction. The chemical shift in ppm is shown on the horizontal axis and the logarithm of the diffusion coefficient on the vertical axis.

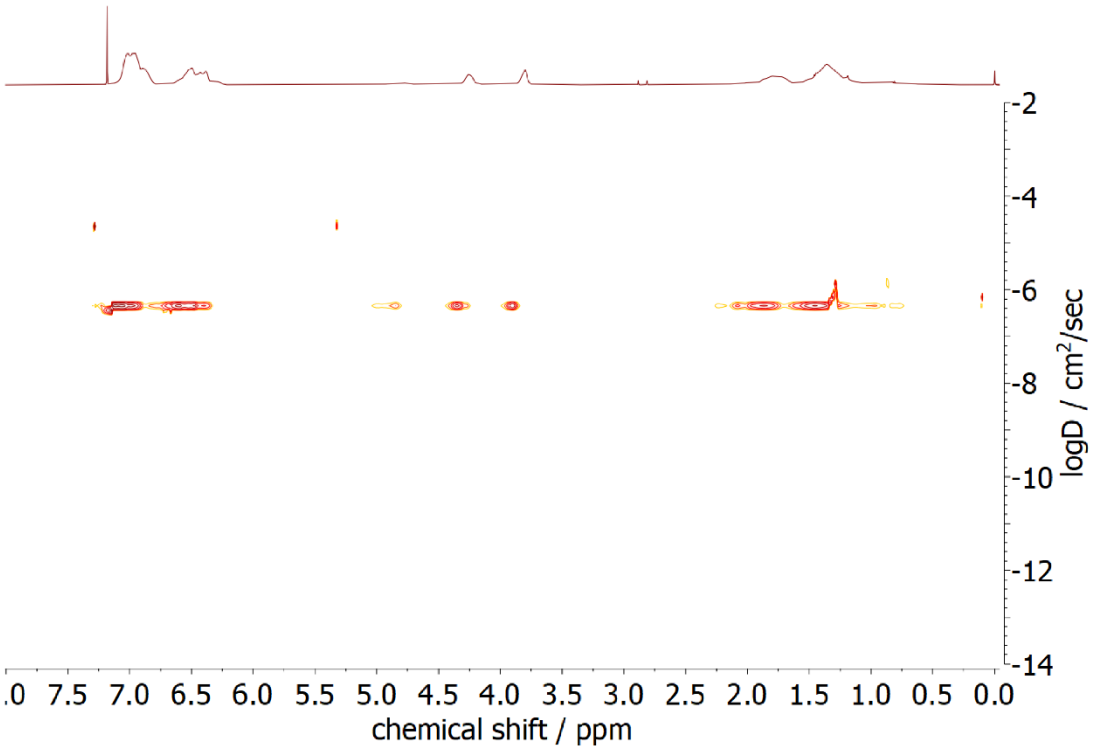

Figure S 16: DOSY spectrum of P-MW-202 (600 MHz, $CDCl_3$, 298 K) after extraction. The chemical shift in ppm is shown on the horizontal axis and the logarithm of the diffusion coefficient on the vertical axis.

DLS measurements

Table S 6: Polydispersity indices (PDIs) determined by DLS of the two species determined by the two-decay fit.

Sample-ID		number	PDI1	PDI2
P-MW-23	before extraction		0.17282	0.13198
	after extraction	A	0.17324	0.14922
		B	0.11585	0.11573
		C	0.11418	0.08929
P-MW-46	before extraction		0.10570	0.08798
and P-R-69	after extraction	A	0.08965	0.08597
		B	0.09892	0.10207
		C	0.06674	0.08574
P-MW-91	before extraction		0.13468	0.16367
	after extraction	A	0.08602	0.18734
		B	0.05216	0.18316
		C	0.04223	0.18667
P-MW-133	before extraction		0.33420	0.15009
	after extraction	A	0.23874	0.15002
		B	0.22651	0.14749
		C	0.18566	0.15386
P-MW-202	before extraction		0.19067	0.20028
and P-F-40	after extraction	A	0.20746	0.18848
		B	0.20400	0.18999
		C	0.20038	0.19233
P-MW-310	before extraction		0.27845	0.19314
	after extraction	A	0.25285	0.24169
		B	0.28642	0.25872
		C	0.29561	0.25797
P-R-92	before extraction		0.24781	0.21415
	after extraction	A	0.22081	0.20229
		B	0.22487	0.19684
		C	0.22420	0.20281
P-R-93	before extraction		0.26076	0.15227
	after extraction	A	0.15609	0.17156
		B	0.16917	0.15274
		C	0.16504	0.15125
P-R-51	before extraction		0.13410	0.10396
	after extraction	A	0.20808	0.16656
		B	0.22074	0.18162

Sample-ID		number	PDI1	PDI2
		C	0.25139	0.20782
P-R-35	before extraction		0.17168	0.20014
	after extraction	A	0.20265	0.21736
		B	0.19720	0.20279
		C	0.18348	0.19640
P-F-72	before extraction		0.30664	0.17417
	after extraction	A	0.32559	0.17191
		B	0.33455	0.16040
P-F-27	before extraction		0.10113	0.23327
	after extraction	A	0.17480	0.17171
		B	0.16086	0.16095
		C	0.15954	0.16259
P-F-13	before extraction		0.18491	0.16343
	after extraction	A	0.18621	0.18591
		B	0.18994	0.18152
		C	0.18937	0.19036
P-F-8	before extraction		0.17972	0.1663
	after extraction	A	0.18097	0.18352
		B	0.16086	0.16095
		C	0.15954	0.16259

Calculation of Hansen Solubility Parameters

In order to estimate the affinities of the solvents used in the LLE to the polymer blocks PS, PMAA and PCE3MA, Hansen solubility parameters were calculated as follows (Eq. (8)),

$$\delta_t=\sqrt{\delta_d^2+\delta_p^2+\delta_{hb}^2} \qquad \text{Eq. (8)}$$

with the total solubility parameter δ_t, the dispersion Hansen solubility parameter δ_d, the polar Hansen solubility parameter δ_p, and the hydrogen-bonding Hansen solubility parameter δ_{hb}.[5,6]

For PMAA, PS, water and dichloromethane, the solubility parameters are known. For PCE3MA, they can be calculated via group contribution method according to Stefanis and Panayiotou (Eq. (9)).[6]

$$f(x)=\left(\sum_i N_i C_i + W\sum_j M_j D_j + X\right) \mathrm{MPa}^{\frac{1}{2}} \qquad \text{Eq. (9)}$$

C_i is the contribution of the first-order group of type i and N_i is the occurrence of it in the molecule, whereas D_j is the contribution of the second-order group of type j and N_j is the occurrence of it in the molecule. X equals 17.3231 $\mathrm{MPa}^{\frac{1}{2}}$ for f(x)= δ_d, 7.3548 $\mathrm{MPa}^{\frac{1}{2}}$ for f(x)= δ_p, and 7.9793 $\mathrm{MPa}^{\frac{1}{2}}$ for f(x)= δ_p. W equals 0 for molecules without second-order groups and 1 with second-order groups. The corresponding values for PCE3MA are listed in Table S 7.

Table S 7: First- and second-order contributions of functional groups inherent in PCE3MA to Hansen solubility parameters δ_d, δ_p, and δ_{hb} [$\mathrm{MPa}^{\frac{1}{2}}$] as well as appearance of the functional groups in the molecule N_i and M_j.[6]

Groups	δ_d	δ_p	δ_{hb}	N_i
	First-order contributions			
$-CH_3$	-0.9714	-1.6448	-0.7813	1
$-CH_2-$	-0.0269	-0.3045	-0.4119	2
>C<	1.2686	2.0838	0.0866	1
COO	0.2039	3.4637	1.1389	1
$ACCH_2-$	0.6933	0.6517	-0.1375	1
ACH	0.1105	-0.5305	-0.4305	3
AC	0.8446	0.6187	0.0084	2
CH_2O(cyclic)	0.2753	0.1994	-0.161	3
	Second-order contributions			M_j
AC-O-C	0.2568	0.8153	0.6092	2

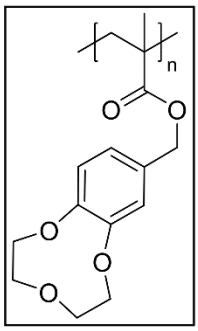

The Hansen solubility parameters for PCE3MA calculated from the group contribution method and the literature values for the Hansen solubility parameters of PS, PMAA, dichloromethane and water are shown in Table S 8 along with the molar volume V_m.

Table S 8: Hansen solubility parameters [$MPa^{\frac{1}{2}}$] and molar volume [mL/mol] for different polymers and solvents.

	δ_d	δ_p	δ_{hb}	δ_t	V_m
PS	21.3[5]	5.8[5]	4.3[5]	22.5	
PMAA	17.39[7]	12.48[7]	15.96[7]	26.7	
PCE3MA	21.82	13.17	6.92	26.4	
Dichloromethane	18.2[5]	6.3[5]	6.1[5]	20.2	63.9[7]
Water	15.5[5]	16[5]	42.4[5]	47.9	18.0[5]

The Flory-Huggins interaction parameter $\chi_{polymer\text{-}solvent}$ can be calculated using Eq. (10) and describes the compatibility of polymer with solvent. α is a universal value which is generally assumed to be 0.6, R is the universal gas constant (8.314 J mol K^{-1}) and T is the temperature (298.15 K). The result is the values in Table S 9.

$$\chi_{12}=\alpha\frac{V_m}{RT}\left((\delta_{d,1}-\delta_{d,2})^2+0.25(\delta_{p,1}-\delta_{p,2})^2+0.25(\delta_{hb,1}-\delta_{hb,2})^2\right) \qquad \text{Eq. (10)}$$

Table S 9: Flory-Huggins interaction parameter $X_{polymer\text{-}solvent}$ of PMAA, PCE3MA and PS with dichloromethane and water.

X	**DCM**	**water**
PS	0.16	1.83
PMAA	0.53	0.78
PCE3MA	0.39	1.55

SEC Traces

The SEC data (RI detector) of the various PS-*b*-PMAA diblock copolymers are shown in Figure S 17 to S 27. The MWs are relative, not absolute. Calibration based on PS standards results in a ratio between the theoretical number-average molecular weight and the number-average molecular weight determined via SEC of approximately 0.6.

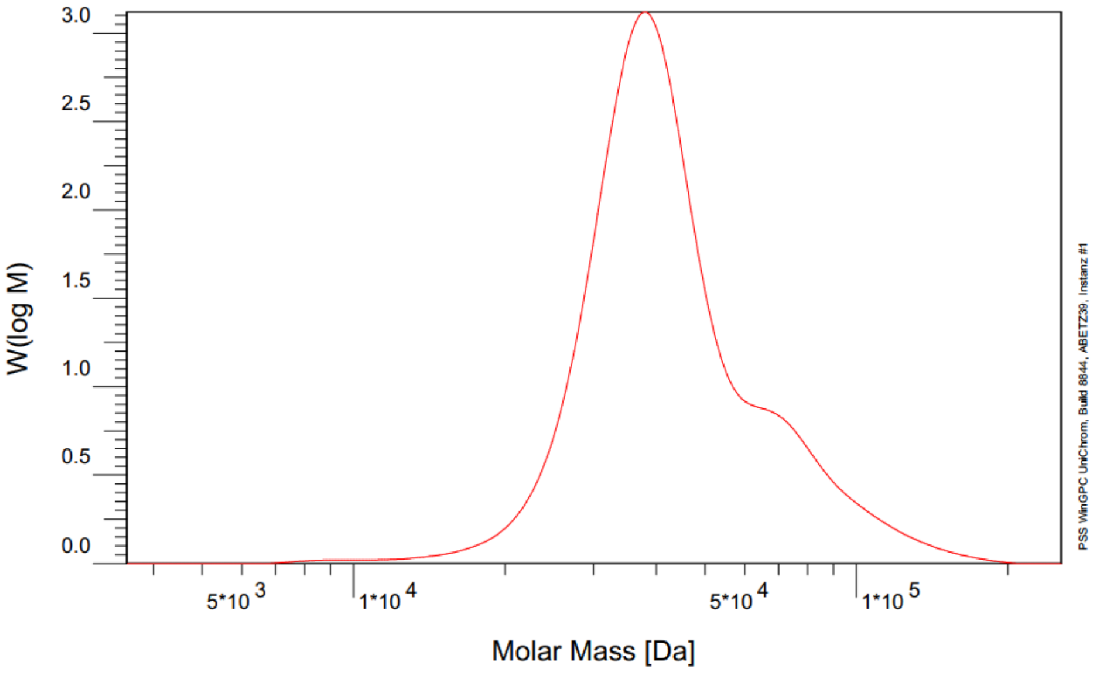

Figure S 17: SEC data for P-MW-23.

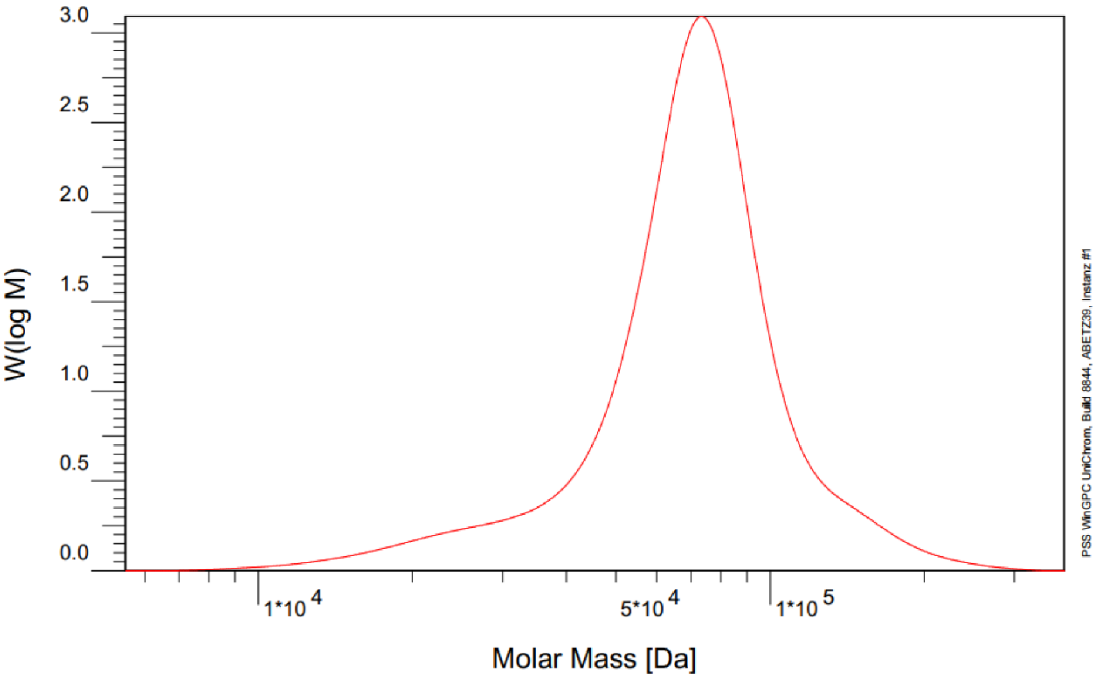

Figure S 18: SEC data for P-MW-46 (equivalent to P-R-69).

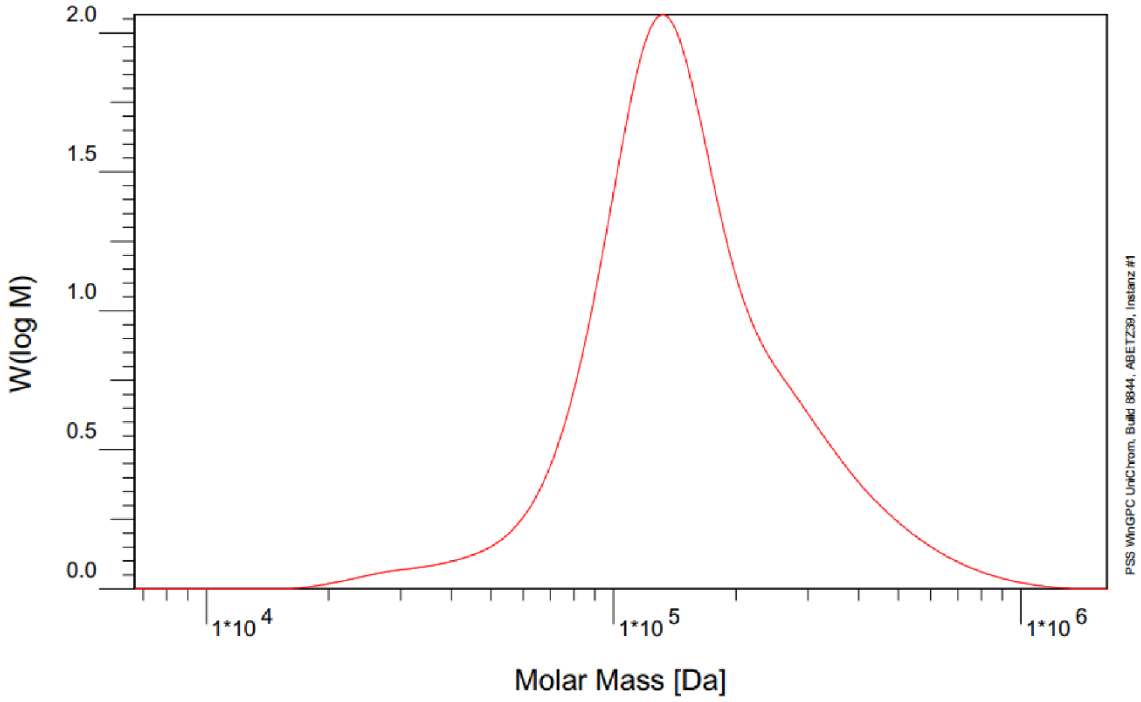

Figure S 19: SEC data for P-MW-91.

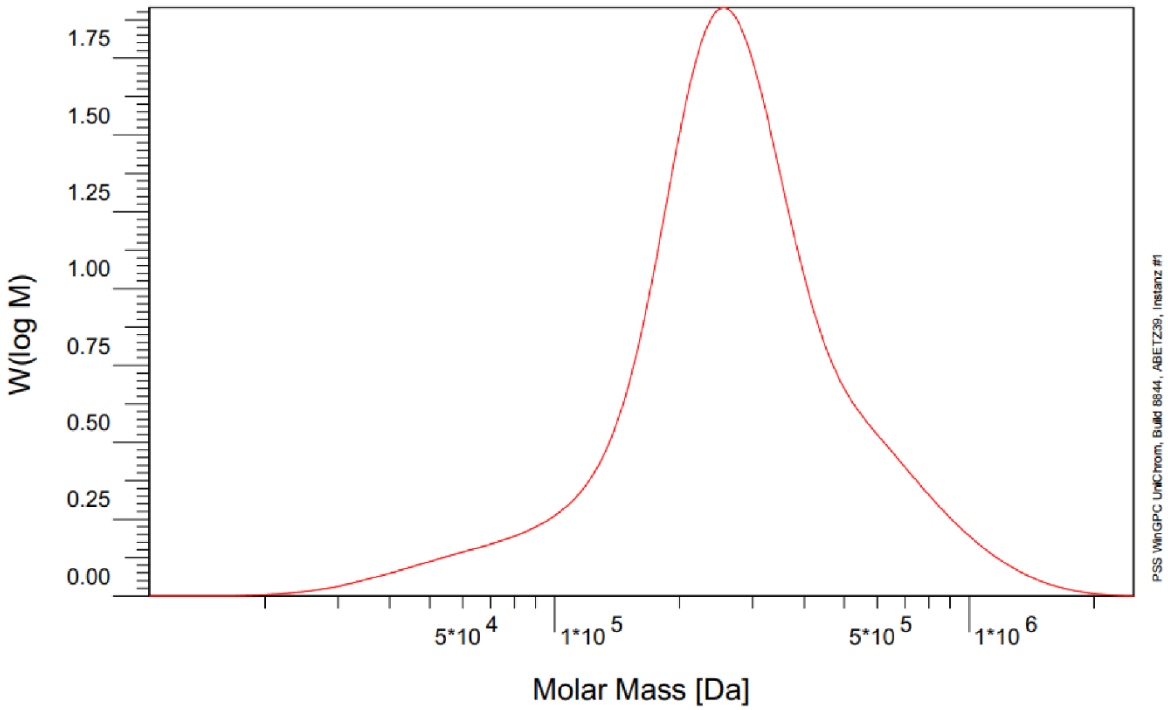

Figure S 20: SEC data for P-MW-133.

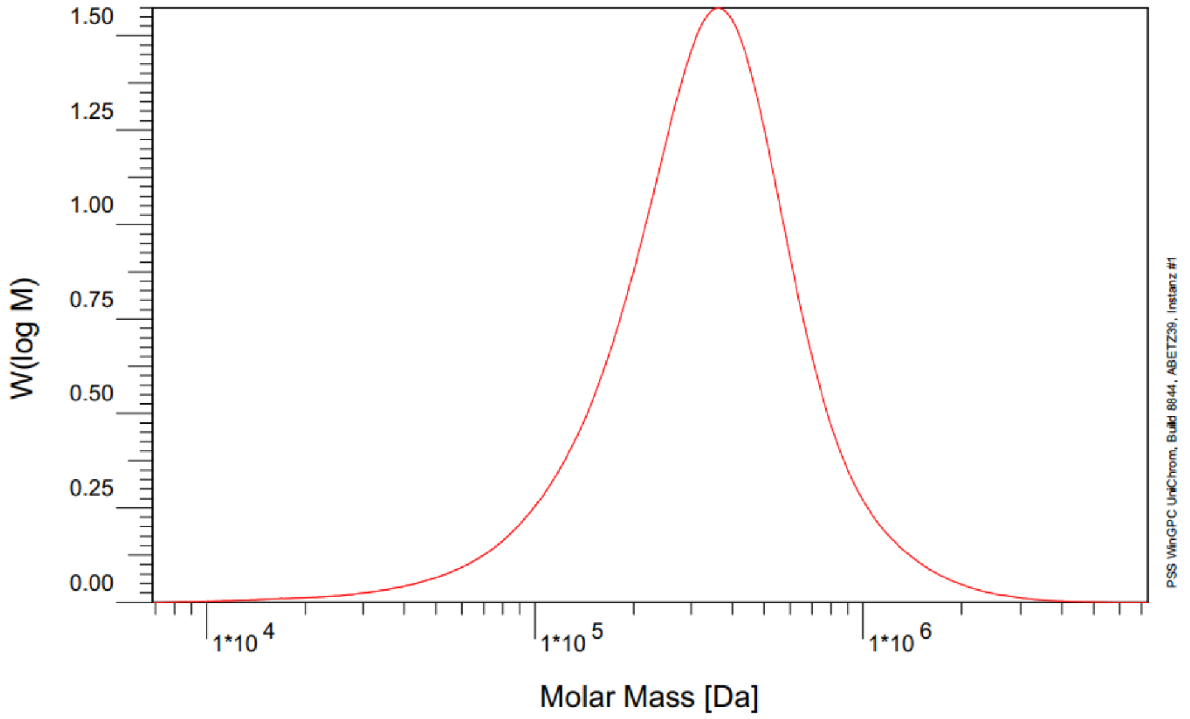

Figure S 21: SEC data for P-MW-202 and the P-F series (P-F-72, P-F-40 (equivalent to P-MW-202), P-F-27, P-F-13, and P-F-8).

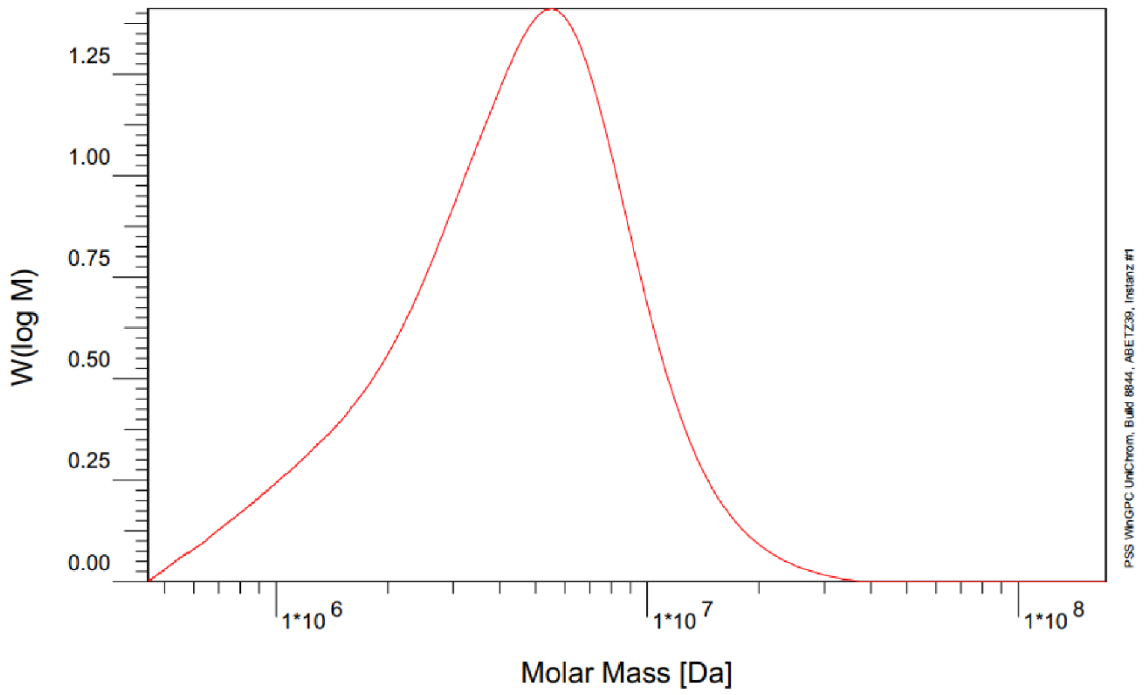

Figure S 22: SEC data for P-MW-310.

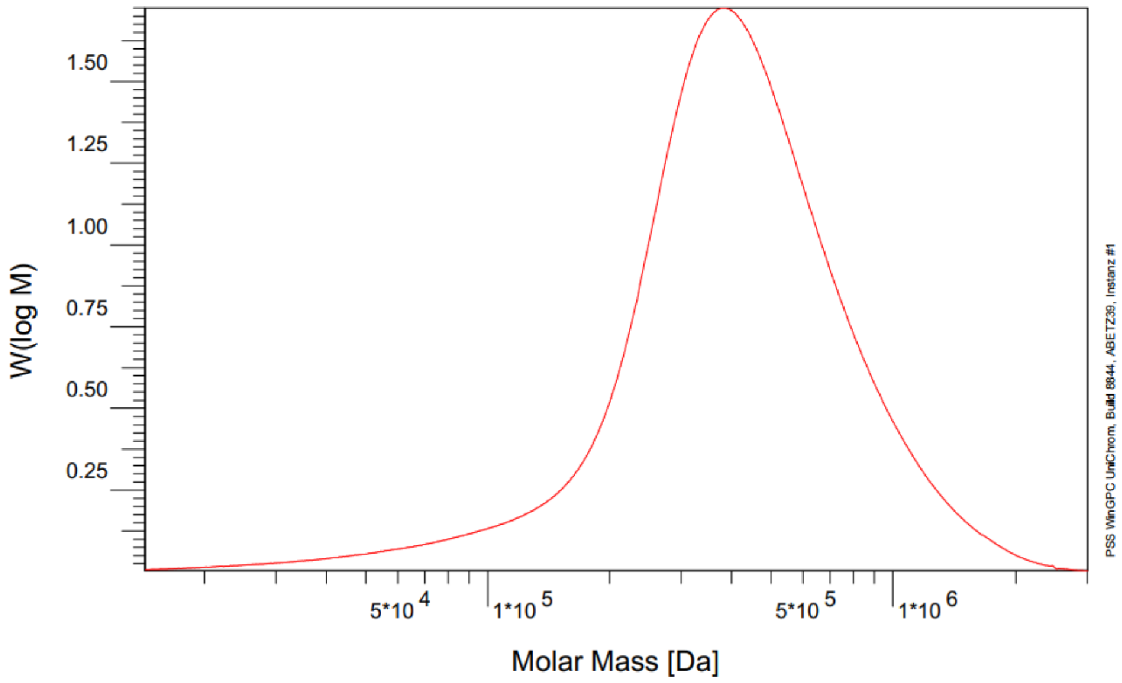

Figure S 23: SEC data for P-R-92.

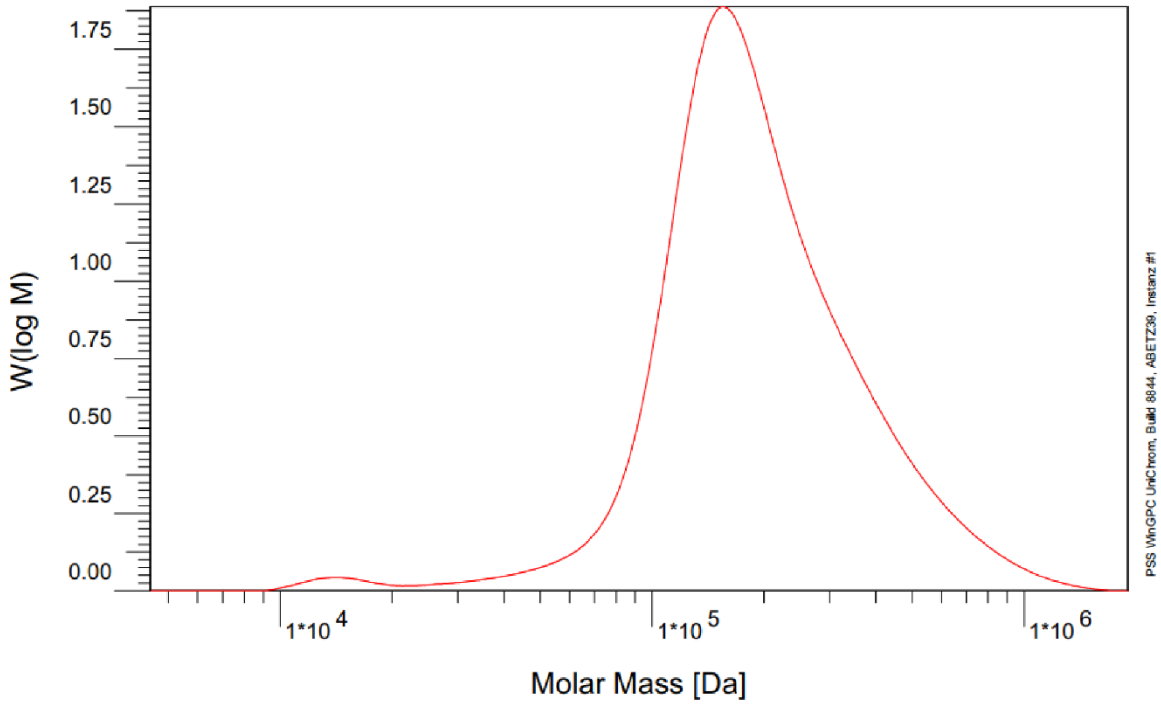

Figure S 24: SEC data for P-R-83.

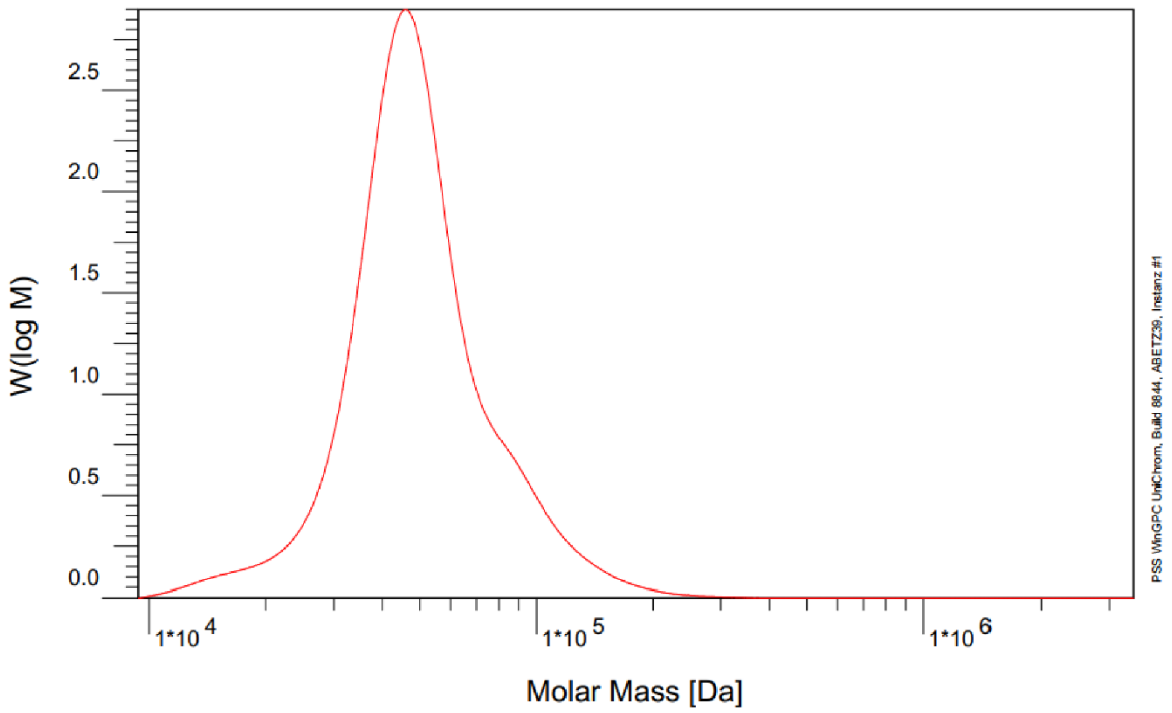

Figure S 25: SEC data for P-R-51.

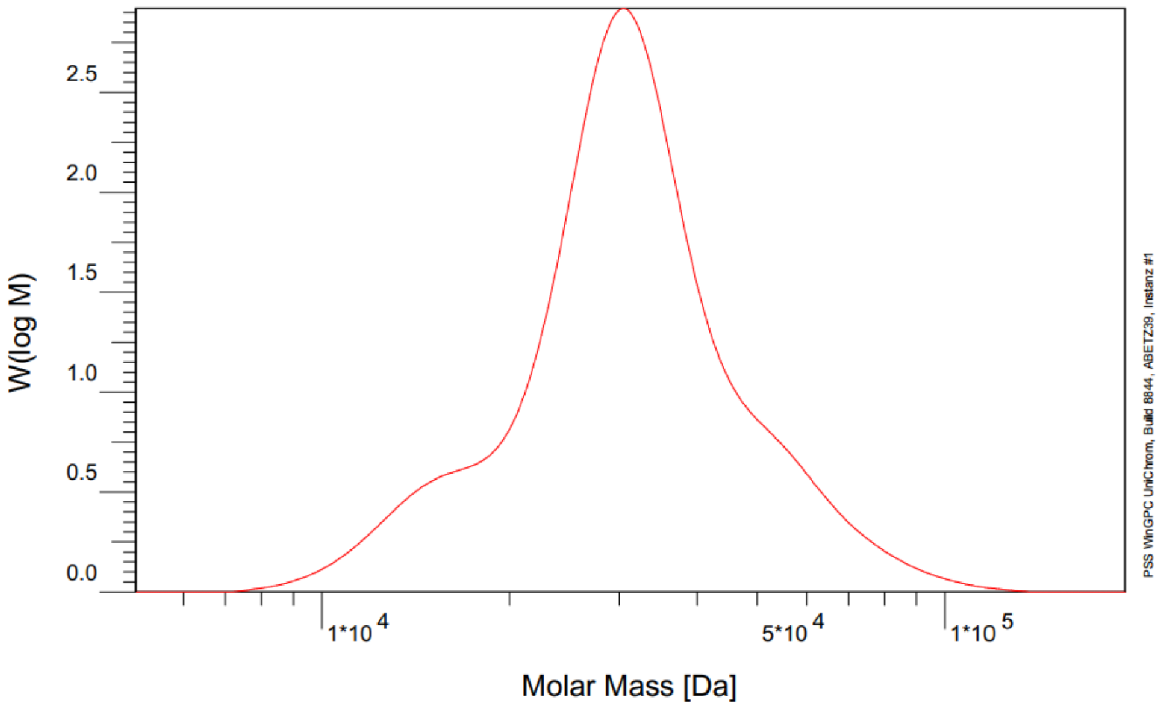

Figure S 26: SEC data for P-R-35. The ratio of theoretical to SEC-determined number-average molecular weight is around 1.2, which is due to the amphiphilic nature of the polymer and the significant deviation of the structure from the PS standard.

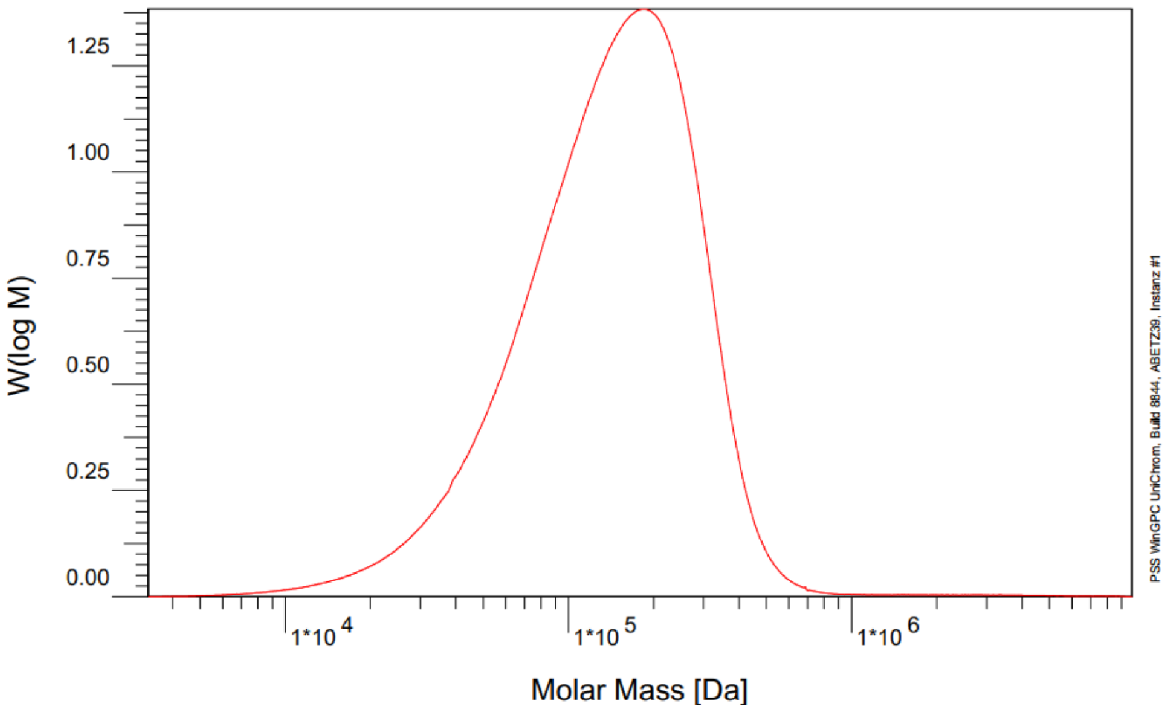

Figure S 27: SEC data for P-C.

Supporting Literature

[1] Xu, E., Smith, A. E., Kirkland, S. E., McCormick, C. L. *Macromolecules*, **2008**, *41*, 8429–8435.

[2] Khazaei, A., Saednia, S., Borazjani, M. K., Saien, J., Kiani, M., Afkhami, A. *Supramol. Chem.*, **2014**, 26, 88–93.

[3] Liu, J. Q., Yang, J. J., Li, J. F., Li, K., Xiao, X. D., Bai, Y. L., Wang, J. W. *Mol. Catal.*, **2017**, *443*, 125–130.

[4] Smith, W. E. *J. Org. Chem.*, **1972**, *37*, 3972–3973.

[5] Hansen, C. M. Hansen Solubility Parameters, Taylor & Francis, Boca Raton, 2nd edn., **2007**, vol. 2.

[6] Stefanis, E., Panayiotou, C. *Int. J. Thermophys.*, **2008**, *29*, 568–585.

[7] James E. Mark Physical Properties of Polymers Handbook, Springer, Cincinnati, 2nd edn., **2007**, vol. 2.

9.4. SUPPORTING INFORMATION FOR PUBLICATION 3

The supporting information are reprinted with permission from S. Jaehnke, V. Abetz, Electrospun, crown ether functionalized PS-b-PMAA block copolymer fibers for Li extraction from aqueous media, *Desalination* (**2025**) 119343 – Copyright 2025 Elsevier B.V.

Supporting Information

Electrospun, Crown Ether Functionalized PS-*b*-PMAA Block Copolymer Fibers for Lithium Extraction from Aqueous Media

Sabrina Jaehnke, Volker Abetz

Experimental Data

Materials

All reagents were purchased from commercial suppliers and used as received, unless it is noted otherwise. Aluminium oxide (basic, 98%, Sigma-Aldrich, Schnelldorf, Germany), 4,4-azobis(4-cyanovaleric acid) (ACVA, 98%, Sigma-Aldrich, Schnelldorf, Germany), benzo-12-crown-4 (98%, TCI Chemicals, Eschborn, Germany), bis-2-chloroethylether (99%, TCI Chemicals, Eschborn, Germany), catechol (99%, TCI Chemicals, Eschborn, Germany), chloroform-d1 (99.8%, Sigma-Aldrich, Schnelldorf, Germany), 12-crown-4 (98%, Sigma-Aldrich, Schnelldorf, Germany), deuterium oxide (D_2O, 99.9%, Deutero, Kastellaun, Germany), dichloromethane (DCM, 99.5%, Grüssing, Filsum, Germany), diisopropyl azodicarboxylate (DIAD, 94%, abcr, Karlsruhe, Deutschland), dimethylformamide (DMF, 99.8 %, Fisher Scientific, Schwerte, Germany), heptane (99.7%, Fisher Scientific, Schwerte, Germany), hexamethylenetetramine (99%, TCI Chemicals, Eschborn, Germany), 2-(hydroxymethyl)-12-crown-4 (97%, Alfa Aesar, Schwerte, Germany), lithium-3,5-diiodosalicylic acid (LIS, 99.9%, Sigma-Aldrich, Schnelldorf, Germany), lithiumhydroxid (LiOH, 98%, TCI Chemicals, Eschborn, Germany), magnesium sulfate (99%, Grüssing, Filsum, Germany), methacrylic acid (MAA, ≥99%, stabilized with hydrochinone monomethyl ether, Merck, Darmstadt, Germany), methanol (MeOH, 99.7%, Fisher Scientific, Schwerte, Germany), sodium bicarbonate ($NaHCO_3$, 99%, Grüssing, Filsum, Germany), sodium borohydride (98%, Alfa Aesar, Schwerte, Germany), sodium ethyl eosin (NaEE, 100%, Carl Roth, Karlsruhe, Germany), tetrahydrofuran (THF, 99.7%, Fisher Scientific, Schwerte, Germany), THF-d8 (99.5%, Deutero, Kastellaun, Germany) trifluoroacetic acid (TFA, 99%, Sigma-Aldrich, Schnelldorf, Germany), triphenylphosphine (TPP, 99%, Merck, Darmstadt, Germany).

Styrene (≥99%, Sigma-Aldrich, Schnelldorf, Germany) was purified by filtering it through basic activated alumina in order to remove the inhibitor (4-tert-butylcatechol). 4-Cyano-4-thioylthiopropylsulfanyl pentanoic acid (CTPPA), (2,3,5,6-tetrahydrobenzo[*b*][1,4,7]-trioxonin-9-yl)methanol (B9C3-MeOH), and (2,3,5,6,8,9-hexahydrobenzo[b][1,4,7,10]tetraoxacyclododecin-12-yl)methanol (B12C4-MeOH) were

synthesized according to the literature.[36–38] Ethyl acetate was purified by distillation and water *via* Milli-Q® purification system (18.1 MΩ cm at 25 °C).

Nuclear Magnetic Resonance (NMR) Spectroscopy

The ^{1}H-Nuclear Magnetic Resonance (NMR) spectra were measured in THF-d_8, $CDCl_3$, and D_2O at room temperature using a 300 MHz Bruker FourierHD, 400 MHz Bruker AVANCE II, or 500 MHz Bruker AVANCE I spectrometer. As a reference for the chemical shifts, the respective solvent signals (δ = 7.26 for $CDCl_3$, δ = 3.58 for THF-d_8, and δ = 4.79 for D_2O) were utilized.

Electrospinning

The electrospinning setup used was conceptualized and constructed at the Helmholtz-Zentrum Geesthacht (Germany). 3–4 mL of sample solution was prepared in DMF/DCM (4/1 V/V) with 20–25 wt% polymer, depending on the viscosity of the solution. The polymer solution was passed through a syringe needle (0.6 mm inner diameter) to which a high voltage was applied, at a constant flow rate (0.5 mL/h). As pump, a Harvard PHD 4400 was used. The distance between the needle tip and the collector plate was held constant throughout the spinning process at 15 cm. The collector plate was equipped with a polyester non-woven (type 05TH-100) and was rotating throughout the spinning process at a constant speed of 10 rotations/sec. Spinning was performed depending on the sample, for 4–6 h. The applied voltage depended on the solutions conductivity and was therefore varied.

Scanning Electron Microscopy (SEM)

Scanning electron microscopy (SEM) characterization was performed with an Merlin SEM (Zeiss, Oberkochen, Germany) using an acceleration voltage of 3 kV or with a LEO GEMINI 1550 (Zeiss, Oberkochen, Germany) using an acceleration voltage of 1 kV (for the fiber's diameter distribution). The polymer samples were dried for 72 h (vacuum, 60 °C) before measurement. Afterwards the samples were sputter-coated (platinum, 1–1.5 nm) with a CCU-010 coating device (Safematic, Switzerland) or for the distribution functions, measured without further coating. The fiber diameters were determined by analyzing 5–10 images per sample (100 fibers with 2 data points /fiber), with a magnification of 2–5 kx, using the software ImageJ (version 1.51f).

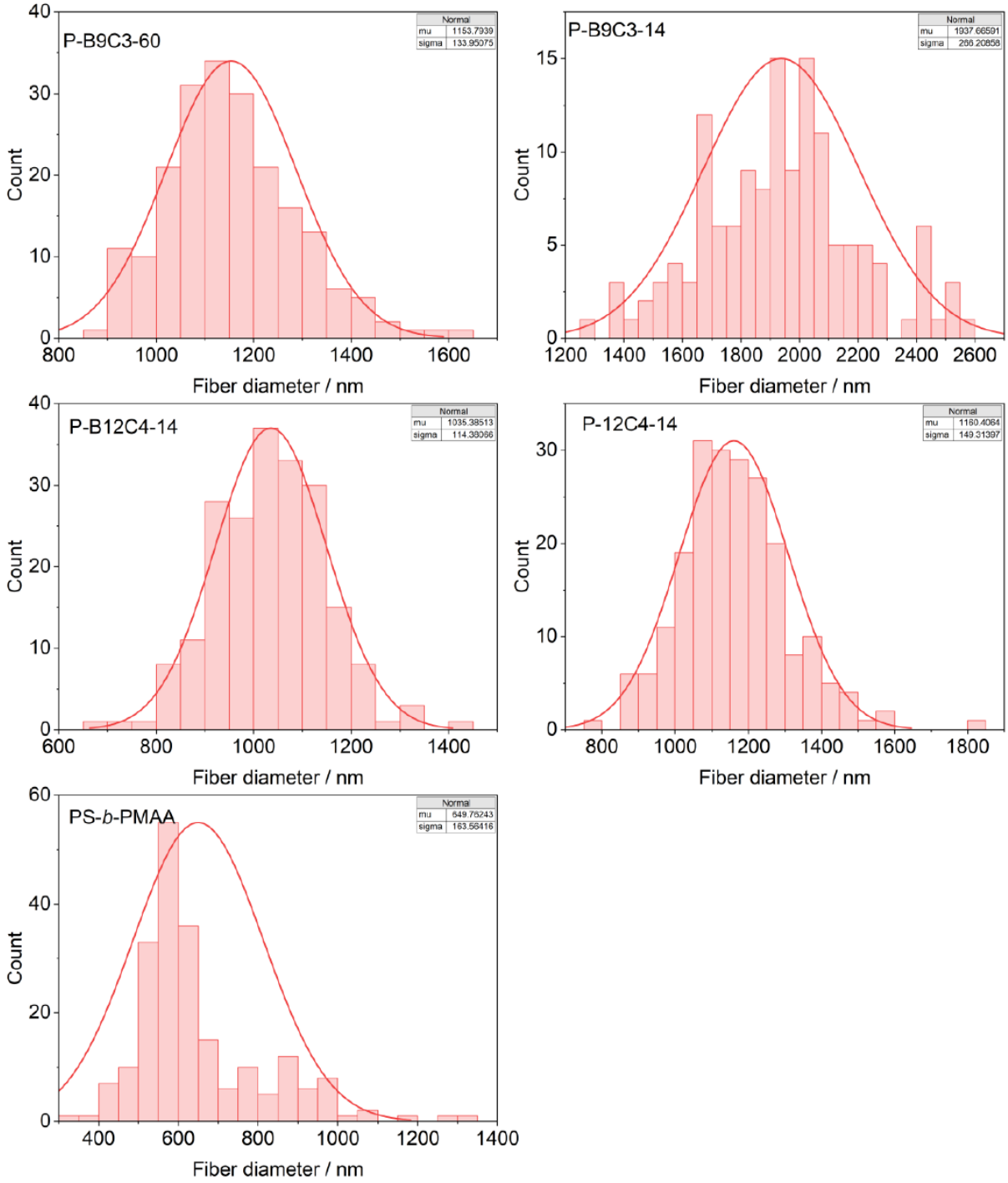

Figure S 1: Distribution functions of the electrospun fibers of functionalized and non-functionalized PS-*b*-PMAA. The mean values (mu) and standard deviation (sigma) are given. The data was grouped into sections of 50 nm with approx. 200 measurement points on a total of 100 fibers (2 measurement points/fiber).

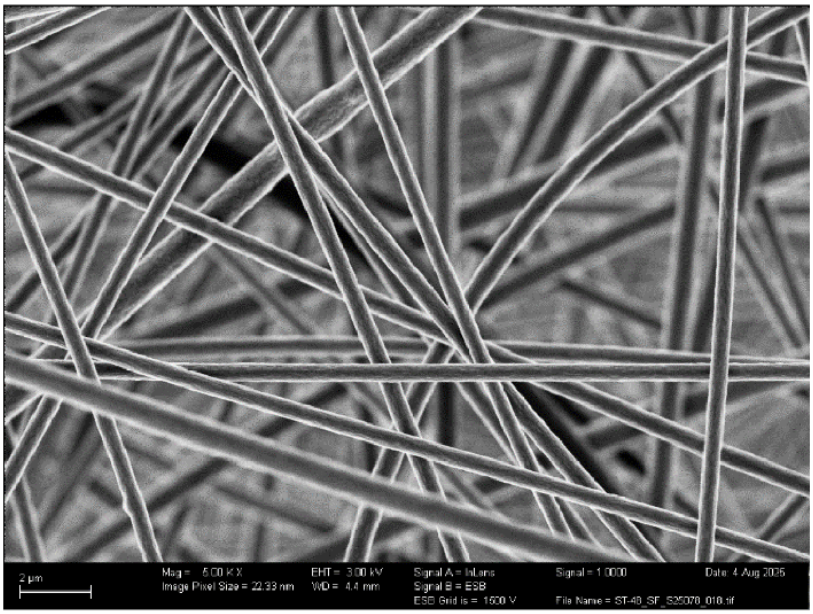

Figure S 2: SEM measurement of PS-*b*-PMAA fibers in 2000x magnitude. Measured by Hereon.

Transmission Electron Microscopy (TEM)

Transmission Electron Microscopy (TEM) measurements of the polymer fiber's cross-sections were analyzed using a Tecnai G2 F20 (FEI, Eindhoven, The Netherlands) in bright-field mode. The acceleration voltage was set to 120 kV. For sample preparation, the polymer fibers were embedded in Epo-Tek 301 (Epoxy Technology, Inc., USA) and ultrathin sections were prepared *via* ultramicrotomy. Staining was performed with RuO_4 for 20 min.

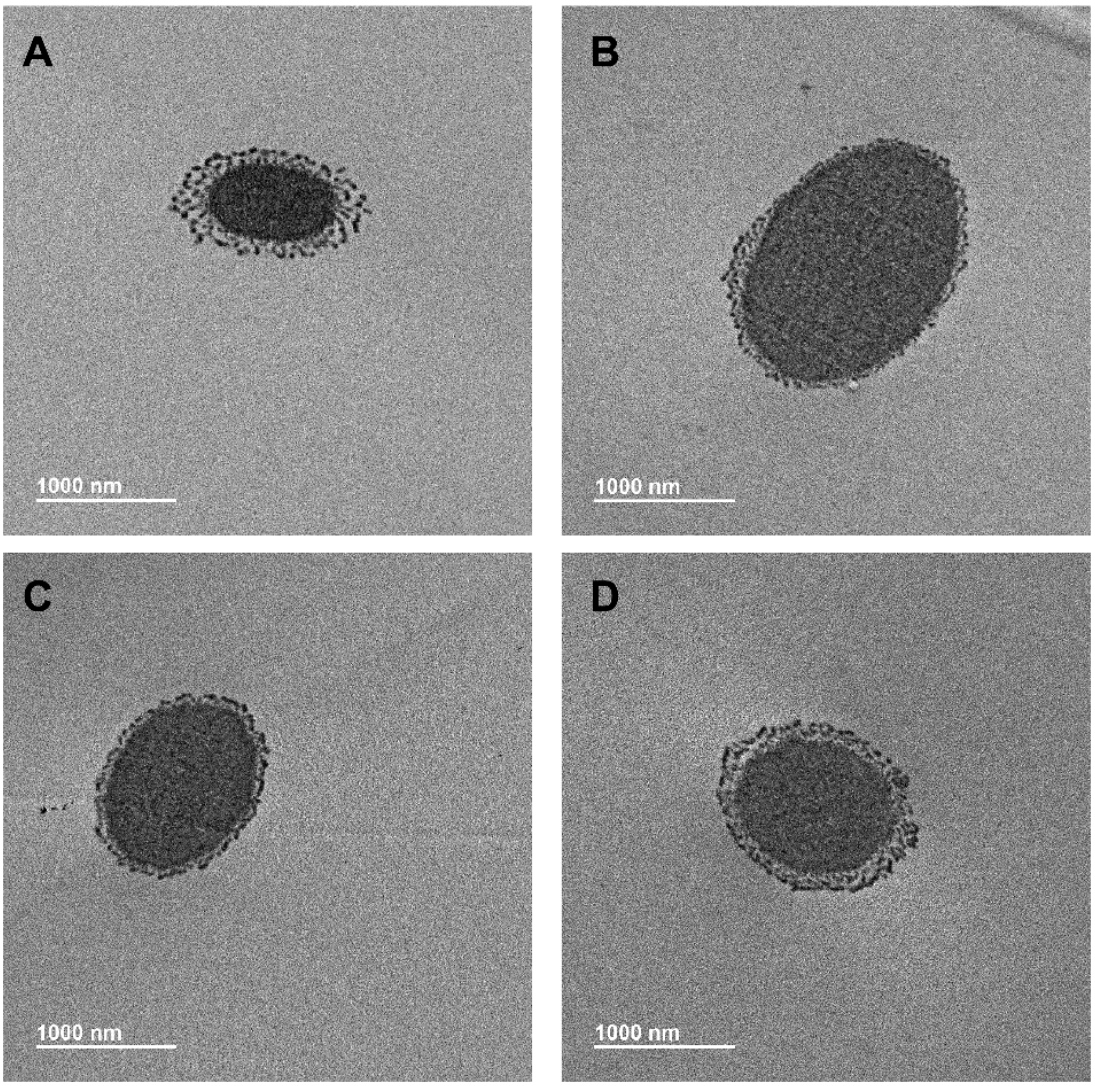

Figure S 3: TEM image of the cross-section of fibers from P-B9C3-60 (A), P-B9C3-14 (B), P-B12C4-14 (C) and P-12C4-14 (D) embedded in epoxy resin and stained with RuO_4. As an average value of 6–12 fibers measured per sample, values of 84±12 nm for A, 77±9 nm for B, 77±16 nm for C, and 119±16 nm for D were calculated for the thickness of the outer layer. The core is somewhat marbled. Due to the large fiber diameters and the shell, no correlation with the polymer length can be found. It is assumed that the core-shell structure is not a self-assembly of the block copolymer, but rather an interaction effect with the polar epoxy resin mixture necessary for the embedment of the fibers.

Size Exclusion Chromatography (SEC)

The molecular weight distribution of the unfunctionalized PMAA-*b*-PS diblock copolymer was determined *via* Size Exclusion Chromatography (SEC). A THF solution (5 wt% TFA; 1 g/L) was prepared. Toluene was utilized as an internal reference. The THF-SEC system contained an Agilent 1260 Infinity Series degasser and pump, and three consecutively slated PSS SDV® columns (100 Å, 1000 Å, 10000 Å). A sample volume of 100 µL was injected and analyzed with a flow rate of 1.0 mL/min at a temperature of 30 °C. Signal detection was ensured by a refractive index detector and a UV detector. For the calibration, a near-monodisperse PS-standard was used.

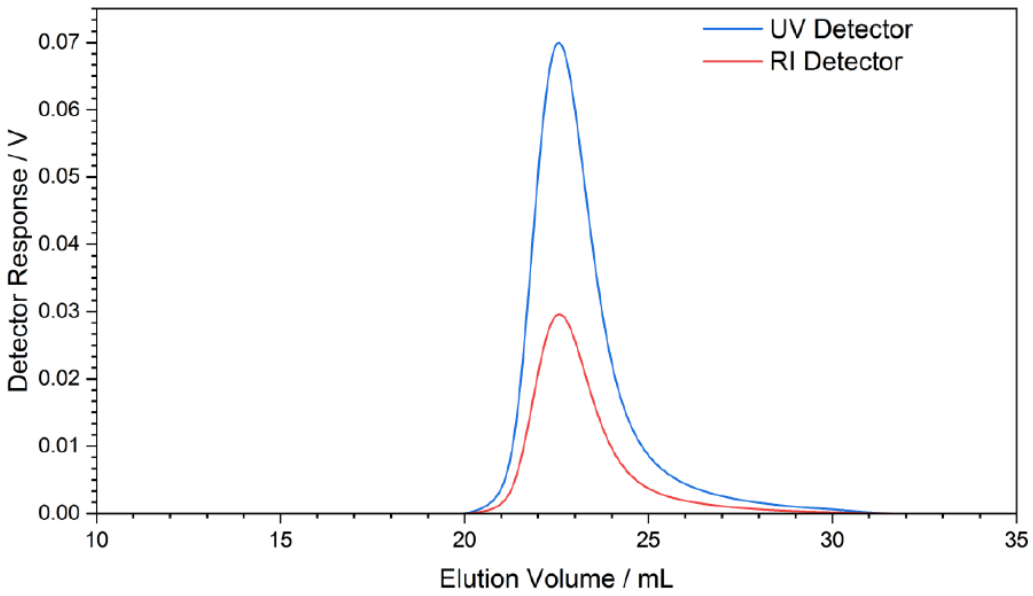

Figure S 4: SEC sample of the unfunctionalized PS-*b*-PMAA in THF (+TFA). The red curve results from the RI detector and the blue curve from the UV detector.

Liquid-Liquid-Extraction

Liquid-liquid extraction (LLE) was performed according to the method described in the literature.[18,19] The CE was dissolved in 2.8 mL DCM and covered with an equal volume of salt solution (salt/CE ratio=0.5). Extraction was performed for 45 min at 500 rpm and 25 °C. After phase separation (60 min), the aqueous phase was either measured directly (for NaEE) or evaporated (LIS) with subsequent addition of 200 µL water. The absorbance of the respective solution was determined at 323 nm (LIS) or 521 nm (NaEE) *via* UV-Vis measurements. Therefore, a spectrophotometer UV5 from Mettler Toledo and the software LabX (version 11.0.1, build 43) was employed. To calculate the salt concentration, calibrations were performed for each salt. These demonstrate a linear correlation (Lambert-Beer law) between salt concentration and absorbance (Figure S2).

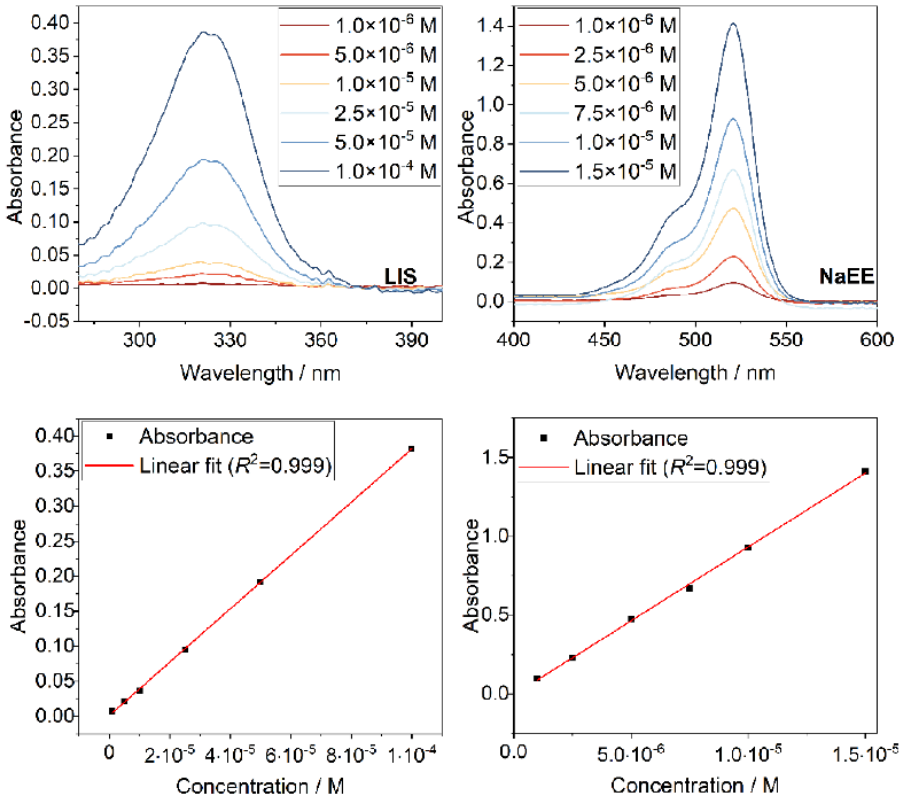

Figure S 5: Correlation of concentration and absorbance for LIS (323 nm, left) and NaEE (521 nm, right), measured *via* UV-Vis.

For the calculation of the capacity q_{CE} (or q_{poly} for SLE), the salt concentrations before and after extraction are required. c_{bc} is determined by the amount of salt used for the extraction and is therefore known. c_{ac} can be derived from the calibration by using the dilution and the absorbance of the solution after extraction.

Solid-Liquid-Extraction

The solid-liquid extractions (SLE) were performed similarly to the LLE. Instead of an organic solvent, however, solid polymer was used as the carrier material for the CE. Therefore, both q_{CE} and q_{poly} could be calculated. In contrast to previous publications by our group, it was decided to provide the capacity of the material rather than the logarithm of the equilibrium constant.[16,18,19,25] In this more application-oriented context, this ensures comparability with other lithium extraction systems known from the literature.[39,40] 2.8 mL of a salt solution was added to the electrospun polymer fibers (salt/CE ratio=0.5). The extraction was carried out analogous to LLE. After extraction, the aqueous phase was either measured directly (NaEE) or subsequently concentrated (LIS). Blank measurements were carried out without polymer or CE. These blank values were used to ensure that only the lithium complexation related to the CE (or functionalized polymer) is considered for the calculation.

Table S 1: Data of the UV-Vis measurements of the different PS-*b*-P(MAA-*r*-CEXMA) polymers obtained in SLE at different times *t* and CEs obtained in LLE with LIS. Shown are molar capacities q_{CE} (in mmol Li/mol CE) and total capacities of the materials q_{poly} (in mmol Li/g polymer) of the three independent measurements, the average values (Av.), and the standard deviation (sd).

t	Sample-ID	q_{CE} 1	q_{CE} 2	q_{CE} 3	Av. q_{CE}	sd q_{CE}	q_{poly} 1	q_{poly} 2	q_{poly} 3	Av. q_{poly}	sd q_{poly}
30 minutes	P-B9C3-60	-	-	-	-	-	$5.12 \cdot 10^{-5}$	-	-	$5.12 \cdot 10^{-5}$	-
	P-B9C3-14	-	-	-	-	-	0	-	-	0	-
	P-B12C4-14	-	-	-	-	-	$9.13 \cdot 10^{-5}$	$1.14 \cdot 10^{-4}$	-	$1.03 \cdot 10^{-4}$	$1.14 \cdot 10^{-5}$
	P-12C4-14	-	-	-	-	-	$2.36 \cdot 10^{-5}$	$2.57 \cdot 10^{-5}$	$2.09 \cdot 10^{-5}$	$2.46 \cdot 10^{-5}$	$1.06 \cdot 10^{-6}$
60 minutes	P-B9C3-60	-	-	-	-	-	$8.11 \cdot 10^{-5}$	-	-	$8.11 \cdot 10^{-5}$	-
	P-B9C3-14	-	-	-	-	-	-	-	-	-	-
	P-B12C4-14	-	-	-	-	-	$1.89 \cdot 10^{-4}$	$1.97 \cdot 10^{-4}$	-	$1.93 \cdot 10^{-4}$	$3.58 \cdot 10^{-6}$
	P-12C4-14	-	-	-	-	-	$5.88 \cdot 10^{-5}$	$5.37 \cdot 10^{-5}$	$5.02 \cdot 10^{-5}$	$5.42 \cdot 10^{-5}$	$3.52 \cdot 10^{-6}$
360 minutes	P-B9C3-60	-	-	-	-	-	$8.35 \cdot 10^{-5}$	$7.08 \cdot 10^{-5}$	$5.13 \cdot 10^{-5}$	$6.64 \cdot 10^{-5}$	$1.33 \cdot 10^{-5}$
	P-B9C3-14	-	-	-	-	-	$3.95 \cdot 10^{-8}$	$1.94 \cdot 10^{-7}$	-	$1.17 \cdot 10^{-7}$	$7.71 \cdot 10^{-8}$
	P-B12C4-14	-	-	-	-	-	$2.08 \cdot 10^{-4}$	$1.99 \cdot 10^{-4}$	$1.53 \cdot 10^{-4}$	$1.87 \cdot 10^{-4}$	$2.41 \cdot 10^{-5}$
	P-12C4-14	-	-	-	-	-	$6.00 \cdot 10^{-5}$	$4.87 \cdot 10^{-5}$	$7.16 \cdot 10^{-5}$	$6.01 \cdot 10^{-5}$	$9.36 \cdot 10^{-6}$
-	B12C4	30	29	26	28	2	-	-	-	-	-
	12C4	19	37	30	29	8	-	-	-	-	-

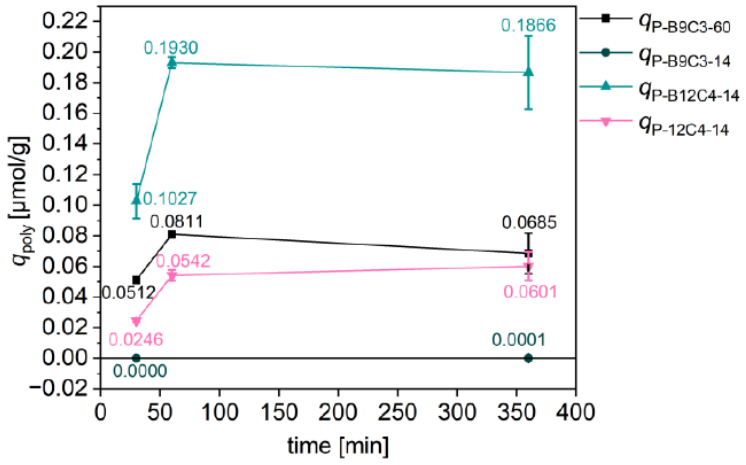

Figure S 6: Representation of the capacity per g of material q_{poly} at different extraction times (30–360 min).

CE functionalization (B9C3-MeOH und B12C4-MeOH)

B9C3 was synthesized according to Khazasei *et al.*[36] B12C4 was purchased commercially. The functionalization of B9C3 is described in the following, with the information for the functionalization of B12C4 provided as well. The synthesis described by Smith *et al.*[44] was performed in a nitrogen atmosphere. B9C3 (123.2 mmol; 14.24 mmol for B12C4) was dissolved in TFA (66.4 mL; 7.68 mL for B12C4) and hexamethylenetetramine (123.2 mmol; 14.24 mmol for B12C4) was added. The reaction was performed at 90 °C for 4 h. Subsequently, Milli-Q water (214 mL; 31 mL for B12C4) was injected and the reaction proceeded for another 90 minutes at unchanged temperature. After r.t. was reached and neutralization with $NaHCO_3$ was performed, the reaction mixture was extracted with DCM. After the organic phases were washed with Milli-Q water, drying over magnesium sulfate was performed. The product mixture was separated and purified *via* column chromatography (silica gel, dry-load, ethyl acetate/heptane (3/1 *V*/*V*)). B9C3-CHO was obtained as a slightly yellowish liquid (10.0 g, 39%), B12C4-CHO as a colorless, highly viscous liquid (2.79 g, 78%). Subsequently, a reduction to B9C3-MeOH (or B12C4-MeOH) was performed as described by Liu *et al.*[38] B9C3-CHO (43.88 mmol; 11.04 mmol for B12C4-CHO) was dissolved in methanol (133 mL; 41 mL for B12C4-CHO) and sodium borohydride (91.92 mmol; 23.19 mmol for B12C4-CHO) was added at a temperature of 0 °C. The mixture was allowed to reheat to r.t.. After 2 h, the mixture was transferred to an excess of Milli-Q water. Extraction was performed with DCM. The combined organic phases were washed with a small amount of water and dried over magnesium sulfate. After removal of solvent, B9C3-MeOH was isolated as a yellowish, highly viscous liquid (42.8 mmol, 98%) without further purification. ^{1}H-NMR (300 MHz, $CDCl_3$, 298 K): δ [ppm] = 7.07–6.90 (m, 3H, -Ph-H), 4.71–4.55 (m, 2H, -CH_2-OH), 4.47–4.26 (m, 4H, Ph-O-CH_2-), 3.98–3.87 (m, 4H, Ph-O-CH_2-CH_2-), 1.73 (t, 1H, -OH). MS (ESI): m/z *calcd.* for $C_{11}H_{14}O_4$ $[M+Na]^+$ 233.0784, *found* 233.0793. B12C4-MeOH was obtained as a yellowish, highly viscous liquid (10.9 mmol, 99%). ^{1}H-NMR (400 MHz, $CDCl_3$, 295 K): δ [ppm] = 7.00–6.87 (m, 3H, -Ph-H), 4.55 (s, 2H, -CH_2-OH), 4.18–4.09 (m, 4H, Ph-O-CH_2-), 3.86–3.79 (m, 4H, Ph-O-CH_2-CH_2-), 3.78–3.74 (m, 4H -O-CH_2-CH_2-O-f), 2.01 (t, 1H, -OH). MS (ESI): m/z *calcd.* for $C_{13}H_{18}O_5$ $[M]^+$ 254.1154, *found* 253.1080.

One-pot synthesis of the PS-b-PMAA diblock copolymer

A synthetic method adapted from Chaduc *et al.* was used.[45] First, the PMAA block was formed in an inert atmosphere. CTPPA (0.320 mmol) was dissolved in MAA (81.9 mmol). DMF (13.7 mmol) was added as a reference for the conversion evaluation. Following the addition of water (28.0 mL), an aqueous solution (1.49 mL, corresponding to 0.032 mmol ACVA and 0.112 mmol $NaHCO_3$) was added. At 0 °C, the mixture was purged with nitrogen for 30 min. An initial sample was taken and the reaction was initiated by transferring the mixture to an

preheated oil bath (80 °C). The reaction proceeded at 80°C for 22 h. A conversion of 99.70% was determined *via* ^{1}H NMR spectroscopy (D_2O). In the second step of the one-pot synthesis, the PS block was synthesized. A further 116 mL of water was added, followed by activated styrene (0.2752 mol) and 2.99 mL of aqueous solution (corresponding to 0.064 mmol ACVA and 0.112 mmol $NaHCO_3$). At 0 °C, the mixture was purged with nitrogen for 30 min. Subsequently, the reaction was started at a temperature of 80°C and terminated after 6 h and a conversion of 99.16% (^{1}H-NMR, THF-d_8). The water was removed, the polymer dissolved in THF, precipitated in *n*-heptane, dried, cooled to -196 °C, and ground to a powder using a ball mill (30 Hz, 5 min). MW (*via* ^{1}H-NMR) 111059 g/mol, *Đ* (*via* SEC)= 1.6 (Figure S 1).

Synthesis of PS-b-P(MAA-r-CE3MA) via Mitsunobu esterification

The synthesis was performed according to Mitsunobu *et al.*[46] The amount of reagents is listed in Table S 2.

Table S 2: Amounts *n* (mmol) of polymer, TPP, DIAD, and hydroxymethyl-functionalized CE, and volume (mL) of THF used.

P-	B9C3-60	B9C3-14	B12C4-14	12C4-14
n(Polymer)	0.018	0.027	0.027	0.027
n(TPP)	4.65	20.9	20.9	20.9
n(DIAD)	4.65	20.9	20.9	20.9
n(CE)	13.9	1.05	1.05	1.05
V(THF)	78	112	112	112

A solution of TPP in half of the THF volume was prepared. DIAD was added dropwise. After 30 min at r.t., a solution of polymer and functionalized CE (in the remaining THF) was added at 0°C. After a reaction time of 24 h at r.t., the reaction was terminated by precipitating the solution in *n*-heptane and washing with methanol. The dried polymer gave a functionalization in relation to the total MAA units (determined by ^{1}H NMR in $CDCl_3$) of 60 % or 14 % as indicated. This was determined as described in the literature[16,19], whereby the ether protons of the respective CE (for example δ = 3.90 ppm for B9C3, δ = 3.85 ppm for B12C4 or δ = 3.70 ppm for 12C4) can be set in relation to the meta-signal of the benzene ring of the PS (δ = 6.85 - 6.15 ppm).

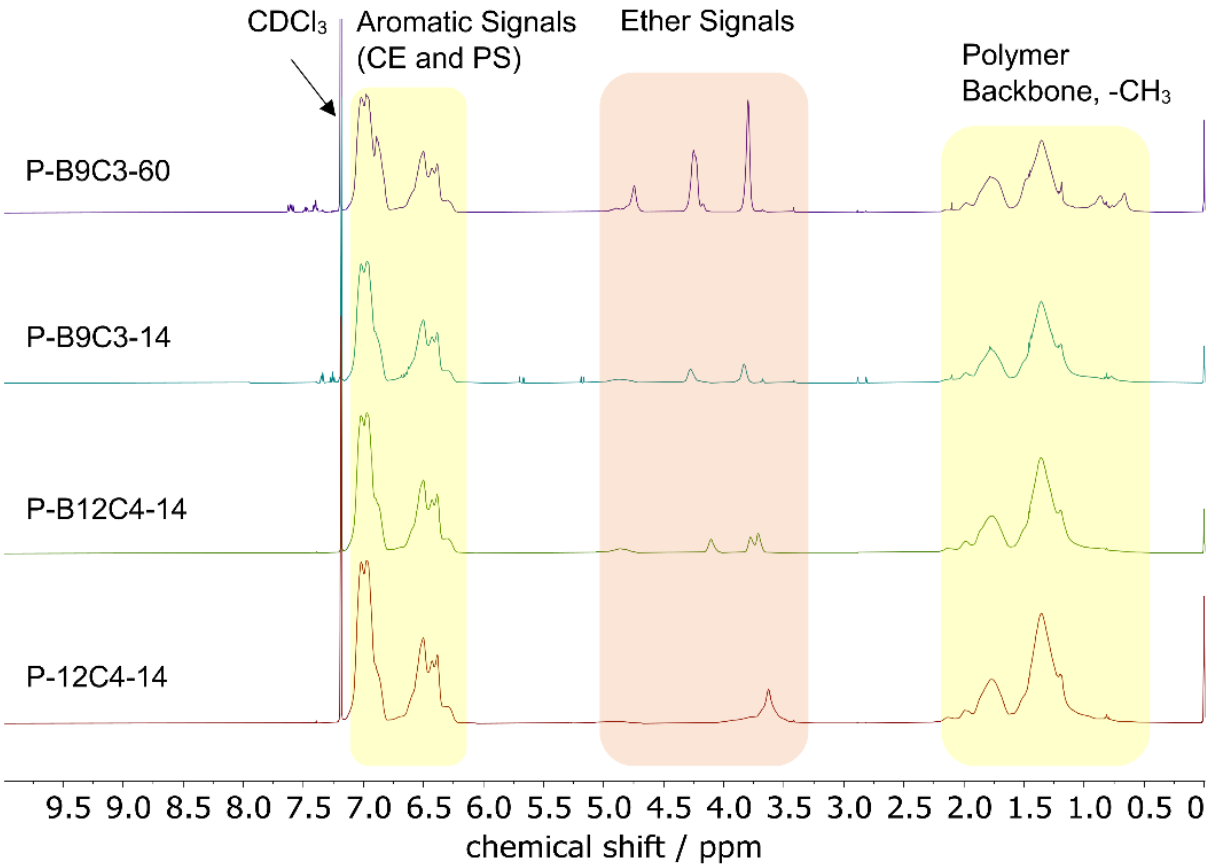

Figure S 7: ^{1}H-NMR Spectrum of P-B9C3-60, P-B9C3-14, P-B12C4-14, and P-12C4-14 (500 MHz, $CDCl_3$, 296 K).

Molecular structure optimizations

The molecular structure optimizations based on Density Functional Theory (DFT) were done with Gaussian 16 (version C.01). The B3LYP exchange-correlation functional was utilized for all calculations, and was combined with Ahlrichs' def–2–TZVP basis set. Furthermore, in order to perform dispersion correction, Grimme's dispersion correction (DFT–D3) was performed.[41–43] The simulated water environment was approximated by an Integral Equation Formalism Polarizable Continuum Model (IEF–PCM) model. For the evaluation of the Hirshfeld partial charges, the Hirshfeld charge implementation in Gaussian 16 was used. Visualization was performed with Avogadro (version 1.1.1).

Example input for Optimization and subsequent Hirshfeld charge calculation:

#p Opt=(ModRedundant,tight) b3lyp/def2tzvp pop=hirshfeld empiricaldispersion=gd3bj scrf=(solvent=water) formcheck

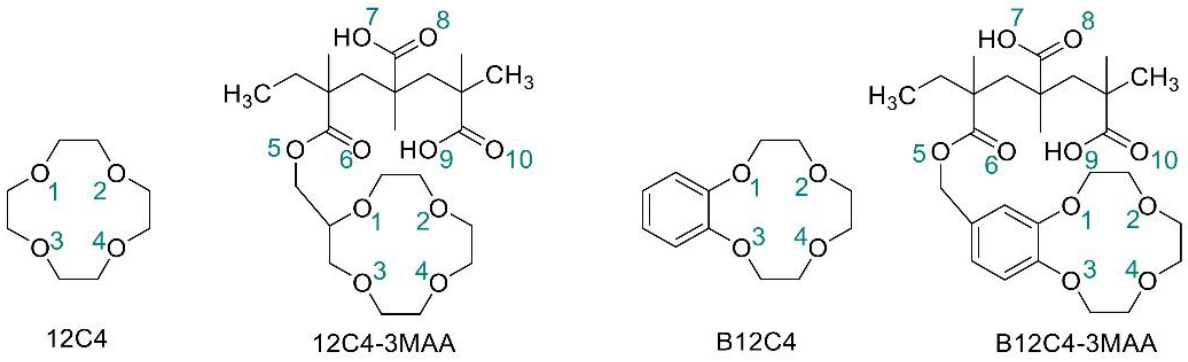

Figure S 8: Illustration of the structures calculated using DFT and assignment of the oxygen atoms for the calculation of the Hirshfeld charges.

Table S 3: Hirshfeld charge differences between the oxygen atoms of 12C4, B12C4, 12C4 multiple (3MAA) ester functionalities, as well as B12C4 with multiple (3MAA) ester functionalities with and without lithium complexation.

	12C4	12C4-3MAA	B12C4	B12C4-3MAA
O1	0.0333	0.0298	0.0031	0.0119
O2	0.0327	0.0413	0.0343	0.0290
O3	0.0328	0.0308	0.0492	0.0065
O4	0.0325	0.0251	0.0382	0.0331
O5	-	0.0074	-	-0.0034
O6	-	0.0025	-	0.0052
O7	-	**0.0383**	-	**0.0415**
O8	-	**0.0455**	-	**0.0539**
O9	-	0.0038	-	**0.0329**
O10	-	**0.0274**	-	**0.0690**

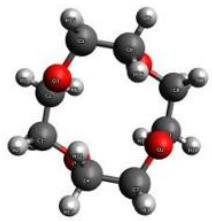

Figure S 9: Simulated molecular structure of 12C4. (Spheres: red = O, dark gray= C, gray= H)

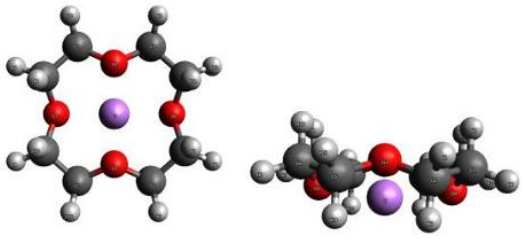

Figure S 10: Simulated molecular structure of the 12C4 lithium complex. (Spheres: red = O, dark gray= C, gray= H, pink= Li)

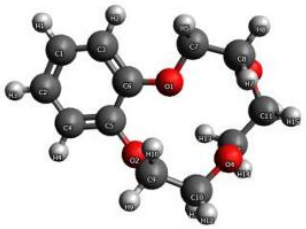

Figure S 11: Simulated molecular structure of B12C4. (Spheres: red = O, dark gray= C, gray= H)

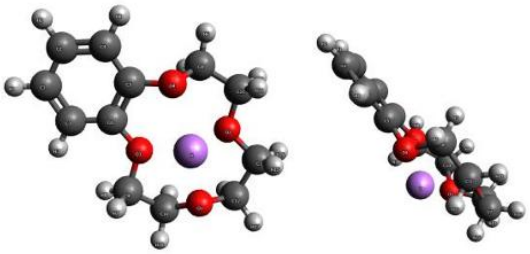

Figure S 12: Simulated molecular structure of the B12C4 lithium complex. (Spheres: red = O, dark gray= C, gray= H, pink= Li)

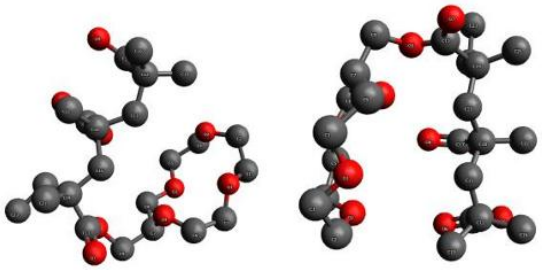

Figure S 13: Simulated molecular structure of 12C4-3MAA from two perspectives. The hydrogen atoms are hidden for reasons of clarity. (Spheres: red = O, dark gray= C)

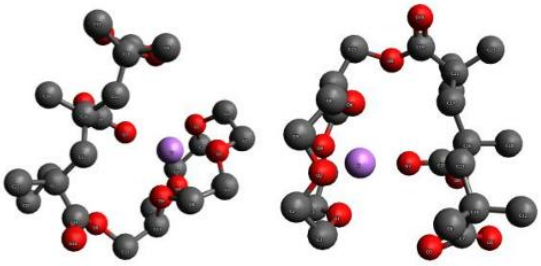

Figure S 14: Simulated molecular structure of the 12C4-3MAA lithium complex. The hydrogen atoms are hidden for reasons of clarity. (Spheres: red = O, dark gray= C, pink= Li)

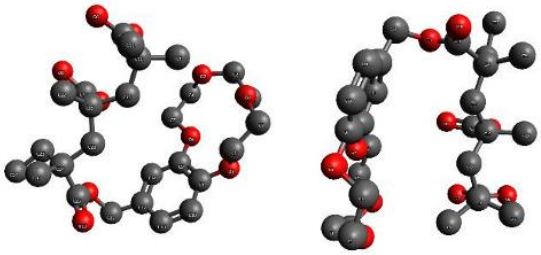

Figure S 15: Simulated molecular structure of B12C4-3MAA from two perspectives. The hydrogen atoms are hidden for reasons of clarity. (Spheres: red = O, dark gray= C)

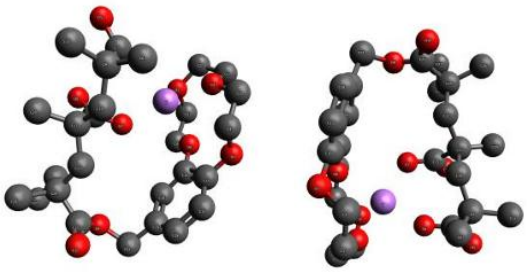

Figure S 16: Simulated molecular structure of the B12C4-3MAA lithium complex. The hydrogen atoms are hidden for reasons of clarity. (Spheres: red = O, dark gray= C, pink= Li)

9.5. SAFETY

The chemicals used in this work and their classification according to GHS are listed in Table 2, the specific CMR classification is listed in Table 3.

Table 2: Chemicals and their classification according to GHS.

Substance	Symbols	Hazard Statement	Precautionary Statement
Acetone	Danger	H225, H319, H336, EUH066	P210, P233, P240, P241, P242, P305+P351+P338
Acetonitrile	Danger	H225, H302+H312+H332, H319	P210, P280, P301+P312, P303+P361+P353, P304+P340+P312, P305+P351+P338
Aluminium oxide (basic)	Not classified as hazardous according to CLP (Regulation (EC) 1272/2008).		
8-Anilino-1-naphthalenesulfonic acid hemimagnesium salt	Warning	H315, H319, H335	P261, P264, P271, P280, P302+P352, P305+P351+P338
Aza-15-Crown-5	Warning	H315, H319, H335	P261, P264, P271, P280, P302+P352, P305+P351+P338
4,4-Azobis(4-cyancovaleric acid)	Danger	H242	P210, P234, P235, P240, P370+P378, P403
Benzo-12-crown-4	Warning	H315-H319	P264-P280-P302+P352+P332+P313+P362+P364-P305+P351+P338+P337+P313
Benzo-9-crown-3	No classification available.		
Bis-(2-chloroethyl)-ether	Danger	H226, H300+H310+H330, H351	P202, P210, P264, P280, P303+P361+P353, P304+P340+P310
Carbon disulfide	Danger	H225, H315, H319, H332, H361fd, H372	P202, P210, P303+P361+P353, P304+P340+P312, P305+P351+P338, P308+P313
Catechol	Danger	H301+H311, H315, H317, H318, H341, H350	P202, P261, P280, P301+P310, P302+P352+P312, P305+P351+P338
Chloroform-d_1	Danger	H302, H315, H319, H331, H336, H351, H361d, H372	P202, P301+P312, P302+P352, P304+P340+P311, P305+P351+P338, P308+P313

Continuation Table 2: Chemicals and their classification according to GHS.

Substance	Symbols	Hazard Statement	Precautionary Statement
12-Crown-4	Danger	H330	P260, P271, P284, P304+P340+P310, P403+P233, P405
15-Crown-5	Warning	H302	P301+P312+P330
4-Cyano-4-thioylthiopropylsulfanyl pentanoic acid	No classification available.		
Deuterium oxide	Not classified as hazardous according to CLP (Regulation (EC) 1272/2008).		
Dichloromethane	Danger	H315, H319, H336, H351	P202, P261, P264, P302+P352, P305+P351+P338, P308+P313
Diisopropyl azodicarboxylate	Danger	H315, H319, H335, H351, H373, H411	P202, P260, P273, P302+P352, P305+P351+P338, P308+P313
N,N'-Dimethylformamide	Danger	H226, H312+H332, H319, H360D	P210, P280, P303+P361+P353, P304+P340+P312, P305+P351+P338, P308+P313
1,4-Dioxane	Danger	H225, H319, H335, H350	P202, P210, P233, P240, P305+P351+P338, P308+P313
Ethyl acetate	Danger	H225, H319, H336	P210, P233, P240, P241, P242, P305+P351+P338
Fuchsin calcium salt	Not classified as hazardous according to CLP (Regulation (EC) 1272/2008).		
2,3,5,6,8,9-Hexahydrobenzo[*b*][1,4,7,10]tetraoxacyclododecine-12-carbaldehyde	No classification available.		
2,3,5,6,8,9-Hexahydrobenzo[*b*][1,4,7,10]-tetraoxacyclododecin-12-yl)methanol	No classification available.		
Hexamethylenetetramine	Danger	H228, H317	P210, P240, P241, P261, P280, P302+P352
Hydrochinone monomethyl ether	Warning	H302, H317, H319, H412	P261, P273, P280, P301+P312, P302+P352, P305+P351+P338

Continuation Table 2: Chemicals and their classification according to GHS.

Substance	Symbols	Hazard Statement	Precautionary Statement
2-(Hydroxymethyl)-12-crown-4	Warning	H315, H319, H335	P261, P264, P271, P280, P302+P352, P305+P351+P338
Lithium hydroxide	Danger	H302, H314	P260, P280, P301+P312, P303+P361+P353, P304+P340+P310, P305+P351+P338
Lithium-3,5-diiodosalycilic acid	Warning	H315, H319, H335	P261, P264, P271, P280, P302+P352, P305+P351+P338
Magnesium sulfate	Not classified as hazardous according to CLP (Regulation (EC) 1272/2008).		
Methacrylic acid	Danger	H302+H332, H311, H314, H335	P261, P280, P301+P312, P303+P361+P353, P304+P340+P310, P305+P351+P338
Methanol	Danger	H225, H301+H311+H331, H370	P210, P233, P280, P301+P310, P303+P361+P353, P304+P340+P311
n-Heptane	Danger	H225, H304, H315, H336, H410	P210, P233, P273, P301+P310, P303+P361+P353, P331
Potassium ethyl eosin	Not classified as hazardous according to CLP (Regulation (EC) 1272/2008).		
Potassium hydroxide	Danger	H290, H302, H314	P234, P260, P280, P301+P312, P303+P361+P353, P305+P351+P338
1-Propanethiol	Danger	H225, H302, H317, H410	P210, P233, P273, P280, P301+P312, P303+ P361+P353
Sodium bicarbonate	Not classified as hazardous according to CLP (Regulation (EC) 1272/2008).		
Sodium borohydride	Danger	H260, H301, H314, H360FD	P231+P232, P260, P280, P303+P361+P353, P304+P340+P310, P305+P351+P338
Sodium ethyl eosin	No classification available.		
Styrene	Danger	H226, H304, H315, H319, H332, H335, H361d, H372, H412	P210, P273, P301+P310, P303+P361+P353, P304+P340+P312, P331

Continuation Table 2: Chemicals and their classification according to GHS.

Substance	Symbols	Hazard Statement	Precautionary Statement
4-Tert-butylcatechol	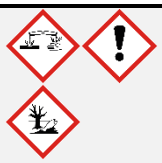 Danger	H302+H312, H314, H317, H410	P260, P273, P280, P301+P312, P303+P361+P353, P305+P351+P338
Tetrahydrofuran	Danger	H225, H302, H319, H335, H336, H351, EUH019	P202, P210, P233, P301+P312, P305+P351+P338, P308+P313
2,3,5,6-Tetrahydrobenzo[*b*][1,4,7] trioxonine-9-carbaldehyde	No classification available.		
2,3,5,6-Tetrahydrobenzo[*b*][1,4,7]-trioxonin-9-yl)methanol	No classification available.		
Tetrahydrofuran-d_8	Danger	H225, H302, H319, H335, H336, H351, EUH019	P202, P210, P233, P301+P312, P305+P351+P338, P308+P313
Trifluoroacetic acid	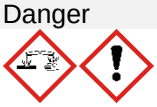 Danger	H314, H332, H412	P261, P273, P280, P303+P361+P353, P304+P340+P310, P305+P351+P338
Triphenylphospine	Danger	H302, H317, H318, H372	P260, P280, P301+P312, P302+P352, P305+P351+P338, P314
p-Toluenesulfonyl chloride	Danger	H290, H315, H317, H318	P280, P302+P352, P305+P351+P338 +P310

Table 3: CMR classification and amount of the substances used in this work.

Substance	CAS-Number	Category	Used Amounts
Catechol	120-80-9	C: 1B	460 g
1,2-Dibromoethan	106-93-4	C: 1B	1.6 g
1,2-Dichloroethan	107-06-2	C: 1B	1 g
N,N'-Dimethylformamide	68-12-2	R: 1B	2309 mL
1,4-Dioxane	123-91-1	C: 1B	290 mL
Sodium borohydride	16940-66-2	R: 1B	22 g

10. DANKSAGUNG

Als allererstes möchte ich Volker nicht nur für die Übernahme der Betreuung meines Promotionsvorhabens bei diesem spannenden Thema, einschließlich der Begutachtung meiner Arbeit sowie dem Beisitz bei meiner Disputation danken, sondern auch für die wunderbare Betreuung in den letzten 4 Jahren. Ich möchte dir danken, dass du wirklich immer ein offenes Ohr hattest, sei es fachlich oder persönlich. Dass du trotz deines wirklich vollen Terminkalenders stets Zeit für deine DoktorandInnen findest ist wirklich nicht selbstverständlich.

Ich danke Dr. Werner Pauer herzlich für das Zweitgutachten meiner Dissertation sowie Dr. Thomas Hackl und Dr. Christoph Wutz für die Bewertung meiner Disputation. Es freut mich sehr, dass Sie mich in dieser entscheidenden Phase begleiten.

Ich danke Prof. Dr. Carmen Herrmann für die angenehme und produktive Zusammenarbeit sowie ihrem Arbeitskreis für die Unterstützung bei DFT-Fragen – besonders Karen für ihre Hilfe bei fachlichen und technischen Anliegen. Birgit danke ich herzlich für ihren Beitrag zur zweiten Publikation, insbesondere für die Softwarebereitstellung und Unterstützung bei der Auswertung.

Ein herzlicher Dank gilt dem NMR-Service der Uni Hamburg, insbesondere Dr. Thomas Hackl für die stets hilfsbereite Unterstützung – vor allem bei der DOSY-Auswertung. Ebenso danke ich dem MS-, EA- und EM-Service für die zahlreichen Messungen und Beratungen, Andreas für die Hilfe bei den AFM-Messungen und Martin für die TGA-, DSC- und GPC-Messungen. Ein großes Dankeschön an die Mitarbeitenden des Hereon (Maryam, Joachim, Martin, Evgeni, Erik, Anke-Lisa, Kristian, Nico und Zhenzhen) für die Einarbeitung in die Methodik und eure Unterstützung bei Fragen. Marcel Schumacher und Prof. Dr. André Gröschel danke ich für die bereichernde Cubosome-Kooperation. Vielen Dank auch an Amrei, Gloria, Karen, Larissa, Patrick und Vincent fürs Korrekturlesen.

Einen ganz wesentlichen Beitrag zu meiner Promotion hat der AK Abetz geleistet – ein Arbeitskreis, dessen Gesichter sich über die Jahre zwar verändert haben, aber dessen Herz immer aus großartigen Menschen bestand und besteht: Amrei, Andja, Florian, Gloria, Iklima, Jingcong, Larissa, Maria, Martin, Marvin, Melle, Nils, Patrick, Philipp, Samar, Sascha, Siraphat und Tilman. Ihr habt diese Zeit für mich geprägt. Danke euch allen für die vielen gemeinsamen Momente, die Bier-Adventskalender, Dart-Spiele, AK-Feiern, die 6x6 Runden, Eispausen, das Lachen und die Unterstützung – es war wirklich eine tolle Zeit mit euch! Besonders danken möchte ich Iklima, von der ich das spannende Thema übernehmen durfte, die mich mit großer Offenheit, Geduld und praktischer Hilfe eingearbeitet hat und mit der ich mein erstes Paper veröffentlichen konnte.

Um den Li-Kreis zu schließen, möchte ich Amrei danken – nicht nur dafür, dass sie das Lithiumthema weiterführen wird (und ich bin überzeugt, dass sie das großartig machen wird), sondern vor allem für ihren Weg an meiner Seite. Vom Praktikum über die Masterarbeit bis zur Kollegin, Büropartnerin und Freundin. Du warst da. Mit Enthusiasmus, Neugier und deinem Humor. Du hast unser Thema mitgestaltet und mir jeden Morgen mit einem Lächeln den Start erleichtert. Danke dafür!

Auch möchte ich Gloria danken. Du warst nicht nur meine Bürokollegin, sondern auch eine echte Stütze im Alltag. Deine Ehrlichkeit, klar und direkt, aber immer mit Empathie, hat mir oft genau das gegeben, was ich gebraucht habe. Du hast mir immer zugehört, mitgedacht und

mit deiner Offenheit und Energie vieles leichter gemacht und mich oft auf den Boden zurückgeholt, wenn ich mich mal wieder in etwas reingesteigert habe. Deine positive Art hat mir immer ein Lächeln aufs Gesicht gezaubert. Danke, dass du da warst und bist – als Kollegin und als Freundin.

Dass Larissa damals für ihre Masterarbeit zu uns kam, war für mich ein Glücksfall – daraus ist eine Freundschaft entstanden, die mir wirklich am Herzen liegt. Danke für die tollen Gespräche und dein offenes Ohr. Ich bin froh, dass es dich gibt. Ein großes Danke auch an Philipp für die tolle Konferenz- und Reisebegleitung nach Kanada. Auch mit Maria verbinde ich viele schöne Erinnerungen. Die erste Zeit gemeinsam mit dir im Büro bedeutet mir sehr viel und ich bin froh, dass ich den gesamten Promotionsweg mit dir gemeinsam gehen durfte.

Ein großes Dankeschön an alle PraktikantInnen, Master- und Bachelor-Studierenden sowie SHKs: Amrei, Andja, Erika, Jette, Joachim, Joel, Larissa, Marc, Marten, Phil, René und Torben. Mit eurem Engagement, eurer Neugier und euren Fragen habt ihr meinen Alltag bereichert und wertvolle Beiträge zur Weiterentwicklung des Themas geleistet. Joachim hat mit seiner Bachelorarbeit den Grundstein für unsere gemeinsame Publikation gelegt, mit viel Eigenverantwortung und echtem Interesse. Besonders freut mich, dass Joachim, Larissa, Amrei und Andja inzwischen Teil des AKs sind. Es ist schön zu sehen, wie sich Wege weiterentwickeln und ein Teil davon sein zu dürfen.

Vielen Dank an meine Freunde und meine Familie, ganz besonders Jelena und Nele. Ihr habt euch immer alle meine Sorgen angehört, mir Ratschläge gegeben und wart unterstützend, auch wenn ich diese nicht befolgt habe. Ihr wart in dieser wirklich anstrengenden Zeit eine riesige Bereicherung für mein Leben und ich bin sehr dankbar, dass es euch gibt.

Ich hatte wirklich keine große Lust auf das PCP, aber es war der Anfang von etwas Unerwartetem und Wertvollem. So habe ich dich kennengelernt, Vincent. Danke, dass du da bist, mich unterstützt, mir Gelassenheit gibst, dir meine Vorträge tapfer zum zehnten Mal anhörst und mich auffängst, wenn der Weg mal zu holprig wird. Ich freue mich auf alles, was noch vor uns liegt.

Der größte Dank gilt jedoch meinen Eltern. Vielen Dank, dass ihr mich 22/7 so bedingungslos unterstützt habt – sei es finanziell oder emotional. Ihr standet immer hinter mir, egal ob ihr meine Entscheidungen nachvollziehen konntet oder nicht. Ihr wart mein fester Anker, wenn alles um mich herum in Bewegung war. Ich bin wirklich unendlich dankbar für euch.

Vielen Dank euch allen, dass ihr Teil dieses Weges wart!

11. EIDESSTATTLICHE VERSICHERUNG

Hiermit versichere ich an Eides statt, die vorliegende Dissertationsschrift selbst verfasst und keine anderen als die angegebenen Quellen und Hilfsmittel benutzt zu haben. Sofern im Zuge der Erstellung der vorliegenden Dissertationsschrift generative Künstliche Intelligenz (gKI) basierte elektronische Hilfsmittel verwendet wurden, versichere ich, dass meine eigene Leistung im Vordergrund stand und dass eine vollständige Dokumentation aller verwendeten Hilfsmittel gemäß der Guten wissenschaftlichen Praxis vorliegt. Ich trage die Verantwortung für eventuell durch die gKI generierte fehlerhafte oder verzerrte Inhalte, fehlerhafte Referenzen, Verstöße gegen das Datenschutz- und Urheberrecht oder Plagiate.

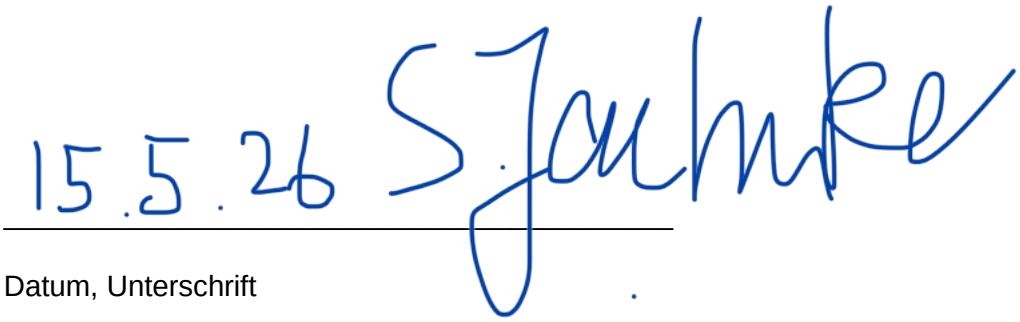

Datum, Unterschrift